TOPSIDE IONOSPHERE ELECTRON DENSITY CONCENTRATION:
OBSERVATION AND THEORY

by

Mao-Fou Wu

B.Sc., Chinese Naval College of Technology

(1955)

M.Sc., University of Chicago

(1965)

SUBMITTED IN PARTIAL FULFILLMENT

OF THE REQUIREMENTS FOR THE

DEGREE OF DOCTOR OF

PHILOSOPHY

at the

MASSACHUSETTS INSTITUTE OF TECHNOLOGY

October, 1969 i.e., 1970

Signature of Author ....

Department of Meteorology, October 27, 1969

Certified by ....

Thesis Supervisor

Accepted by ....

Chairman, Departmental Committee on Graduate Students

WITHDRAWN FROM MIT LIBRARIES
Lindgren
MASS. INST. TECH.
JUN 1 1970

TOPSIDE IONOSPHERE ELECTRON DENSITY CONCENTRATION: OBSERVATION AND THEORY

by

Mao-Fou Wu

Submitted to the Department of Meteorology on October 27, 1969 in partial fulfillment of the requirment for the degree of Doctor of Philosophy.

ABSTRACT

The ionospheric F-region is noted for its many anomalies, which may be defined as the departure in measured electron concentrations from the values predicted by straightforward application of Chapman layer theory. The anomalies have long been studied from ground based ionosonde data. In this study, three years of Alouette I satellite data on the topside ionosphere, between the F2 peak and 1000 km, have been analyzed. The equatorial anomaly and the seasonal anomaly appear clearly in the diagrams which show similar features to those observations from the bottomside ionosphere. In addition, an electron trough in the night time ionosphere has been verified as a permanent feature.

The three dimensional continuity equation of electron density has been solved numerically. The production rate and recombination coefficient are calculated based on Hinteregger's (1965) solar EUV flux as well as CIRA 1965, model 2 data. The results agree quite well with the observational data collected by the Alouette I satellite.

Rishbeth and Setty proposed in 1961 that the creation of the seasonal anomaly is due to the seasonal change of the neutral atmospheric compositions. This hypotheses has been confirmed through numerical calculations in this study. It is found that a fifty percent increase in atomic oxygen during winter and a fifty percent increase in oxygen and nitrogen molecules during summer are enough to make a clear appearance of the seasonal anomaly.

The theory of formation of the equatorial anomaly was reexamined. From Alouette I for 1963, we found that the equatorial anomaly makes its first appearance at about 11:00 local time. The time period of formation of the equatorial anomaly is on the order of 2 to 3 hours. Next, the plasma transportation time was calculated, and diagrams of the ionization flux were drawn. We confirmed that the plasma upward drift produced by the electric field is the most likely the physical cause of the equatorial anomaly. However, based on flux calculations, it is suggested that the plasma is likely to move directly toward the

maximum instead of via the 840 km height in the equatorial plane, as was thought by many workers.

The Muldrew trough is found to be a permanent feature of the ionosphere. The trough occurs under all magnetic conditions even when $K_p = 0$. The boundary of low plasma region matches Carpenter's "knee" quite well. It is believed that the escape of the charged particles from the ionospheric level to outer space along the open field lines could be the direct cause of this trough. The escape effect can reach to the region below 60° geomagnetic latitude through DP2 current system. In addition, the influence of electric drift produced by the electrojet as first proposed by Newell should also be considered during disturbed time. A nighttime source is definitely needed in the trough region. The solar wind and the precipitating electrons are the most likely nighttime energy sources.

The correlation coefficient between h_mF2 and the vertical transport velocity has been calculated. It is found that the up and down plasma motions should play an important role in altering the F2 peak height during storm time. Thus, a suggestion has been made that bodily motion is significant to the change of electron densities.

Thesis Supervisor: Reginald E. Newell

Title: Professor of Meteorology

ACKNOWLEDGEMENTS

I would like to express my gratitude to Professor R.E. Newell for his kind supply of the original Alouette I topside sounder data, and for his advice and encouragement throughout the course of this study. The writer is deeply indebted to Professor V.P. Starr for his interest and kind support. Professor N.A. Phillips helped to check equations, numerical method and made lots of valuable comments, Dr.A. Nishida read whole manuscript and made quite a few comments, Dr. D.F. Strobel discussed a part of the thesis thoroughly, and Dr. M.K. Mak assisted in computer programming. For this the author is very grateful.

The computational work was done on the IBM 360 at the M.I.T. computer center.

Mrs. Susan Nemeti helped with much of the data plotting, and Miss Isabel Kole drafted all of the diagrams, Miss Mary Bagarella punched cards and Mrs. Marie L. Gabbe typed the text. I wish to express my sincere thanks to all these people.

Finally, my thanks are due to my wife Julia for her patience and constant help.

This research was supported by the National Science Foundation under grant number GA-1310X, and by the U.S. Atomic Energy Commision under contract number AT(30-1) 2241.

TABLE OF CONTENTS

Acknowledgements 4

List of Figures 8

List of Tables 13

1. INTRODUCTION 14

    1.1. Data Sources 15

    1.2. Observation From Alouette I Satellite 18

    1.3. The Problems And My Approach 24

    1.4. Outline of Contents 24

2. DERIVATION OF EQUATIONS 43

    2.1. Basic Equations 43

    2.2. Assumptions 44

    2.3. Scale Analysis 45

    2.4. Derivation of Plasma Velocities 57

    2.5. Equation of Continuity For Electron 63

3. NUMERICAL SOLUTIONS 65

    3.1. Introduction 65

    3.2. Three-dimensional Model of Continuity Equation 66

    3.3. Numerical Scheme 72

    3.4. Boundary Conditions 72

    3.5. Computer Results 76

    3.6 Neutral Winds Effect 81

    3.7. Error Remarks 84

4. SEASONAL ANOMALY IN F REGION 102

4.1. Introduction 102

4.2. Current Theories 102

4.3. Observational Pictures From Satellite View 105

4.4. Possible Cause of Seasonal Anomaly 106

4.5. Conclusion 111

5. EQUATORIAL ANOMALY 127

5.1. Introduction 127

5.2. Satellite Picture of Equatorial Anomaly 128

5.3. Travel Time Calculation--Route 1 129

5.4. Questionable Argument On The Plasma Transportion Route 130

5.5. Proposed Transportation Process--Route 2 131

5.6. Vertical Profile View 132

5.7. Conclusion And Suggestion 133

6. ELECTRON TROUGH IN THE NIGHT IONOSPHERE 140

6.1. Introduction 140

6.2. General Features 140

6.3. K_p Effect 144

6.4. Current Theories 145

6.5. Possible Cause of The Trough 147

6.6. Electron Density Depletion Due To Electrojet 153

6.7. Energy And Flux 156

6.8. Seasonal Changes of The Trough 160

6.9. Conclusion 161

7. F2 PEAK HEIGHT AND VERTICAL TRANSPORT VELOCITY 166

7.1. Introduction 166

7.2. Observational Results of h_mF2 168

7.3. Vertical Transport Velocity 169

7.4. The Relation Between F2 Peak And The Vertical Transport Velocity 172

7.5. Conclusion And Discussion 174

8. SUMMARY AND CONCLUDING REMARKS 184

References 188

Appendix 198

Biographical Note 202

LIST OF FIGURES

1.1 Daytime meridional cross sections of the electron density from Alouette I topside sounder. 26

1.2. Daytime meridional cross sections of the electron density from Alouette I topside sounder 27

1.3 Daytime meridional cross sections of the electron density from Alouette I topside sounder 28

1.4 Daytime meridional cross sections of the electron density from Alouette I topside sounder 29

1.5 Daytime meridional cross sections of the electron density from Alouette I topside sounder 30

1.6 Daytime meridional cross sections of the electron density from Alouette I topside sounder 31

1.7 Nighttime meridional cross section of the electron density from Alouette I topside sounder 32

1.8 Nighttime meridional cross section of the electron density from Alouette I topside sounder 33

1.9 Nighttime meridional cross sections of the electron density from Alouette I topside sounder 34

1.10 Nighttime meridional cross sections of the electron density from Alouette I topside sounder 35

1.11 Nighttime meridional cross sections of the electron density from Alouette I topside sounder 36

1.12 Nighttime meridional cross sections of the electron density from Alouette I topside sounder 37

1.13 Nighttime meridional cross sections of the electron density from Alouette I topside sounder 38

1.14 Diurnal variations of equatorial anomaly in the months of January, February and March, 1963. 39

1.15 Diurnal variations of equatorial anomaly in the months of April, May and June, 1963. 40

1.16 Diurnal variations of equatorial anomaly in the months of July, August and September, 1963. 41

1.17 Diurnal variations of equatorial anomaly in the months of October, November and December, 1963 42

3.1 Meridional cross sections of electron density at 12 through 19 hours computed from equation of continuity 85

3.2 Meridional cross sections of electron density at 20 through 3 hours computed from equation of continuity 86

3.3 Meridional cross sections of electron density at 4 through 11 hours computed from equation of continuity 87

3.4 Diurnal variation of vertical electron density profiles at 5° latitude computed from equation of continuity 88

3.5 Diurnal variation of vertical electron density profiles at 40° latitude computed from equation of continuity 89

3.6 Diurnal variation of vertical electron density profiles at 75° latitude computed from equation of continuity 90

3.7 Diurnal variation of h_mF2 91

3.8 Diurnal variation of N_mF2 at 5°, 40° and 75° latitudes 92

3.9 World curves of N_mF2 at the equinox 93

3.10 Latitudinal variation of total electron content between 150 km and 1000 km heights 94

3.11 Latitudinal variation of total electron content between 150 km and 1000 km heights 95

3.12 Latitudinal variation of total electron content between 150 km and 1000 km heights 96

3.13 Latitudinal variation of total electron content between 150 km and 1000 km heights 97

3.14 Latitudinal variation of total electron content between 150 km and 1000 km heights 98

3.15 Latitudinal variation of total electron content between 150 km and 1000 km heights 99

3.16 Latitudinal variation of electron density at constant 100 heights at 12 and 2 HRS, with and without winds

3.17 N-h profiles at 12 HR for the cases of no wind, with drift, and winds 101

4.1 Latitudinal variation of N_mF2 from Alouette I in geographic latitude 113

4.2 Latitudinal variations of N_mF2 from Alouette I in dip latitude 114

4.3 Latitudinal variation of h_mF2 from Alouette I corresponding to N_mF2 in Fig. 4.1 115

4.4 N-h profiles from Alouette I in June and December 116

4.5 Latitudinal variation of total electron content computed from Alouette I data 117

4.6 Meridional cross section of electron density distribution for normal case computed from steady state equation of continuity 118

4.7 (a) Ratio of electron density between winter and summer for normal case; (b) N-h profile in the normal case 119

4.8 N-h profiles at 35° latitude (a) with downward wind (b) with meridional wind 120

4.9 Ratio of electron density between winter and summer (a) with downward wind (b) with northward wind 121

4.11 Ratio of electron density between winter and summer (a) $(O)_w/(O)_s = 1.8$ (b) $(O)_w/(O)_s = 1.4$ 122

4.12 Ratio of electron density between winter and summer 123
(a) $(O)_w/(O)_s = 1.4$; $(N_2+O_2)_s/(N_2+O_2)_w = 1.4$
(b) $(O)_w/(O)_s = 1.3$; $(N_2+O_2)_s/(N_2+O_2)_w = 1.3$

4.13 Ratio of electron density between winter and summer 124
(a) $(O)_w/(O)_s = 1.5$; $(N_2+O_2)_s/(N_2+O_2)_w = 1.5$
(b) $(O)_w/(O)_s = 2.0$; $(N_2+O_2)_s/(N_2+O_2)_w = 2.0$

4.14 N-h profiles at 35 ° latitude computed by adjusting O, N_2 and O_2 in winter and summer 125

4.15 N-h profiles at 35° latitude in winter and summer for different cases 126

5.1 Earth dipole field lines showing relative positions in the equatorial plane 134

5.2 Time charts for ionization loss and for transportation from different source levels to the various heights along 20 degree field line 135

5.3 (a) Mericional cross section of electron density distribution at 13 HR for stational atmosphere and without drift (b) Flux vectors 136

5.4 (a) Meridional cross section of electron density distribution at 13 HR, with meridional neutral winds and no drift (b) Flux vectors 137

5.5 (a) Merdional cross section of electron density distribution at 13 HR, with upward drift and no wind (b) Flux vectors 138

5.6 (a) Meridional cross section of electron density distribution at 13 HR, with downward drift and no wind (b) Flux vectors 139

6.1 Comparison between positions of the trough center and the Carpenter knee 162

6.2 (a) Equivalent current system of DP1 (b) Equivalent current system of DP2 163

6.3 Meridional cross sections of electron density at midnight (a) without drift (b) with E-S drift of ± 40 m/sec 164

6.4 Meridional cross sections of electron density at midnight (a) E-S drift of ±50 m/sec (b) with E-S drift of ±60 m/sec 165

7.1 Latitudinal variation of h_mF2 from Alouette I in March and June 176

7.2 Latitudinal variation of h_mF2 from Alouette I in September and December 177

7.3 Latitudinal variation of h_mF2 during quiet and storm times in March 178

7.4 Latitudinal variation of h_mF2 during quiet and storm times in September 179

7.5 Vertical transport velocity in March 180

7.6 Vertical transport velocity in June 181

7.7 Vertical transport velocity in September 182

7.8 Vertical transport velocity in December 183

LIST OF TABLES

2.1 Numerical values of various terms in the equations (2.9), (2.10) and (2.11) 53

2.2 Numerical values of various terms in the equations (2.13), (2.14) and (2.15) 54

6.1 Trough center positions, horizontal and vertical electron density gradients in different month and K_p from Alouette I 142

6.2 Position of trough in total electron content (after Liszka, 1967) 144

7.1 Correlation coefficient between h_mF2 and vertical transport velocity 173

CHAPTER 1

INTRODUCTION

Since rocket and satellite data became available, research on the ionosphere has come to a new era. The old method for exploring the ionospheric region is through radio-wave sounding conducted from the ground. The relationship between density and frequency can be expressed approximately by

$$N_e = 1.24 \times 10^4 f^2 \qquad (1.1)$$

where N_e = electrons/cm^3, and f = wave frequency in Mc/sec. If the ionosphere is horizontally stratified with N_e increasing upward, a plane wave propagated vertically will be reflected at an altitude where the equation (1.1) is satisfied. Based on this technique, the vertical electron density distribution up to the maximum in the ionized layer (which is the so-called F2 peak) can be measured. The electron concentration at the F2 peak is designated as N_mF2. The frequency corresponding to N_mF2 is called the "critical" or "penetration" frequency (denoted as f_oF2). When the wave frequency exceeds the critical frequency, it passes through the ionosphere without reflection. Consequently, the ground measurements only give the electron density distribution up to the F2 peak in the "bottomside" of the ionosphere and cannot provide any information above the F2 peak which is located at about 300 km. Since the total electron content in the topside ionosphere is about three times the content present in the bottomside, the electron density distribution above the F2 peak is very important in determining the behavior of the whole ionosphere. The topside sounders can thus supplement the ground measurements and provide a complete topside electron density profile up to the satellite. The first topside ionosphere probing was performed by the Alouette I satellite launched in 1962 followed by a second satellite, Explorer XX, in 1964. The satellite is the most powerful tool to study the physics of the ionosphere and has already provided immense amounts of information about the upper atmospheric conditions. Our knowledge concerning the topside ionosphere has thus been extended a great deal. While older problems such as the seasonal anomaly and the equatorial anomaly, are still in open debate, new interesting features have been discovered by satellites. For example, a nighttime electron trough in high latitudes was found by Muldrew in 1965 from an analysis of four months of Alouette I data. The physical causes of the various F region anomalies and features remain to be investigated, and this is the object of the present work.

1.1 Data sources

Vertical electron density profiles were collected by the Alouette I satellite for the period September 1962-March 1966. This satellite was launched from California on September 29, 1962 by the National Aeronautics and Space Administration of the USA. It is under the sponsorship of the NASA, the Defense Research Board of Canada (now the Communications Research Center) and the United

Kingdom. The satellite was injected into a near polar, 1000 km circular orbit, to measure the electron density distributions on the upper side of the ionosphere. The spatial coverage of the data is over North and South America, ranging from 40°W to 110°W, and from 80°N to 55°S (geographic location). There are 13 ground telemetry stations in different world-wide locations providing a necessary geographic coverage. The speed of the satellite is 27,500 km/hr, and the period of the satellite orbit is 105.5 minutes. The sweeping frequency is from 0.5 to 11.5 Mc/s in approximately 11 seconds. Since the apogee (1031 km) and the perigee (996 km) of this satellite are almost the same, it gives a good data sounding. The orbital plane rotates relative to the sun-earth line by 2 degrees per day. Thus, with south- and north-going passes, the diurnal variation of the ionosphere can be obtained in about 90 days. The magnetic dip angle, f_oF2 and the total number of electrons in a column one square centimeter in horizontal cross section extending from the satellite to the height of reflection corresponding to f_oF2 were also given in the 8 volumes of the Alouette I data books which were obtained from the Defense Research Board.

K_p indices, Zurich sunspot numbers and data on the principal magnetic storms were taken from the Journal of Geophysical Research (JGR) for the period of 1962-1966.

Solar extreme ultraviolet radiation (EUV) data were picked from Hinteregger's work (1965) in Space Research V.

Neutral atmospheric data came from CIRA (Cospar International reference Atmosphere) 1965.

Geomagnetic data were obtained from the Handbook of Geophysics and Space Environments published in 1965.

1.2. Observations from Alouette I satellite

1.2.1. The morphology of daytime and nighttime electron density distribution.

(a) Method of data processing.

Data are classified according to month. Daily measurements are further divided into four periods of time. They are: morning section (05:00 a.m. - 11:00 a.m.), daytime section (11:00 a.m. - 17:00 p.m.), evening section (17:00 p.m. - 21:00 p.m.), and nighttime section (21:00 p.m. - 05:00 a.m.). After that, further subgroup work was done based on K_p index. The next step is to take the average of those data belonging to the same category. Finally, those averaged values were plotted in the meridional plane at constant heights for each 100 km interval and at dip angle interval of 10 degrees. Isopleth were drawn on each graph. It is noted that the data are scattered over the North and South American continents. The average taken is based on the magnetic dip and the longitudinal difference is ignored.

(b) Daytime ionosphere: The average daytime electron density distributions for each month and different K_p indices are shown in Figs. 1.1-1.6. In these time sections, the electron density distributions are characterized by smooth and gradual variations at all latitudes and altitudes. Two peaks of high electron concentration are shown clearly at about 17 degrees both north and south of the dip equator during equinox season. These were discovered from bottomside measurements and are termed the equatorial anomaly. The heights of the maxima are at about 300 km. A minimum electron density can be seen over the dip equator from 300 km to about 600 km height. The distributions of electron density are under solar and geomagnetic control, as can be seen from the field-alignment of electron concentrations (see for example the detail profiles by King et al., 1964) as well as the sunward shifting of the maximum electron density positions in the high altitudes. Small peaks appear quite often in the high latitudes above 75°N and 50°S dip during disturbed days ($K_p \geq 4$).

In the months of June and August, the average daytime electron densities are asymmetric with respect to the dip equator. The maximum electron density is larger and more pronounced in the summer (northern) hemisphere than in the winter (southern) hemisphere. This is consistent with the subsolar point. Below 400 km, geomagnetic control is strong, whereas at higher altitudes, the equatorial anomaly is not obvious, and solar control gradually exerts a stronger influence. This is illustrated by the sunward movement of the electron density maximum from dip latitude of 17°N at 400 km to the dip latitude of 30°N at 1000 km in Fig. 1.3A.

During the months of November and December, the daytime electron densities are nearly symmetric with respect to the dip equator. The maximum electron densities at high altitudes are located just a few degrees south of the dip equator. This is because that the subsolar positions along the 75°W meridian during these months are between 3°S and 10°S dip latitudes.

During the equinox seasons, the daytime electron densities are larger in the northern hemisphere than in the southern hemisphere.

The Equatorial Anomaly is not symmetric with respect to the dip equator, because the subsolar positions are between 4°N and 21°N dip latitudes. Again, solar control is very apparent. This can be seen in the month of September in Fig. 1.4 and Fig. 1.5.

(c) Nighttime ionosphere: The average nighttime electron density distributions for each month and different K_p indices are shown in Figs. 1.7-1.13. In this period of time, the electron density distributions are characterized by more wave-like structure. Geomagnetic control is weak. Two relative maximum electron densities are still seen at approximately the same places as during the daytime, although they are not clear. The latitudinal gradients are larger comparing with the daytime values. A relatively low electron density region (often termed a trough and sometimes Muldrew's trough after its discoverer) is located at about 74°N dip latitude and is clearly seen for all K_p indices. At latitudes higher above the trough location, the density always increases for all seasons and all magnetic conditions.

During the months of November and December, electron densities are greater in the Southern Hemisphere than in the Northern Hemisphere. It is interesting to note that above about 40°S dip, the nighttime electron densities are greater than the daytime values at the same height levels. This diurnal anomalous behavior was found long ago from bottomside ionospheric data (Rastogi, 1960; Sato and Rourke, 1964). The horizontal density gradient is smaller in low latitudes, but very large in the high latitudes. A special feature should be noticed in these months, namely that the isopleths are sloped in one direction from the Southern Hemisphere down to the Northern Hemisphere. Therefore, densities tend to decrease all the way from Southern Hemisphere to the Northern Hemisphere. The exception is the peak occurring at about 50°N dip latitude in the month of December.

In the month of June, the slope of the equi-density line is reverse in direction such that the greater electron densities are present in the Northern Hemisphere. The trough in the Northern Hemisphere disappears below the height of 500 km for K_p = 1 and 2. However, in the Southern Hemisphere, the trough does exist (see Fig. 1.9b,c). Isopleths show more wavelike structures.

In the equinox season, the nighttime electron densities are nearly symmetric with respect to the dip equator. Under quiet magnetic conditions, the isopleths of electron density are almost horizontal; while under storm times, alternate crests and troughs are prominent.

1.2.2. Diurnal variations of Equatorial Anomaly

(a) Method of data processing

Because of the period of satellite procession, it needs about three months to deduce a complete diurnal picture of electron density distribution. However, it is believed that the seasonal effect is not serious (King et al., 1964), therefore, even though the data on successive local times were obtained on different days within three months period, yet they still can give a good feature of the diurnal variations. Based on this hypothesis, we took the entire 1963 year data, and divided them into four periods, e.g. January-March, April-June, July-September and October-December. Furthermore, since our interest is to see the electron density distributions around equatorial area; therefore, the latitudinal coverage of data analyses is within 40° north and south of the dip equator. The isopleths of constant electron density were drawn in the rectangular coordinates in which the ordinate represent the height above the earth surface and the abscissa represent the dip latitude. The dates, K_p index, local time range and the longitudinal range are denoted on each diagram. Four diurnal pictures of the electron density distributions are shown in Figs. 1.14-1.17.

(b) Descriptions of the diagrams

Fig. 1.14 shows the diurnal variations of the equatorial anomaly for the period from January through March. Before 10 o'clock in the morning, the shape of the contour is dome-like and extends up to the satellite height at 1000 km. The feature of these contours is that of a single maximum centered on the magnetic equator, there is no anomaly. About 11:00 local time, two maxima of electron density start to occur below the height of about 600 km. They are located at about 12-15° on either side of the dip equator. At this moment, however, the contours above 600 km height still remain dome-like structure. As time goes on, the equatorial anomaly widens and the electron densities at the two maxima increase until about 14:00 local time. At this hour, the two maxima shift to about 20 degrees north and south dip latitudes. The contours above 600 km height have also become flat. The equatorial anomaly lasts until 18:00 local time, and then start to decay.

Fig. 1.15 shows the diurnal variations of the equatorial anomaly for the months of April, May and June. In this period of time, the equatorial anomaly also starts to appear at about 11:00 local time. However, this time it lasts until mid-night and then gradually disappears.

Fig. 1.16 shows the diurnal variations of the equatorial anomaly for the months from July to September. Still, it appears at almost the same time as before. The big difference is that the locations of the two maxima are situated further away from the dip equator. They are at about 25 to 30 degrees dip latitudes, and are asymmetric with respect to the dip equator. The maxima are more pronounced in the northern magnetic hemisphere which is in summer at this time. The equatorial anomaly begins to decay at about 22:00 local time.

Fig. 1.17 shows the diurnal variations of the equatorial anomaly for the months of October, November and December. The first appearance of the equatorial anomaly is still at about 11:00 local time. The locations of the two maxima are at about 13° on either side of the equator at first, later they move to about 20° north and south at about 14:00 local time and stay there for about two hours and after that they shift back to the original places. The decay epoch begins at about 23:00 local time. The maximum density in the southern magnetic hemisphere is larger than that in the northern hemisphere.

1.2.3. Seasonal difference of N_mF2

Fig. 4.1 shows the latitudinal variations of N_mF2 (maximum electron concentration at the F2 peak) both in summer and in winter. It is clearly seen that the F2 peak electron density is larger in winter than in summer around noon hour in the latitude range of 32°-62°N. This difference has traditionally been termed the seasonal anomaly. Fig. 4.4 shows the N-h profiles at 35° and 40°N geographic latitudes. The detailed descriptions are given in Section 4.3.

1.3. The problems and my approach

The F region seasonal anomaly, the equatorial anomaly and the Muldrew trough are the main problems in this study. In the first part of my approach an effort is made to present a topside view of these problems through extensive data analyses. The purpose is to show both spatial and temporal variations in different seasons, local time and under different geomagnetic conditions in order to confirm whether these problems are permanent or temporal in nature. Then, possible physical causes are proposed through data analyses as well as theoretical calculations. All physical quantities such as solar EUV flux, neutral atmospheric structure etc. in the model were chosen within the same period of year as the satellite data were collected, so that the comparison between the computed results and the observational facts can be made under reasonable and similar conditions.

1.4. Outline of contents

Chapter 1 gives the data sources and points out the problems. Chapter 2 shows the whole derivation of the equations. Chapter 3 presents numerical solutions of the model. Chapters 4, 5, 6 are the main part which investigate the physical causes of the seasonal anomaly, equatorial anomaly and the nighttime electron trough respectively.

The final chapter deals with the F2 peak height and its relationship to the vertical transport velocity.

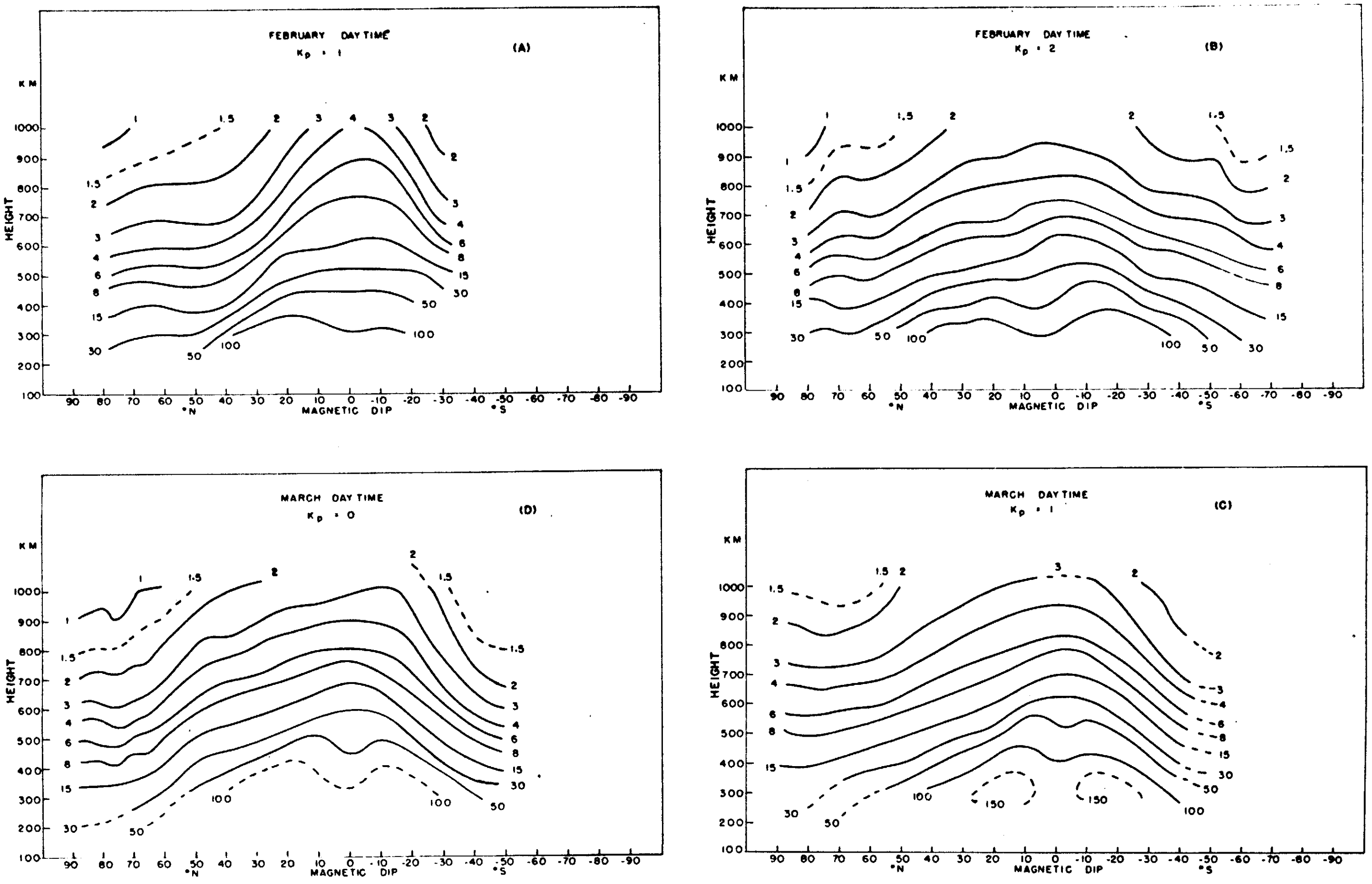

Fig. 1.1. Daytime meridional cross sections of the electron density from Alouette I topside sounder. Units: 10^4 el/cm^3.

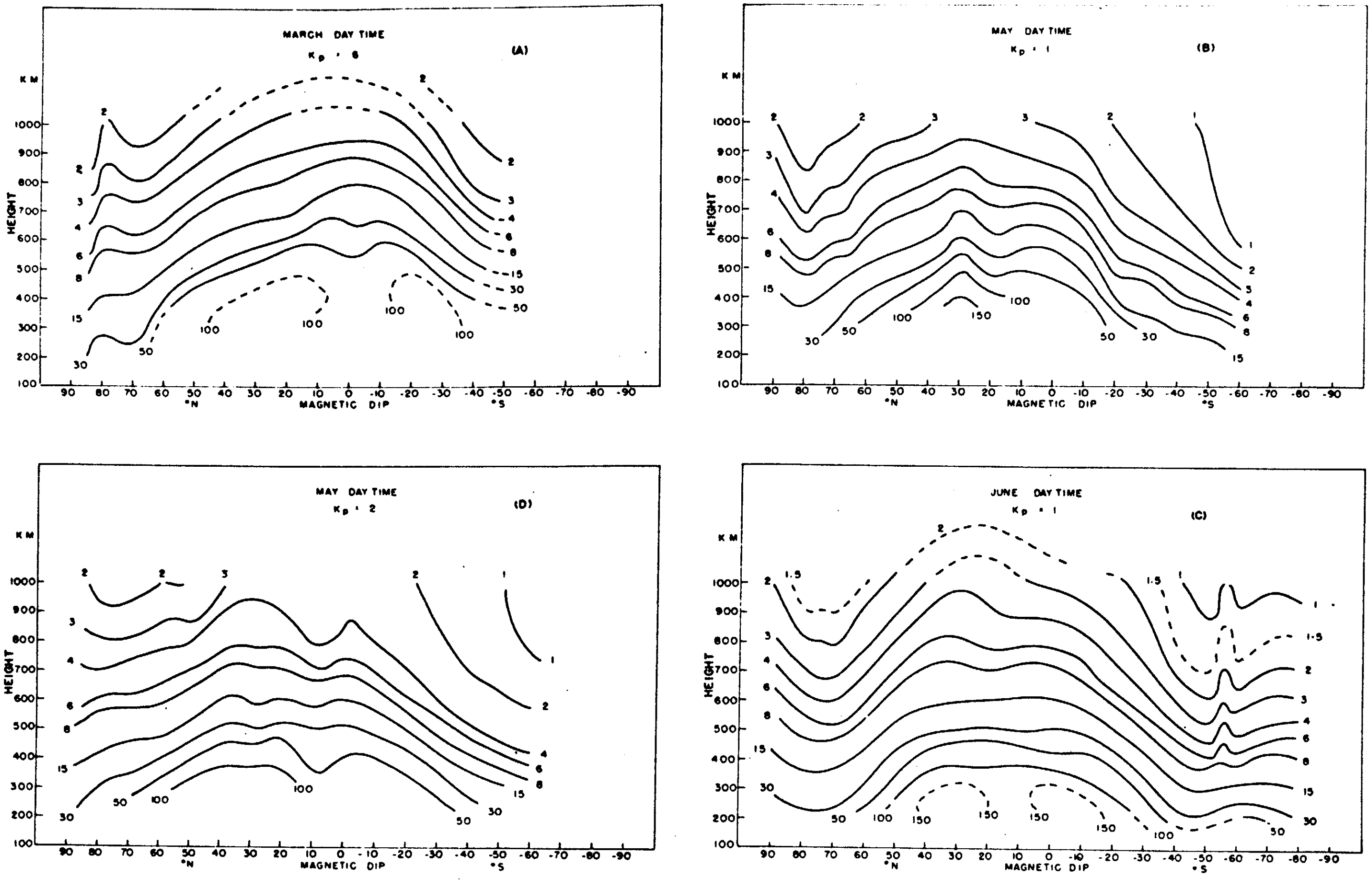

Fig. 1.2. Daytime meridional cross sections of the electron density from Alouette I topside sounder. Units: 10^4 el/cm^3.

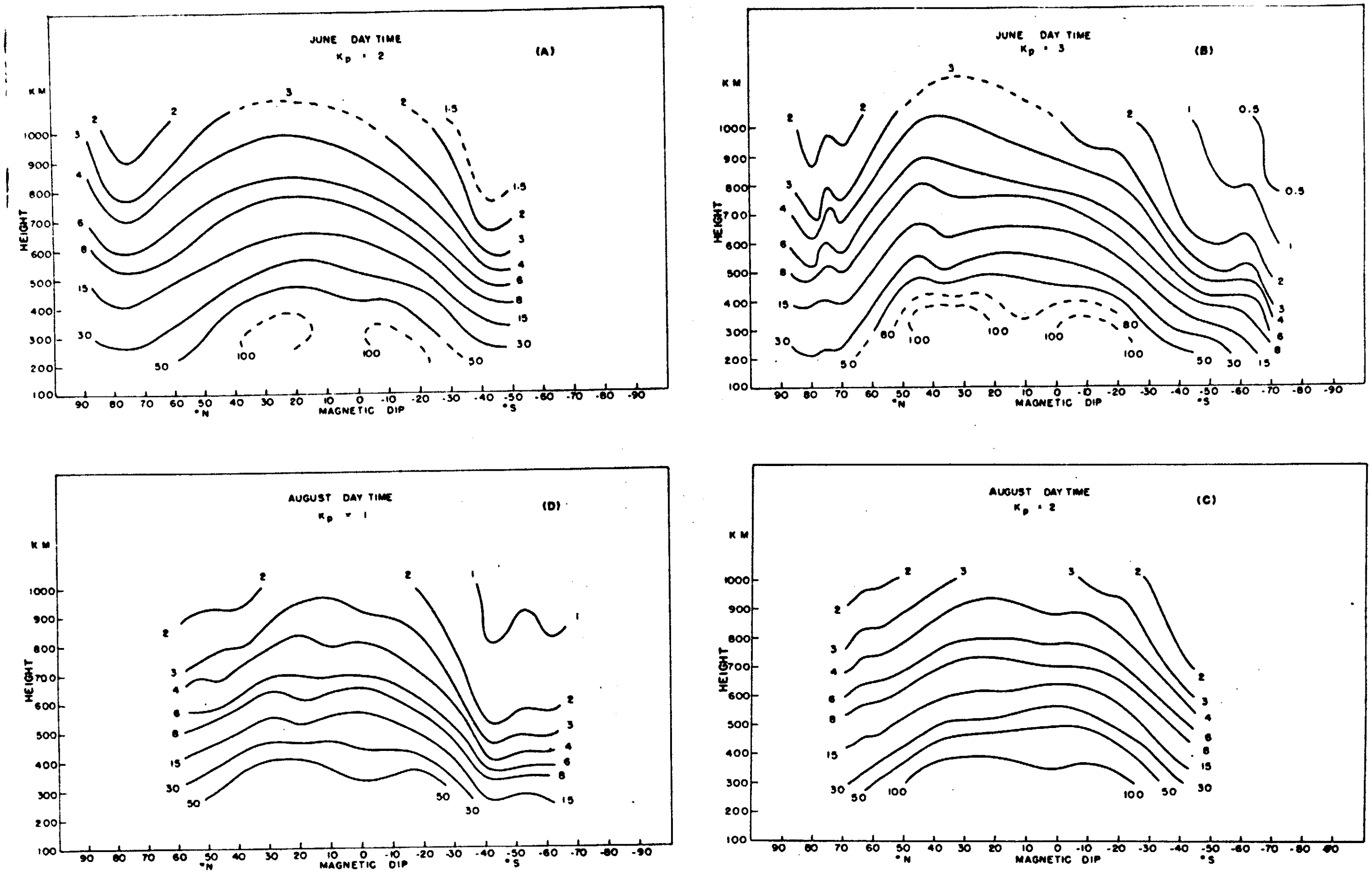

Fig. 1.3. Daytime meridional cross sections of the electron density from Alouette I topside sounder. Units: 10^4 el/cm^3.

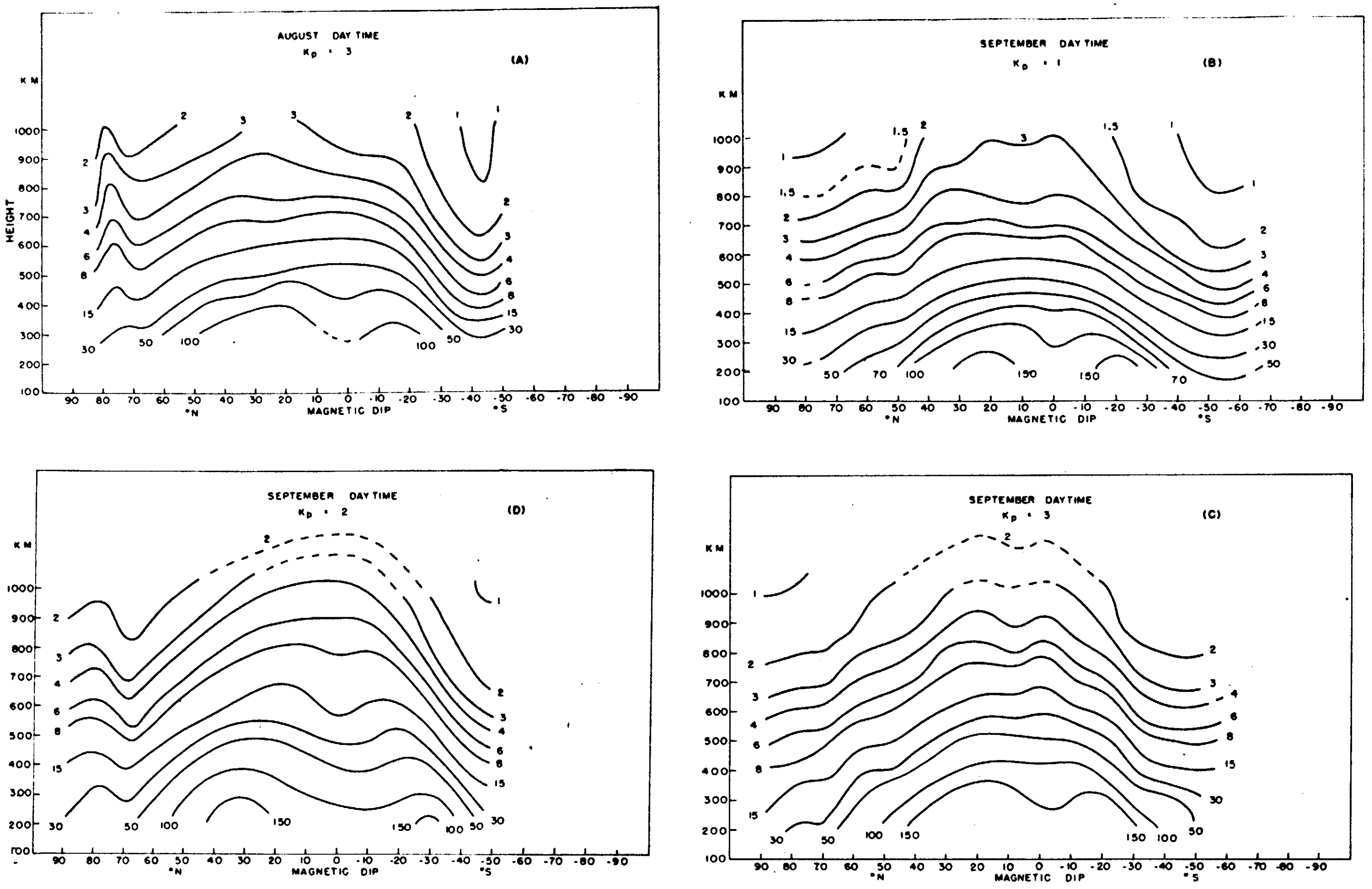

Fig. 1.4. Daytime meridional cross sections of the electron density from Alouette I topside sounder. Units: 10^4 el/cm^3.

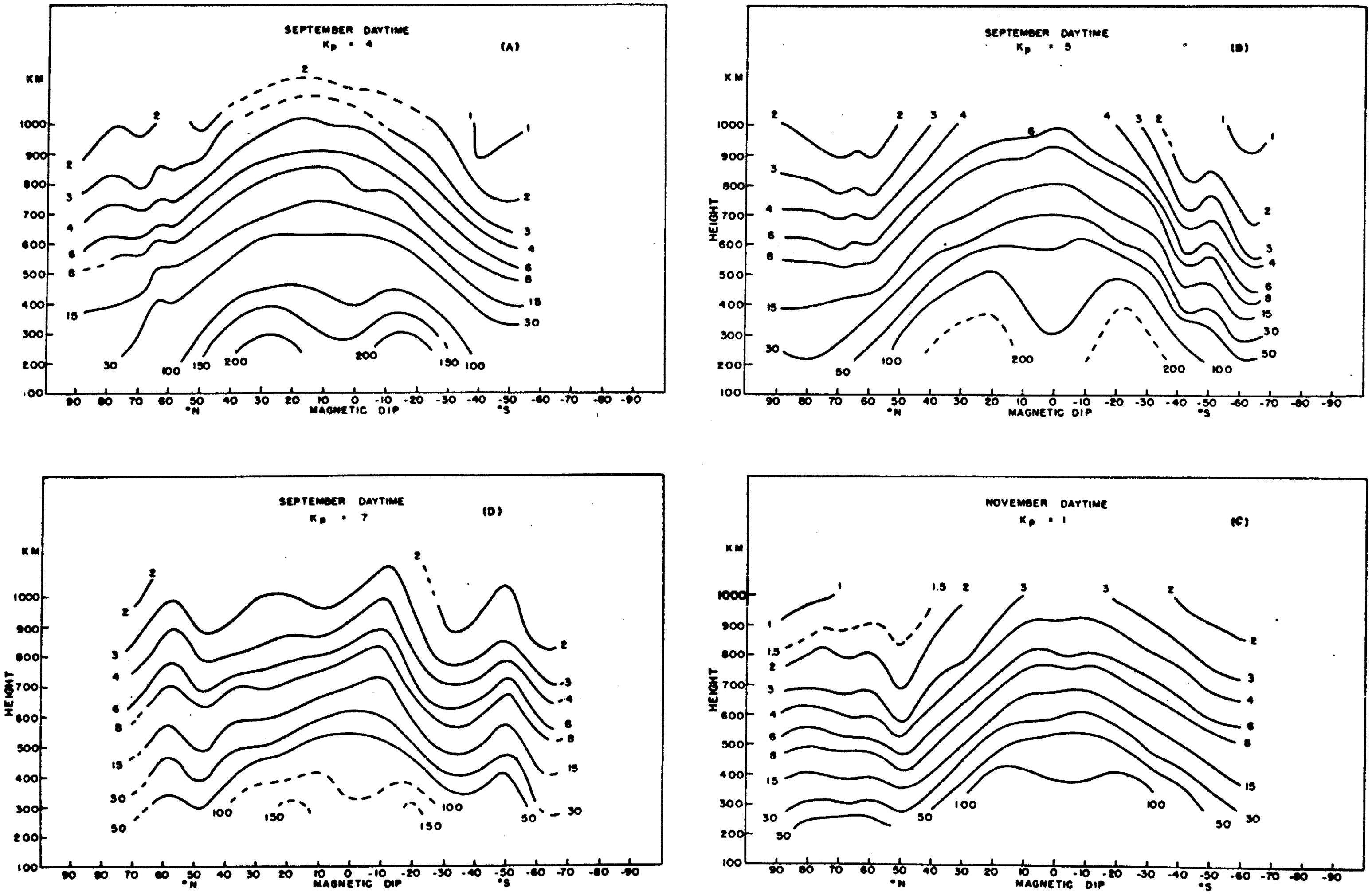

Fig. 1.5. Daytime meridional cross sections of the electron sounder. Units: 10^4 el/cm^3.

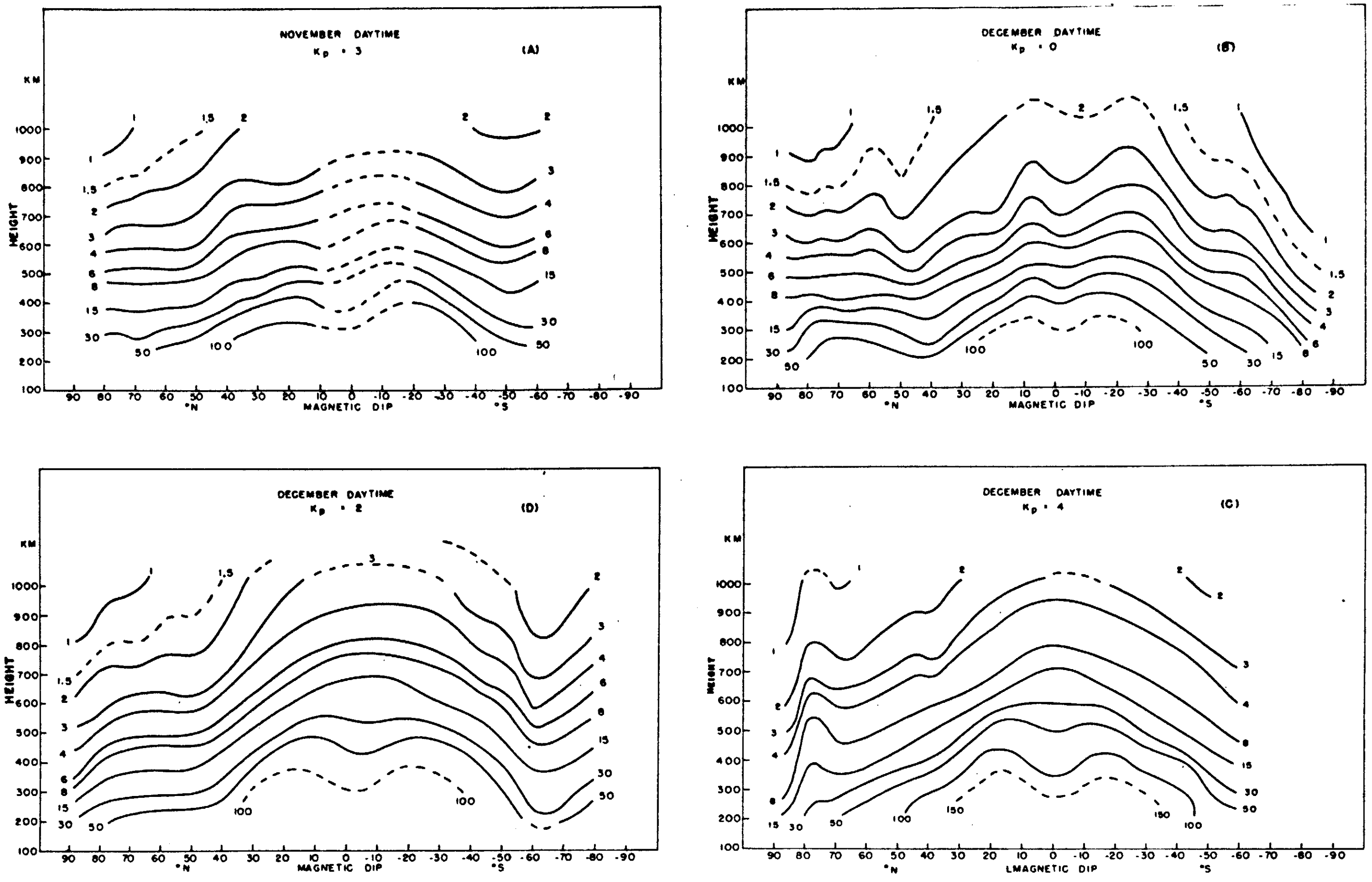

Fig. 1.3. Daytime meridional cross sections of the electron density from Alouette I topeside sounder. Units: 10^4 el/cm^3.

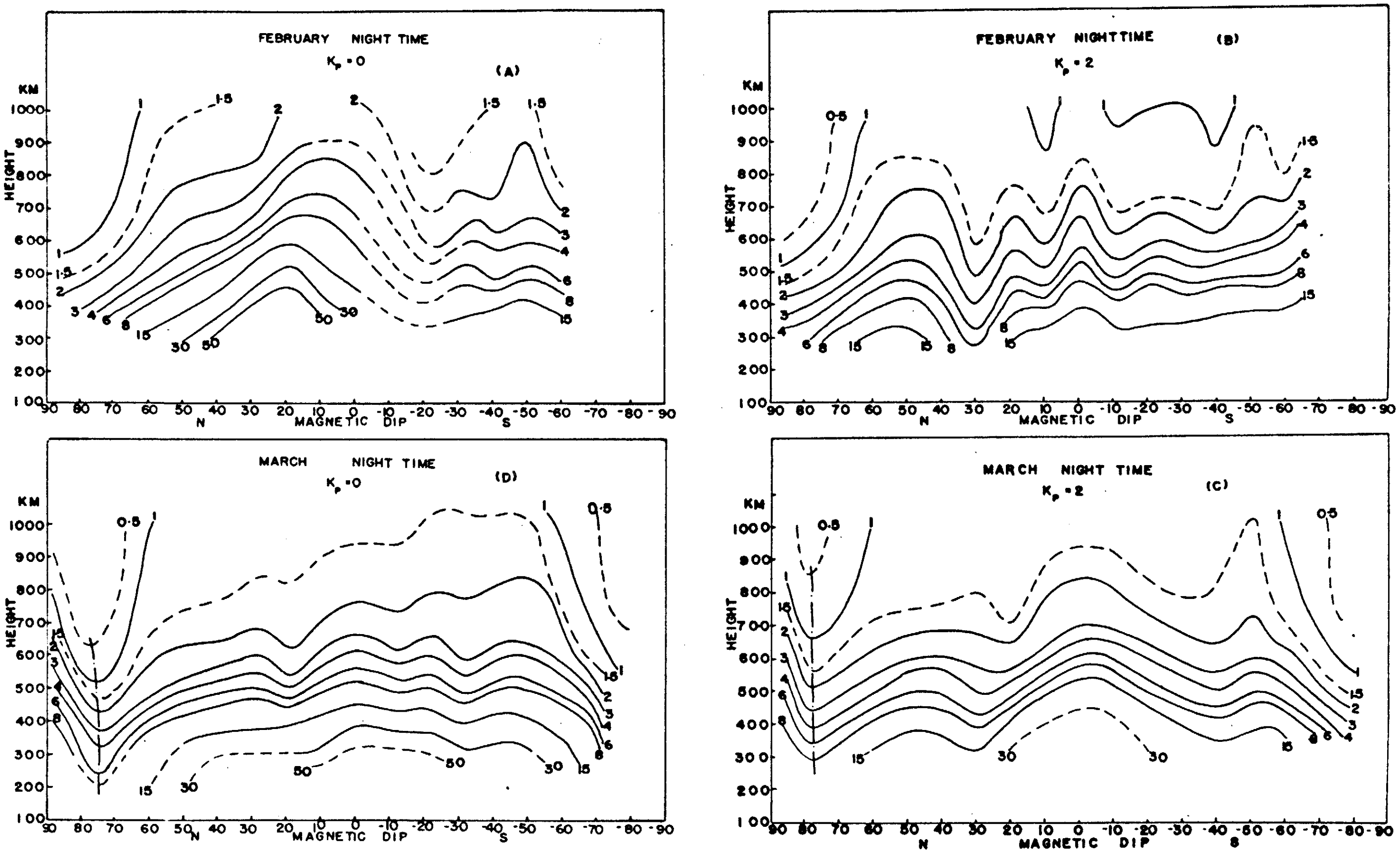

Fig. 1.7. Nighttime meridional cross section of the electron density from Alouette I topside sounder. Units: 10^4 el/cm^3.

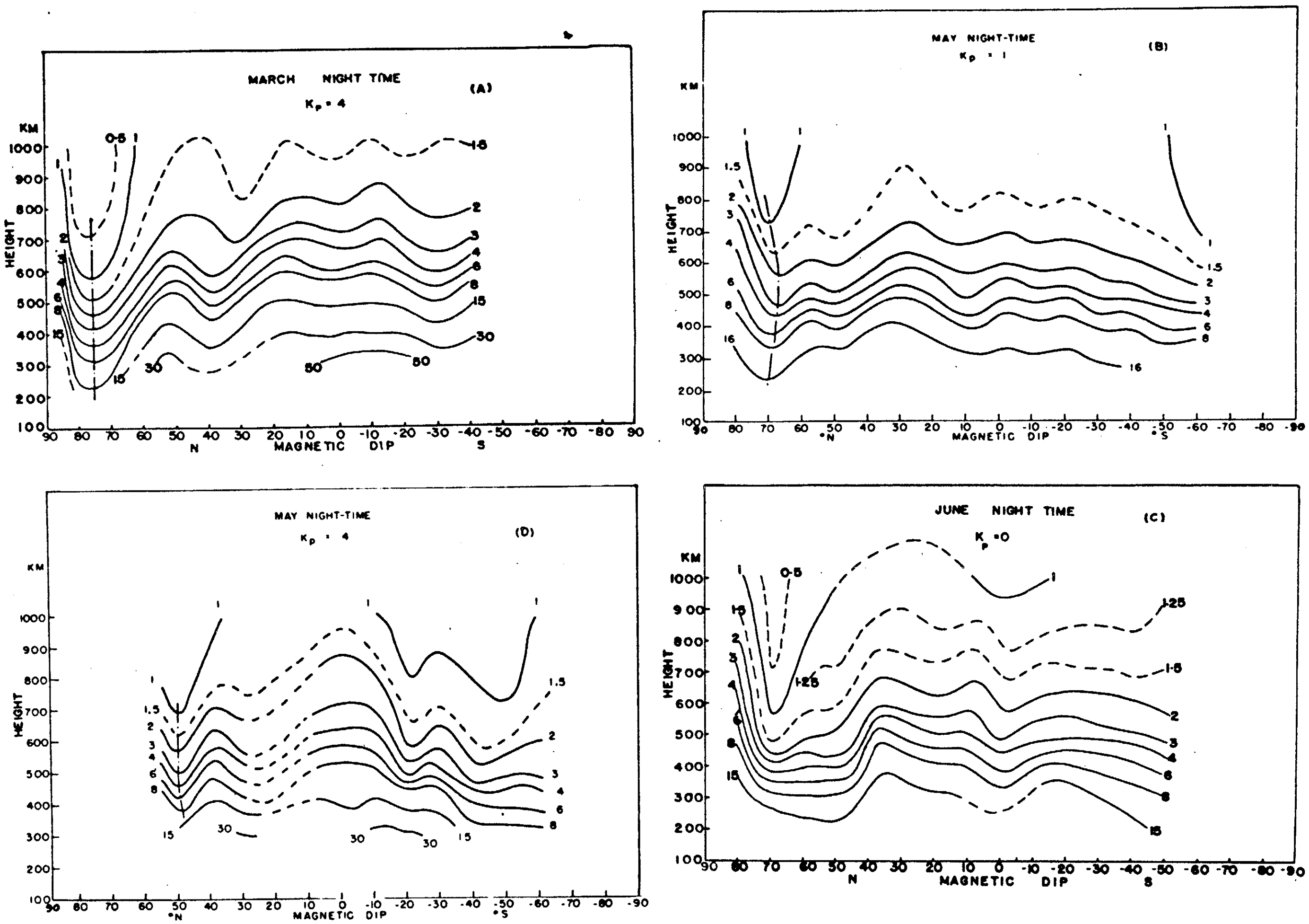

Fig. 1.8. Nighttime meridional cross section of the electron density for Alouette I topside sounder. Units: 10^4 el/cm^3.

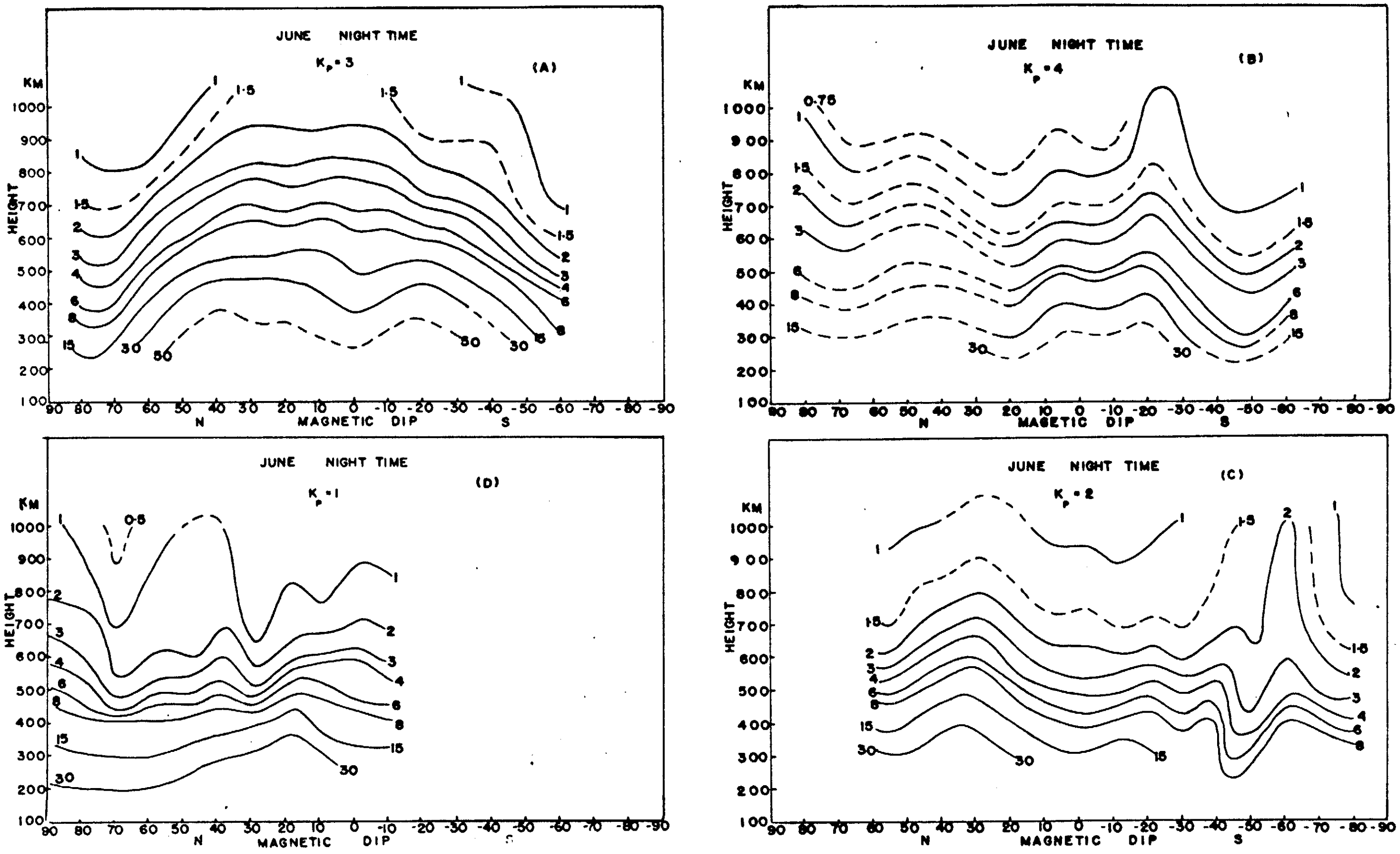

Fig. 1.9. Nighttime meridional cross section of the electron density from Alouette I topside sounder. Units: 10^4 el/cm^3.

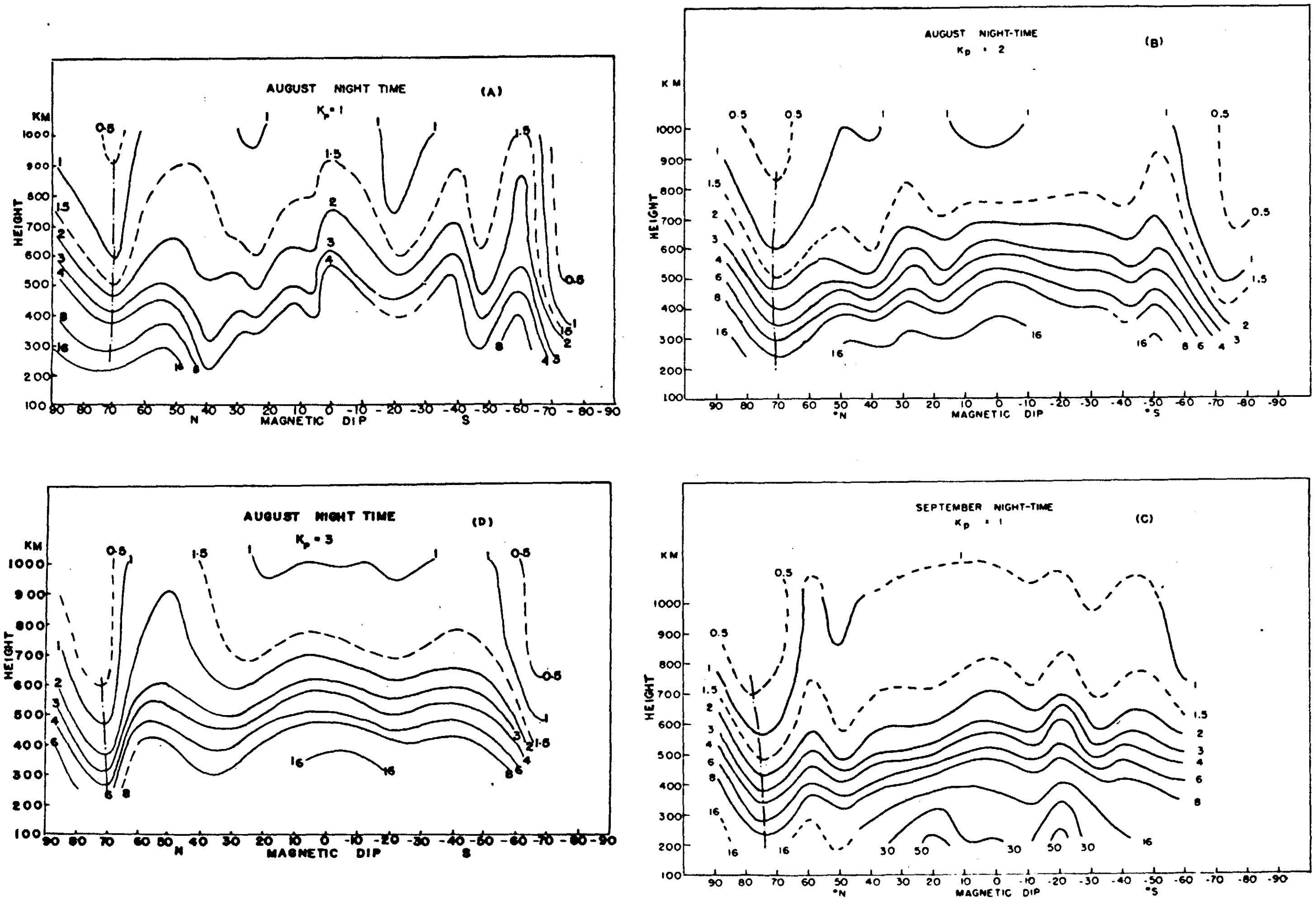

Fig. 1.10. Nighttime meridional cross section of the electron density from Alouette I topside sounder. Units: 10^4 el/cm^3.

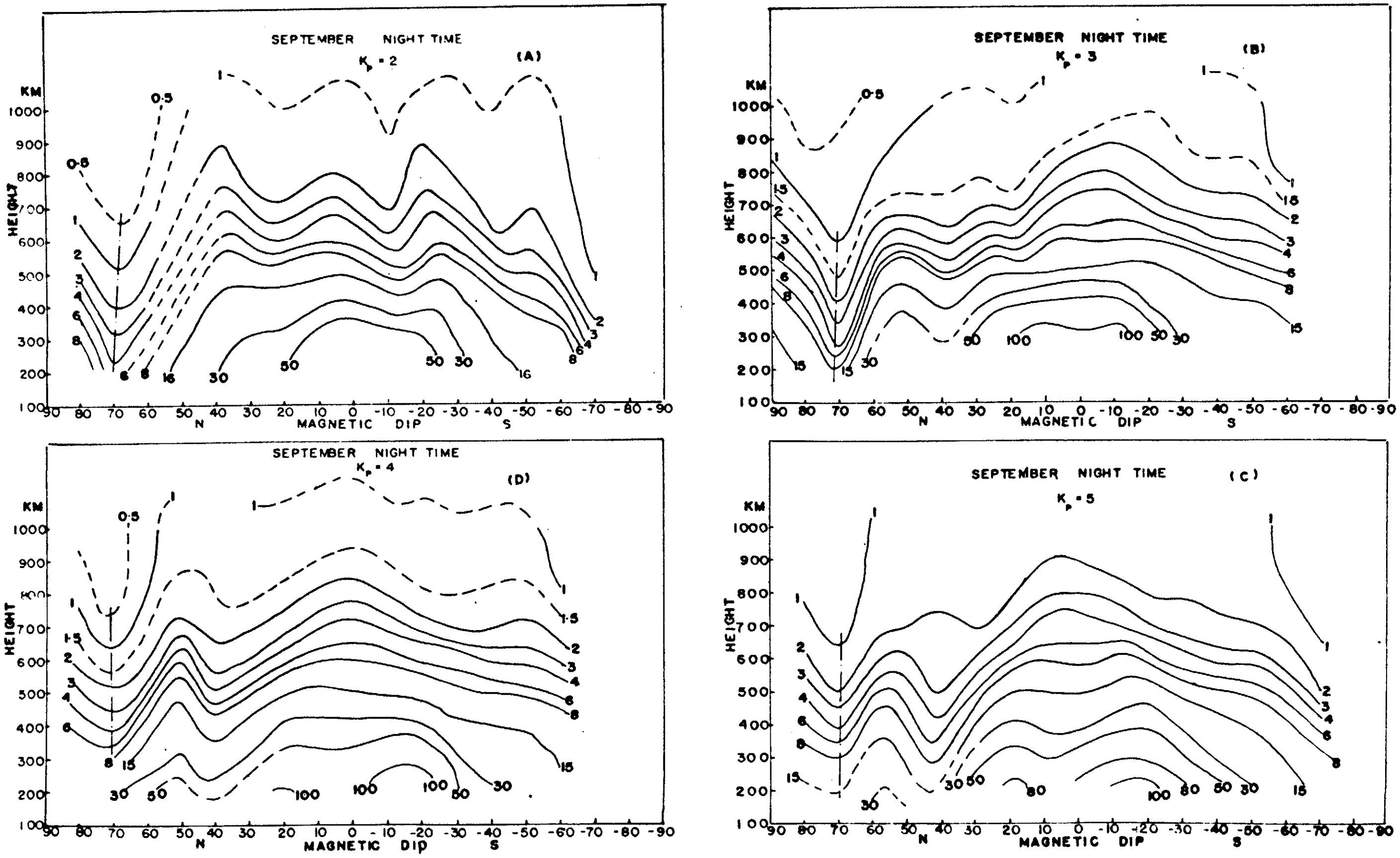

Fig. 1.11. Nighttime meridional cross section of the electron density from Alouette I topside sounder. Units: 10^4 el/cm^3.

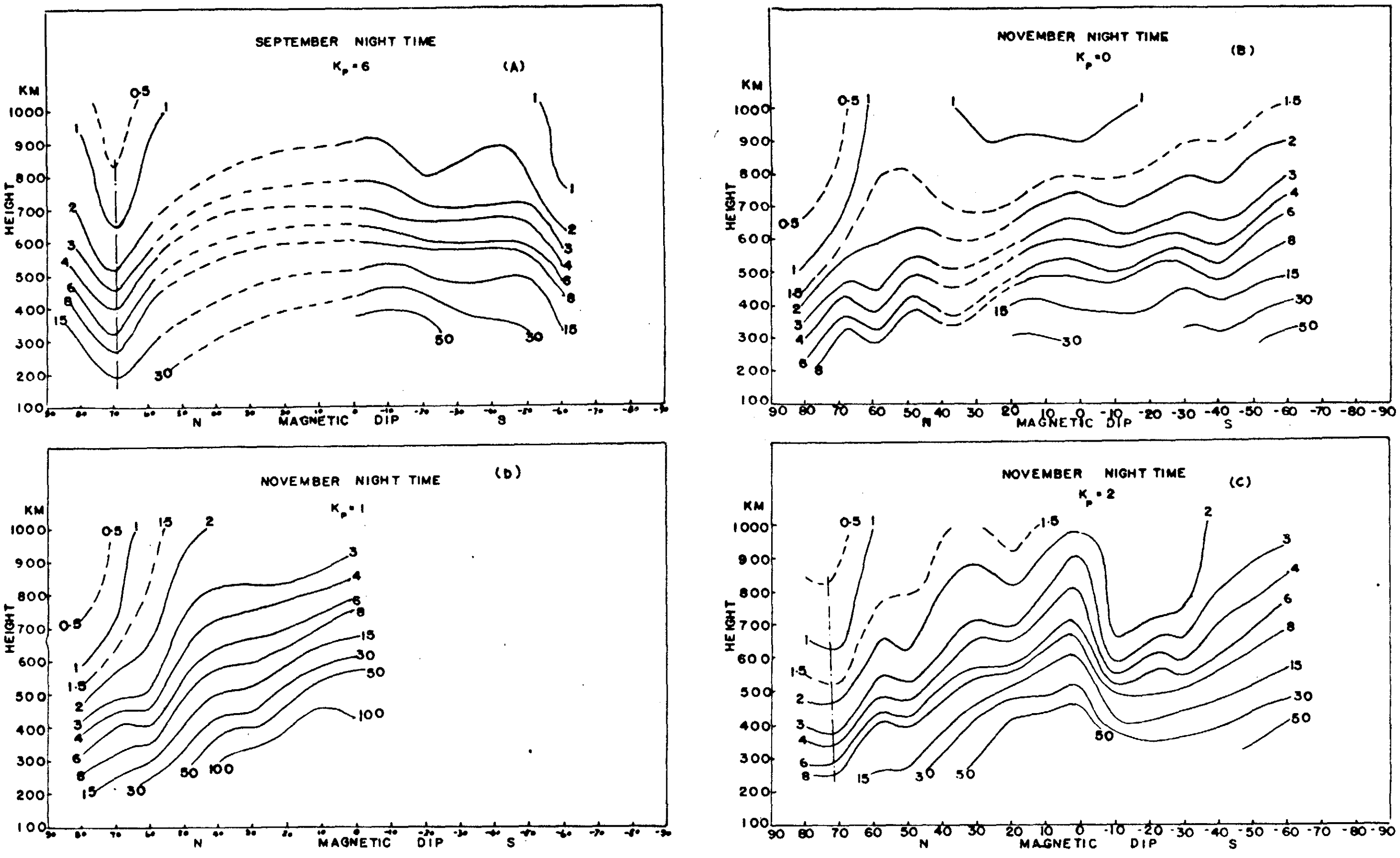

Fig. 1.12. Nighttime meridional cross section of the electron density from Alouette I topside sounder. Units: 10^4 el/cm^3.

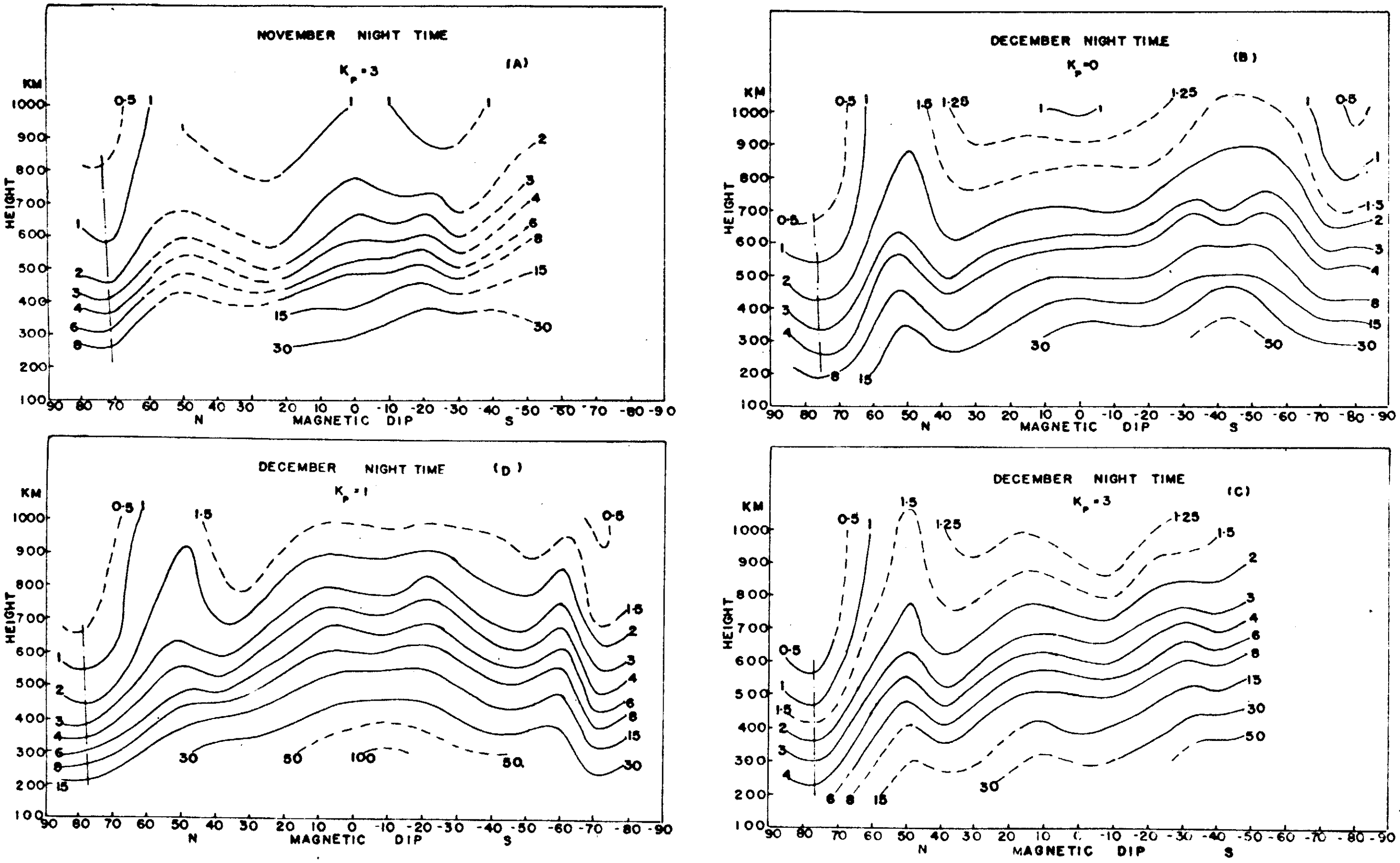

Fig. 1.13 Nighttime meridional cross section of the electron density from Alouette I topside sounder. Units: 10^4 el/cm^3.

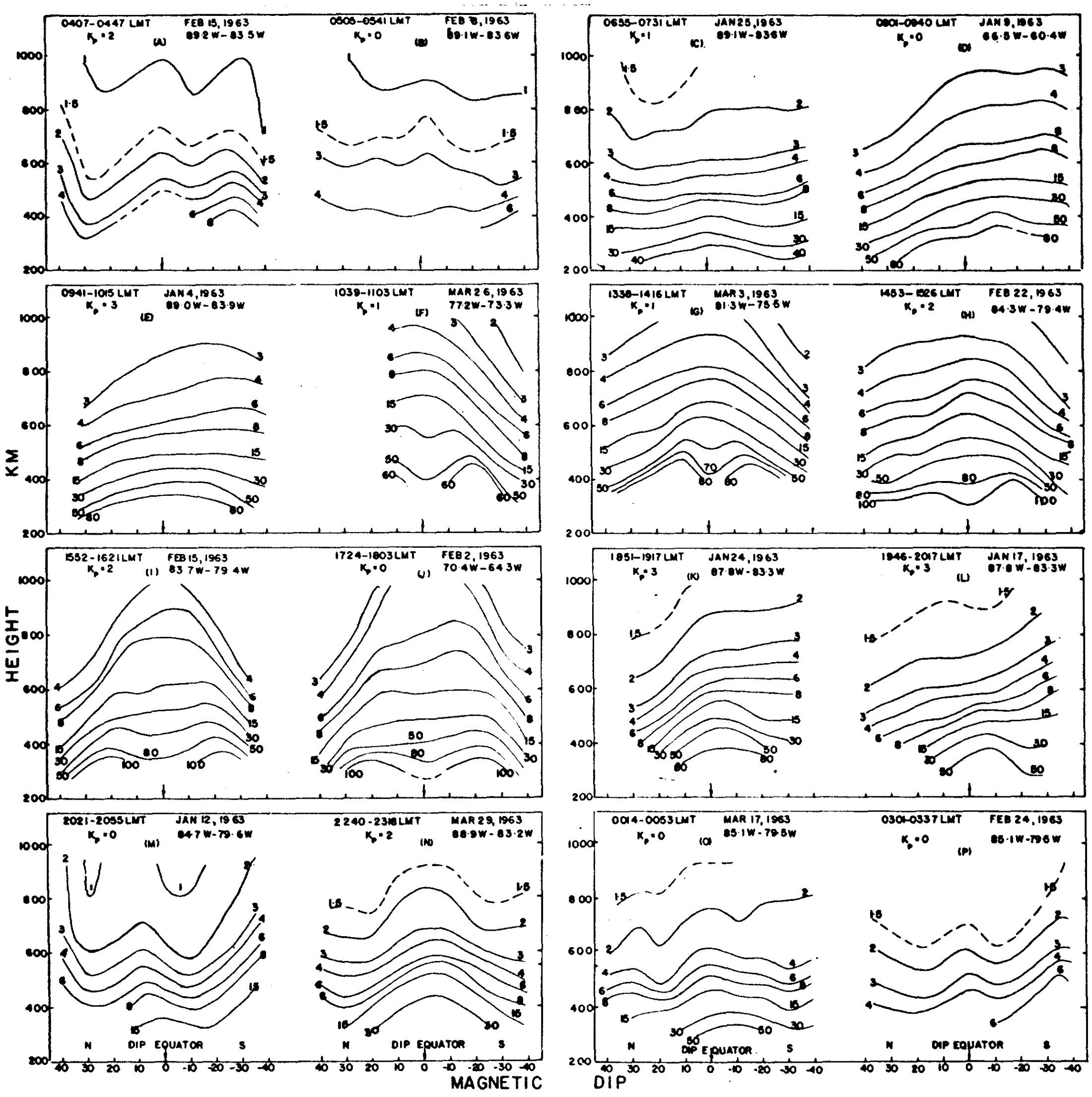

Fig. 1.14. Diurnal variations of equatorial anomaly in the months of January, February and March, 1963. The arrows denote the dip equators. Units: 10^4 el/cm^3.

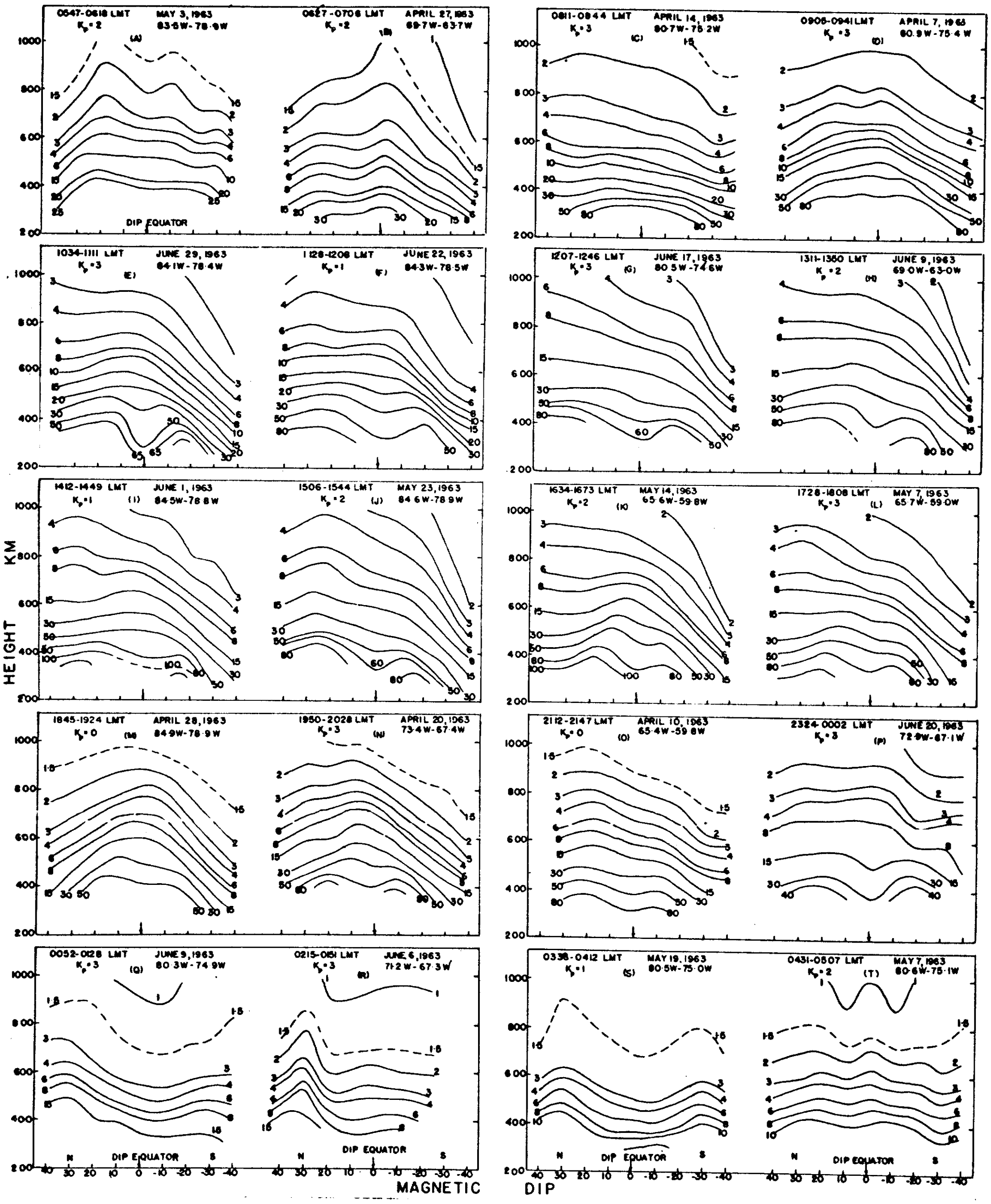

Fig. 1.15. Diurnal variations of equatorial anomaly in the months of April, May and June, 1963. The arrows denote the dip equators. Units: 10^4 el/cm^3.

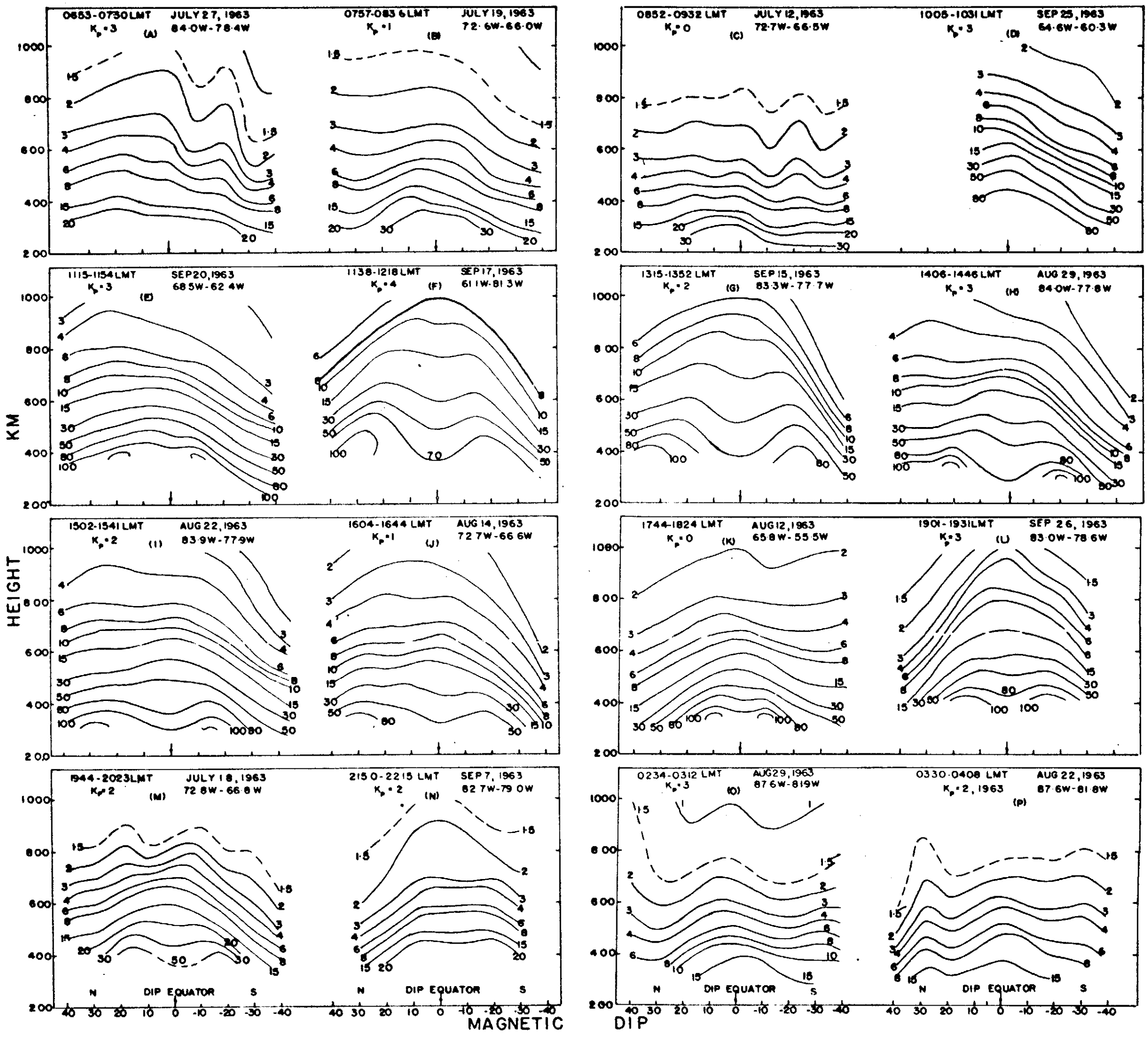

Fig. 1.16. Diurnal variations of equatorial anomaly in the months of July, August and September, 1963. The arrows denote the dip equators. Units: 10^4 el/cm^3.

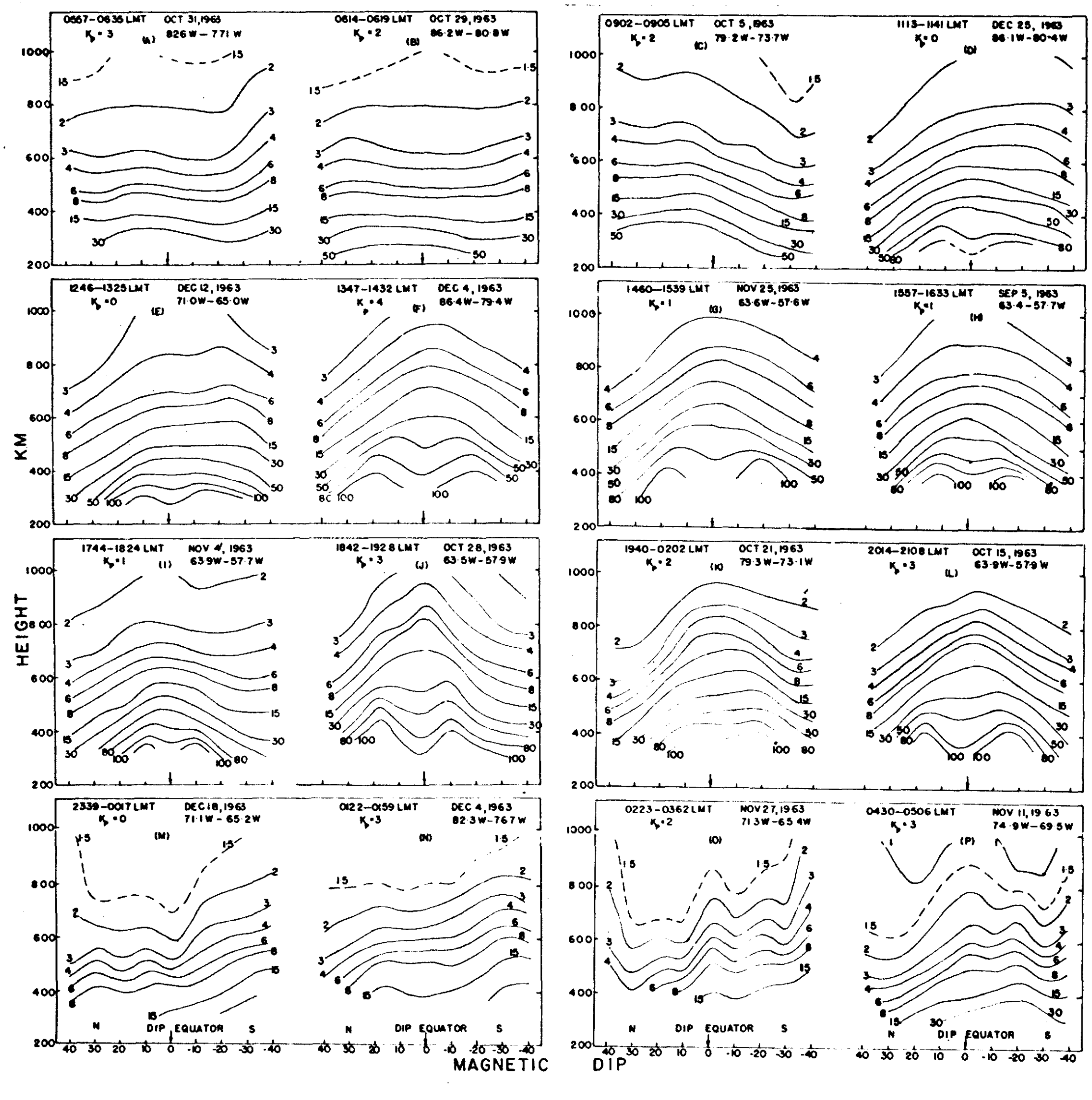

Fig. 1.17. Diurnal variations of equatorial anomaly in the months of October, November and December, 1963. The arrows denote the dip equators. Units: 10^4 el/cm^3.

CHAPTER 2

DERIVATIONS OF EQUATIONS

2.1. Basic equations

The vector equation of motion* for a gas with r constituents reads as follows:

$$N_r m_r \frac{d\vec{V}_r}{dt} = -\nabla P_r - 2N_r m_r \vec{\Omega} \times \vec{V}_r + N_r m_r \vec{g} + N_r e(\vec{E} + \vec{V}_r \times \vec{B}) + \sum_s m_{rs} \nu_{rs} N_r (\vec{V}_s - \vec{V}_r) + div\, \vec{\tau} \qquad (2.1)$$

Where:

$\frac{d\vec{V}_r}{dt}$ = Total derivative of the local mean velocity $\vec{V}_r$ with respect to time

N_r = Number density of r'th constituent

m_r = r'th particle mass

p_r = Partial pressure from r'th particle

μ = Viscosity coefficient

$\vec{g}$ = Acceleration due to gravity

e = Ionic charge

$\vec{E}$ = Electric field

$\vec{B}$ = Magnetic induction

---

*The classical name of the "Navier-Stokes" equation came from the fluid dynamics aspect. Recently some authors borrowed this name for charged particles in the field of gas dynamics. For example, Stube (1968) takes this name for the motions of the charged particles, Shercliff (1965) uses "modified Navier-Stokes" equation in the magnetohydrodynamics. Here we prefer to follow very general terminology as "equation of motion".

$\vec{\Omega}$ = Angular velocity of the earth

$\vec{V}_r$, $\vec{V}_s$ = Velocities of r'th and s'th type particles

ν_{rs} = Collision frequency between r'th and s'th constituent gases

$$\operatorname{div} \vec{\tau} = \mu \left[\frac{1}{3} \nabla (\nabla \cdot \vec{V}_r) + \nabla^2 \vec{V}_r \right] - \frac{2}{3} \nabla \cdot \vec{V}_r \, \nabla \mu$$

$$+ (\nabla \mu \cdot \nabla) \vec{V}_r + \nabla (\vec{V}_r \cdot \nabla \mu) - (\vec{V}_r \cdot \nabla) \nabla \mu$$

The partial pressure from r'th constituent gas can be written as:

$$P_r = N_r k T_r \tag{2.2}$$

Where:

k = Boltzman's constant

T_r = Temperature of r'th gas

Equation of continuity:

$$\frac{\partial N}{\partial t} = Q_r - L_r(N) - \operatorname{div}(N_r \vec{V}_r) \tag{2.3}$$

Where:

Q_r = Rate of production of r'th particle per unit volume

$L_r(N)$ = Rate of loss of r'th particle per unit volume

2.2. Assumptions

(1) Ionic atomic oxygen is the only positive ion and is singly charged. This is based from satellite results which show that in the region from 250 km to 950 km, the principal positive ion is mass 16 (Ratcliffe, 1960; Hanson and Moffett, 1966). The transition altitude from atomic oxygen to helium is at about 1200 km in the

early afternoon and about 600 km during the night (Bowen et al., 1964). The average transition level is at about 920 km (Hines, 1965).

(2) The negatively charged particles are electrons and $N_e = N_i = N$.

(3) μ is constant, therefore $\nabla\mu = 0$.

(4) The electric current in the dynamo region is quasi-horizontal in nature.

(5) Neutral atmospheric structure is function of local time and height. The latitudinal variation has been neglected.

(6) Photoionization of atomic oxygen is the only contribution to the production of electrons.

2.3. Scale analysis

Applying equations (2.1) and (2.2) for positive ion, we have

$$\begin{aligned} N_i m_i \frac{d\vec{V}_i}{dt} = & -\nabla k N_i T_i - 2 N_i m_i \vec{\Omega} \times \vec{V}_i + N_i m_i \vec{g} \\ & + N_i e (\vec{E} + \vec{V}_i \times \vec{B}) + m_e \nu_{ei} N_i (\vec{V}_e - \vec{V}_i) \\ & + m_i \nu_{in} N_i (\vec{V}_n - \vec{V}_i) + \mu\left[\frac{1}{3}\nabla(\nabla\cdot\vec{V}_i) + \nabla\vec{V}_i \right] \end{aligned} \tag{2.4}$$

Dividing equation (2.4) by $N_i m_i$ and decomposing it into three components, we have:

$$\begin{aligned}\frac{\partial u_i}{\partial t} + u_i\frac{\partial u_i}{\partial x} + v_i\frac{\partial u_i}{\partial y} + w_i\frac{\partial u_i}{\partial z} &= -\frac{k}{\rho_i}\,\frac{\partial(N_i T_i)}{\partial x}\\ &+ 2\Omega\, v_i \sin\phi - 2\Omega\, w_i \cos\phi + \frac{e}{m_i}E_x\\ &- \frac{eB}{m_i} v_i \sin I - \frac{eB}{m_i} w_i \cos I + \frac{m_e}{m_i}\nu_{ei}(u_e - u_i)\\ &+ \nu_{in}(u_n - u_i) + K_i\left[\frac{1}{3}\frac{\partial(\nabla\cdot\vec{V}_i)}{\partial x} + \frac{\partial^2 u_i}{\partial x^2} + \frac{\partial^2 u_i}{\partial y^2} + \frac{\partial^2 u_i}{\partial z^2}\right]\end{aligned} \tag{2.5}$$

$$\begin{aligned}\frac{\partial v_i}{\partial t} + u_i\frac{\partial v_i}{\partial x} + v_i\frac{\partial v_i}{\partial y} + w_i\frac{\partial v_i}{\partial z} &= -\frac{k}{\rho_i}\,\frac{\partial(N_i T_i)}{\partial y}\\ &- 2\Omega u_i \sin\phi + \frac{eB}{m_i} u_i \sin I + \frac{e}{m_i}E_y\\ &+ \frac{m_e}{m_i}\nu_{ei}(v_e - v_i) + \nu_{in}(v_n - v_i)\\ &+ K_i\left[\frac{1}{3}\frac{\partial(\nabla\cdot\vec{V}_i)}{\partial y} + \frac{\partial^2 v_i}{\partial x^2} + \frac{\partial^2 v_i}{\partial y^2} + \frac{\partial^2 v_i}{\partial z^2}\right]\end{aligned} \tag{2.6}$$

$$\begin{aligned}\frac{\partial w_i}{\partial t} + u_i\frac{\partial w_i}{\partial x} + v_i\frac{\partial w_i}{\partial y} + w_i\frac{\partial w_i}{\partial z} &= -\frac{k}{\rho_i}\,\frac{\partial(N_i T_i)}{\partial z}\\ &+ 2\Omega u_i \cos\phi - g + \frac{e}{m_i}E_z + \frac{eB}{m_i} u_i \cos I\\ &+ \frac{m_e}{m_i}\nu_{ei}(w_e - w_i) + \nu_{in}(w_n - w_i)\\ &+ K_i\left[\frac{1}{3}\frac{\partial(\nabla\cdot\vec{V}_i)}{\partial z} + \frac{\partial^2 w_i}{\partial x^2} + \frac{\partial^2 w_i}{\partial y^2} + \frac{\partial^2 w_i}{\partial z^2}\right]\end{aligned} \tag{2.7}$$

Where x, y, z are positive toward east, north and zenith respectively.

$\nu_i = \frac{\mu}{N_i m_i}$ = Kinematic viscosity

I = Inclination of earth's magnetic field, positive in the northern hemisphere.

ϕ = Latitude

$\rho_i = N_i m_i$ = Mass density of ion gas

T_i = Temperature of ion gas

ν_{ei} = Collision frequency between electrons and ions (Chapman and Cowling, 1958).

ν_{in} = Collision frequency between ions and neutral particles.

u, v, w are the velocity components in the x, y, and z directions; while the subscripts of i, e, and n stand for ion, electron and neutral particles respectively.

Introduce primed quantities as non-dimensional quantities as follows:

$$\vec{V}^{i,e,n} = \vec{V}_o^{i,e,n} V'_{i,e,n} \; ; \quad \begin{matrix} x \\ y \end{matrix} = L \begin{matrix} x' \\ y' \end{matrix} \; ; \quad z = H z'$$

$$\nabla = \frac{1}{L} \nabla' \; ; \quad \nabla^2 = \frac{1}{L^2} \nabla^{2\prime} ; \quad N_i = N_o^i N_i'$$

$$T_i = T_o^i T_i' \; ; \quad \Omega = \Omega_o \Omega' \; ; \quad t = \frac{t'}{4\Omega_o} \tag{2.8}$$

$$B = B_o B' \; ; \quad R^{i,e,n} = \frac{V_o^{i,e,n}}{L\,\Omega_o}$$

$$\omega_i = \frac{e B_o}{m_i} \; ; \quad \vec{E} = (E_{ox}, E_{oy}, E_{oz}) \vec{E}'$$

Substituting (2.8) into equations (2.5), (2.6), (2.7), we have:

$$\begin{aligned}
&4R^{i}\frac{\partial u_i'}{\partial t'} + R^{i2}\left(u_i'\frac{\partial u_i'}{\partial x'} + v_i'\frac{\partial u_i'}{\partial y'}\right) + \frac{W_0^{i}}{H\Omega_0}R^{i}w_i'\frac{\partial u_i'}{\partial z'}\\
&= -\frac{k}{\rho_i}\frac{N_0^{i}T_0^{i}}{\Omega_0^2L^2}\frac{\partial(N_i'T_i')}{\partial x'} + 2R^{i}\Omega' v_i'\,Sin\phi\\
&\quad -\frac{2W_0}{\Omega_0 L}\Omega' w_i'\,Cos\phi + \frac{eE_{0x}}{m_i\Omega_0^2L}E_x' - \frac{\omega_i}{\Omega_0}R^{i}B'v_i'\,Sin\,I\\
&\quad -\frac{\omega_i}{\Omega_0^2}\frac{W_0^{i}}{L}w'B'\,Cos\,I + \frac{m_e}{m_i}\frac{\nu_{ei}}{\Omega_0}\left(R^{e}u_e' - R^{i}u_i'\right)\\
&\quad +\frac{\nu_{in}}{\Omega_0}\left(R^{n}u_n' - R^{i}u_i'\right) + K_i\left[\frac{1}{3}\frac{R^{i}}{\Omega_0L^2}\frac{\partial}{\partial x'}\left(\frac{\partial u_i'}{\partial x'} + \frac{\partial v_i'}{\partial y'} + \frac{W_0L}{HV_0}\frac{\partial w_i'}{\partial z'}\right)\right.\\
&\quad \left. +\frac{R^{i}}{\Omega_0L^2}\left(\frac{\partial^2u_i'}{\partial x'^2} + \frac{\partial^2u_i'}{\partial y'^2}\right) + \frac{R^{i}}{\Omega_0H^2}\frac{\partial^2u_i'}{\partial z'^2}\right]
\end{aligned}\tag{2.9}$$

$$\begin{aligned}
&4R^{i}\frac{\partial v_i'}{\partial t'} + R^{i2}\left(u_i'\frac{\partial v_i'}{\partial x'} + v_i'\frac{\partial v_i'}{\partial y'}\right) + \frac{W_0^{i}}{H\Omega_0}R^{i}w_i'\frac{\partial v_i'}{\partial z'}\\
&= -\frac{k\,N_0^{i}T_0^{i}}{\rho_i\Omega_0^2L^2}\frac{\partial(N_i'T_i')}{\partial y'} - 2R^{i}\Omega' u_i'\,Sin\phi + \frac{eE_{0y}}{m_i\Omega_0^2L}E_y'\\
&\quad +\frac{\omega_i}{\Omega_0}R^{i}B'u_i'\,Sin\,I + \frac{m_e}{m_i}\frac{\nu_{ei}}{\Omega_0}\left(R^{e}v_e' - R^{i}v_i'\right)\\
&\quad +\frac{\nu_{in}}{\Omega_0}\left(R^{n}v_n' - R^{i}v_i'\right) + K_i\left[\frac{1}{3}\frac{R^{i}}{\Omega_0L^2}\frac{\partial}{\partial x'}\left(\frac{\partial v_i'}{\partial x'} + \frac{\partial v_i'}{\partial y'} + \frac{W_0^{i}L}{HV_0^{i}}\frac{\partial w_i'}{\partial z'}\right.\right.\\
&\quad \left.\left. +\frac{R^{i}}{\Omega_0L^2}\left(\frac{\partial^2v_i'}{\partial x'^2} + \frac{\partial^2v_i'}{\partial y'^2}\right) + \frac{R^{i}}{\Omega_0H^2}\frac{\partial^2v_i'}{\partial z'^2}\right]\right.
\end{aligned}\tag{2.10}$$

$$4\frac{\partial w_i'}{\partial t'} + R^i\left(u_i'\frac{\partial w_i'}{\partial x'} + v_i'\frac{\partial w_i'}{\partial y'}\right) + \frac{W_o}{H\Omega_o} w_i' \frac{\partial w_i'}{\partial z'}$$

$$= -\frac{k N_o^i T_o^i}{\rho_i \Omega_o H W_o^i}\frac{\partial(N_i' T_i')}{\partial z'} + 2\frac{V_o^i}{W_o^i}\Omega' u_i' \cos\phi$$

$$- \frac{g_o}{\Omega_o W_o^i} g' + \frac{eE_z^o}{m_i\Omega_o W_o} E_z' + \frac{\omega_i}{\Omega_o}\frac{V_o^i}{W_o^i} B' u_i' \cos I$$

$$+ \frac{m_e}{m_i}\frac{\nu_{ei}}{\Omega_o}(w_e' - w_i') + \frac{\nu_{in}}{\Omega_o}(w_n' - w_e')$$

$$+ K_i\left[\frac{1}{3}\frac{R^i}{HW_o^i}\frac{\partial}{\partial z'}\left(\frac{\partial u_i'}{\partial x'}+\frac{\partial v_i'}{\partial y'}\right) + \frac{1}{3}\frac{1}{H^2\Omega_o}\frac{\partial}{\partial z'}\left(\frac{\partial w_i'}{\partial z'}\right) + \right.$$

$$\left.\frac{1}{\Omega_o L^2}\left(\frac{\partial^2 w_i'}{\partial x'^2}+\frac{\partial^2 w_i'}{\partial y'^2}\right) + \frac{1}{\Omega_o H^2}\frac{\partial^2 w_i'}{\partial z'^2}\right] \qquad (2.11)$$

The following typical values are taken in our analysis.

$\left.\begin{array}{l} u^{i,e} \\ v^{i,e} \\ w^{i,e} \end{array}\right\} = 100$ m/sec $\qquad \Omega_o = 7\text{x}10^{-5}$ sec^{-1}

$\left.\begin{array}{l} u_o^n \\ v_o^n \end{array}\right\} = 100$ m/sec (Geisler, 1967; Kohl and King, 1967)

$w_o^n = 5$ m/sec $\qquad H = 5\text{x}10^4$ m

$L = 10^6$ m $\qquad T_o^i = 1500$ ^{o}K

$B_o = 0.3$ gauss $= 3\text{x}10^{-5}$weber/m^2; $N_n = 10^{14}$ m^{-3} (at 400 km height)

$N_o^{i,e} = 10^{11}\ \mathrm{m}^{-3}$;

$m_i = 2.5\mathrm{x}10^{-26}\,\mathrm{kgm}$;

$g_o = 10\ \mathrm{m/sec}^2$;

$E = 10^{-2}\ \mathrm{volt/m}$;

$\nu_{en} = 20\ \mathrm{sec}^{-1}$; (at 300 km)

$\nu_{in} = 5\times10^{-1}\ \mathrm{sec}^{-1}$ (at 300 km)

$k = 1.38\mathrm{x}10^{23}\ \mathrm{j.deg}^{-1}$

$m_e = 9.1\mathrm{x}10^{-31}\ \mathrm{kgm}$

$e = 1.6\mathrm{x}10^{-19}\ \mathrm{coul}$

$\omega_i = 200\ \mathrm{sec}^{-1}$

$\omega_e = 5\mathrm{x}10^{6}\ \mathrm{sec}^{-1}$

See Martyn 1958; Chapman and Cowling, 1958

$K_i = 5\mathrm{x}10^{3}\ \mathrm{m}^2\ \mathrm{sec}^{-1}$ (Kaufman, 1960; Spitzer, 1962; Linhart, 1961)

Table 2.1 shows different values for the coefficients of each term from equation (2.9), (2.10), and (2.11).

In the similar way, we can apply equations (2.1) and (2.2) to the electron and use the same scaling process as we did for ion. Thus we get non-dimensional equations of motion for electrons. Table 2.2 gives the numerical values of their different terms.

$$4 R^e \frac{\partial u_e'}{\partial t'} + (R^e)^2 \left(u_e' \frac{\partial u_e'}{\partial x'} + v_e' \frac{\partial u_e'}{\partial y'} \right) + \frac{W_o^e}{H\Omega_o} R^e w_e' \frac{\partial u_e'}{\partial z'}$$

$$= - \frac{k N_o^e T_o^e}{\rho_o \Omega_o^2 L^2} \frac{\partial (N_e' T_e')}{\partial x'} + 2 R^e \Omega' v_e' \,\mathrm{Sin}\,\phi$$

$$- \frac{2 W_0^e}{\Omega_0 L} \Omega' w'_e \cos\phi - \frac{e E_{0x}}{m_e \Omega_0^2 L} E_x' + \frac{\omega_e}{\Omega_0} R^e B' v'_e \,\mathrm{Sin}\, I$$

$$+ \frac{\omega_e W_0^e}{\Omega_0^2 L} w' B' \,\mathrm{Cos}\, I + \frac{\nu_{ei}}{\Omega_0} (R^i u'_i - R^e u'_e)$$

$$+ \frac{\nu_{en}}{\Omega_0} (R^n u'_n - R^e u'_e) + K_e \Bigg[\frac{R^e}{3 \Omega_0 L^2} \frac{\partial}{\partial x'} \left(\frac{\partial u'_e}{\partial x'} + \frac{\partial v'_e}{\partial y'} + \frac{W_0^e L}{H V_0^e} \frac{\partial w'_e}{\partial z'} \right)$$

$$+ \frac{R^e}{\Omega_0 L^2} \left(\frac{\partial^2 u'_e}{\partial x'^2} + \frac{\partial^2 u'_e}{\partial y'^2} \right) + \frac{R^e}{\Omega_0 H^2} \frac{\partial^2 u'_e}{\partial z'^2} \Bigg] \qquad (2.13)$$

$$4 R^e \frac{\partial v'_e}{\partial t'} + (R^e)^2 \left(u'_e \frac{\partial v'_e}{\partial x'} + v'_e \frac{\partial v'_e}{\partial y'} \right) + \frac{W_0^e}{H \Omega_0} R^e w'_e \frac{\partial v'_e}{\partial z'}$$

$$= - \frac{k N_0^e T'_e}{\rho_i \Omega_0^2 L^2} \frac{\partial (N'_e T'_e)}{\partial x'} - 2 R^e \Omega' u'_e \,\mathrm{Sin}\phi - \frac{e E_{0y}}{m_e \Omega_0^2 L} E_{0y}'$$

$$- \frac{\omega_e}{\Omega_0} R^e B' u'_e \,\mathrm{Sin}\, I + \frac{\nu_{ei}}{\Omega_0} (R^i v'_i - R^e v'_e)$$

$$+ \frac{\nu_{en}}{\Omega_0} (R^n v'_n - R^e v'_e) + K_e \Bigg[\frac{R^e}{3 \Omega_0 L^2} \frac{\partial}{\partial x'} \left(\frac{\partial v'_e}{\partial x'} + \frac{\partial v'_e}{\partial y'} + \frac{W_0^e L}{H V_0^e} \frac{\partial w'_e}{\partial z'} \right)$$

$$+ \frac{R^e}{\Omega_0 L^2} \left(\frac{\partial^2 v'_e}{\partial x'^2} + \frac{\partial^2 v'_e}{\partial^2 y'} \right) + \frac{R^e}{\Omega_0 H^2} \frac{\partial^2 v'_e}{\partial z'^2} \Bigg] \qquad (2.14)$$

$$4 \frac{\partial w'_e}{\partial t'} + R^e \left(u'_e \frac{\partial w'_e}{\partial x'} + v'_e \frac{\partial w'_e}{\partial y'} \right) + \frac{W_0^e}{H \Omega_0} w'_e \frac{\partial w'_e}{\partial z'}$$

$$= - \frac{k N_0^e T_0^e}{\rho_0 \Omega_0 H W_0^e} \frac{\partial (N'_e T'_e)}{\partial z'} + 2 \frac{V_0^e}{W_0^e} \Omega' u'_e \,\mathrm{Cos}\phi$$

$$\begin{aligned}
&-\frac{g_0}{\Omega_0 W_0^e}\, g' - \frac{eE_{0z}}{m_e \Omega_0 W_0^e} E_z' - \frac{\omega_e}{\Omega_0}\frac{V_0^e}{W_0^e} B' u_e' \cos I \\
&+\frac{\nu_{ei}}{\Omega_0}\left(w_i' - w_e'\right) + \frac{\nu_{en}}{\Omega_0}\left(w_n' - w_e'\right) \\
&+K_e\left[\frac{R^e}{3HW_0^e}\frac{\partial}{\partial z'}\left(\frac{\partial u_e'}{\partial x'}+\frac{\partial v_e'}{\partial y'}\right) + \frac{1}{3H^2\Omega_0}\frac{\partial}{\partial z'}\left(\frac{\partial w_e'}{\partial z'}\right)\right. \\
&\left.+\frac{1}{\Omega_0 L^2}\left(\frac{\partial^2 w_e'}{\partial x'^2}+\frac{\partial^2 w_e'}{\partial y'^2}\right)+\frac{1}{\Omega_0 H^2}\frac{\partial^2 w_e'}{\partial z'^2}\right] \qquad (2.15)
\end{aligned}$$

Where:

$$K_e = \frac{\mu}{N_e m_e}$$

$\rho_e = N_e m_e$ = Mass density of electron gas

T_e = Temperature of electron gas

$$R^e = \frac{V_0^e}{\Omega_0 L}$$

$\omega_e = \dfrac{eB}{m_e}$ = Gyrofrequency of electrons

The other symbols have the same meaning as defined previously.

Table 2.1. Numerical values of various terms in the equations (2.9), (2.10), and (2.11)

Quantity	Numerical Value	Quantity	Numerical Value
$R^i = \frac{V_o^i}{\Omega_o L}$	1.4	$\frac{W_o^i R^i}{\Omega_o H}$	42
$R^n = \frac{V_o^n}{\Omega_o L}$	1.4	$\frac{k N_o^i T_o^i}{\rho_o \Omega_o H W_o^i}$	$2.4\text{x}10^{3}$
$\frac{k N_o^i T_o^i}{\rho_o \Omega_o^2 L}$	$1.7\text{x}10^{2}$	$\frac{W_o^i}{\Omega_o L}$	1.4
$\frac{V_o^i}{W_o^i}$	1	$\frac{g_o}{W_o^i \Omega_o}$	$1.4\text{x}10^{3}$
$\frac{e}{m_i \Omega^2 L} E_{ox}$ or E_{oy}	$1.3\text{x}10^{7}$	$\frac{e E_{oz}}{m_i \Omega_o W_o^i}$	9.10^{6}
$\frac{\omega_i}{\Omega_o} R^i = \frac{\omega_i}{\Omega_o^2} \frac{W_o^i}{L}$	$3.8\text{x}10^{6}$	$\frac{\omega_i}{\Omega_o} \frac{V_o^i}{W_o^i}$	$2.7\text{x}10^{6}$
$\frac{\nu_{in}}{\Omega_o} R^n$	10^{4}	$\frac{\nu_{in}}{\Omega_o}$	$7\text{x}10^{3}$
$\frac{K_i R^i}{3 \Omega_o L^2}$	$3.5\text{x}10^{-5}$	$\frac{K_i R^i}{3 L^2 \Omega_o} \frac{W_o^i L}{H V_o^i}$	$6.5\text{x}10^{-4}$
$\frac{K_i R_o^i}{\Omega_o H^2}$	$4\text{x}10^{-3}$	$\frac{K_i R^i}{3 H W_o^i}$	$4.75\text{x}10^{-4}$
$\frac{K_i}{3 H^2 \Omega_o}$	$1\text{x}10^{-2}$	$\frac{K_i}{\Omega_o L^2}$	$7.5\text{x}10^{-5}$

Table 2.2 Numerical values of various terms in the equations (2.13), (2.14), and (2.15)

Quantity	Numerical Value	Quantity	Numerical Value
$R^e = \frac{V_0^e}{\Omega_0 L}$	1.4	$\frac{W_0^e R^e}{\Omega_0 H}$	42
$R^n = \frac{V_0^n}{\Omega_0 L}$	1.4	$\frac{k\ N_0^e T_0^e}{\rho_0 \Omega_0 H W_0^e}$	$6.6\text{x}10^7$
$\frac{k\ N_0^e T_0^e}{\rho_0 \Omega_0^2 L^2}$	$4.7\text{x}10^6$	$\frac{W_0^e}{\Omega_0 L}$	1.4
$\frac{V_0^e}{W_0^e}$	1	$\frac{g_0}{\Omega_0 W_0^e}$	$1.4\text{x}10^3$
$\frac{e}{m_e \Omega_0^2 L} E_{0x}$ or E_{0y}	$3.5\text{x}10^{11}$	$\frac{e\ E_{0z}}{m_e \Omega_0 W_0^e}$	$2.45\text{x}10^{11}$
$\frac{\omega_e}{\Omega_0} R^e = \frac{\omega_e}{\Omega_0^2} \frac{W_0^2}{L}$	$1\text{x}10^{11}$	$\frac{\omega_e}{\Omega_0} \frac{V_0^e}{W_0^e}$	$7.4\text{x}10^{10}$
$\frac{\nu_{en}}{\Omega_0} R^n$	$4\text{x}10^5$	$\frac{\nu_{en}}{\Omega_0}$	$3\text{x}10^5$
$\frac{K_e R^e}{3 \Omega_0 L^2}$	1	$\frac{K_e R^e}{3 L^2 \Omega_0} \frac{W_0^e L}{H V_0^e}$	20
$\frac{K_e}{\Omega_0} \frac{R^e}{H^2}$	$1.1\text{x}10^2$	$\frac{K_e R^e}{3 H W_0^e}$	13.2
$\frac{K_e}{3 H^2 \Omega_0}$	$2.8\text{x}10^2$	$\frac{K_e}{\Omega_0 L^2}$	2.0

From the above scale analysis, we have found the following facts:

1. Inertia term

This term is extremely small compared with other terms. Physically, the validity of neglecting inertia term requires that the time interval between collisions should be much smaller than the time in which macroscopic features of the flow are changing. The time scale for macroscopic feature change in our problem is on the order of few hours, whereas for ions and electrons the collision time is in a few seconds. The inertia term will be of the same importance as the pressure term if $|V_i| \sim 10^9$ m/sec, which is not true in the F region.

2. Pressure term

For both the ion and electron gases, the horizontal pressure terms are two order of magnitude smaller than the vertical pressure components. For the ion gas, the vertical pressure force is the same order of magnitude as the gravitational force, while for electron gas the vertical pressure force is much larger than the gravitational force.

3. Lorentz force and electric force terms

These two forces are dominant terms and almost in balance with each other. In fact, all other forces can be neglected in the large scale motions of the ionization in which the electro-static force and the Lorentz force are just in balance.

4. Viscous term

The viscous force is also a minor term compared with the Lorentz force. It is also smaller than the pressure force and can be neglected.

5. Coriolis force

This term is of the same order of magnitude as inertia term and can be omitted.

6. Ion drag terms

In F region, the plasma has a tendency for electrons and ions to move together in order to prevent any large current. Thus $V_i - V_e \ll V_i$ and $\nu_{ie}(V_e - V_i) \ll \nu_{in}(V_n - V_i)$. From Table 2.1 and 2.2, we find that these terms are also smaller compared with Lorentz force term. However, they should be treated as equally important as pressure terms.

Remarks: It should be mentioned that different conclusions may occur if motions are in different scales. Certainly, the scaling factor should be different. As for the neutral gas, the velocity scaling factor may differ quite a lot, because of the absence of the electro-static force and the Lorentz force. The large scale vertical motions of the neutral gas are much smaller than horizontal motions in contrast to the case of charged particles in which the vertical velocity is comparable to the horizontal velocity. Therefore, the inertia term may not be ignored in the equation of motion for the neutral gas.

2.4. Derivation of plasma velocities

After examining each term by making a scale analysis, we now have confidence to write down the equations of motion for the ion and electron gases, and then solve for their velocities in terms of other quantities.

For ions:

$$0 = -\frac{k}{\rho_i}\frac{\partial(N_iT_i)}{\partial x} + \frac{eE_x}{m_i} - \frac{eB}{m_i}v_i \sin I - \frac{eB}{m_i}w_i \cos I + \nu_{in}(u_n - u_i) \qquad (2.16)$$

$$0 = -\frac{k}{\rho_i}\frac{\partial(N_iT_i)}{\partial y} + \frac{e}{m_i}E_y + \frac{eB}{m_i}u_i \sin I + \nu_{in}(v_n - v_i) \qquad (2.17)$$

$$0 = -\frac{k}{\rho_i}\frac{\partial(N_iT_i)}{\partial z} - g + \frac{e}{m_i}E_z + \frac{eB}{m_i}u_i \cos I + \nu_{in}(w_n - w_i) \qquad (2.18)$$

For electrons:

$$0 = -\frac{k}{\rho_e}\frac{\partial(N_eT_e)}{\partial x} - \frac{e}{m_e}E_x + \frac{eB}{m_e}v_e \sin I + \frac{eB}{m_e}w_e \cos I \qquad (2.19)$$

$$0 = -\frac{k}{\rho_e}\frac{\partial(N_eT_e)}{\partial y} - \frac{e}{m_e}E_y - \frac{eB}{m_e}u_e \sin I \qquad (2.20)$$

$$0 = -\frac{k}{\rho_e}\frac{\partial(N_eT_e)}{\partial z} - \frac{e}{m_e}E_z - \frac{eB}{m_e}u_e \cos I \qquad (2.21)$$

Since the current system in the dynamo region is assumed quasi-horizontal in nature, therefore, our further assumption is that $w_e = w_i$. Thus we can solve for u_e, u_i, v_e, v_i, $w_e = w_i (= w)$ and E_z from six equations (2.16-2.21) in terms of other quantities.

Eliminating u_e between (2.20) and (2.21), we have

$$E_z = E_y \mathrm{Ctn}\, I - \left[\frac{k}{Ne} \frac{\partial (NT_e)}{\partial z} - \mathrm{Ctn}\, I \frac{\partial (NT_e)}{\partial y} \right] \tag{2.22}$$

Substituting (2.22) into (2.18) and rearranging equations (2.16), (2.17), (2.18), we have:

$$u_i + \frac{\omega_i}{\nu_{in}} \mathrm{Sin}\, I\, v_i + \frac{\omega_i}{\nu_{in}} \mathrm{Cos}\, I\, w_i = \frac{eE_x}{m_i \nu_{in}} + u_n - \frac{k}{\rho_i \nu_{in}} \frac{\partial (NT_i)}{\partial x} \tag{2.23}$$

$$\frac{\omega_i}{\nu_{in}} \mathrm{Sin}\, I\, u_i - \qquad v_i + \qquad 0 = -\frac{eE_y}{m_i \nu_{in}} - v_n - \frac{k}{\rho_i \nu_{in}} \frac{\partial (NT_i)}{\partial y} \tag{2.24}$$

$$\begin{aligned} \frac{\omega_i}{\nu_{in}} \mathrm{Cos}\, I\, u_i + \qquad 0 - \qquad w_i = {} & -\frac{eE_y}{m_i \nu_{in}} \mathrm{Ctn}\, I - w_n + \frac{k}{\rho_i \nu_{in}} \frac{\partial (N(T_i + T_e))}{\partial z} \\ & - \frac{k}{\rho_i} \mathrm{Ctn}\, I \frac{\partial (NT_e)}{\partial y} + \frac{g}{\nu_{in}} \end{aligned} \tag{2.25}$$

It is easy to solve u_i, v_i, w_i in terms of other quantities from (2.23), (2.24) and (2.25). The results are as follows:

$$\begin{aligned} U_i = \frac{1}{1+\left(\frac{\nu_{in}}{\omega_i}\right)^2} \Bigg\{ & -\frac{E_y}{B}\,\mathrm{Csc}\,I + \frac{k}{\rho_i \omega_i}\left[\mathrm{Sin}\,I \frac{\partial (NT_i)}{\partial y} - \frac{\mathrm{Cos}^2 I}{\mathrm{Sin}\,I}\frac{\partial (NT_e)}{\partial y} \right. \\ & \left. + \mathrm{Cos}\,I \frac{\partial (N(T_i+T_e))}{\partial z} \right] + \frac{g}{\omega_i}\mathrm{Cos}\,I + \left(\frac{\nu_{in}}{\omega_i}\right)^2 U_n \\ & + \frac{\nu_{in}}{\omega_i}\left[\frac{E_x}{B} - \mathrm{Sin}\,I\, V_n - \mathrm{Cos}\,I\, W_n - \frac{k}{\rho_i \omega_i}\frac{\partial (NT_i)}{\partial x} \right] \Bigg\} \end{aligned} \qquad (2.26)$$

$$\begin{aligned} V_i = \frac{1}{1+\left(\frac{\nu_{in}}{\omega_i}\right)^2} \Bigg\{ & \frac{E_x}{B}\mathrm{Sin}\,I + \frac{E_y}{B}\frac{\nu_{in}}{\omega_i} + V_n\left[\mathrm{Cos}^2 I + \left(\frac{\nu_{in}}{\omega_i}\right)^2 \right] \\ & + \frac{\nu_{in}}{\omega_i} U_n \mathrm{Sin}\,I + \mathrm{Cos}\,I\,\mathrm{Sin}\,I\left(\frac{g}{\nu_{in}} - W_n \right) \\ & + \frac{k\,\mathrm{Cos}\,I}{\rho_i \nu_{in}}\left[\frac{\partial (N(T_i+T_e))}{\partial z}\mathrm{Sin}\,I - \frac{\partial (N(T_i+T_e))}{\partial y}\mathrm{Cos}\,I \right] \\ & - \frac{k}{\rho_i \omega_i}\left[\mathrm{Sin}\,I \frac{\partial (NT_i)}{\partial x} + \frac{\nu_{in}}{\omega_i}\frac{\partial (NT_i)}{\partial y} \right] \Bigg\} \end{aligned} \qquad (2.27)$$

$$w_i = \frac{1}{1+\left(\frac{\nu_{in}}{\omega_i}\right)^2}\left\{\frac{E_x}{B}\cos I + \frac{E_y}{B}\cos I\,\frac{\nu_{in}}{\omega_i \sin I} - \sin I\cos I\left(v_n - \frac{\nu_{in}}{\omega_i \sin I}u_n\right)\right.$$

$$+ w_n \sin^2 I\left[1 + \left(\frac{\nu_{in}}{\omega_i \sin I}\right)^2\right] + \frac{k}{\rho_i \nu_{in}}\cos I \sin I\left[\frac{\partial(NT_i)}{\partial y} - \frac{\nu_{in}}{\omega_i \sin I}\frac{\partial(NT_i)}{\partial x}\right]$$

$$+\left[\frac{k \sin I \cos I}{\rho_i \nu_{in}}\frac{\partial(NT_e)}{\partial y} - \frac{g}{\nu_{in}}\sin^2 I\right.$$

$$\left.\left. - \frac{k \sin^2 I}{\rho_i \nu_{in}}\frac{\partial(N(T_i+T_e))}{\partial z}\right]\left[1 + \left(\frac{\nu_{in}}{\omega_i \sin I}\right)^2\right]\right\} \qquad (2.28)$$

In the F region, $\frac{\nu_{in}}{\omega_i} \ll 1$, and if $I > 2^\circ$, then $\frac{\nu_{in}}{\omega_i \sin I} \ll 1$, so, it is a good approximation to neglect all terms which contain the factor of $\frac{\nu_{in}}{\omega_i}$ and $\left(\frac{\nu_{in}}{\omega_i}\right)^2$. Making this adjustment, and using equation (2.19) and (2.20) we finally obtain equations for u_e, u_i, v_e, v_i and $w_e = w_i$ as follows:

$$u_i = -\frac{E_y}{B}\csc I + \frac{1}{\omega_i}\left\{g \cos I + \frac{k}{\rho_i}\sin I\left[\frac{\partial(NT_i)}{\partial y} - \mathrm{Ctn}^2 I\,\frac{\partial(NT_e)}{\partial y}\right]\right.$$

$$\left. - \frac{k}{\rho_i}\cos I\,\frac{\partial(N(T_i+T_e))}{\partial z}\right\} \qquad (2.29)$$

$$v_i = \frac{E}{B}\sin I - \cos^2 I\, v_n - \cos I \sin I\, w_n$$

$$+ \frac{\cos I \sin I}{\nu_{in}}\left[g + \frac{k}{\rho_i}\frac{\partial(N(T_i+T_e))}{\partial z}\right] - \frac{k}{\rho_i \nu_{in}}\cos^2 I\,\frac{\partial(N(T_i+T_e))}{\partial y} \qquad (2.30)$$

$$
\begin{aligned}
w_i = w_e = {} & \frac{E_x}{B}\cos I - \sin I \cos I \, v_n + \sin^2 I \, w_n \\
& + \sin I \cos I \, \frac{k}{\rho_i \nu_{in}} \, \frac{\partial (N(T_i + T_e))}{\partial y} \\
& - \frac{\sin^2 I}{\nu_{in}} \left[g + \frac{k}{\rho_i} \, \frac{\partial (N(T_i + T_e))}{\partial z} \right]
\end{aligned}
\tag{2.31}
$$

$$
u_e = - \frac{E_y}{B} \csc I - \frac{k}{\rho_e \omega_e \sin I} \, \frac{\partial (N T_e)}{\partial y}
\tag{2.32}
$$

$$
\begin{aligned}
v_e = {} & \frac{E_x}{B} \sin I + \cos^2 I \, v_n - \cos I \sin I \, w_n \\
& + \frac{\cos I \sin I}{\nu_{in}} \left[g + \frac{k}{\rho_i} \, \frac{\partial (N(T_i + T_e))}{\partial z} \right] - \frac{k}{\rho_i \nu_{in}} \cos^2 I \, \frac{\partial (N(T_i + T_e))}{\partial y} \\
& + \frac{k}{\rho_e \omega_e \sin I} \, \frac{\partial (N T_e)}{\partial x}
\end{aligned}
\tag{2.33}
$$

Let us examine a little more the details about those terms in the RHS of the equations (2.29) through (2.33) to see the importance of the different parameters in governing the plasma velocities.

(a) East-west velocity: Since $\omega_i \sim 200 \text{ sec}^{-1}$, the maximum contribution from gravity to this velocity is 0.05 m/sec. According to Evans (1967), the vertical temperature gradients for electrons during the daytime are 2 °K/km and 6 °K/km at the heights above and below 300 km. For ions it is about 4 °K/km. The nighttime values are always less. Therefore, the maximum contribution from the temperature term to u_i in the equation (2.29) is on the order of 10^{-2} m/sec and the contribution from horizontal temperature terms should be less except at the equator. As for the contribution from the vertical gradient of N, we can prove that it is on the same order of magnitude as from gravity. Take $N = N_o e^{-z/2H}$, where $H = k(T_i+T_e)/m_i g$, then $\frac{\partial N}{\partial z} = -N/H$. It follows that $\left[\text{Cos } I\ k(T_i+T_e)/\rho_i\right] \cdot \frac{\partial N}{\partial z} = \text{Cos } I \cdot g$. Take $E_y = 10^{-3}$ volt/m, $B = 0.3\text{x}10^{-4}$ weber/m^2 we have $E_y/B = 33$ m/sec. It is obvious that the major contribution to the east-west ion velocity comes from N-S electric field.

In a similar way, we may prove that the contributions to E-W velocity of electron from the temperature as well as horizontal gradient of N are smaller comparing with the electric field. It is noticed that $\omega_e \sim 10^6\ \text{sec}^{-1}$.

(b) North-south velocity: Take $v_n = 100$ m/sec, $w_n = 5$ m/sec, $\nu_{in} = 0.5\ \text{sec}^{-1}$ (at 300 km), $E_x = 10^{-3}$ volt/m, then the contributions from the vertical gradients of the temperature as well as N are the same amount as from the gravity. The horizontal gradients of both T and N are smaller. It turns out that the E-W electric field, meridional neutral wind and diffusion due to gravity and pressure have the same importance to the N-S ion or electron velocity.

(c) Vertical velocity: The same conditions hold for the vertical velocity as for the N-S velocities. However, one important feature should be mentioned here. In the equation (2.31), all terms except the electric field term are multiplied by a common factor of Sin I. Consequently, at the equator, where I = 0, the only contribution to the vertical velocity is due to N-S electric field.

From above examination, we have some idea that the plasma velocities are influenced by three major contributors, namely: electric field, neutral winds and the diffusion due to gravity and the pressure. The relative importance of these three factors are weighted by the inclination of the earth magnetic field through the terms of Sin I and Cos I.

2.5. Equation of continuity for electron

In the F region, the loss term is of the attachment type, i.e. L = β N, where β is the recombination coefficient. Taking the earth as perfect dipole, then the rotation axis coincides with the magnetic axis. The continuity equation for electrons will be:

$$\frac{\partial N}{\partial t} = Q - \beta N - \frac{\partial \Phi_z (a+z)^2}{(a+z)^2 \partial z} - \frac{1}{(a+z)\,\mathrm{Cos}\,\phi}\left[\frac{\partial \Phi_\lambda}{\partial \lambda} + \frac{\partial \Phi_\phi \mathrm{Cos}\,\phi}{\partial \phi}\right] \tag{2.34}$$

Where:

$$\Phi_\lambda = N u_e \cong -\frac{E_y}{B_o}\,\frac{(1+\frac{z}{a})^3}{2\,\mathrm{Sin}\,\phi}\,N \tag{2.35}$$

$$\begin{aligned}\Phi_\phi = N V_e \cong \frac{N}{1+3\,\mathrm{Sin}^2\phi}\Bigg\{ & \frac{E_x}{B_o}\left(1+\frac{z}{a}\right)^3 2\,\mathrm{Sin}\,\phi + V_n\,\mathrm{Cos}^2\phi \\ & -\mathrm{Sin}\,2\phi\, W_n + \frac{g}{\nu_{in}}\,\mathrm{Sin}\,2\phi\left(1+\frac{\partial H}{\partial z}\right) - \frac{g}{\nu_{in}}\,\frac{\mathrm{Cos}^2\phi}{(a+z)}\,\frac{\partial H}{\partial \phi} \\ & + \frac{gH}{N\nu_{in}}\left[\mathrm{Sin}\,2\phi\,\frac{\partial N}{\partial z} - \frac{\mathrm{Cos}^2\phi}{(a+z)}\,\frac{\partial N}{\partial \phi}\right]\Bigg\}\end{aligned} \tag{2.36}$$

$$\Phi_z = N W_e \cong \frac{N}{1+3\sin^2\phi}\left\{\frac{E_x}{B_o}\left(1+\frac{z}{a}\right)^3\cos\phi - V_n \sin 2\phi \right.$$

$$+ 4W_n \sin^2\phi + \frac{g}{\nu_{in}}\frac{\sin 2\phi}{(a+z)}\frac{\partial H}{\partial\phi} - \frac{g}{\nu_{in}} 4\sin^2\phi\left(1+\frac{\partial H}{\partial z}\right)$$

$$\left. + \frac{gH}{N\nu_{in}}\left[\frac{\sin 2\phi}{(a+z)}\frac{\partial N}{\partial\phi} - 4\sin^2\phi\,\frac{\partial N}{\partial z}\right]\right\} \qquad (2.37)$$

a = Radius of the earth

z = Height above earth surface, positive toward zenith

ϕ = Latitude angle, positive toward north

λ = Longitude, positive toward east

B_o = Magnetic field intensity at the surface of the earth

$$H = \frac{k(T_i+T_e)}{m_i g}$$

The other symbols have the same meaning as defined previously.

CHAPTER 3

NUMERICAL SOLUTIONS

3.1. Introduction

The equation of continuity is not only complicated, but also contains many unknown quantities. It is almost impossible to get an analytic solution. Even for numerical ones, we still have to make many assumptions in order to simplify the equation. Different simplified treatments of this equation have been done by many authors. By and large, their results agree with the observational facts. Rishbeth (1967a) used neutral winds as input data to see the effect on the ionospheric F2-peak. Kendall and Windle (1968) examined the ion drag with electrodynamic drift. Thomas and Venables (1967) made a numerical calculation for a non-thermoequilibrium case (i.e. $T_e \neq T_i$). Yeh (1968) investigated F2 region ionospheric behavior by varying different physical parameters such as production rate, loss coefficient etc.. However, in these authors' models, the horizontal flux was omitted for simplicity. Therefore, their results only represent the mid-latitude behavior. Baxter (1967) integrated the continuity equation along each field line and thus gave the latitudinal variation of electron density. Baxter and Kendall (1968) used the same method except that they included electrodynamic drifts in order to explain the equatorial anomaly. Abur-Robb et al. (1969) and Abur-Robb (1969) inserted neutral winds and electrodynamic drift in their time-varying solutions of the full continuity equation. The results of these authors, though offering three-dimensional pictures, still have some drawbacks. First, the atmospheric temperature was treated as isothermal. Secondly, their integration technique was as follows: they started at one end of the field line and integrated the continuity equation step by step until the other end was reached. The boundary values at both ends were initialized. They assigned different sets of values to the physical parameters such as production rate, recombination rate, scale height etc. The results of this approach depend much on the physical constants chosen in their models. Furthermore, a common drawback to all workers' efforts was that they used Chapman's theoretical formula to compute electron production rate which may differ a lot from the actual results created by the solar radiation flux.

3.2. Three-dimensional model of continuity equation

As strongly suggested by Sato (1968), a three-dimensional model of the continuity equation should be worked out in order to get better results. Here is our model: in view of those drawbacks mentioned above, we do our best to survey all data measured separately in order to make our model as close to reality as possible. The horizontal flux is retained in the equation of continuity and the electron production rate is calculated from actual solar radiation flux.

We divide the solar spectrum below 1027 A into 68 divisions in the manner described by Hinteregger et al. (1965). Thus the production rate is given by

$$Q = \sum_{\Delta\ell=1}^{68} \mathcal{E}_\ell \, \sigma'_\ell \, n(o) F^{\ell}(\infty) \, e^{-\tau_\ell} \tag{3.1}$$

Where:

$\mathcal{E}_\ell$ = Production efficient

σ'_ℓ = Photo-ionization cross-section in cm

n(0) = Number density of atomic oxygen in cm^{-3}

$F^{\ell}(\infty)$ = Solar flux interval ℓ outside the atmosphere in photo/cm^2 sec.

The optical path is given by

$$\tau_\ell = \int_z^\infty \left[\sigma^\ell(o)n(o) + \sigma^\ell(O_2)n(O_2) + \sigma^\ell(N_2)n(N_2) \right] Sec\,\chi \, dz \tag{3.2}$$

Where $\sigma^\ell(o)$, $\sigma^\ell(O_2)$, $\sigma^\ell(N_2)$ are the absorption cross-section for the neutral constituents of 0, 0_2 and N_2 at wavelength ℓ, and χ is solar zenith angle.

In this chapter, we only consider equinoctial conditions. The winter and summer cases are investigated in chapter 4, in which the seasonal anomaly is discussed. For equinoctial condition, we have:

$$\text{Cos}\,\chi = \text{Cos}\,\phi \ \text{Cos}\,\lambda$$

The loss of ionization in the F-region is controlled by the following chemical reaction:

$0^+ + 0_2 \dashrightarrow 0_2^+ + 0$ $\quad k_1$

$0_2^+ + e \dashrightarrow 0' + 0''$ $\quad \alpha_1$

$0^+ + N_2 \dashrightarrow NO^+ + N$ $\quad k_2$

$N^+ + e \dashrightarrow N' + 0'$ $\quad \alpha_2$

Where α_1, α_2, k_1, k_2 are rate coefficients. Since $\alpha \gg k$, the atom-ion interchange reactions control the electron loss process in the F region. The loss coefficients are given by

$$\beta = k_1\ n(N_2) + k_2\ n(0_2)\ \text{sec}^{-1} \tag{3.3}$$

Where:

$k_1 = 3\text{x}10^{-12}\ (T_n/300)^{-1.5}\ \text{cm}^3/\text{sec}$ see: Mitra et al. (1967)

$k_2 = 4\text{x}10^{-11}\ (T_n/300)^{-1.5}\ \text{cm}^3/\text{sec}$ Smith et al. (1968

T_n = Temperature of neutral gas

The neutral atmosphere data were picked from model 2 of CIRA 1965, which corresponds to the solar minimum case. Incidently, the EUV data for the range from 1300 A to 250 A are for the quiet solar day of July 10, 1963. The other part of wavelengths below 250 A was measured on May 2, 1963. The year of 1963 was in the solar minimum activity period. We chose these data because our satellite data is in this year. We prefer to have theoretical and observational results under similar outside circumstances in order to make a better comparison.

To date, there are no neutral winds data available, nor the global electric fields. As for the ion and electron temperatures, only Evan's data (1967, 1968) are good. He used the Millston Hill Ionospheric Radar (42.6°N, 71.5°W geographic coordinates) and deduced temperature continuously for the year of 1964. Under such poor conditions, it is very difficult to satisfy our expectation. However, as we mentioned before, our approach to the problems is to do what we can in order to collect all reasonable data in our numerical model of the continuity equation. Therefore we calculated the scale heights of ion and electron based on Evans' average ion and electron temperatures. The diurnal variation and height variation of H were also calculated in the same manner. Certainly, we have to ignore the horizontal variations of both temperature and neutral atmospheic densities for lack of data.

For the first trial, our solution is for the stationary atmosphere. Electrostatic force is also ignored. Later, in chapters 5 and 6, we will include the electric field to explain the equatorial anomaly and the effect on the Muldrew trough. The neutral wind effect is discussed briefly in section 3.6.

The continuity equation for the stationary atmosphere and without electric field is as follows:

$$\frac{\partial N}{\partial t} = C_1(z,\phi,t)\frac{\partial^2 N}{\partial z^2} + C_2(z,\phi,t)\frac{\partial^2 N}{\partial z \partial \phi} + C_3(z,\phi,t)\frac{\partial^2 N}{\partial \phi^2}$$

$$+ C_4(z,\phi,t)\frac{\partial N}{\partial z} + C_5(z,\phi,t)\frac{\partial N}{\partial \phi} + C_6(z,\phi,t)N$$

$$+ C_7(z,\phi,t) \qquad (3.4)$$

Where:

$$C_1(z,\phi,t) = \frac{4g(z)H(z,t)}{\nu_{in}(z,t)}\,\frac{\sin^2\phi}{(1+3\sin^2\phi)} \qquad (3.5)$$

$$C_2(z,\phi,t) = -\frac{2g(z)H(z,t)}{\nu_{in}(z,t)}\,\frac{\sin(2\phi)}{(1+3\sin^2\phi)(a+z)} \qquad (3.6)$$

$$C_3(z,\phi,t) = \frac{g(z)H(z,t)}{\nu_{in}(z,t)} \frac{\cos^2\phi}{(1+3\sin^2\phi)(a+z)^2} \tag{3.7}$$

$$\begin{aligned} C_4(z,\phi,t) = {} & \frac{4\sin^2\phi}{(1+3\sin^2\phi)} \frac{\partial}{\partial z}\left[\frac{g(z)H(z,t)}{\nu_{in}(z,t)}\right] \\ & + \frac{4g(z)}{\nu_{in}(z,t)}\left(1+\frac{\partial H}{\partial z}\right)\frac{\sin^2\phi}{(1+3\sin^2\phi)} \\ & - \frac{g(z)H(z,t)}{(a+z)\nu_{in}(z,t)} \frac{\partial}{\partial \phi}\left[\frac{\sin(2\phi)}{1+3\sin^2\phi}\right] \\ & + \frac{g(z)H(z,t)}{\nu_{in}(z,t)} \frac{\sin(2\phi)}{(1+3\sin^2\phi)(a+z)} \\ & - \frac{8g(z)H(z,t)\sin^2\phi}{(a+z)\nu_{in}(z,t)(1+3\sin^2\phi)} \end{aligned} \tag{3.8}$$

$$\begin{aligned} C_5(z,\phi,t) = {} & -\frac{\sin 2\phi}{(1+3\sin^2\phi)} \frac{\partial}{\partial z}\left[\frac{g(z)H(z,t)}{\nu_{in}(z,t)(a+z)}\right] \\ & - \frac{g(z)H(z,t)}{\nu_{in}(z,t)(a+z)^2} \frac{\sin\phi\cos\phi}{(1+3\sin^2\phi)} \\ & - \frac{g(z)H(z,t)}{\nu_{in}(z,t)(a+z)^2} \frac{\partial}{\partial \phi}\left[\frac{\cos^2\phi}{(1+3\sin^2\phi)}\right] \\ & - \frac{g(z)}{\nu_{in}(z,t)(a+z)}\left(1+\frac{\partial H}{\partial z}\right)\frac{\sin(2\phi)}{(1+3\sin^2\phi)} \\ & + \frac{2g(z)H(z,t)}{\nu_{in}(z,t)(a+z)^2} \frac{\sin 2\phi}{(1+3\sin^2\phi)} \end{aligned} \tag{3.9}$$

$$C_6(z,\phi,t) = \frac{4\sin^2\phi}{(1+3\sin^2\phi)}\frac{\partial}{\partial z}\left[\frac{g(z)}{\nu_{in}(z,t)}\left(1+\frac{\partial H}{\partial z}\right)\right]$$

$$-\frac{2\,g(z)}{\nu_{in}(z,t)(a+z)}\left(1+\frac{\partial H}{\partial z}\right)\frac{\sin^2\phi}{(1+3\sin^2\phi)}$$

$$-\frac{g(z)}{\nu_{in}(z,t)(a+z)}\left(1+\frac{\partial H}{\partial z}\right)\frac{\partial}{\partial\phi}\left[\frac{\sin 2\phi}{1+3\sin^2\phi}\right]-\beta$$

$$-\frac{8\,g(z)}{\nu_{in}(z,t)(a+z)}\frac{\sin^2\phi}{(1+3\sin^2\phi)}\left(1+\frac{\partial H}{\partial z}\right) \qquad (3.10)$$

$$C_7(z,\phi,t) = Q \qquad (3.11)$$

3.3. Numerical scheme

In order to guarantee computational stability, we use the implicit method (Crank and Nicholson, 1947; Thompson, 1961; Richtmyer, 1967) for all terms in the RHS of equation (3.4) and the backward difference method for LHS term. We set 560 mesh points in the meridian plane, and apply equation (3.4) to each point. Thus we have 560 simultaneous linear equations which can be written in matrix form (see Appendix I for detail). The solution can be obtained easily by reversing the matrix by using a version of Gaussian elimination through internal function of the IBM 360. Later we increased mesh points to 1120, thus obtaining 1120 simultaneous equations. The two sets of results were compared. We found that the maximum difference is only 3%; therefore we believe that our solving technique is better than those obtained by using a two-dimensional model.

3.4. Boundary conditions

3.4.1. Lower boundary

At about 150 km both local change of electron density and plasma diffusion are much smaller than the production rate and chemical loss. This means that at any instant in daylight hours the rate of electron production and the rate of electron decay approximately balance each other. The electrons are then said to be in quasi-equilibrium (Ratcliffe, 1960). After sunset the decay rate is very fast in the E and lower F regions. The governing equation can be expressed approximately as

$$\frac{\partial N}{\partial t} = -\beta N$$

$$\text{or} \qquad N = N_o e^{-t/\tau_{chm}} \qquad (3.12)$$

where $\tau_{chm} = 1/\beta$ is a chemical time constant. Since $\tau_{chm} = 10$ sec at 150 km height, it needs only few seconds for one exponential decay. For these reasons, ionospheric workers always take the photoequilibrium state as the lower boundary condition in solving the continuity equation. For example, Strobel (1968) sets his lower boundary at 120 km height, Baxter and Kendall (1968) took 180 km altitude as the lower base and require quasi-equilibrium there.

The physics in the D-region is quite different from the F region. The presence of negative ions and the existence of attachment and detachment processes make the loss term no longer linearly dependent upon electron density. We can no longer assume that atomic oxygen is the main constituent; instead, we have to consider NO, N_2 and O_2 in the production of electrons. Furthermore, ionization sources are solar X-rays, Lyman α and cosmic rays. Therefore, the governing equations are much more complicated in the D-region. So, it is not a good idea to place the lower boundary level in the D region.

Based on the above explanations, the lower boundary in our model calculations is set at 150 km where we require the ionization density to be in photochemical equilibrium, i.e.

$$N = \frac{Q}{k_1 \, n(N_2) + k_2 \, n(O_2)} \qquad (3.12)$$

3.4.2. Upper boundary

At 1000 km height, the diurnal variation of electron density is small, being about 3 at low latitudes and 1.5 at mid- and high-latitude regions (Brace et al., 1967), while at the F2 peak, the diurnal change may reach one order of magnitude. The electron density distribution pattern does not vary much at such heights as diffuse equilibrium predominates. We use the averaged observational figures measured by Alouette I for the upper boundary values which is set at 1000 km height.

3.4.3. Equatorial lateral boundary

According to Goldberg (1969), there are two approaches in dealing with the equatorial F2 region ionosphere, i.e. the causal approach and the semiphenomenological approach. The causal approach postulates specific mechanism for the basic cause of the geomagnetic anomaly (Kendall, 1962; Maeda, 1963; Kendall and Windle, 1965; Hanson and Moffett, 1966; Baxter, 1967). The semiphenomenological approach does not assume that the physical cause to the problem is known. Instead, it accepts the vertical density profile at the magnetic equator or some other density profile crossing magnetic field lines as an observed boundary condition, and then proceeds to calculate the electron density at other latitudes and altitudes (Goldberg and Schmerling, 1962; Goldberg et al., 1964; Chandra and Goldberg, 1964; Baxter and Kendall, 1965).

During the equinox, since solar radiation is symmetric with respect to the equator, it is a good method to use $\partial N/\partial \phi = 0$ as the equatorial lateral boundary condition. Baxter (1967) has used this symmetric condition to solve a time varying diffusion equation for the F2 layer. However, in our numerical model, we chose averaged N-h profiles measured by the Alouette I topside sounder for the equatorial boundary values. We prefer to follow second approach because although this chapter, refers to the equinox, when we discuss the seasonal anomaly in chapter 4, we have to solve both summer and winter conditions for which $\partial N/\partial \phi = 0$ is no longer valid. Therefore in order to use the same computer program for different seasons with only minor corrections, we used actual N-h profiles at the equator for the boundary condition.

3.4.4. Polar lateral boundary

During the equinox, the production rate of electrons is zero at the pole. The electrons created in the lower latitudes cannot be transported to the pole unless there is electric field drift. Thus, in our simple model for the present chapter, the electron density should be zero at the polar boundary. In the F region, the electron density is under both solar and geomagnetic control. The electron density is lower in the polar region due to the weak production rate. For the purpose of comparison, we have made calculations by using $N = 0$ and $N \neq 0$ for the polar boundary condition. The results do not show much difference in the interior regions (see section 3.5.1). Therefore, we take $N = 0$ for the polar boundary condition in this chapter.

3.5. Computer results

3.5.1. General remarks

Our computer results are very good. Not only is the magnitude of the electron density close to the real one, the distribution pattern in the whole ionosphere is also quite similar to the Alouette I results. We started at 12 o'clock, omitted the $\frac{\partial N}{\partial t}$ term at this moment and solved the steady state equation. The values we got at this time were used as initial input data. We then kept the $\frac{\partial N}{\partial t}$ term and proceeded until a periodic solution came out. It is noted that we may start at any local time to calculate the initial values. The periodic solution should be the same, except that the iteration time on which the periodic values comes out will differ. The periodic solution appears at about 30 model hours whereas Strobel's model (1968) needed three simulated days and Yeh (1968) spent at least two days to obtain his periodic results. We first used 15 minutes and 50 km for time step and grid interval, then 5 minutes and 25 km. It was found that the maximum difference in N is not over 5%. Furthermore, when we changed the top boundary values of N by 30%, the results showed only 3% of the influence to those points in the third row from the boundary, and beyond that the effect is getting smaller and there is no change at all in the interior region. We also used $N = 0$ and $N \neq 0$ for the polar lateral boundary condition, the results in these two cases were compared. We found that the maximum difference in the row next to the polar boundary (2.5^{o} latitude away) is less than 0.9%. In the second row to the polar boundary, the maximum difference is less than 0.2%, and no essential change in interior region.

In equation (2.34) the third term on the RHS was inadvertently taken as $\frac{\partial \Phi_z}{\partial z}$ instead of $\frac{\partial \Phi_z (a+z)^2}{(a+z)^2 \partial z}$ in this set of calculation. The effect of the error on the results is discussed in section 3.7.

The only disadvantage in our technique is that it requires a large memory space. The maximum capacity of IBM 360 is 45000 bits. We have already used 41000 bits in our numerical computations. We, therefore, cannot decrease grid intervals any further.

3.5.2. Meridional electron density cross section

Figs. 3.1-3.3 show the periodic solution of the electron density distribution in the meridional plane by solving equation (3.4). The electric field and the neutral winds were not included at this moment. The results agree excellently with observational facts both in magnitude and in their distribution patterns. One important fact, which this calculation revealed, should be mentioned. During the daytime, the maximum electron density at the peak occurs at about 4° or 5° away from the equator. This shifting is due to downward diffusion due to gravity and pressure. After sunset, N_mF2 begins decreasing, as expected. However, the location of the peak moves toward 15 degrees after 22 hours and stays until sunrise. This phenomenon could be due to horizontal movement of plasma from the equator. We shall come back to this point as we examine the total vertical content diagrams.

3.5.3. Vertical N-profiles

Figs. 3.4-3.6 show the diurnal variation of electron densities in vertical profiles at 5, 40 and 75 degrees latitude. Again the profiles resemble the observational facts. Above about 500 km, all curves appear as straight lines in the logarithmic scale showing electrons in diffusion equilibrium.

3.5.4. Diurnal variation of h_mF2

From meridional cross sections, we see that h_mF2 is about 300 km at the equator and decreases to 250 km in the polar region during the daytime hours and rises to 350 km after sunset for the stationary atmosphere. In order to see more clearly, we plotted the diurnal variation of h_mF2 in Fig. 3.7 for 5 and 40 degrees. The solid lines represent h_mF2 without neutral winds. Two interesting features should be noticed here. First, after sunset at 18 hours, the h_mF2 rises about 50 km at both 5 and 40 degrees latitude. The highest height of the F2 peak is around 20 hours. However, for low latitudes this increasing h_mF2 remains until sunrise, while for mid-latitudes it falls back at 23 hours. Second, after sunrise at 6 hours, h_mF2 drops suddenly to its lowest position until 8 o'clock, then rises gradually to the normal daytime condition. The sudden drop is more pronounced at low latitudes as is clearly seen in Fig. 3.7. This phenomenon is due to a sudden increase in the production rate of electrons by solar radiation at about 180 km height.

3.5.5. Diurnal variation of N_mF2

Fig. 3.8 shows the diurnal variation of maximum electron density at 5, 40 and 75 degrees latitude. The maximum N_mF2 occurs at about 16 hours and the minimum N_mF2 is at 6 hours, just before sunrise, at

5 degrees latitude. The ratio of daytime maximum to nighttime minimum is about 5. Note that the decrease of electron density is rapid at the beginning of sunset between 18 and 20 hours. Then it decays slowly until the minimum value is reached, at the time before sunrise. After sunrise, the rate of ionization increases rapidly between 6 and 8 hours, then slows down.

At mid and high latitudes, the maximum N_mF2 appears at about 13 hours. The minimum N_mF2 occurs at the same time as in low latitudes. The diurnal ratio of maximum N_mF2 to minimum N_mF2 decreases as latitude increases, being approximately 3 in high latitudes. The decay rate after sunset is smaller in the higher latitudes than in lower ones. Worldwide curves of N_{max} have been plotted in Fig. 3.9. The contours are similar to experimental world curves as given by Martyn (1959).

3.5.6. Total electron content

The total electron content between 150 km and 1000 km has been integrated. The latitudinal variations of N_t for the whole 24-hour period for one hour intervals have been drawn in Figs. 3.10-3.15. The most interesting feature, as we mentioned earlier, is that starting at sunrise, and throughout the whole day until sunset, the total electron content per square centimeter cross-section is always highest at the equatorial region, as it should be. After sunset, N_t decreases in all latitudes. However, the rate of decrease is much larger in the equatorial belt within 5 degrees. As time goes on, the rapid decrease of N_t in the equatorial belt is associated with an increase of N_t in the subtropics at about 15°. This increase of electron content in the subtropical region is clearly due to horizontal movement of plasma from the equator along the field lines. The physical argument is this: during daytime, the ionization created by solar EUV radiation is higher in the equatorial region than at any other places. When the sun goes down, the ionization between 1000 km and F2 peak cannot be destroyed through chemical reaction within few hours time. Thus the plasma will slide down along the field lines due to the pressure gradients. Since the field line of 1000 km height at the equatorial plane links the height of 400 km at about 17°, the north bound of latitude where the plasma appears to increase after sunset is about 17 degrees.

Wright (1960) found that at Bogota (15°N geomagnetic latitude), N_{max} increases during the night. He claimed that the intense ionization at night is due to transport from regions near the equator. Rao (1963) also reported an observational fact of postsunset rise in f_oF2 in the transition region, extending from about 30 to 40 dip. Sato (1968a) gave more detailed descriptions of this nighttime abnormal enhancement of F_2 region electron density. The most remarkable geomagnetic latitude where the anomalous enhancement occurs is at 16°-17° as described by Sato. The major enhancement appears between 20 and 24 hr. A recent paper by Brown, et al., (1968) reported that the oxygen red lines are enhanced after mid-night in Hawaii (14° magnetic latitude). They estimated that a column content of 1.08×10^{13} electron per cm^2 column is needed for a burst with a lifetime of 1.5 hr. But the winter mid-night value of electron content in Hawaii is about $(0.44 \pm 0.12) \times 10^{13}$ electron/cm^2 - col. Therefore, a source of electron is required.

According to Peterson (1966), the electrons recombine above 90 km almost exclusively by dissociative recombination with the molecular ions, O_2^+ and NO^+:

$$O_2^+ + e \longrightarrow O + O + 6.96 \text{ ev}$$

$$NO^+ + e \longrightarrow N + O + 2.76 \text{ ev}$$

The molecular ions came from the following reactions:

$$O^+ + O_2 \longrightarrow O_2^+ + O + 1.53 \text{ ev}$$

$$O^+ + N_2 \longrightarrow NO^+ + N + 1.09 \text{ ev}$$

Dissociative recombination in the F region appears to be the dominant process, in the night and at low latitudes, for the production of excited oxygen atoms that give rise to the 6300 $\mathring{A}$ night glow.

In Fig. 3.12, the peak column content occurs at about 15° latitude, and is about 1.8×10^{13} electrons/cm^2 - col which is roughly the required value for one burst of airglow as estimated by Brown, et al., (1968). Therefore, I suggest that the increased electrons at 15° latitude during the night come from the equatorial region and that a part of the electron source which makes the airglow comes from this mechanism as well as from the other ionization sources.

3.6. The effect of neutral winds

Undoubtedly, the effect of neutral winds on the electron density distribution is very important (Rishbeth, 1967a, 1968b).

Especially in the mid-latitude area, the nighttime electrons could be reserved through wind effect (King and Kohl, 1965; Strobel, 1968). The north-south asymmetry in N_mF2 could also be caused by wind blowing from one hemisphere to the other (Abur-Robb and Windle, 1969). In this section, we do not intend to give a full discussion on winds. Our purpose is to present some evidence about the role of the winds by making numerical calculations including winds. Since we know that the meridional winds tend to blow toward the pole during the day and toward the equator at night (Geisler, 1966, 1967; Kohl and King, 1967), the model of meridional wind chosen is simple harmonic, being poleward during the period 0600-1800 hr local time and equatorward for the remaining period. The latitudinal distribution of wind is similar to Fig. 4.10 with peak at 45° latitude where the diurnal maximum amplitudes are 40 m/sec and 80 m/sec at 12 and 24 hours respectively. For simplicity, the height variation of wind is neglected. In this idealized wind model, the modification of equation (3.4) is simple. Only coefficients C_4, C_5 and C_6 need to be modified. We require to add a term $V_n(t)\,\mathrm{Sin}\,t\,\mathrm{Sin}^2 2\phi/(1+3\mathrm{Sin}^2\phi)$ to C_4, and subtract $\dfrac{V_n(t)\,\mathrm{Sin}\,t\,\mathrm{Cos}^2\phi\,\mathrm{Sin}\,2\phi}{(a+z)(1+3\,\mathrm{Sin}^2\phi)}$, and

$$\frac{V_n(t)\,\mathrm{Sin}\,t}{(a+z)}\left[\frac{-3\,\mathrm{Sin}\,\phi\,\mathrm{Sin}\,2\phi\,\mathrm{Cos}\,\phi+2\,\mathrm{Cos}^2\phi\,\mathrm{Cos}\,2\phi}{(1+3\,\mathrm{Sin}^2\phi)}-\frac{3\,\mathrm{Cos}^2\phi\,\mathrm{Sin}^2 2\phi}{(1+3\,\mathrm{Sin}^2\phi)^2}\right]$$

from C_5 and C_6 respectively. The effects of the winds are clearly seen in Figs. 3.7, 3.16 and 3.17. The main features are summarized as follows:

(a) Effect on h_mF2

Fig. 3.7 shows the wind effect on the F2 peak height. In the low latitudes, h_mF2 decreases during the day by about 15 km and increases about 40 km during the night. In mid and high latitudes h_mF2 does not change much during daytime hours. This is probably due to the fact that the field lines are steeper in mid and high latitudes compared to those in the low latitudes. Therefore, the horizontal wind effect should be getting smaller as the dip angle gets higher.

(b) Effect on electron density

Below about 600 km and above the F2 peak, the electron density tends to increase a little for constant height levels during the night, and to decrease during the day. Fig. 3.16 shows those changes for 300 and 400 km at 12 hour and for 400 and 500 km at 2 hour. The N-h profiles with and without winds are also plotted in Fig. 3.17 at 5 and 10 degrees of latitudes and at 12 hour. It is seen in Fig. 3.17b that the descending of h_mF2 is accompanied by a decrease of N_mF2. This is due to the larger recombination rate in the lower altitudes. The fact that the electron density is insensitive to the winds above 600 km is partly due to the lower recombination rate and partly due to the smaller collision frequency whereby the diffusion plays the dominant role.

3.7. Error remarks

It should be noted that during numerical calculations we inadvertently used $\partial \Phi_z/\partial z$ for $\partial \Phi_z (a+z)^2/(a+z)^2 \partial z$ in equation (2.34). Thus we lost the $2\Phi_z/(a+z)$ term which in turn meant that we lost the last term for C_4, C_5 and C_6 in equations (3.8), (3.9) and (3.10) respectively. The other C's (C_1, C_2, C_3, C_7) did not change. Fortunately, this mistake does not make a serious error in the results, because each lost term in C_4, C_5 and C_6 contains a factor of $1/(a+z)$ which is very small. We checked the numerical figures for each term in C_4, C_5 and C_6 and found that only C_5 is significantly altered. In order to estimate the maximum error created by missing the terms in equation (3.4), we calculated equation (3.4) with corrected and uncorrected coefficients of the C's. We found that the maximum error is less than 0.8% which occurs at 250 km height and at 45° latitude.

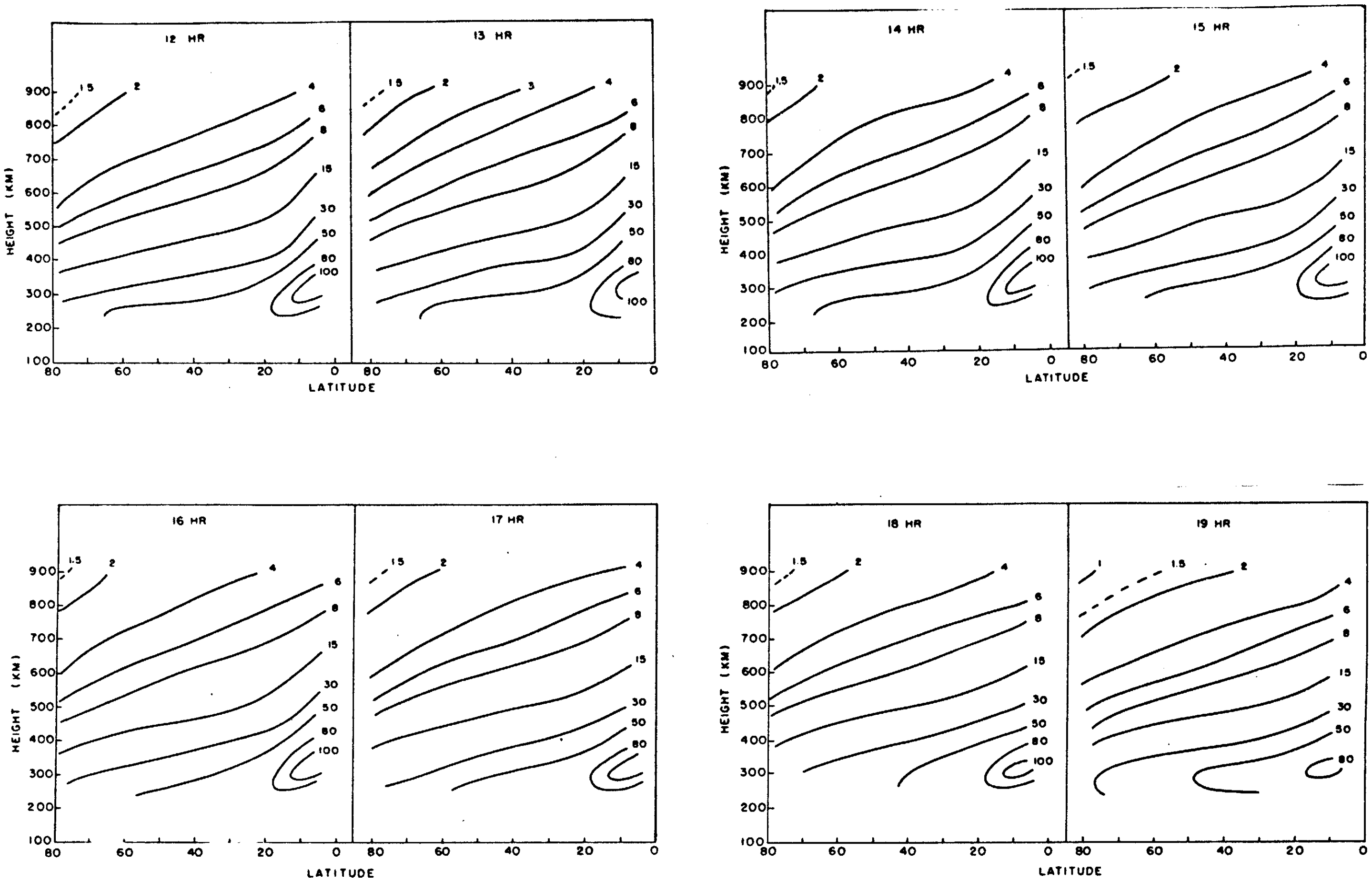

Fig. 3.1. Meridional cross sections of electron density at 12 through 19 hours computed from equation of continuity. Units 10^4 el/cm^3.

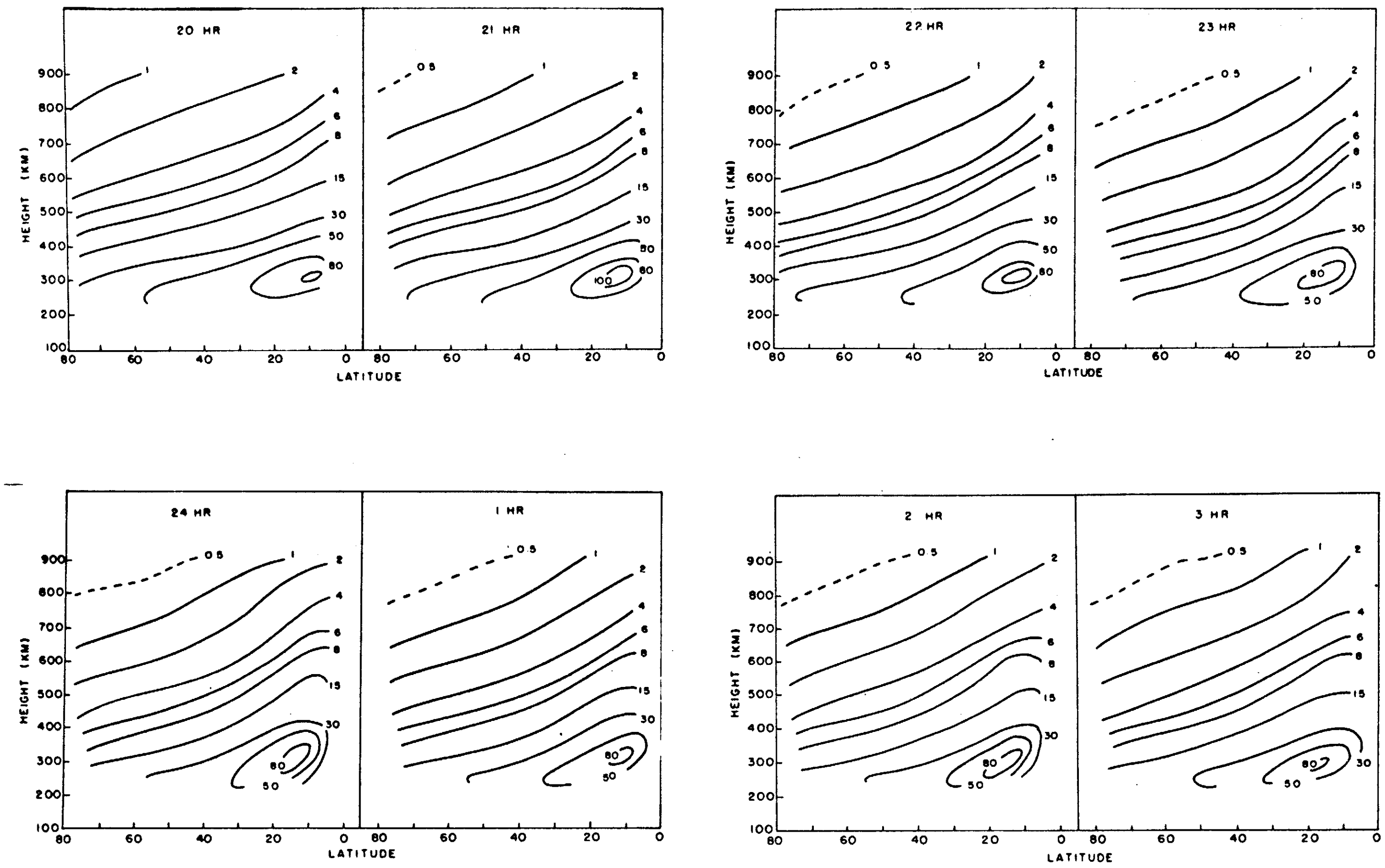

Fig. 3.2. Meridional cross sections of electron density at 20 through 3 hours computed from equation of continuity. Units 10^4 el/cm^3.

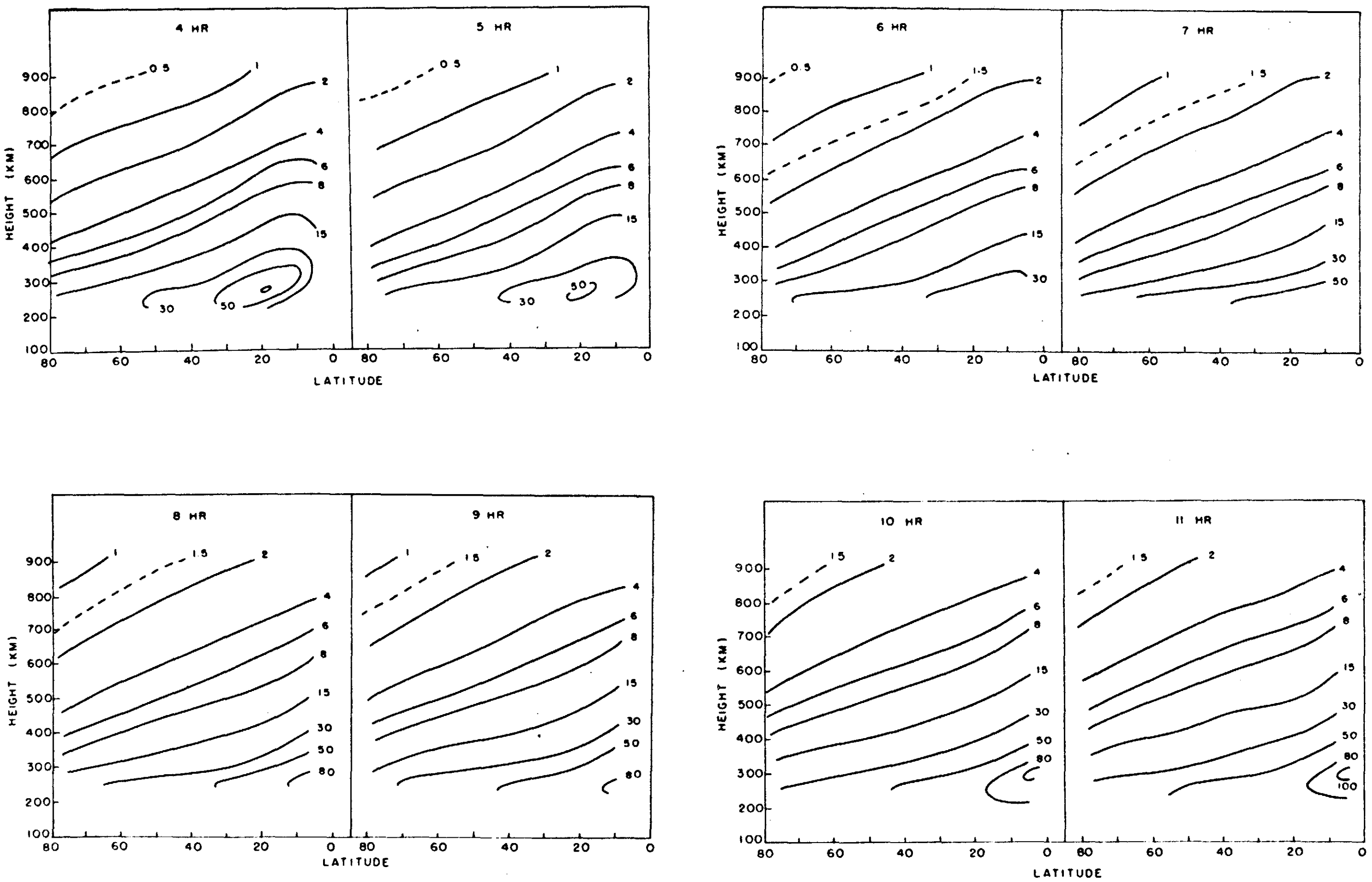

Fig. 3.3. Meridional cross sections of electron density at 4 through 11 hours computed from equation of continuity. Units 10^4 el/cm^3.

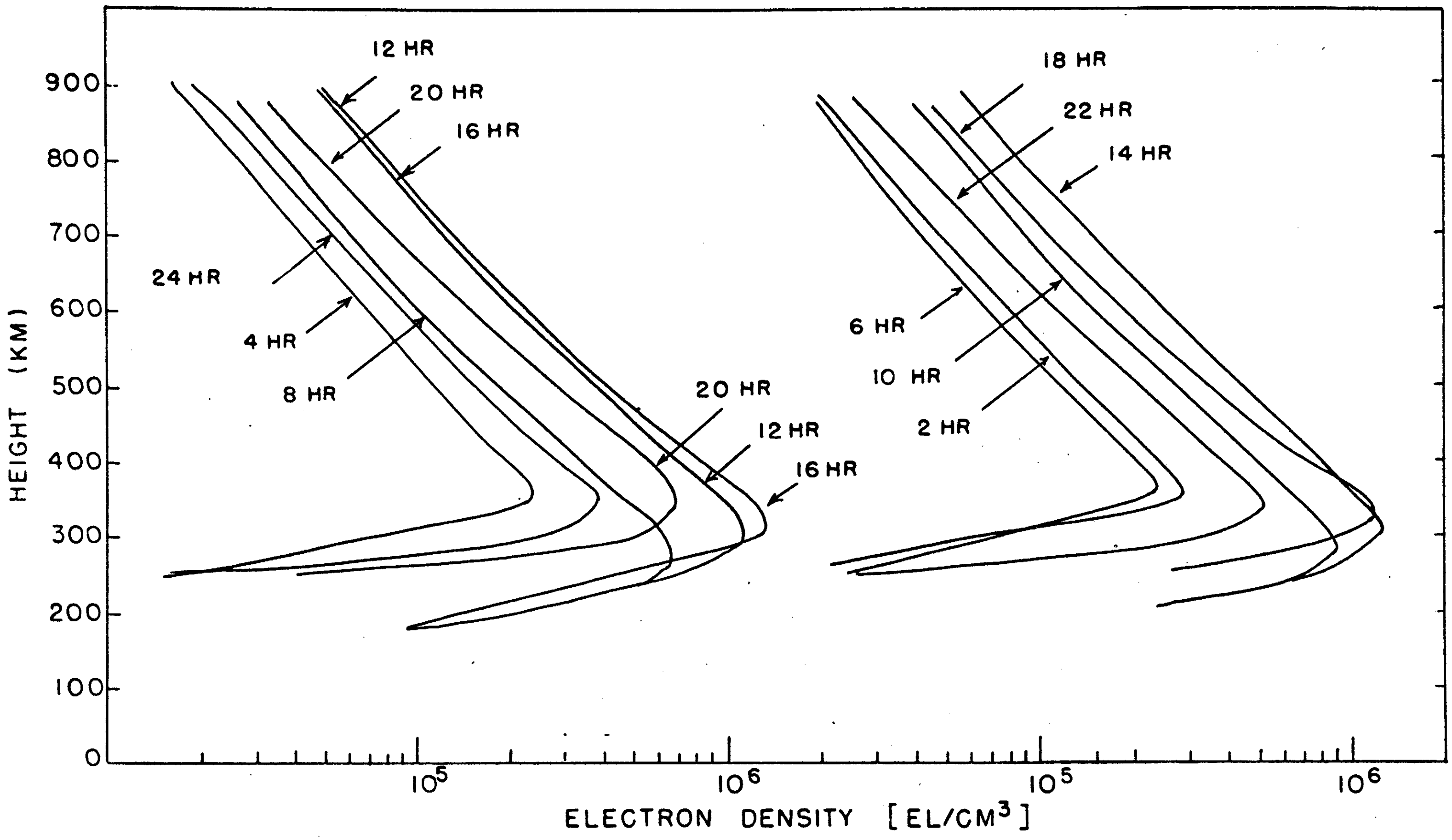

Fig. 3.4. Diurnal variation of vertical electron density profiles at 5° latitude computed from equation of continuity.

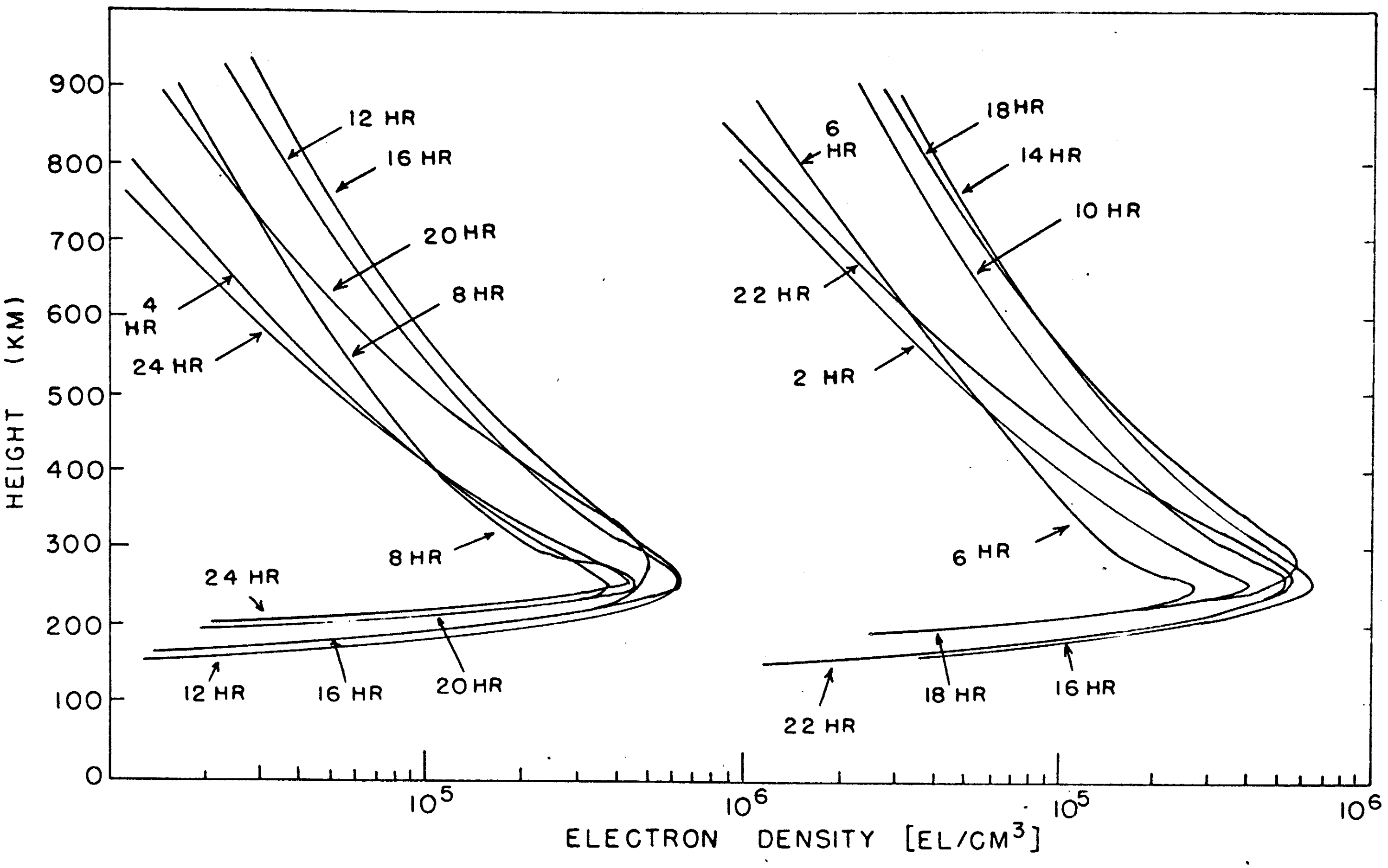

Fig. 3.5. Diurnal variation of vertical electron density profiles at 40° latitude computed from equation of continuity.

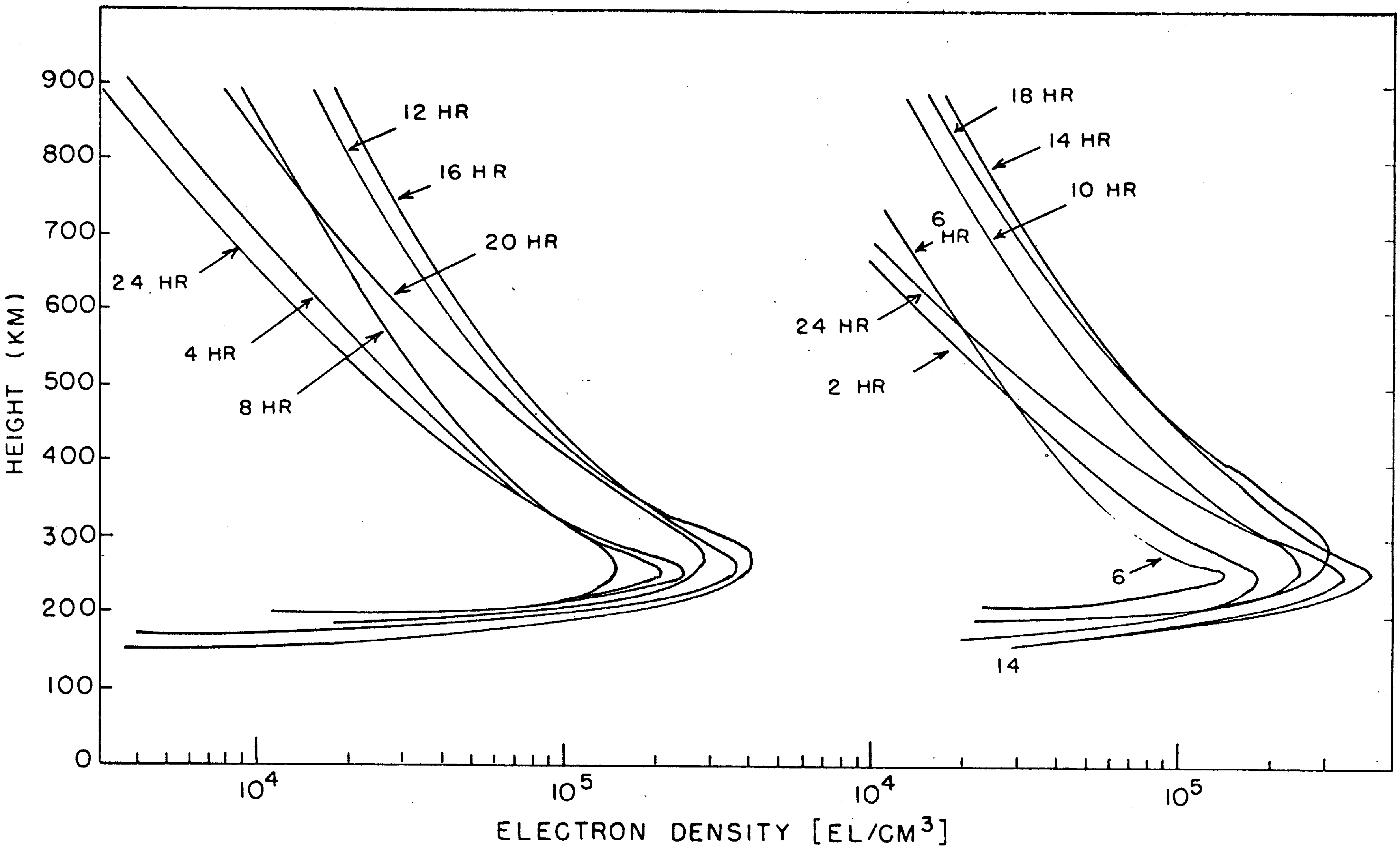

Fig. 3.6. Diurnal variation of vertical electron density profiles at 75° latitude computed from equation of continuity.

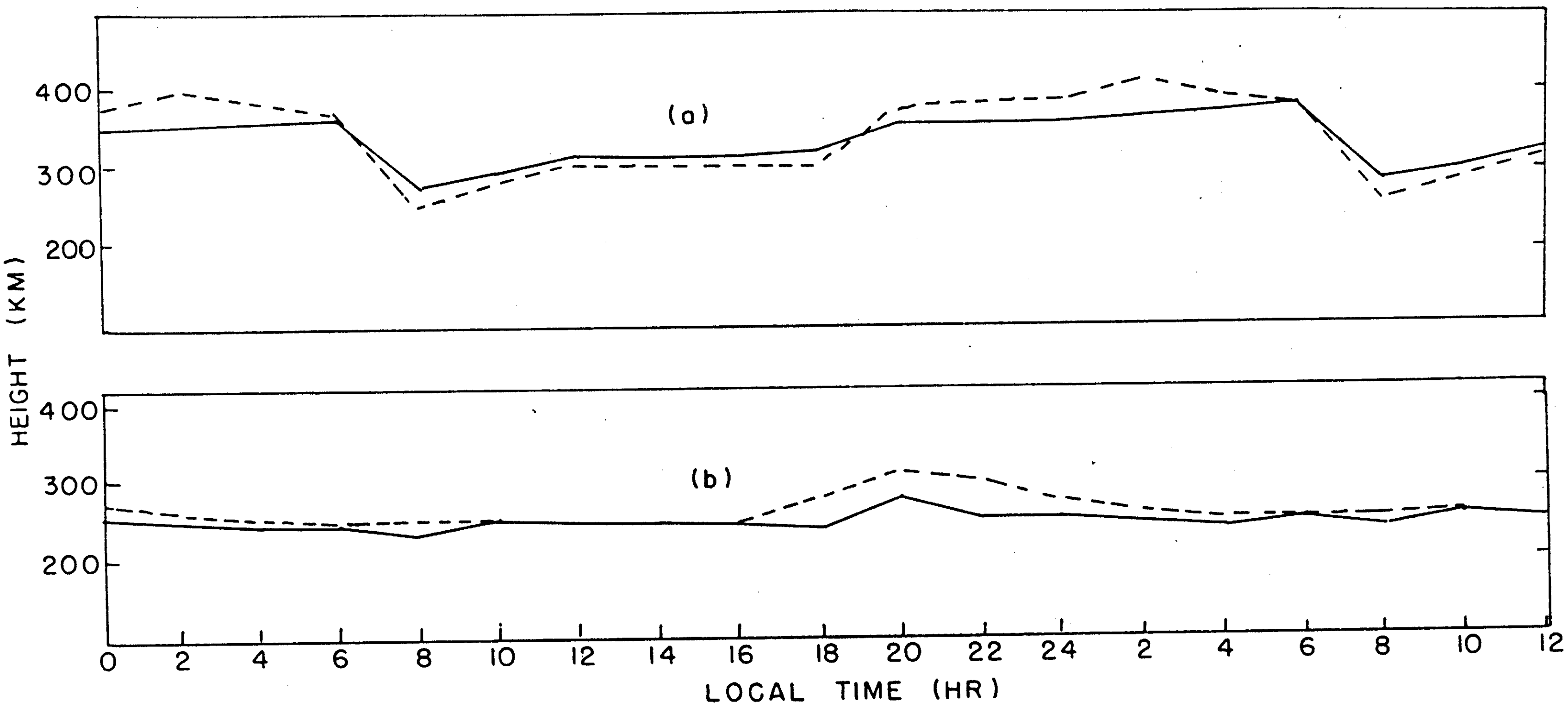

Fig. 3.7. Diurnal variation of hmF2. The solid curve represents the stationary atmosphere case, the dashed for the case with neutral winds, being 40 m/sec toward pole at 12 HR and 80 m/sec toward equator at 24 HR. (a) at 5° lat., (b) at 40° lat.

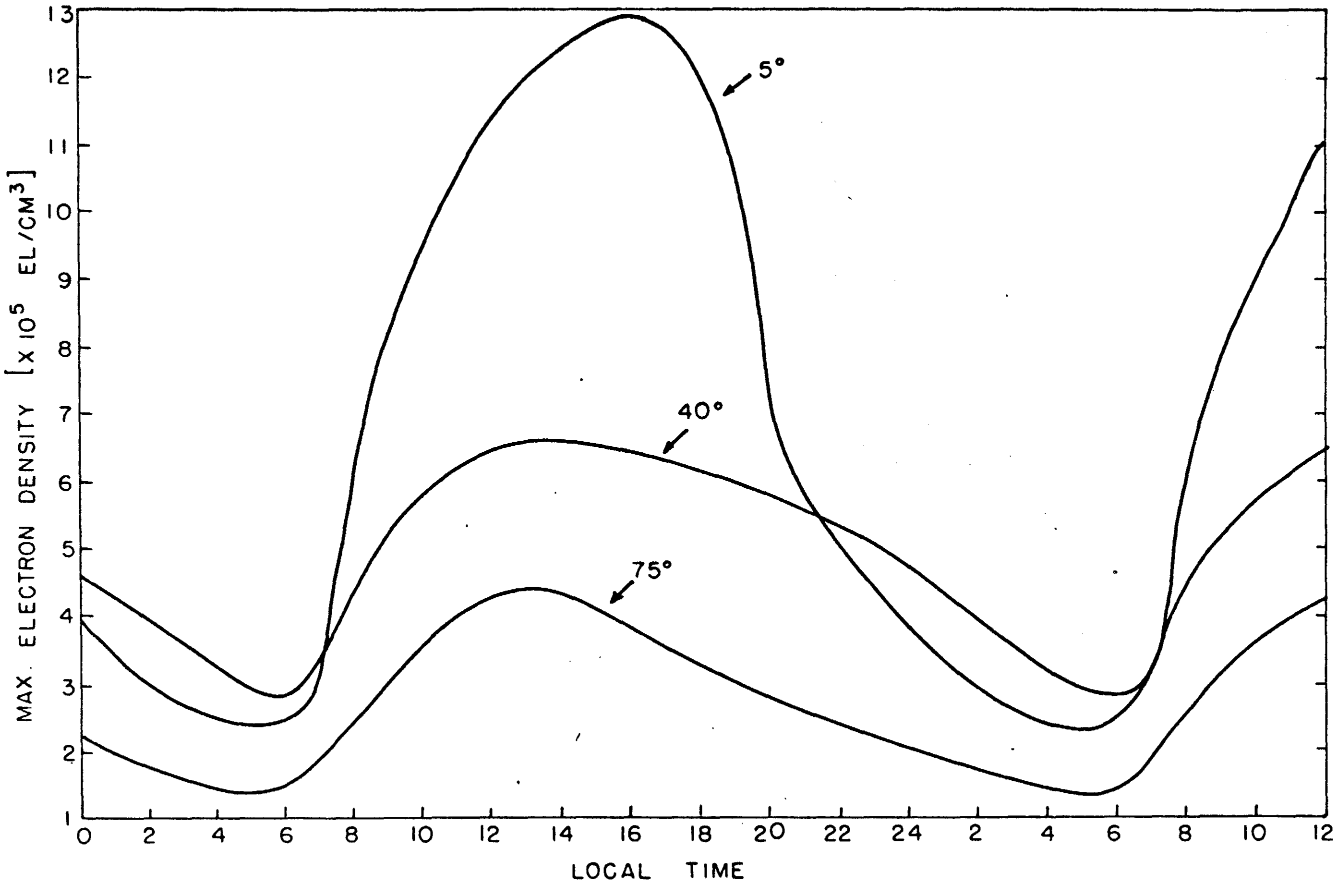

Fig. 3.8. Diurnal variation of N_{max}F2 at 5°, 40°, and 75° latitudes.

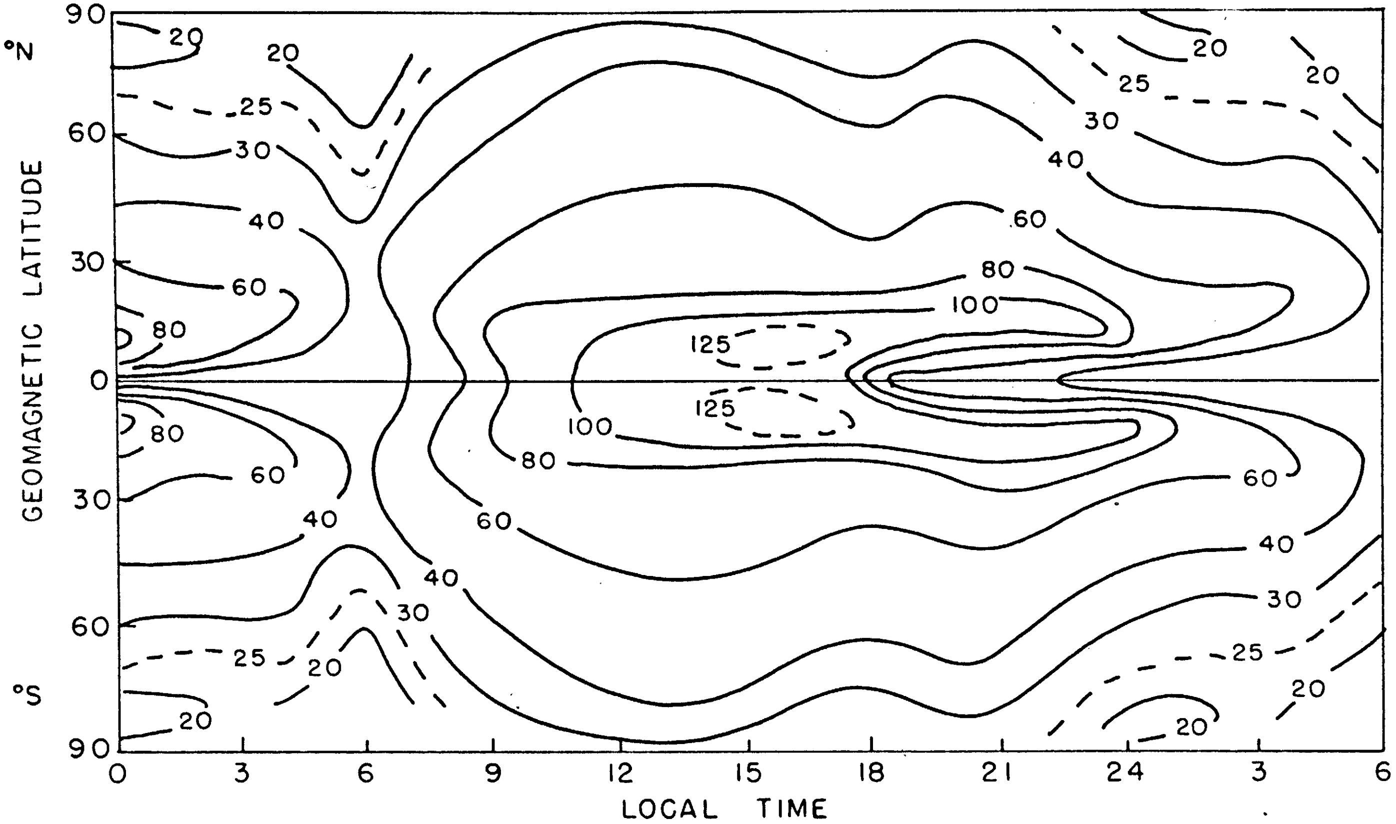

Fig. 3.9. World curves of $N_{max}F2$ at the equinox. Units: 10^4 el/cm^3.

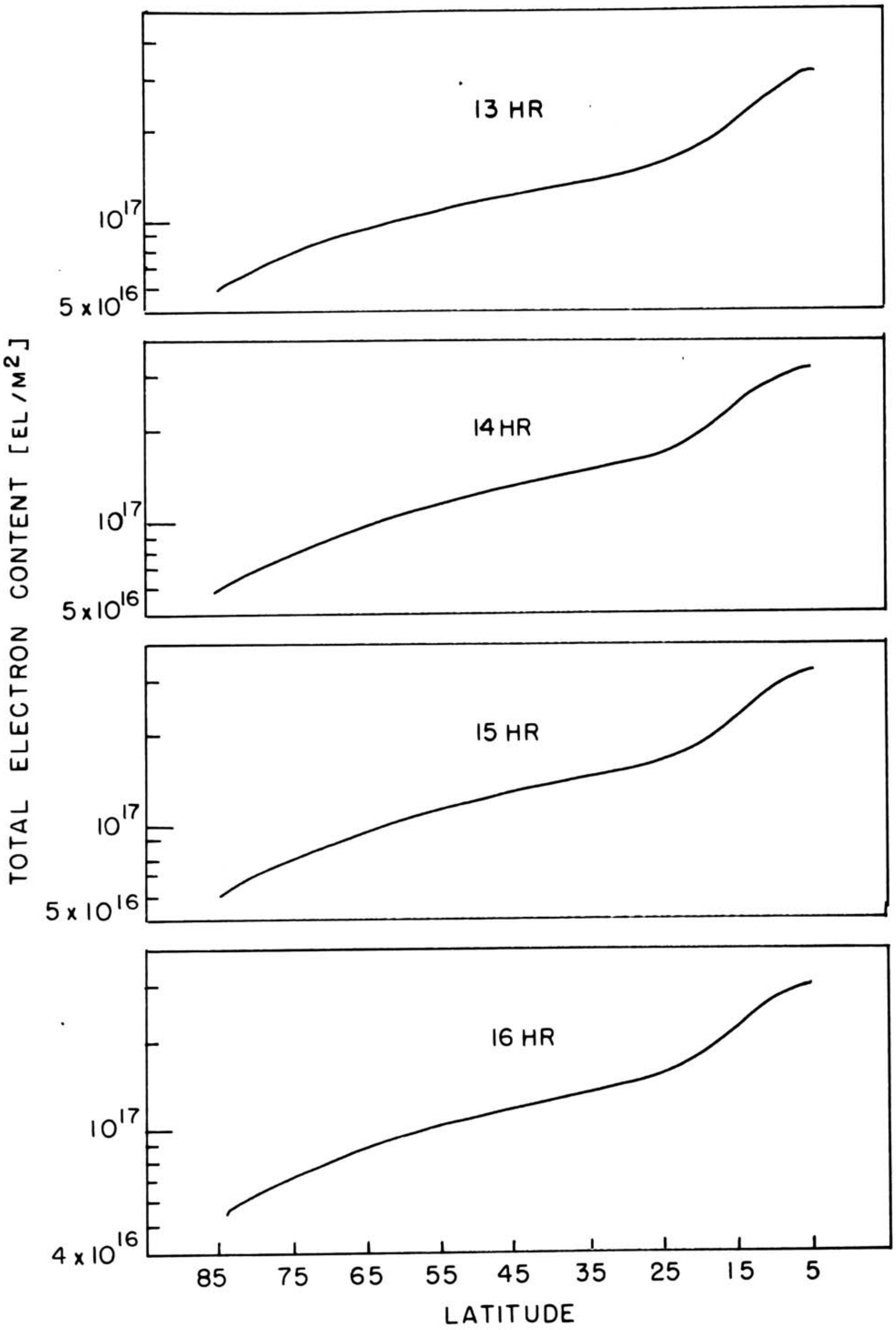

Fig. 3.10. Latitudinal variation of total electron between 150 km and 1000 km heights.

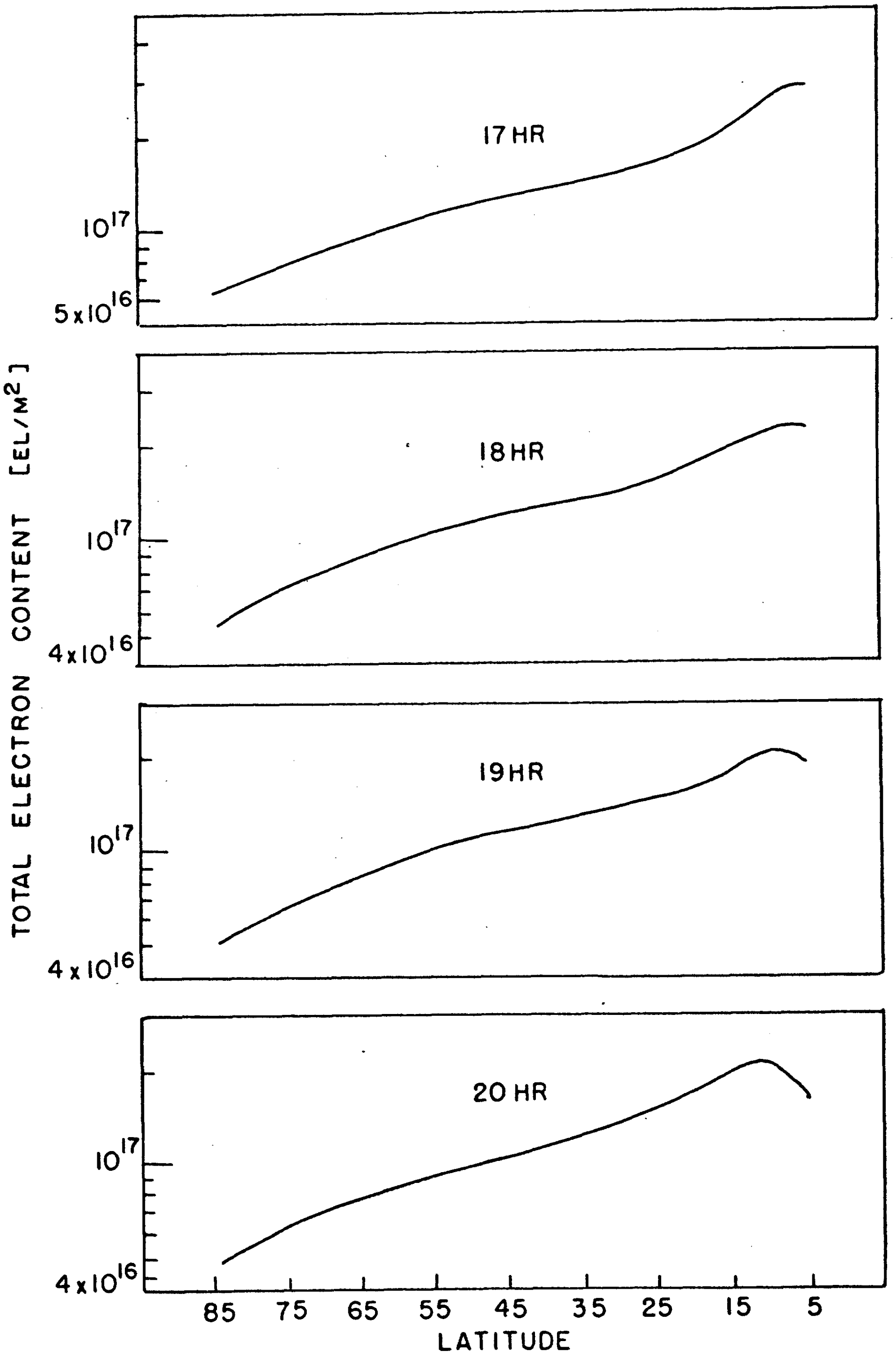

Fig. 3.11. Latitudinal variation of total electron content between 150 km and 1000 km heights.

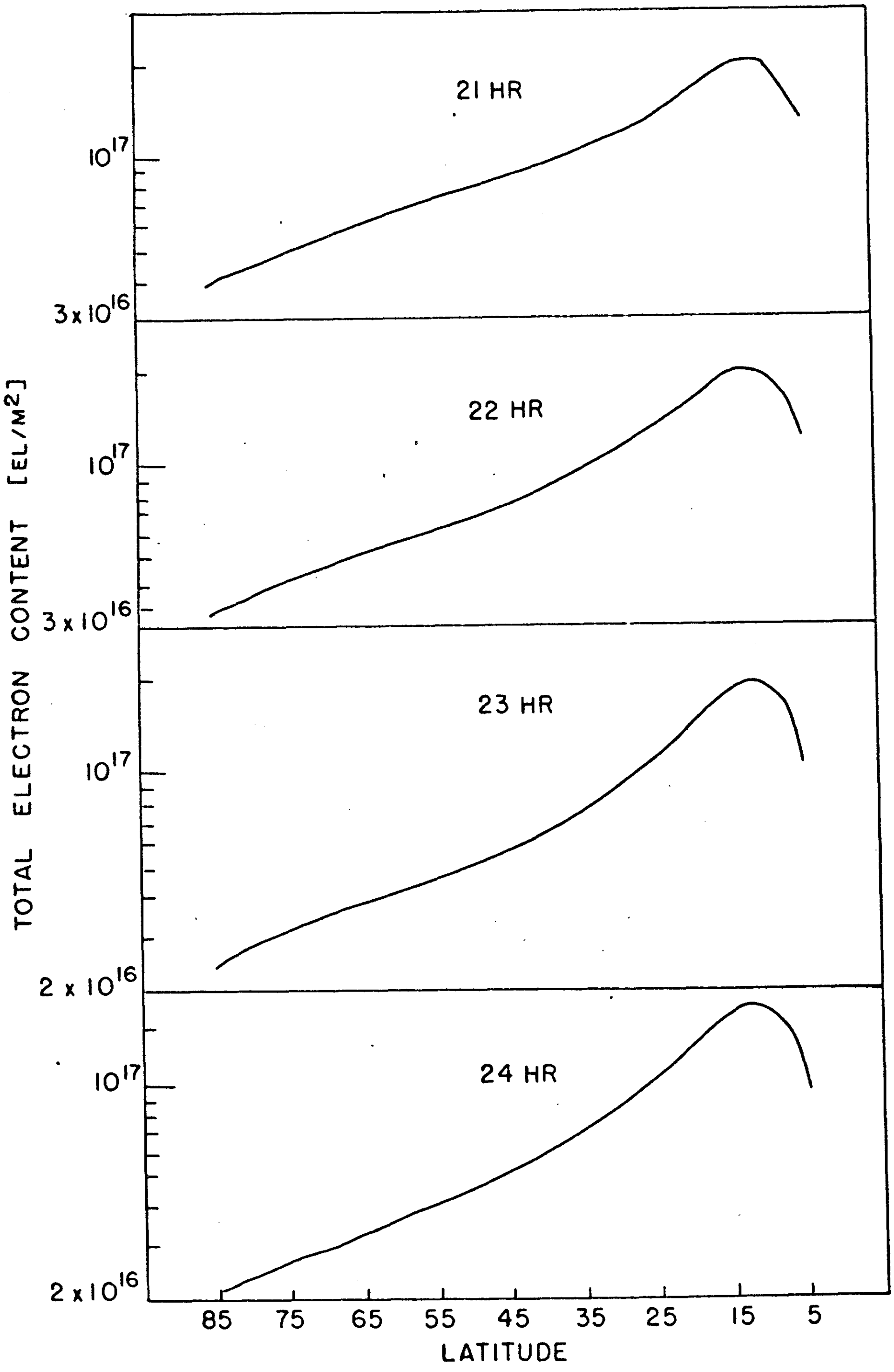

Fig. 3.12. Latitudinal variation of total electron content between 150 km and 1000 km heights.

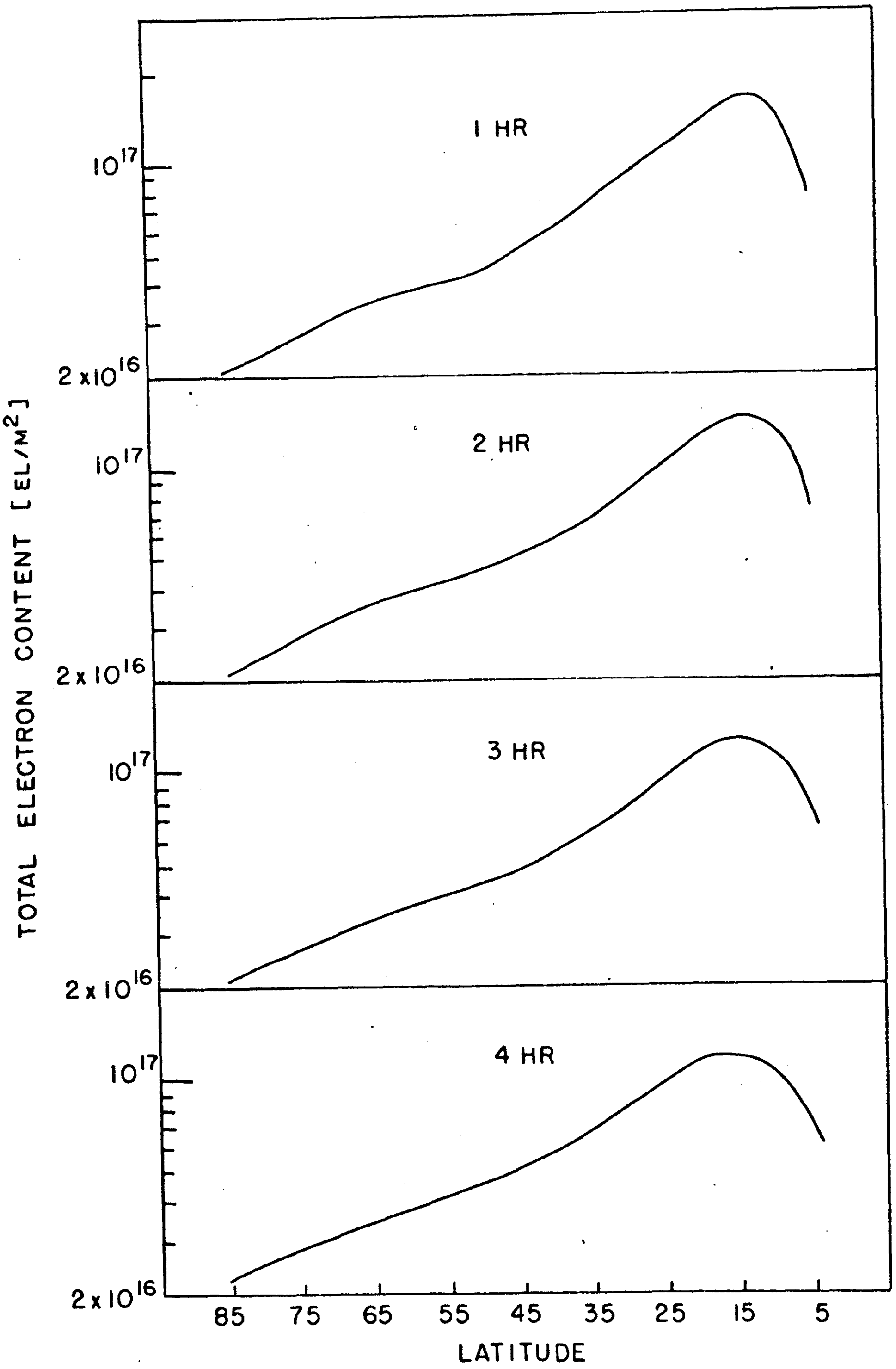

Fig. 3.13. Latitudinal variation of total electron between 150 km and 1000 km heights.

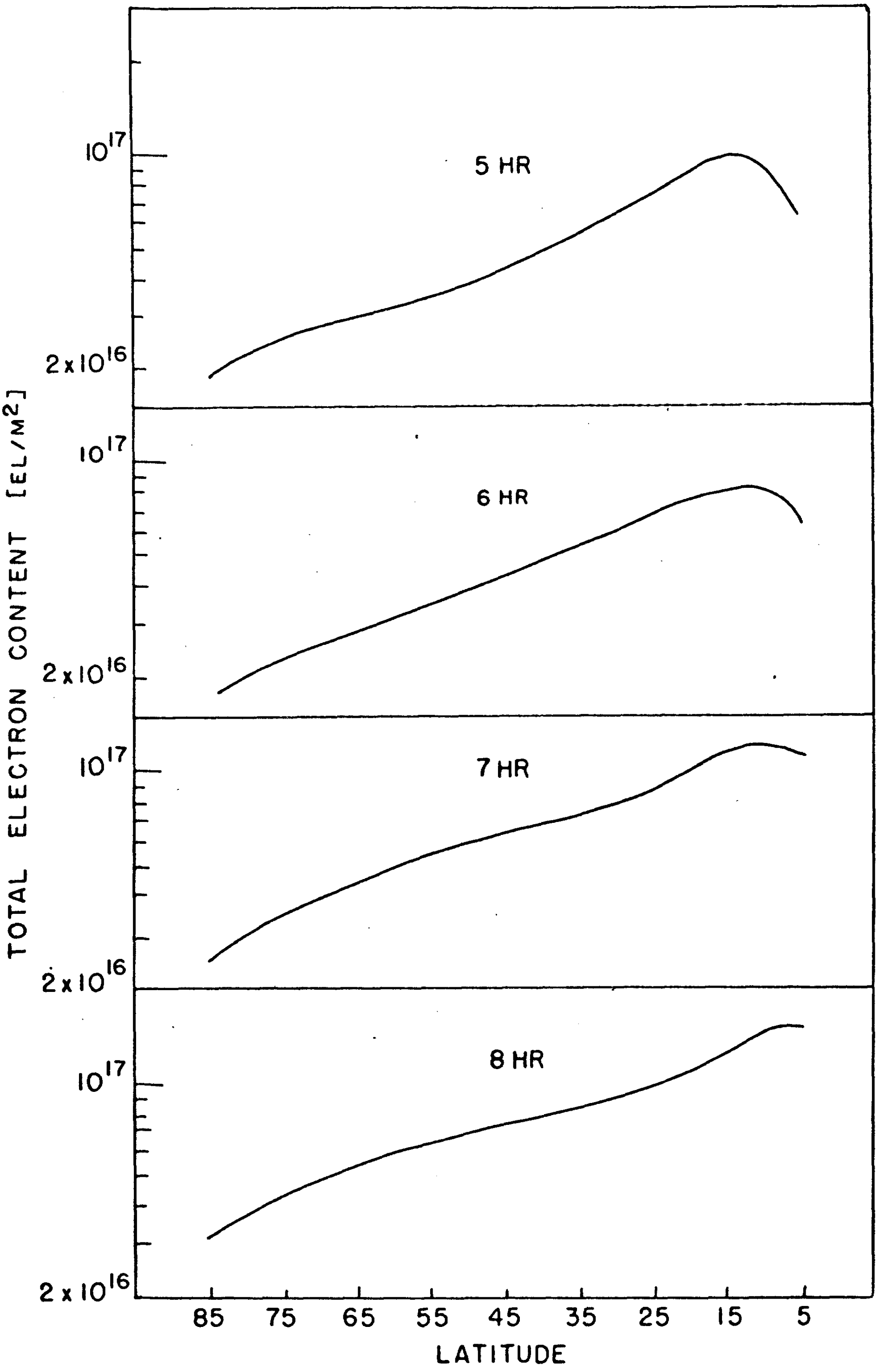

Fig. 3.14. Latitudinal variation of total electron content between 150 km and 1000 km heights.

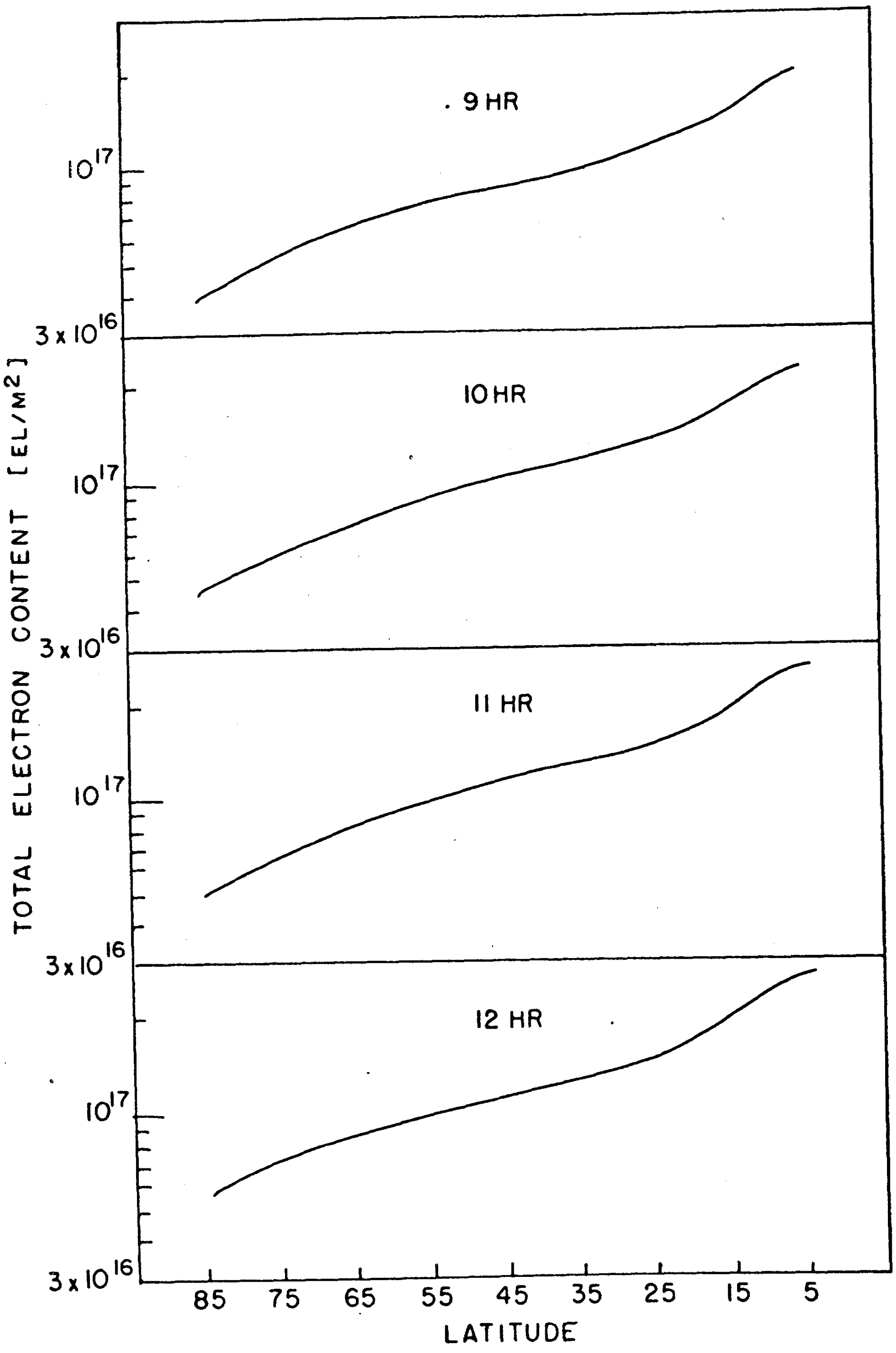

Fig. 3.15. Latitudinal variation of total electron content between 150 km and 1000 km heights.

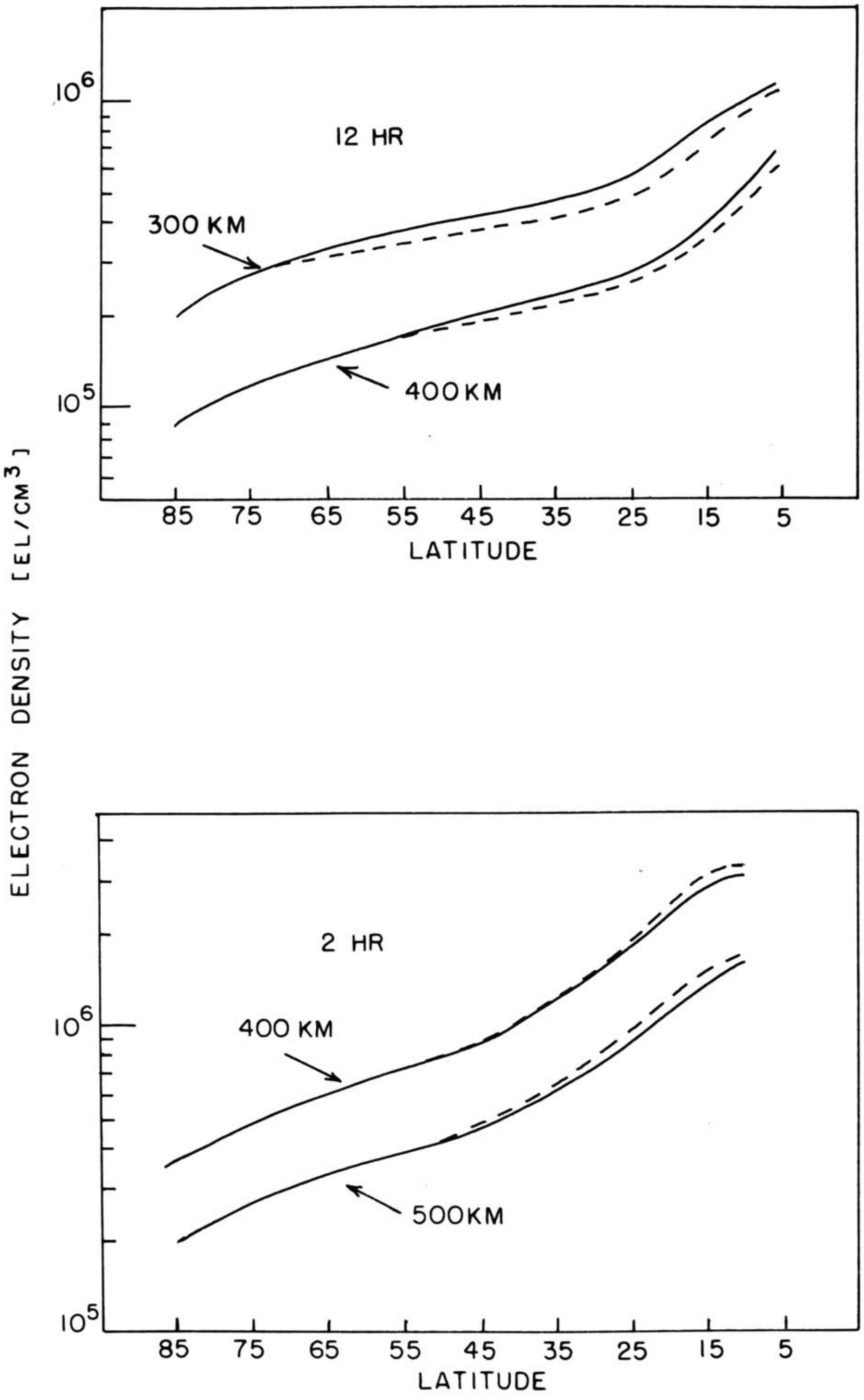

Fig. 3.16. Latitudinal variation of electron density at constant heights at 12 and 2 hrs. The dashed curves represent the case in which a poleward wind of 40 m/sec at midday and an equatorward wind of 80 m/sec at midnight, the solid curves without winds.

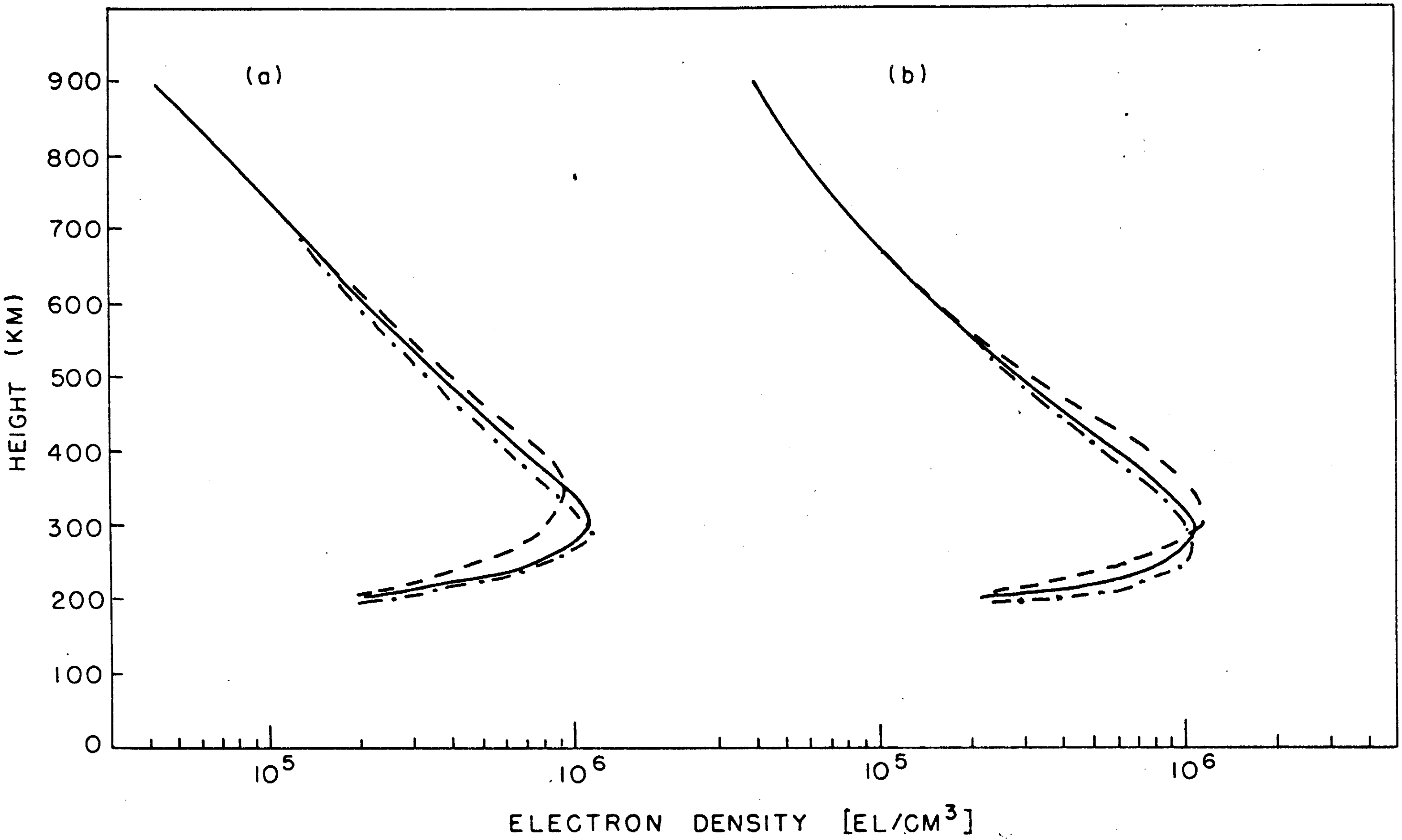

Fig. 3.17. N-h profiles at 12 HR. The solid curves represent the case of a stationary atmosphere, dashed with upward drift velocity of 20 m/sec below 10° latitude at 12 HR, the dotted-dashed with wind of 40 m/sec toward pole. (a) at 5° lat. (b) at 10° lat.

CHAPTER 4

SEASONAL ANOMALY IN F REGION

4.1. Introduction

During midday, F-region critical frequencies (f_oF2) are greater in December than in June. This phenomenon is particularly pronounced in the midlatitudes in the Northern Hemisphere, and is called the 'seasonal or winter anomaly'. The physical courses of this anomaly have a long historical debate. Although many suggestions have been made, yet a satisfactory theory is still lacking. Up to the present, at least half of a dozen proposals have been discussed among different scientists. Each one states his own evidence and fights against that of the others. However, none of them possesses a sufficient reason to convince each other. In this chapter, I would like to present a brief review of the current theories first, and then I shall present my own computations and evidence obtained through analyzing the satellite data, and join the debating crowd.

4.2. Current theories

4.2.1. Seasonal change of neutral atmosphere composition

In the F-region, electrons are mainly produced by the photoionization of atomic oxygen. The radiation absorbed by molecular nitrogen does not contribute appreciatively to the observed ionization, because molecular ions are short-lived in the F-region. However, since the loss rate depends on both O_2 and N_2 concentrations, a seasonal variation of $(O)/(N_2)$ ratio can certainly make a change in the production rate and loss rate which could result in an increase or decrease of the electron densities for different seasons. This theory was proposed by Rishbeth and Setty (1961), favored by Wright (1964), and opposed by Thomas (1964) and Yeh (1968).

4.2.2. Diffusion from the opposite hemisphere

During winter, the input of solar energy in the Southern Hemisphere is more than in the Northern Hemisphere. The electrons created in the warmer summer hemisphere may diffuse along the magnetic field lines to the conjugated points in the winter hemisphere. This model was proposed by Rothwell (1961, 1963). Against this were Hanson and Ortenburger (1961), Kohl (1966), Becker (1966), Rishbeth (1968a). Their reason of objection is that this process is too slow. However, Thomas (1964) accepted this idea and claimed that the downward flux of electrons from above the peak of the F_2-layer is the most likely cause of the winter spur.

4.2.3. Plasma interchange between the ionosphere and the magnetosphere.

The magnetosphere is a reservor for a large amount of ionization. An interchange of magnetic tubes will bring more plasma into the ionosphere. This hydromagnetic pumping theory was proposed by Piddington in 1964. He claimed that the F_2 seasonal anomaly and some other ionosphere effects can be explained in terms of pumping mechanism. The plasma can get into the winter-daytime ionosphere and out of the winter-nighttime ionosphere through that process. This theory was seriously criticized by Rishbeth (1968).

4.2.4. Convective theory

During the Northern Hemisphere winter, more input energy is found in the Southern Hemisphere. A large scale circulation could be induced at ionospheric levels due to the heat contrast between the two hemispheres. Warm air with more molecular species will rise over the summer hemisphere and thus increase the recombination rate of electrons, whereas, over the cold winter polar region, a descending current must be set up, with a resulting enrichment of atomic oxygen and an increase in the production rate. This theory was proposed by Johnson (1964), Kellogg (1961), King (1964), and supported by Wright (1964), but opposed by Thomas (1963) and Belrose (1965). A recent paper by Duncan (1969) strongly recommended this theory. Actually, this theory has the same physical idea as described in Section 4.2.1.

It is noted that there is no quantitative investigations on the process which brings more atomic oxygen to the winter hemisphere. The level of maximum gradient of atomic oxygen mixing ratio is at about 96 km height in Kellogg's work (1961). A further research is certainly needed in order to prove the validity of this convective theory.

4.2.5. Other theories, such as 'electrodynamic drift' (Martyn, 1953; Maeda, 1953, 1955), 'thermal expansion' (Appleton, 1935), 'Corpuscular ionization' (Croom et al., 1960; Thomas, 1963), and 'Neutral wind' (King and Kohl, 1965) have been discussed among various scientists.

4.3. Observational pictures from satellite view

Since most of the published papers concerning the seasonal anomaly are based on ground measurements, therefore, the view point is from the bottom side of ionosphere. It should be worthwhile to examine this problem from the topside ionosphere. It is the purpose of this section to discuss this topside view from the satellite data.

Fig. 4.1 shows the latitudinal variation of N_mF2 around noon hours for June 11 and December 19, 1963. Both data are picked for solar quiet condition at $K_p = 2$. The dots represent summer data while the cross points represent N_mF2 in winter. It is clearly seen from this diagram and from a similar set of data not shown here that the maximum electron density is certainly greater in winter than in summer between 30^oN and 62^oN. The ratio of N_mF2 in winter to N_mF2 in summer is on the average about 1.3. Below 30^oN, N_mF2 is large in summer. Note that in the Southern Hemisphere, polewards of 20^oS, the local summer value of N_mF2 is greater than the local winter value. There is no anomaly. Fig. 4.2 shows the same data plotted in dip latitude. We see that both kinds of analyses fit the smooth lines. It is hard to tell whether the seasonal anomaly is under geographic or magnetic control.

Fig. 4.3 shows the latitudinal variations of h_mF2 corresponding to Fig. 4.1. It is interesting to note that the winter F2 peak height is, in the area of seasonal anomaly, about 40 km lower than in summer time.

Fig. 4.4 shows the vertical profiles of electron density distribution at different latitudes. These diagrams tell us that the electron densities are larger in winter only at around and below F2 peak. Above about 300 km, the summer value of electron density is larger than winter value – that is to say there is no anomaly occurrence. We have integrated the total electrons per one centimeter square base from 400 km to 1000 km height at latitude range of 13°N to 40°S and from 300 km to 1000 km height intervals for all other latitudes. We calculated N_t (total electron density) in this way because while the summer F2 peak height is usually above 300 km in low latitudes, there is no satellite data available below the peak height. We plotted N_t versus geographic latitudes as shown in Fig. 4.5. We can see that N_t is always larger during summer days for all latitudes. The anomaly is absent as far as total electron content is concerned during the solar minimum year.

Becker (1966) noted, too, that the total electron content in winter may be less than in summer, while N_mF2 is still greater in winter.

4.4. Possible cause of seasonal anomaly

Winds and compositional changes are considered the most probable causes of the F2 region seasonal anomaly. The physical idea of formation of the seasonal anomaly due to neutral winds is as follows:
The meridional wind is about twice as strong in winter as in summer around noon hours at mid-latitudes (Kohl and King, 1967; Geisler, 1966, 1967). The direction of the wind is poleward. It follows that a

stronger downward movement of ionization will occur during winter noon hours. The rate of downward transport of plasma may be faster than its recombination rate. Thus N_mF2 is made larger than it should be. According to Doupnik and Nisbet (1968), the altitude of the F2-peak tends to follow the variations of the transport velocities, occurring at the lowest altitudes when the velocities are mostly negative (downward). The observational data shows that h_mF2 is lower in winter than in summer. This is consistent with the wind theory. In this section, we test both the theories of winds and compositional changes by solving the continuity equation for the steady state case.

4.4.1. Meridional cross sections of electron density in winter and in summer.

Before including neutral winds and the changes in the atmospheric composition in our continuity equation, we will present two diagrams showing the meridional cross sections of the electron density distribution in the normal case. By 'normal case', we mean that the same neutral atmosphere density distribution is taken in the calculations for winter and summer seasons. We have only adjusted the solar zenith angle, the mean distance between the sun and the earth, and the temperature difference. Fig. 4.6 shows the electron density distribution in the normal case. It should be noted that in the summer hemisphere and above the 700 km height level, the electron density distribution tends to be under solar control, because the largest density is located around 20 degrees when the sun is overhead. The same thing happens in the winter hemisphere. Two maxima of density occur at about 10 degrees north and south of the equator. Another fact we would like to point out is that the densities are much lower above 65 degrees in the winter hemisphere owing to the darkness at this moment.

The density ratios between winter and summer seasons at each point were calculated and the results plotted in the diagram (Fig. 4.7). In this diagram, we note that the ratios are less than one, except around equatorial belt where we have more insolation from the sun since we used 6 percent more solar flux in winter due to the shorter mean distance. There is no seasonal anomaly in the mid-latitudes. The ratio decreases monotonically from the equator to the pole.

4.4.2. The effect of the winds

We used the same model for the computation except that we imposed neutral winds. Fig. 4.9b shows the results of the ratios for the case of including meridional winds. The meridional wind distributions which we used as input in our model equations are sketched as follows:

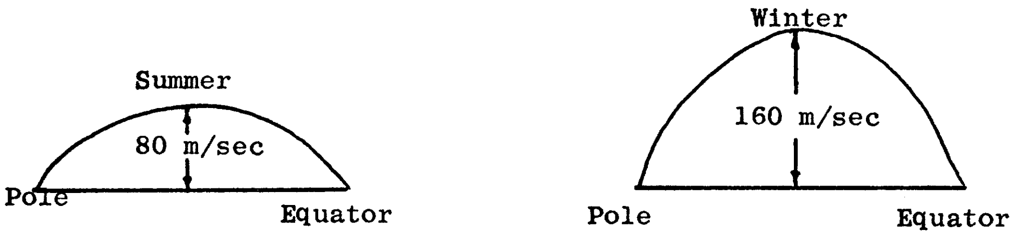

(a) Fig. 4.10 (b)

There is no essential change between Figs. 4.7a and 4.9b in the region above about 400 km. There are some changes below the F2 peak. The isoline of ratio one extends toward 30 degrees latitude in the meridional wind model. The density at the heights below the F2 peak is a little larger in winter when there is a stronger poleward wind. However, the N_mF2 is actually smaller than the previous case. This can be seen clearly from vertical density profiles as shown in Fig. 4.8b. The physical reason is this: since the recombination coefficient is getting larger in the lower altitude, it is unfavorable for the lower h_mF2 in winter to have a large value of N_mF2.

We also tested the vertical wind effect. The magnitudes of the vertical wind included in the winter hemisphere is 5 m/sec and is downward. Fig. 4.9a shows the isolines of the ratio, and Fig. 4.8a the vertical N-profile. The results still do not show any anomaly feature.

4.4.3. The effect of the atmospheric composition change

For the first trial, we increased the atomic oxygen only in the winter hemisphere in the latitude range of 30 to 60 degrees, keeping the other parameters the same. The only influence in the continuity equation is the production rate. The results are shown in Fig. 4.11 of which the sub-figure (a) shows the case when the ratio of atomic oxygen between winter and summer is 1.8, while sub-figure (b) shows the case when the ratio of atomic oxygen between winter and summer is 1.4. We learned that the seasonal anomaly hardly occurs even under the condition of the case (a) when winter atomic oxygen has been increased 80 percent.

For the second trial, we increased the atomic oxygen in the winter hemisphere, and also systematically increased the molecular gases, N_2 and O_2 in the summer hemisphere. Thus we found that the production rate increases in winter and the loss rate increases in summer (Figs. 4.12 and 4.13 show the results). The anomaly appears clearly in the latitude range of 25 to 60 degrees. It seems that a 50% increase of atomic oxygen in winter and 50% increase of nitrogen and oxygen in summer are enough for the formation of the seasonal anomaly as compared with the observational facts. In order to get an exact picture, we present the vertical electron density profiles both from computed values and from Alouette satellite data for comparison. Fig. 4.7b shows the vertical electron density profiles in the normal case. Under this case, the winter values are always less than the summer values for all heights. As the atomic oxygen increases in winter and nitrogen and oxygen increase in summer, the relative values of electron densities at F2 peak change in such a way that N_mF2 increases in winter and decreases in summer. Finally it reaches to the point when winter N_mF2 is greater than the values in summer. Fig. 4.14 shows these results for 50 and 100 percent changes of the atmospheric composition. The peak density ratio between winter and summer is about 1.25.

An important point which I would like to make is that in winter, as N_mF2 increases due to the enrichment of O, the peak height is getting lower at the same time, while in summer, the h_mF2 is rising, as N_mF2 decreases. This is consistent with the fact that the h_mF2 is lower in winter than in summer (Fig. 4.15).

I would also like to point out another interesting feature which occurs in all predicted diagrams. Namely, there are almost no significant changes of densities above about 400 km. The density variations are sensitive to the composition change of the neutral atmosphere only at around and below F2 peak. This is because physically both solar production rate and recombination terms lose their importance in high altitudes where diffusion is dominant.

4.5. Conclusion

The seasonal anomaly was discovered long ago from the bottomside ionospheric measurements (Appleton, 1935; Appleton and Naismith, 1935). Our satellite data show the similar features.

It is most likely that the composition change of the atmosphere is the probable cause of the F-region seasonal anomaly. We have shown that a fifty percent change in atomic oxygen, oxygen and nitrogen is enough to make a clear appearance of the greater N_mF2 in winter. Furthermore, the rising of h_mF2 in summer and the falling of h_mF2 in winter from computed values also agree quite well with the observational picture.

Norton and Warnoch (1968) have deduced the concentration of O_2 by using attenuation of solar radiation technique. Their values are: $N(O_2) = 1.5x10^{12}$ cm^{-3} in winter and $N(O_2) = 2.3x10^{12}$ cm^{-3} in summer at the height of 100 km. Rocket data as well as satellite measurements all show that the densities of molecular species in winter are different from what are in summer (Keating and Prior, 1967; Manersberger et al., 1968). Mahoney (1968) has done numerical calculations using one-dimensional models. He found that the ratio of n(0) to n(O_2) and n(N_2) are larger in winter. Seasonal changes of β of the order of 1.5:1 with smaller value in winter was found by King (1961) and French (1966). All these evidences show that a fifty percent of change in the neutral atmosphere is a conservative estimation.

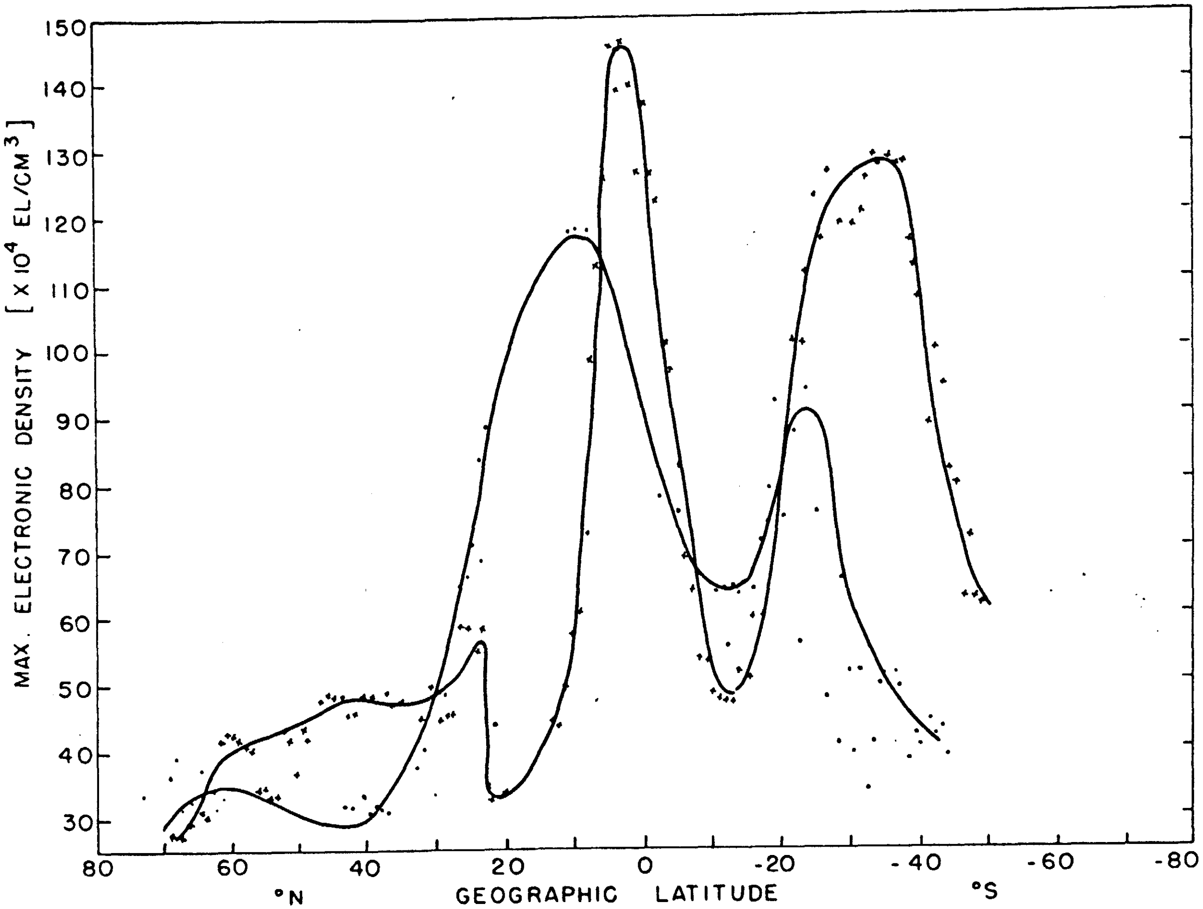

Fig. 4.1. Latitudinal variations of N_mF2 from Alouette I in geographic latitude. Cross points are for Dec. 19, 1963, 1120-1318 LMT; dots for June 11, 1963, 1224-1247 LMT, both data are under $K_p = 2$.

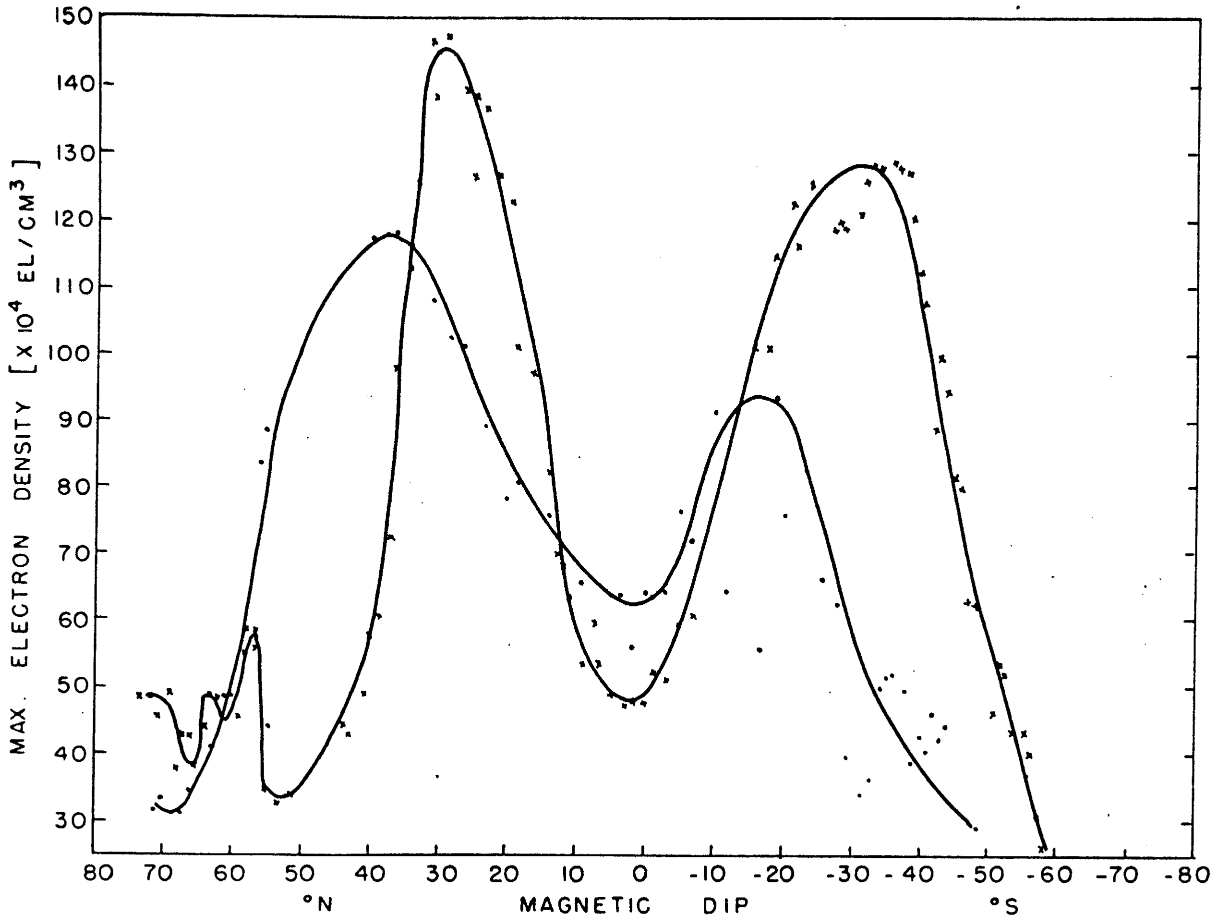

Fig. 4.2. Latitudinal variations of N_mF2 from Alouette I in dip latitude, same data as in Fig. 4.1.

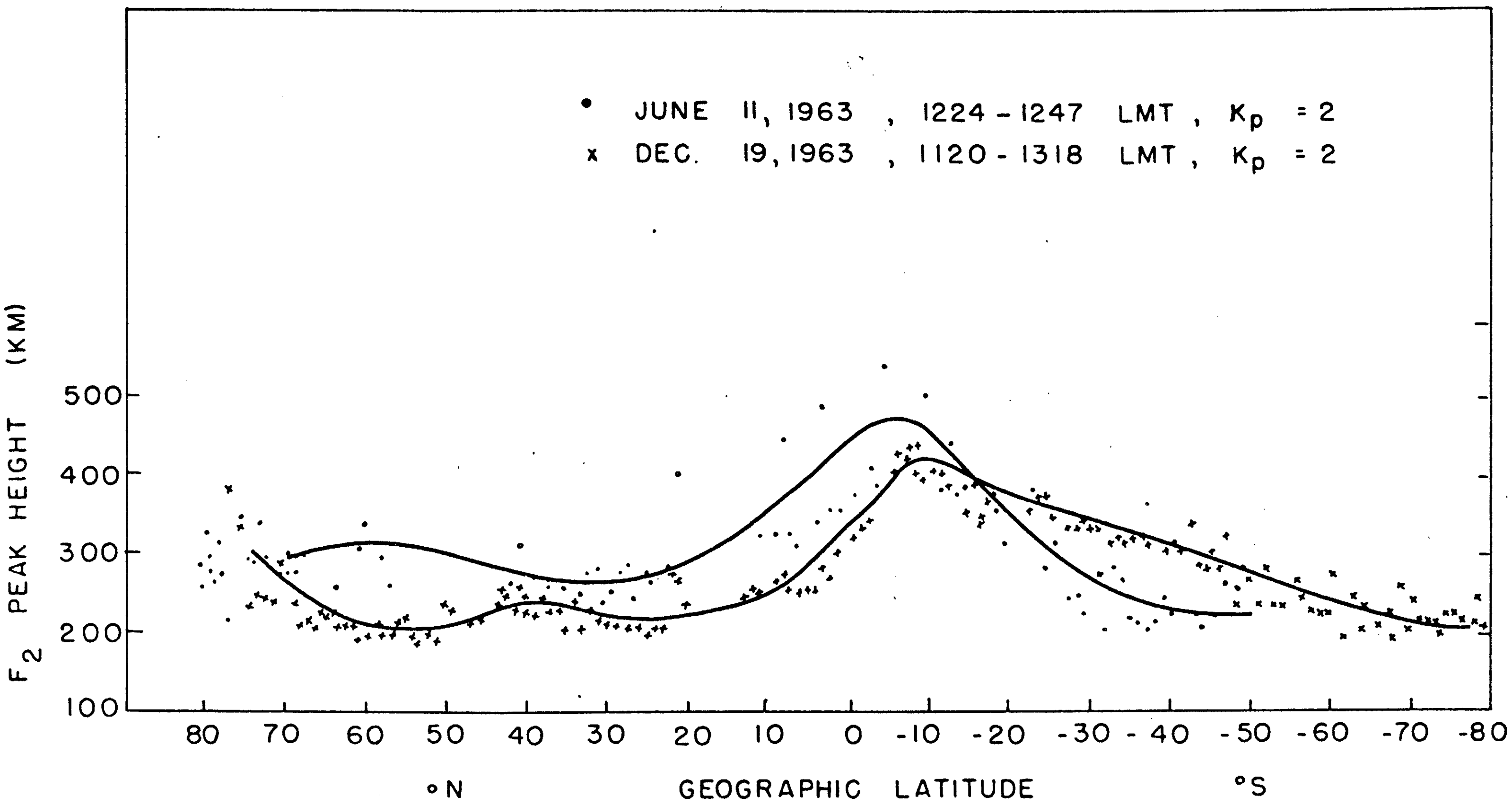

Fig. 4.3. Latitudinal variations of h_mF2 from Alouette I, corresponding to N_mF2 in Fig. 4.1.

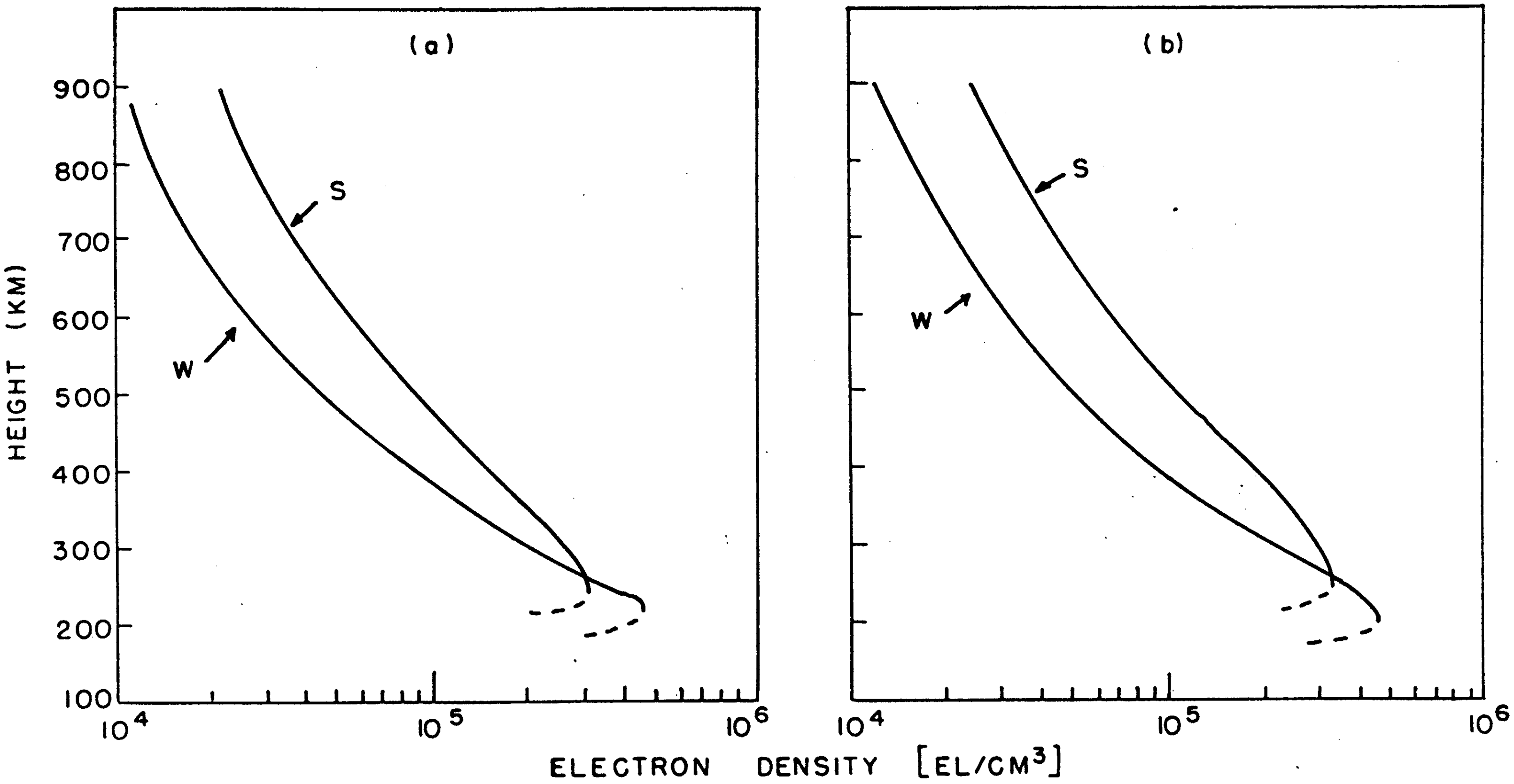

Fig. 4.4. N-h profiles from Alouette I. S represents June 11, W December 19, 1963. (a) at 40° lat., (b) at 35° lat., $K_p = 2$.

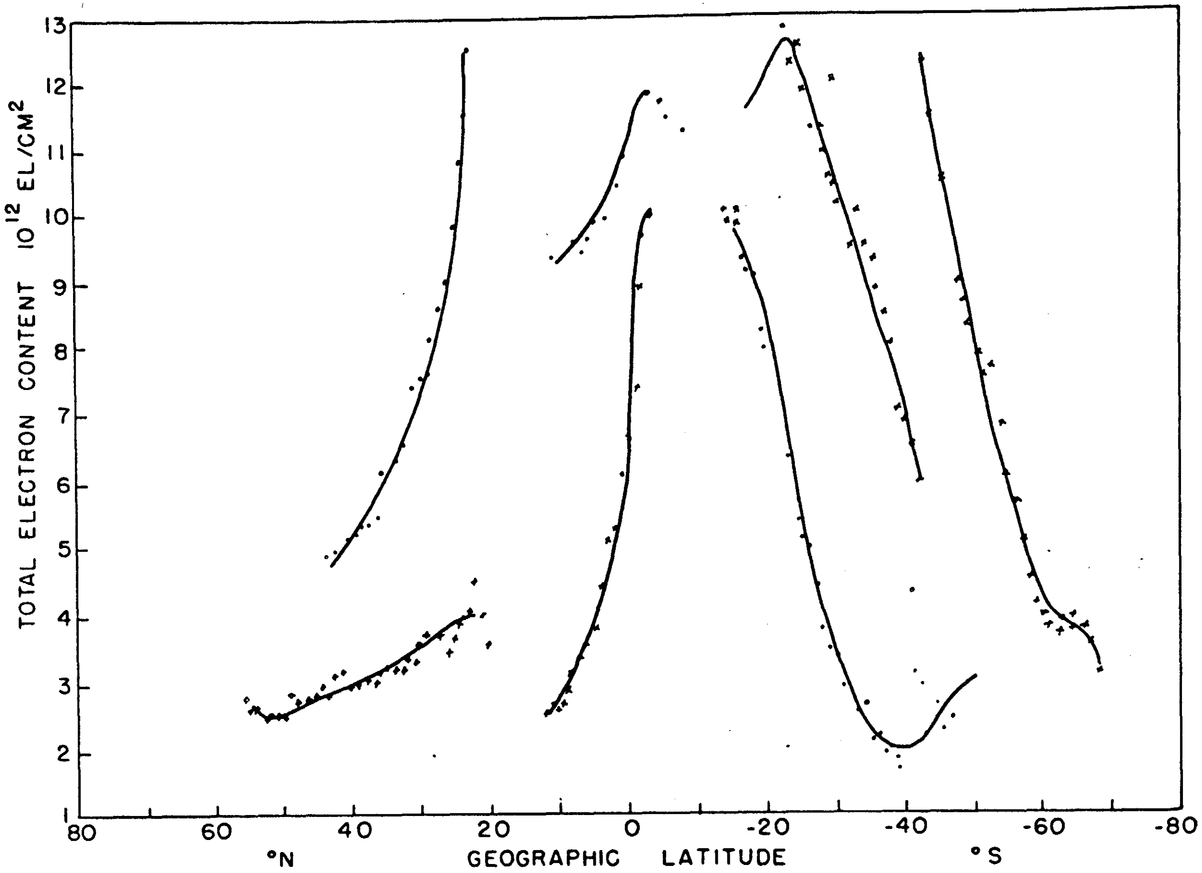

Fig. 4.5. Latitudinal variation of total electron content. The height intervals are from 400 km to 1000 km between 13°N and 40°S, and from 300 km to 1000 km for other latitudes. Cross points are for December 19 and dots June 11, 1963, $K_p = 2$.

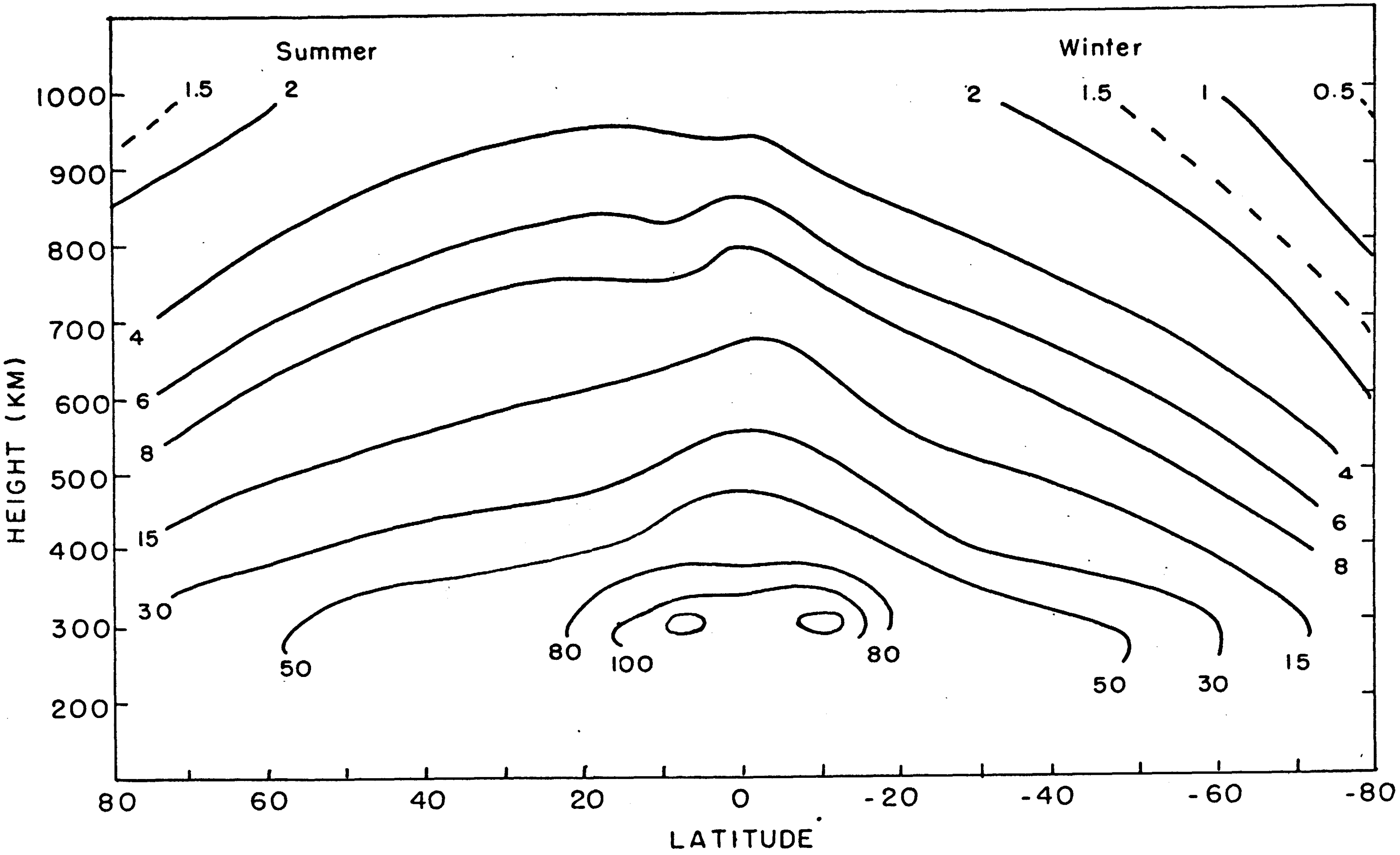

Fig. 4.6. Meridional cross section of electron density distribution for normal case computed from steady state equation of continuity. Solar zenith angle, mean distance between earth and the sun, and temperature are adjusted but with no change in neutral atmospheric structure.

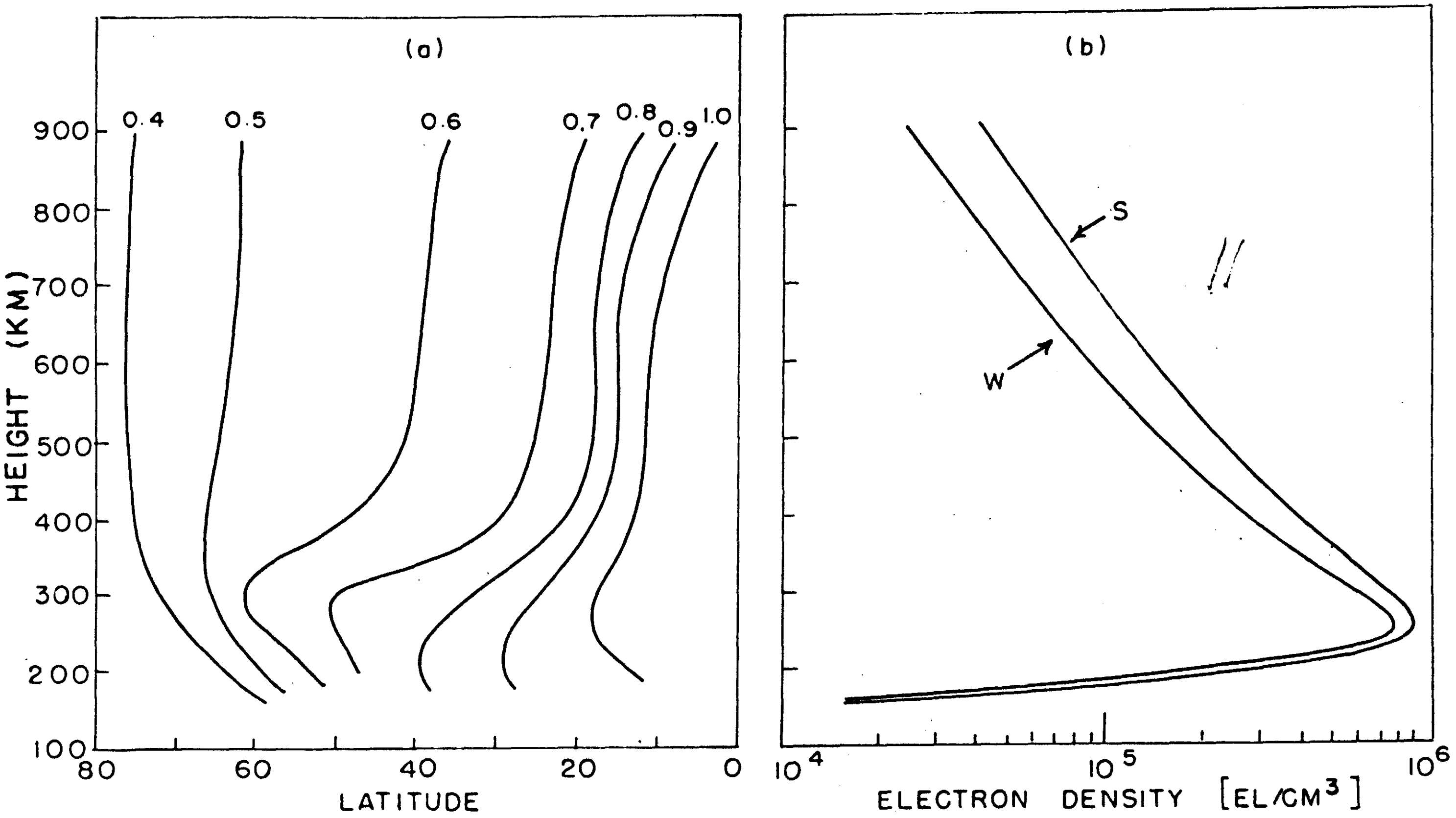

Fig. 4.7. (a) Ratio of electron density between winter and summer for normal case; (b) N-h profile at 35° lat. in normal case. S stands for summer, W winter.

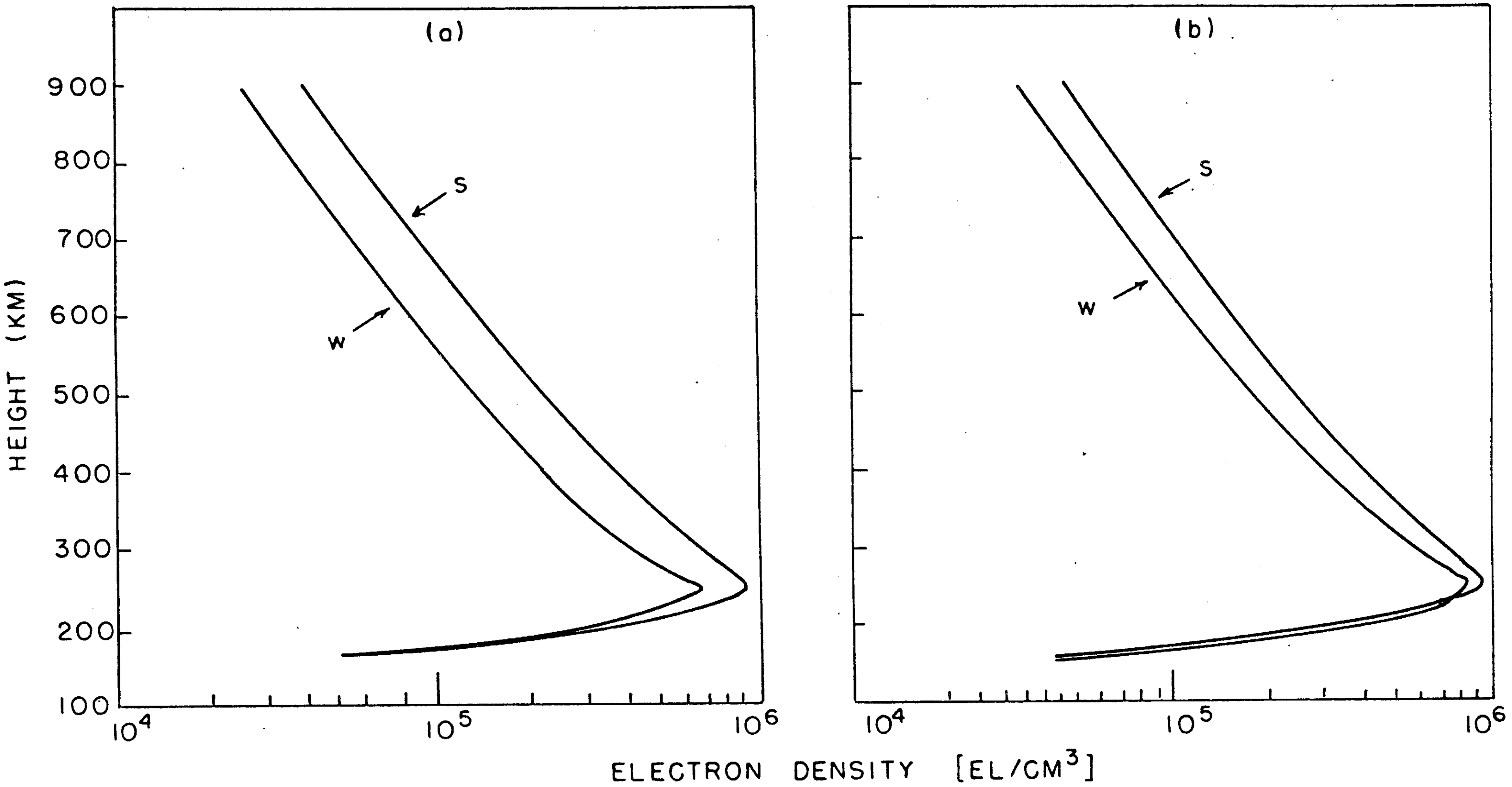

Fig. 4.8. N-h profiles at 35° latitude. (a) with vertical wind of -5 m/sec, (b) with meridional wind as sketched in Fig. 4.10. S stands for summer, W winter.

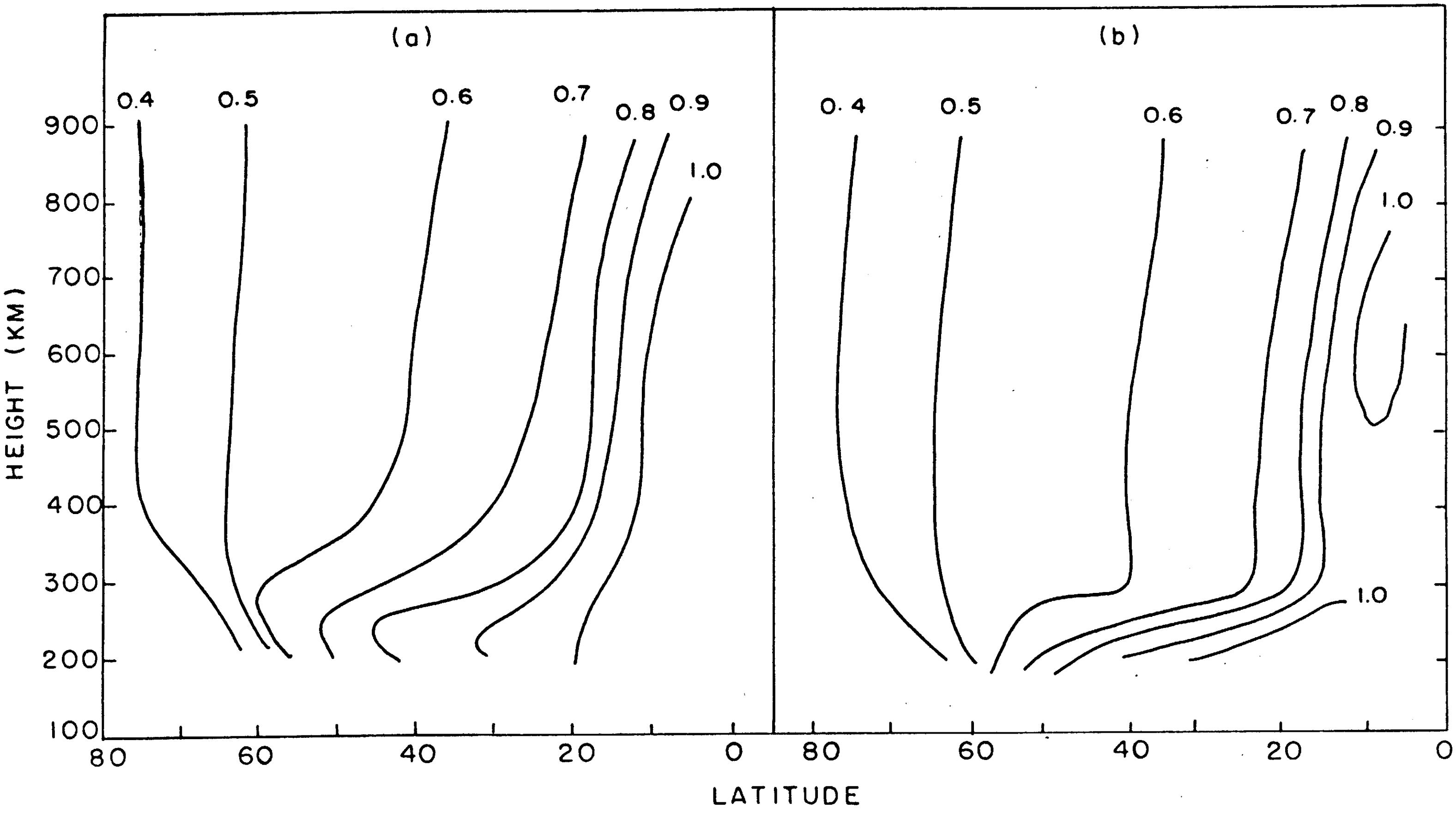

Fig. 4.9. Ratio of electron density between winter and summer. (a) with vertical wind of -5 m/sec, (b) with northward wind as sketched in Fig. 4.10.

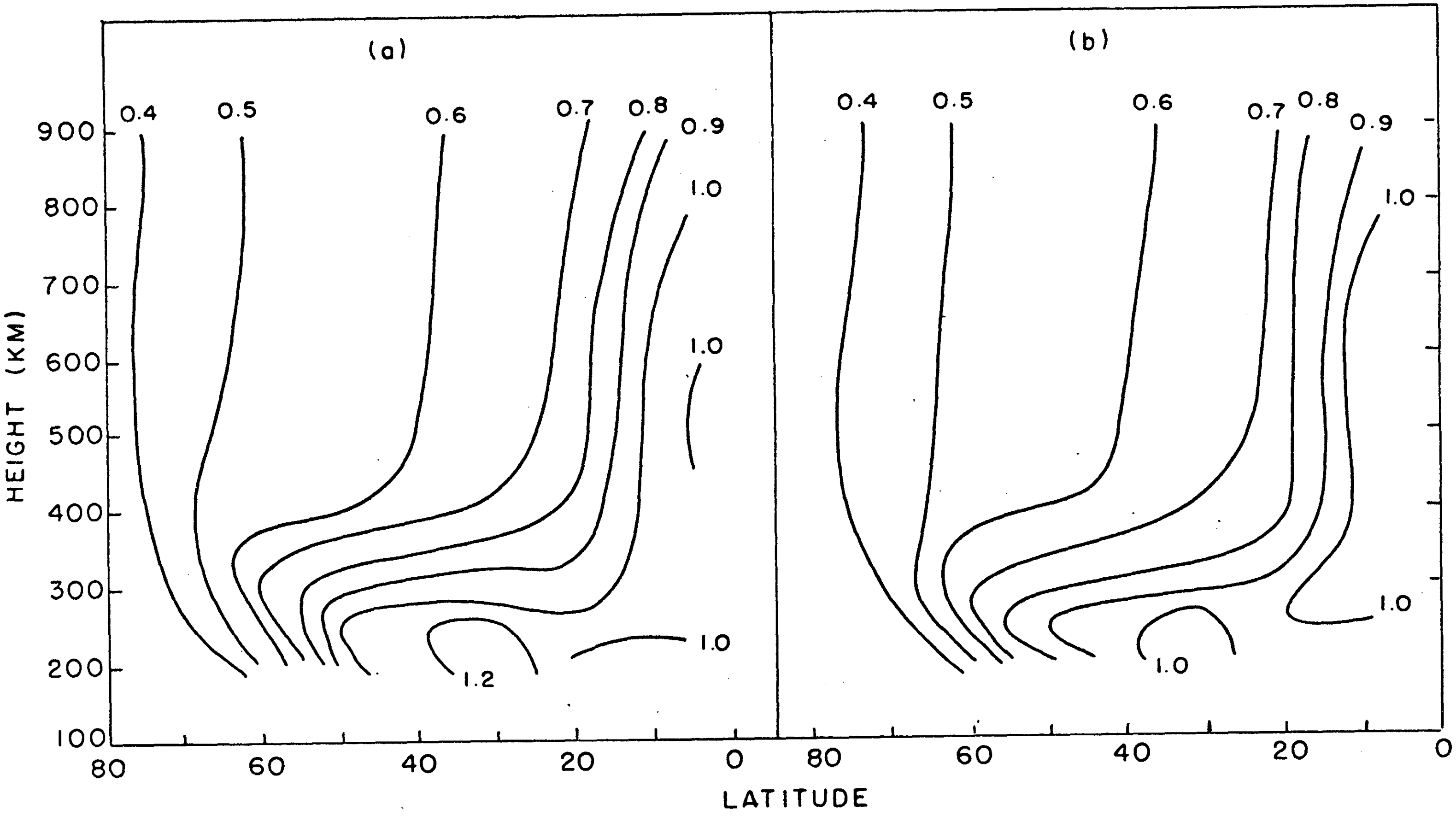

Fig. 4.11. Ratio of electron density between winter and summer. (a) $(O)_w/(O)_s = 1.8$; (b) $(O)_w/(O)_s = 1.4$.

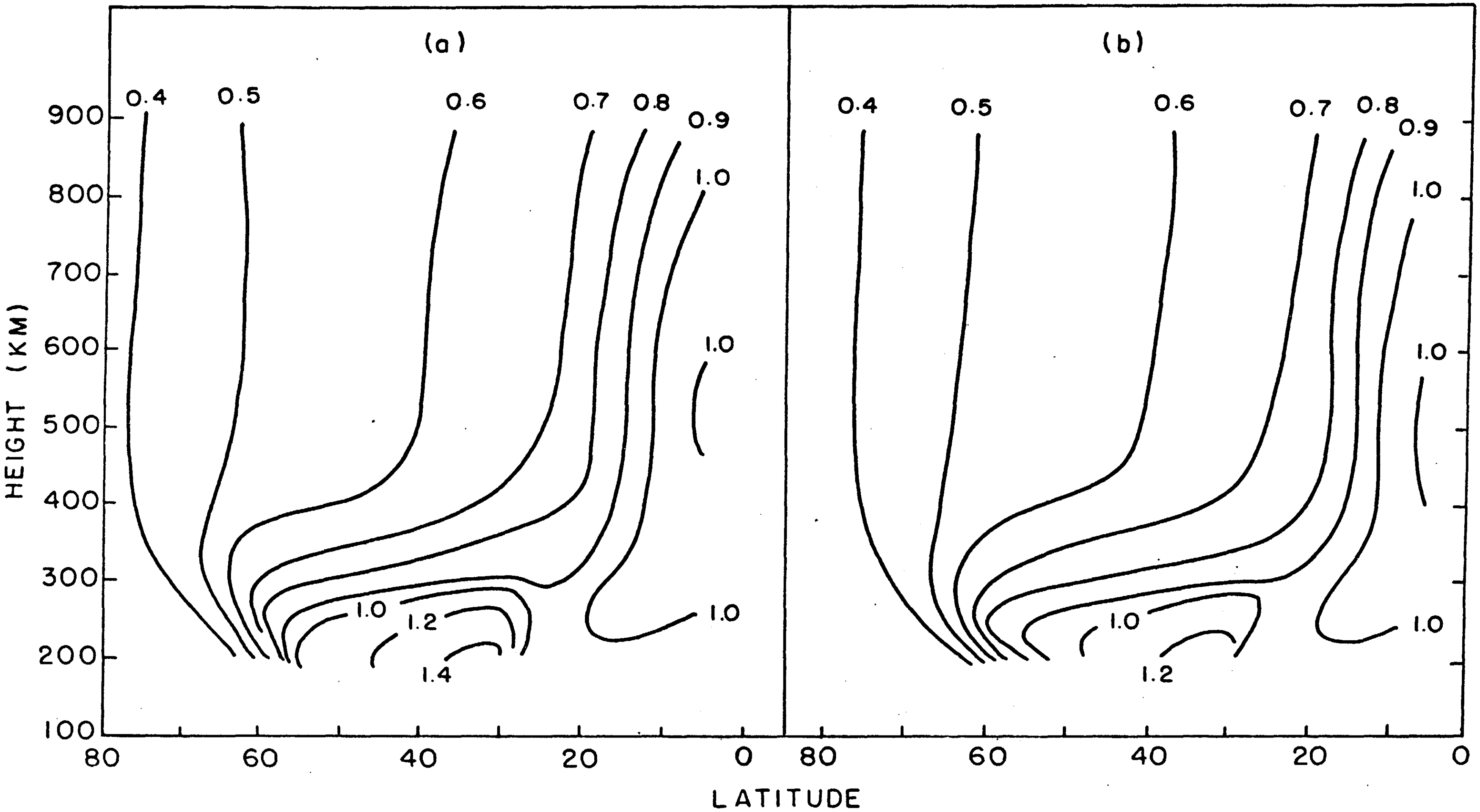

Fig. 4.12. Ratio of electron density between winter and summer.

(a) $(O)_w/(O)_s = 1.4$; $(N_2+O_2)_s/(N_2+O_2)_w = 1.4$,

(b) $(O)_w/(O)_s = 1.3$; $(N_2+O_2)_s/(N_2+O_2)_w = 1.3$.

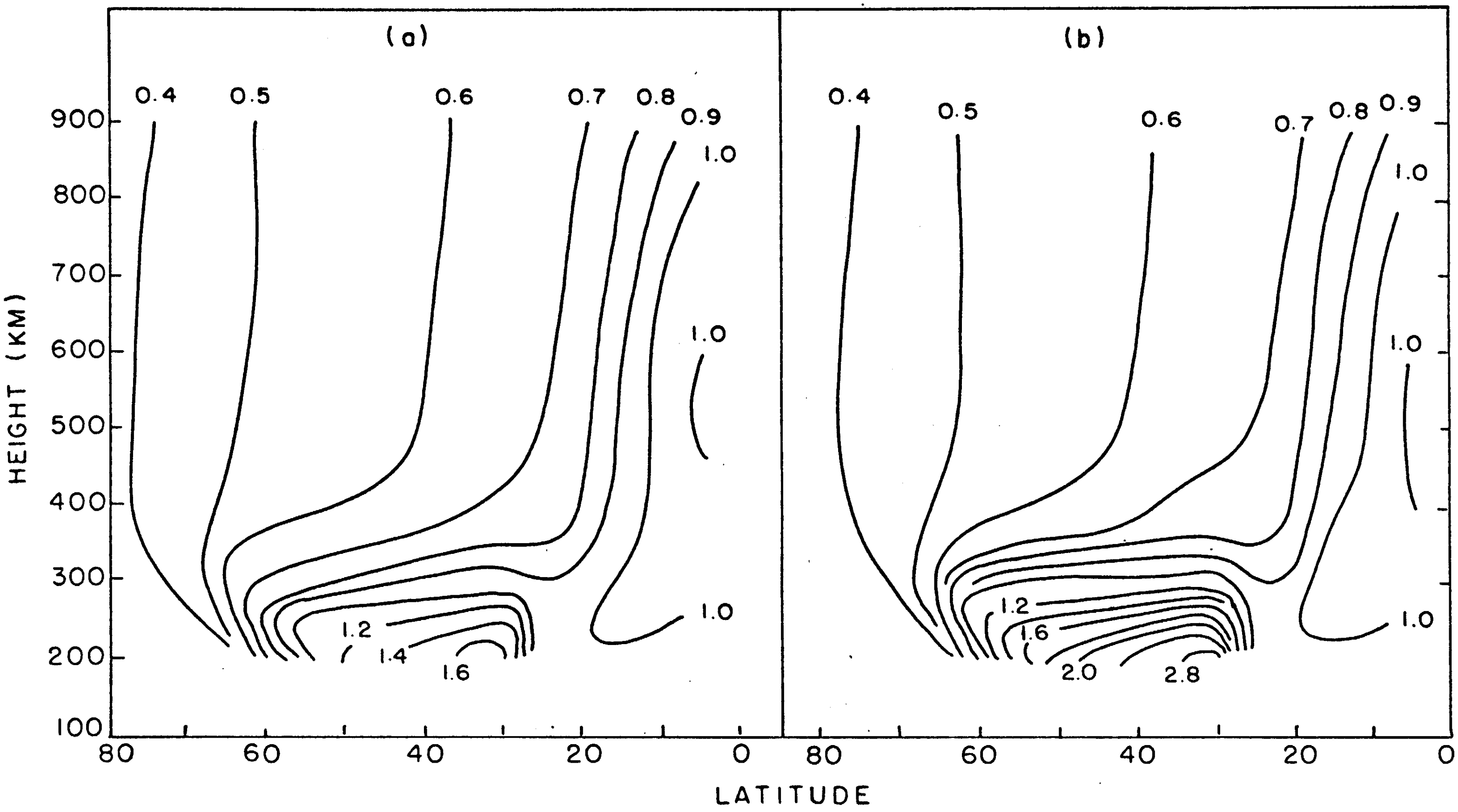

Fig. 4.13. Ratio of electron density between winter and summer.

(a) $(O)_w/(O)_s = 1.5$; $(N_2+O_2)_s/(N_2+O_2)_w = 1.5$,

(b) $(O)_w/(O)_s = 2.0$; $(N_2+O_2)_s/(N_2+O_2)_w = 2.0$.

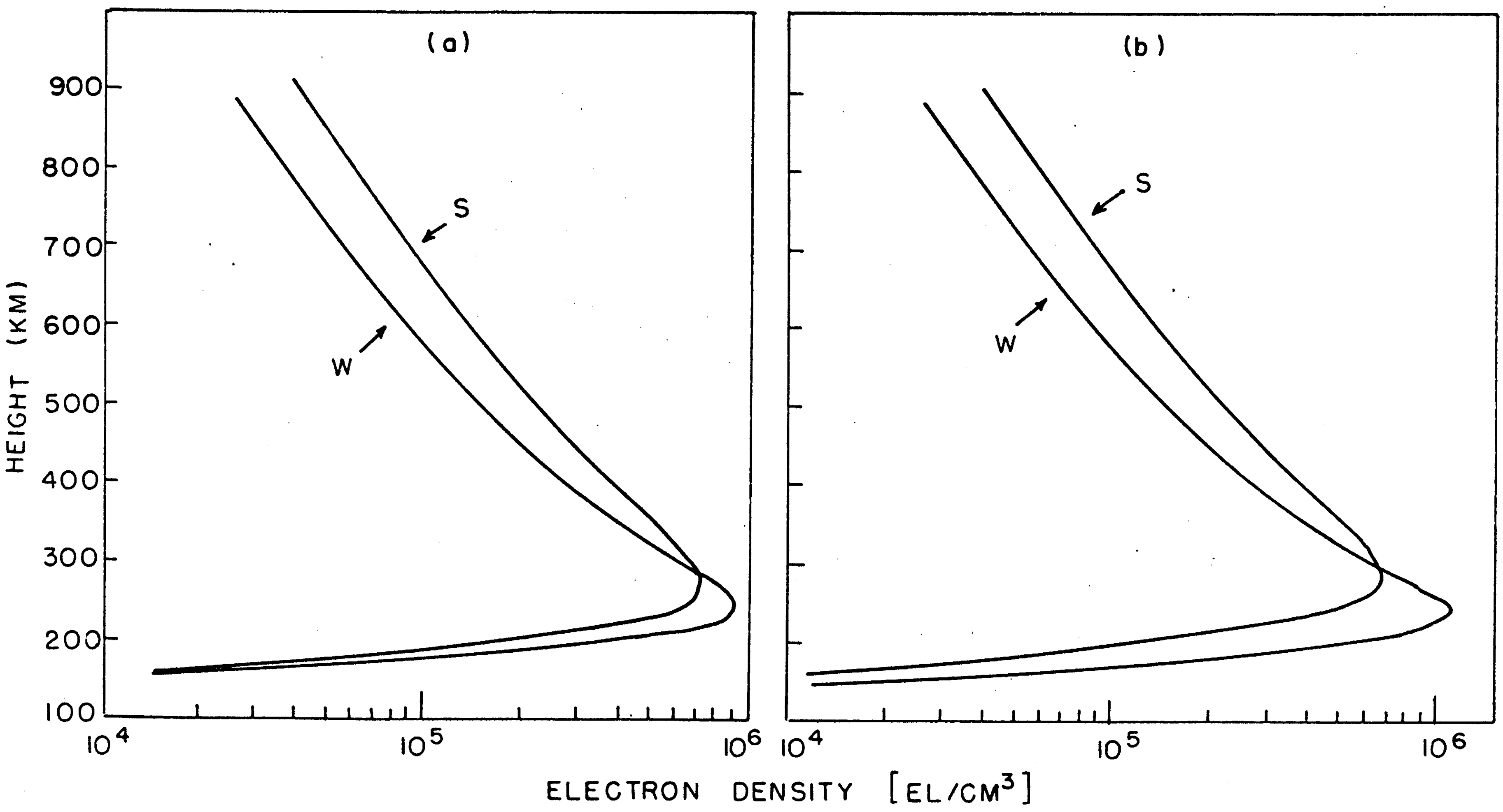

Fig. 4.14. N-h profiles at 35° latitude computed by adjusting O, N_2 and O_2 in winter and summer.
(a) $(O)_w/(O)_s = 1.5$; $(N_2+O_2)_s/(N_2+O_2)_w = 1.5$
(b) $(O)_w/(O)_s = 2.0$; $(N_2+O_2)_s/(N_2+O_2)_w = 2.0$.

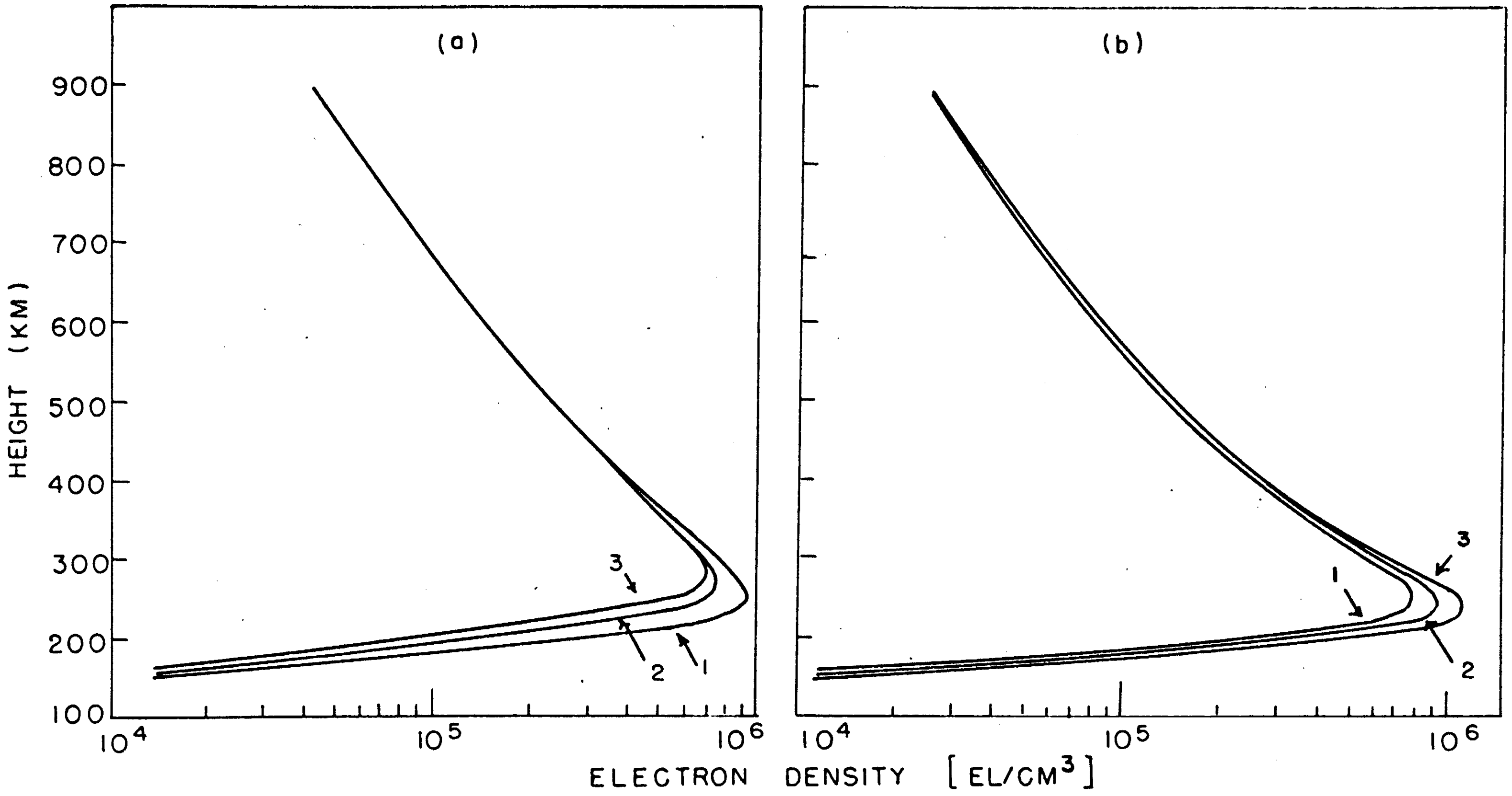

Fig. 4.15. N-h profiles at 35° latitude. (a) Summer: Label 1 represents normal case, label 2 50% increase of O_2+N_2, label 3 100% increase of O_2+N_2.
(b) Winter: Label 1 represents normal case, label 2 50% increase of O, label 3 100% increase of O.

CHAPTER 5

EQUATORIAL ANOMALY

5.1. Introduction

Since Appleton (1946) discovered this peculiar feature in the equatorial ionospheric F-region, several different explanations of the anomaly have been given. The fact is that when f_oF2 values at noon are plotted against magnetic latitude there is a minimum at the equator and two maxima at about 15 degrees north and south.

Mitra (1946) thought that the ionization produced at heights up to 600 km over the equator might diffuse down along the field lines under gravity and pile up at the places where the maxima occur. Martyn (1954) modified this idea by saying that the ionized particles were originally created at a lower height over the equator and were lifted up by the electromagnetic force early in the day and then slid down. Appleton (1954) once proposed that the contraction and expansion of the layer may do the job. Duncan (1960) made a comparison of data at Chimbote, Peru (magnetic dip 7°N) and at Panama (dip 37°N), and found that the critical frequencies in the two locations were negatively correlated, thus Martyn's transport mechanism was confirmed. Bramley and Peart (1965) integrated the continuity equation for the equilibrium case, and found that a vertical drift of a few meters per second is enough to produce the equatorial trough. Kendall and Windle (1968) showed that the electrodynamic drift is really more important than ion-drag. A recent paper by Baxter and Kendall (1968) integrated the equation of continuity for the time dependent case and inserted different vertical drift velocities - 10, 15, and 25 m/sec - to show how the maxima change their positions with time.

It seems that the transport process is a generally accepted physical cause of the equatorial anomaly. In this chapter, we are going to re-examine this problem carefully.

5.2. Satellite picture of equatorial anomaly

The structure and behavior of the topside equatorial anomaly have been described in section 1.2.2. Here, a short summary will be given.

(a) After sunrise and before 10:00 local time, the latitudinal distribution of electron concentration across the equatorial area shows a single maximum above the dip equator. There is no anomaly.

(b) At about 11:00 local time, two maxima of electron density occur on either side of the dip equator in all seasons.

(c) The anomaly starts to develop below about 600 km height; then gradually the contours of constant electron density above 600 km change their shape from a dome-like to a flat structure. The anomaly is most developed near 16:00 LMT. The decay epochs are different for different seasons. The life time of the equatorial anomaly is longest during summer months, from 11:00 to midnight; and shortest in winter, from 11:00 to 22:00 LMT.

(d) In general, the equatorial anomaly is not symmetric with respect to the magnetic equator. The anomaly crest in the summer hemisphere is larger and the height of constant electron density contour is higher in summer than in winter.

5.3. Travel time calculation – Route 1

Assume that the earth is a perfect dipole, as is done by most authors. From Fig. 5.1, we see that in order to have maxima at 15° north and south and at about 300 km height, the ionization produced in the equatorial F-region must be lifted to about 840 km height, so that it can slide down along the 20° field line and reach the correct places. Hereafter we refer to this transportation route as route 1. The largest vertical drift velocity used by Baxter and Kendall is 25 m/sec. We can estimate how much time is needed for ionization raised from different levels to 840 km in the equatorial plane.

The velocity of diffusion along the field line due to gravity (neglecting the pressure effect) is given by

$$V = \frac{g \times \sin\phi}{\nu_{in}(1 + 3\sin^2\phi)^{1/2}} \tag{5.1}$$

where ν_{in} is collision frequency, and ϕ the magnetic latitude. If we use Chapman's formula for collision frequency, and neutral particle densities from CIRA 1965, the sliding time, t_s , can be calculated from 840 km to different heights along the field line of 20 degrees and is shown in Fig. 5.2. Duncan (1960) made the same calculation on this part. However, if the source ionization is in the lower ionosphere over the equator, we have to add the lifting time from the different levels to 840 km. Curves t_1, t_2, t_3, and t_4 in Fig. 5.2 show these total times for different source levels.

The chemical time constant is given by $\tau_{chm} = \left[K_1 N(O_2) + K_2 N(N_2)\right]^{-1}$, where $K_1 = 3\times10^{-12}(T_n/300)^{-1.5}$ cm^3/sec, $K_2 = 4\times10^{-11}(T_n/300)^{-1.5}$ cm^3/sec,

T_n being the temperature of the neutral atmosphere (see Fehsenfeld et al., 1965; Copsey et al., 1966; Donahue, 1966; and Mitra et al., 1967). Again CIRA 1965 data were used to calculate τ_{chm} which is plotted in Fig. 5.2. In order to insure that these ionized particles coming from equatorial F-region pile up at some high levels at 15° north and south without being diminished through recombination, we require the minimum critical values for heights and times as shown in the intersection points A, B, C, D, in Fig. 5.2. Below the heights of the intersection points, the ionization decays so rapidly by recombination that a build-up is prevented. The curves show that the height ranges of forming maxima are from 320 km to 326 km which are reasonable. However, if we check the total time required for the transportation, we find that the minimum time is about 400 minutes or 6.7 hours for the ionization starting to lift at 350 km over the equator and that a longer time is needed for the ionization starting at lower levels.

5.4. Questionable argument on the plasma transportation route

From the observational facts, as described in sections 1.2.2 and 5.2, we realize that at 09:00 or 10:00 LMT, the crest of electron concentration is over the equator, and at 12:00 hour, the equatorial anomaly is well formed. The bottom side ionosphere data from ground measurements also gives the same formation time of the anomaly (Appleton, 1954). This evidence shows that the time period of forming equatorial anomaly is on the order of 2 to 3 hours. However, the calculations made in section 5.3 require at least 6.7 hours. There is a time discrepancy, if we take route 1 for the plasma transportation.

5.5. Proposed transportation process — Route 2

In order to see how ionization is transported from place to place, we solved the equation of continuity and plotted the electron density distribution and the associated flux vectors. First, we included only diffusion due to gravity and partial pressure. Fig. 5.3 shows the meridional cross section of electron density distribution and their transport fluxes. It is clear that a center of maximum electrons is located at about 5 degrees of latitude, not exactly at the equator. This shifting of the maximum electron density center away from the equator is due to diffusion by gravity and ionization gradient as suggested by Mitra (1946). The flux vectors which always show NE-SW directions suggest that the plasma is sliding along the field lines either upwards or downwards. Next, we imposed a meridional wind in the equation of continuity and ran the same program again. The wind model was described in section 3.6. The results are shown in Fig. 5.4. We found that during the daytime the electron density decreases, and h_mF2 drops, and the center of the maximum density does not change. All flux vectors are poleward (see Fig. 5.4b). Finally, we tested the electric drifting theory. It is seen in equation (2.31) that if the electric field, E_x, is positive (eastward), then the vertical drift is upward; while E_x is negative (westward) the drift is downward. According to Maeda (1963), the vertical drift is upward during the day and downward during the night. We thus specify a vertical drift velocity at the equatorial belt of 5° wide and assume that the electrodynamic 'ExB' drift is simple harmonic in time with amplitude of 20 m/sec. The phase is such that the maximum upward drift occurs at noon and maximum downward drift at midnight. This time the computer results show an interesting distribution of electron densities and their associated fluxes. The center of the maximum moves to about 13 degrees where the electron flux is convergent (See Fig. 5.5).

The flux vectors show that most of the electrons do not travel along route 1; instead, they like to go to the right place almost horizontally from the equatorial region. Furthermore, Fig. 5.5 shows that above 15 degrees and between 350 km and 450 km, the flux vectors are toward the center of maximum density. Thus a convergence is formed there.

Fig. 5.6 shows the computer results for the condition similar to that illustrated in Fig. 5.5 except that the direction of the drift is reversed. This time, the location of maximum moves toward the equator, and the anomaly disappears.

5.6. Vertical profile view

Another method of checking the electric drifting effect is to take a vertical cross section. Fig. 3.17 presents this kind of view. The peak heights are moving up both at 5 and 10 degrees latitude. The electron densities increase above the peak as they should, because ionization is pushed upward by the electric force. However, electron density at the new peak decreases at 5 degrees, but increases at 10 degrees latitude. This suggests that some electrons moved away from the lower latitudes to the higher latitudes.

5.7. Conclusion and suggestion

We confirm that the plasma drift produced by the electric field is most likely the physical cause of the equatorial anomaly. However, we stress that the main route of transportation is not via 840 km height in the equatorial plane. Instead, the plasma moves almost horizontally toward the place where the maximum density occurs. We also suggest that the ionization accumulated at the center of maximum density is not coming only from the equator. The ionization produced by solar EUV radiation within, say, 7 degrees of the equatorial belt will also contribute. As one compares Fig. 5.3 with Fig. 5.5, one will find that electron densities are decreasing below 7-10 degrees latitude at the time when the maximum center is gaining its ionization.

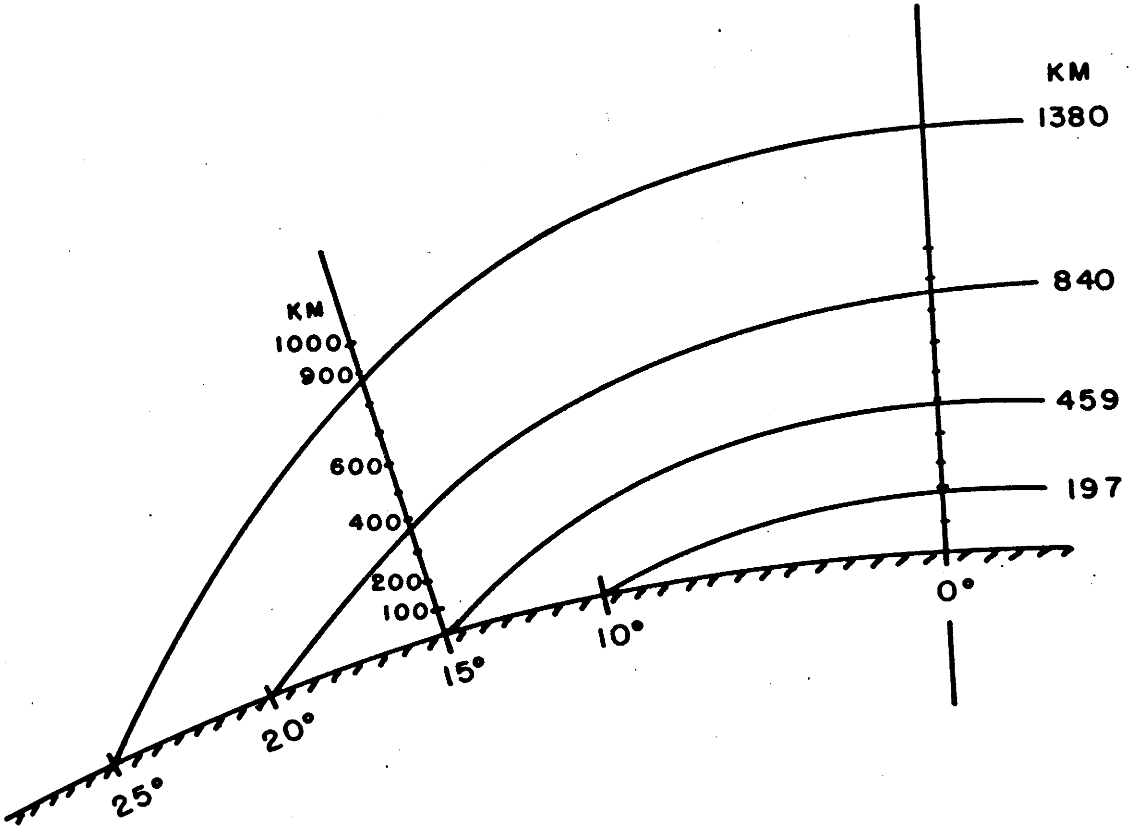
KM
1380
840
459
197
KM
1000
900
600
400
200
100
25°
20°
15°
10°
0°

Fig. 5.1. Earth dipole field lines showing relative positions in the equatorial plane.

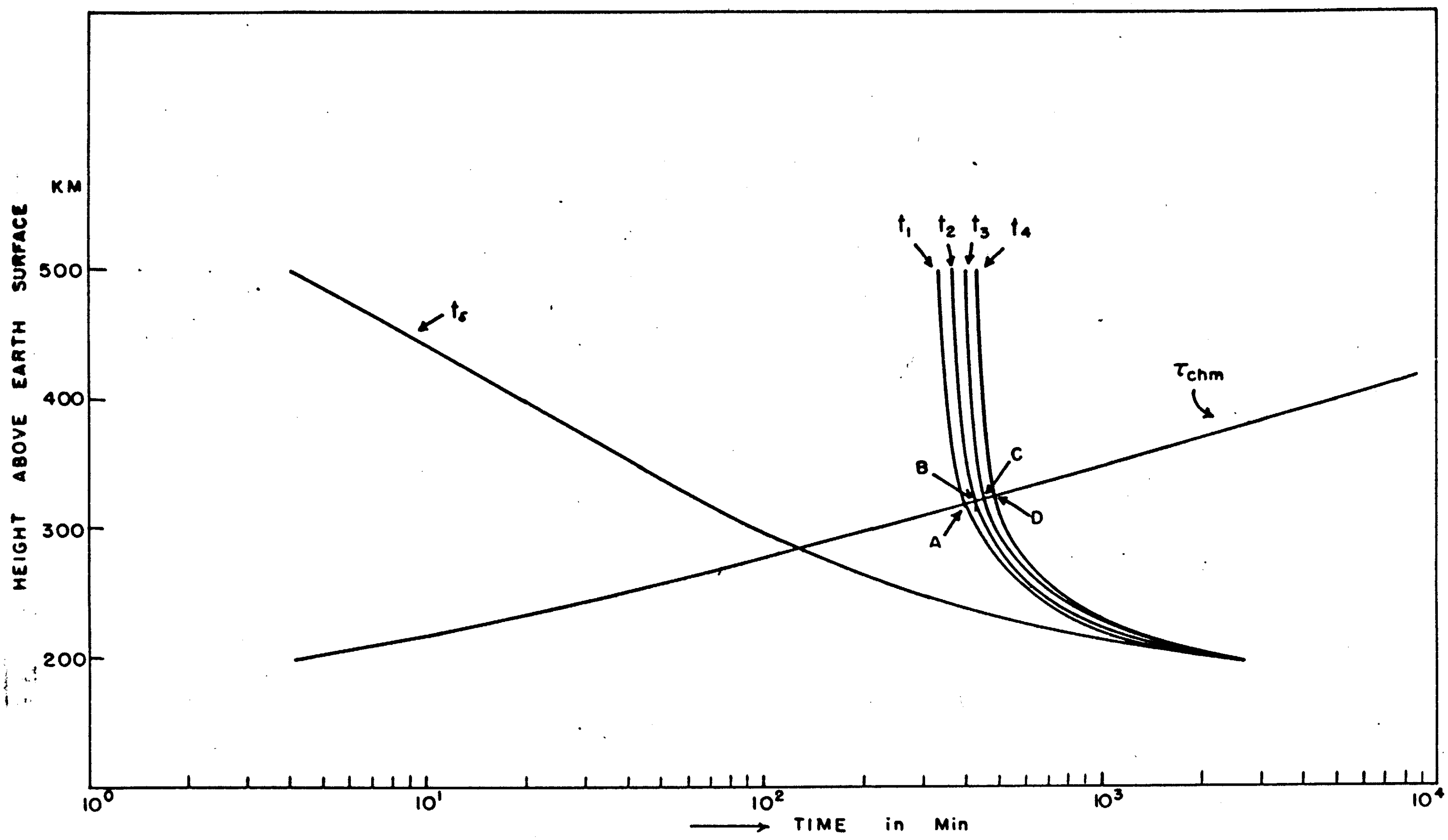

Fig. 5.2. Time charts for ionization loss and for transportation from different source levels to the various heights along 20 degree field line. τ_{chm} = chemical time constant; t_s = sliding time starting at 840 km; t_1, t_2, t_3, and t_4 = total times starting from 350, 300, 250, and 200 km height above the equator, respectively.

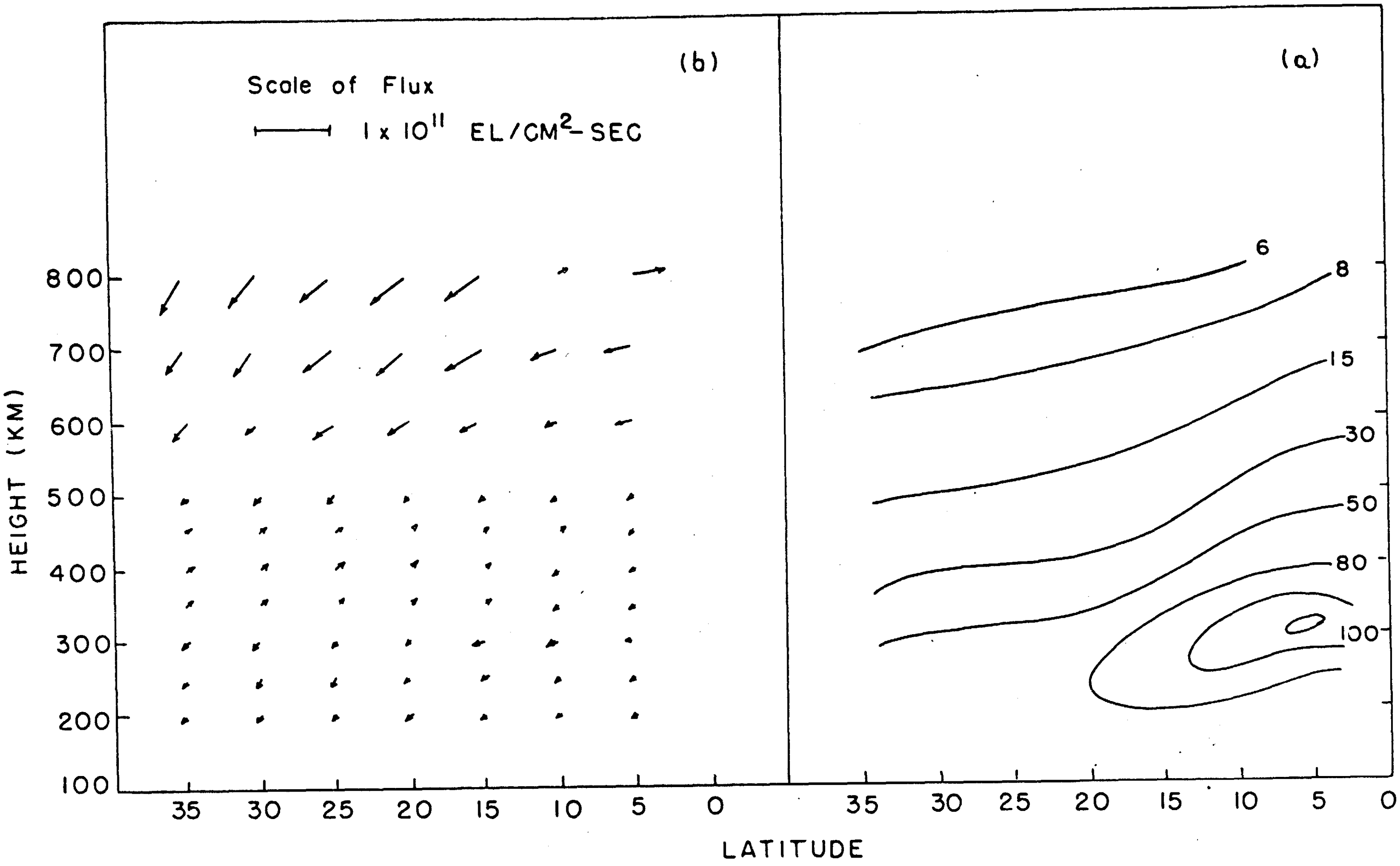

Fig. 5.3. (a) Meridional cross section of electron density distribution at 13 HR for stationary atmosphere and without drift. Units: 10^4 el/cm^3.
(b) Flux vectors associated with (a).

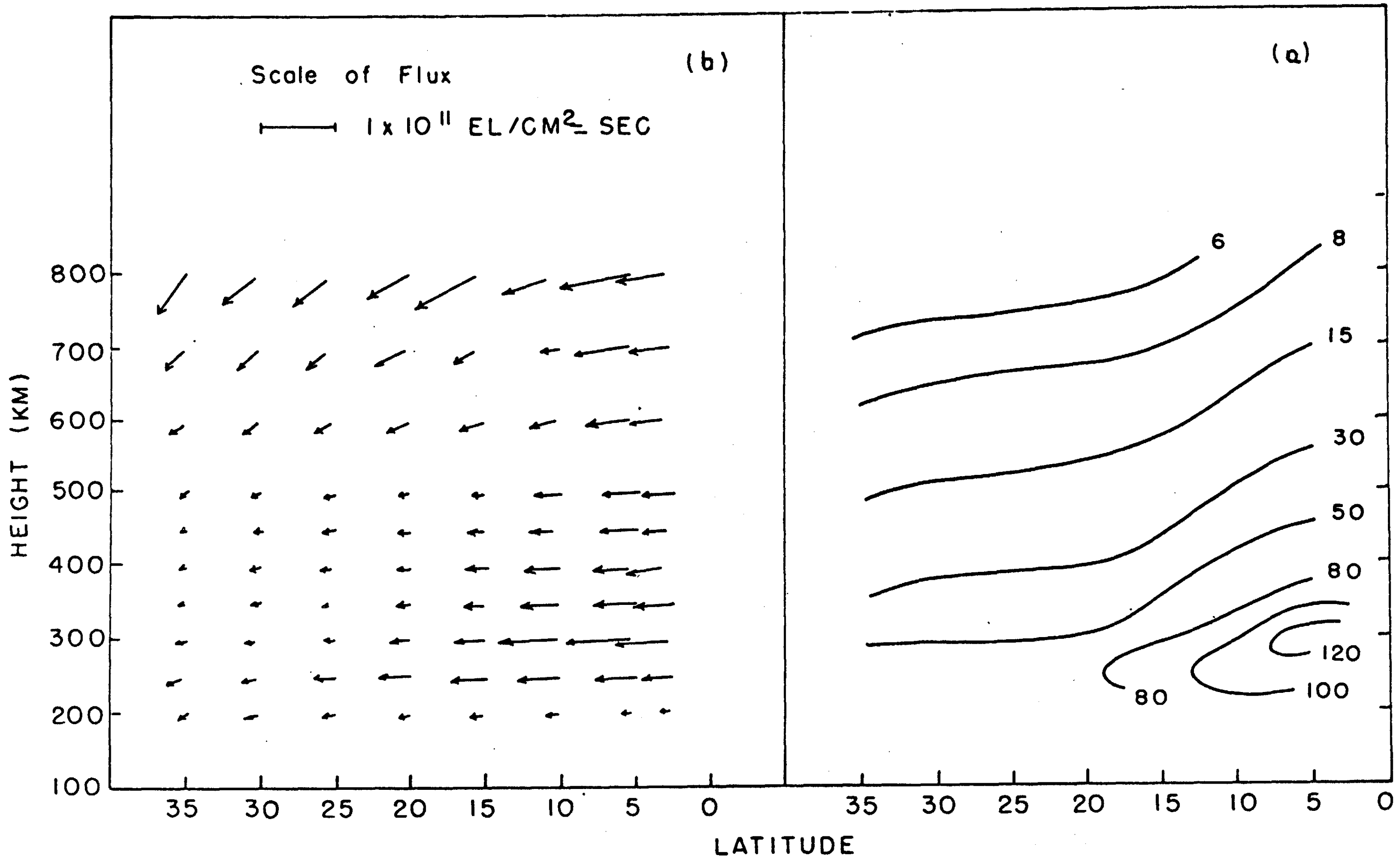

Fig. 5.4. (a) Meridional cross section of electron density distribution at 13 HR for the case with meridional neutral winds of 80 m/sec at 12 HR and 160 m/sec at 24 HR and without drift. (b) Flux vectors associated with (a).

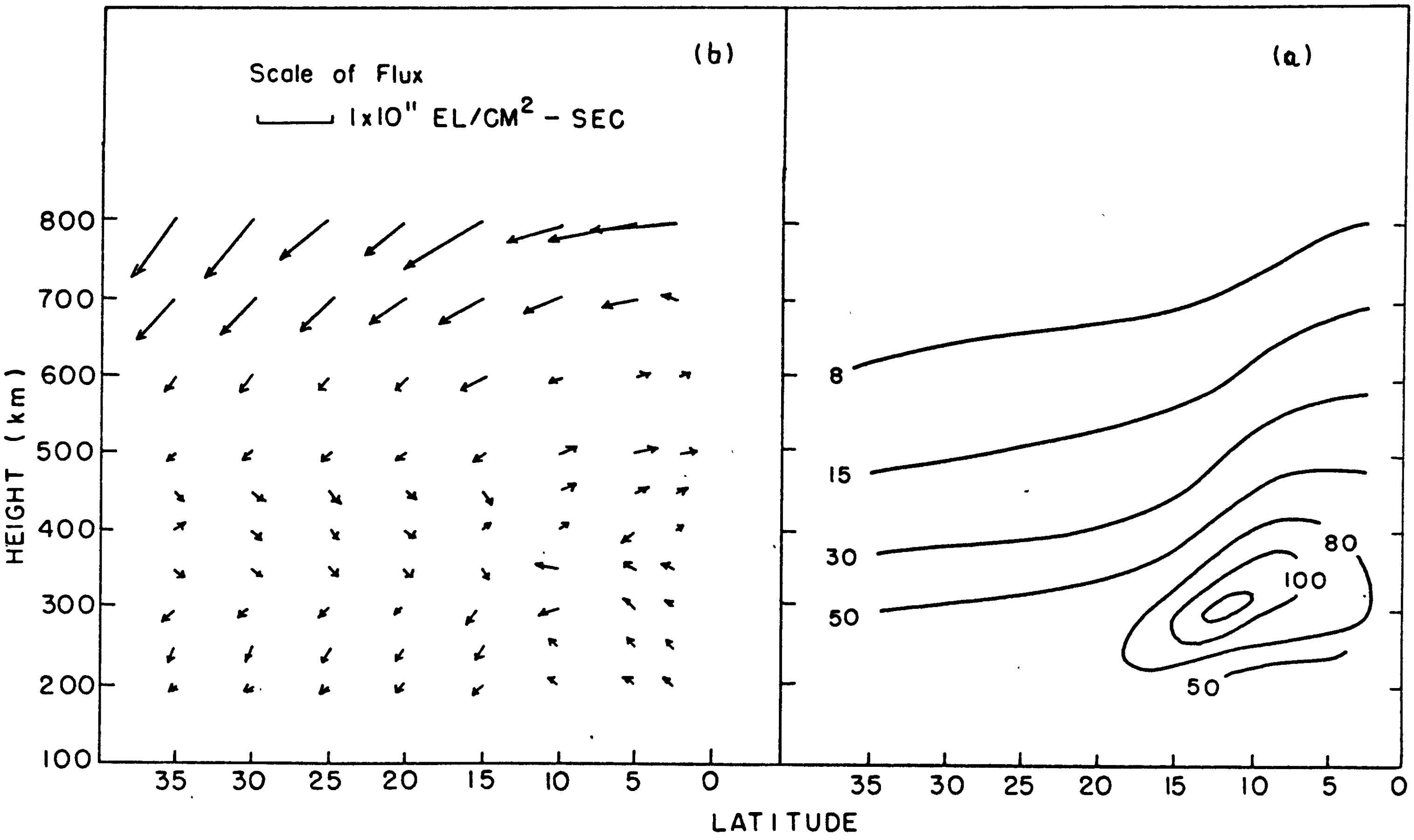

Fig. 5.5. (a) Meridional cross section of electron density distribution at 13 HR for the case with upward drift of 20 m/sec and without winds. Units: 10^4 el/cm^3. (b) Flux vectors associated with (a).

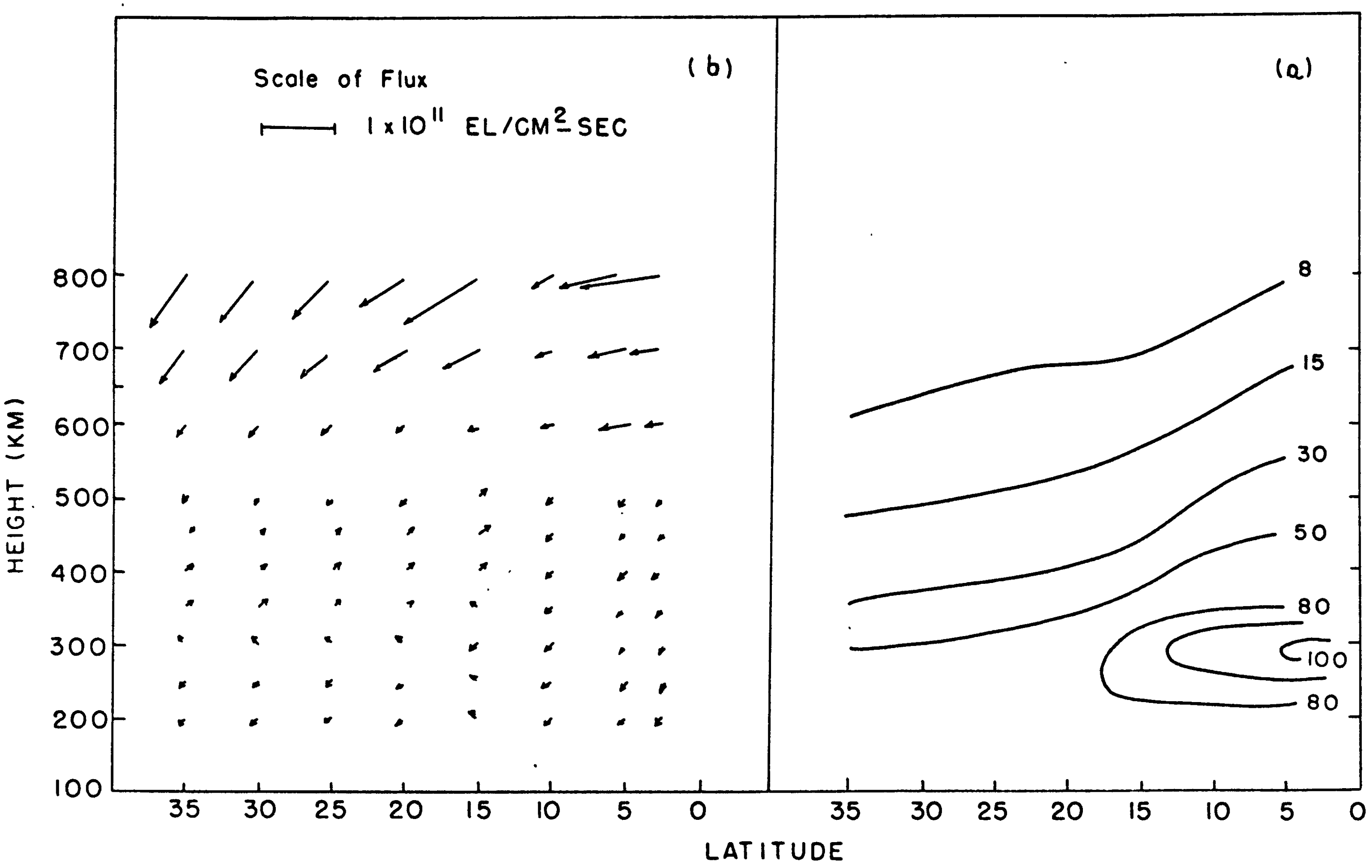

Fig. 5.6. (a) Meridional cross section of electron density distribution at 13 HR for the case with downward drift of 20 m/sec and without winds. Units: 10^4 el/cm^3.
(b) Flux vectors associated with (a).

CHAPTER 6

ELECTRON TROUGH IN THE NIGHT IONOSPHERE

6.1. Introduction

Muldrew (1965) was the first one who analyzed Alouette I data for the period of September 29, 1962 to January 2, 1963 and found that the electron density decreases extremely during the night hours in the high latitude ionosphere. Since then lots of observational data were collected in different regions and at different times both by satellite and by ground radar stations (Sharp, 1966; Calvert, 1966; Liszka, 1967; Nishida, 1967). The permanent feature of this night time trough has been confirmed.

The physical causes of this trough are still in open debate. In this chapter, we are going to examine this problem a little further by analyzing three years satellite data. Its general features, K_p effect, and seasonal variations will be described extensively. The possible causes will also be suggested.

6.2. General features

We found that the trough is present for all magnetic conditions during the night. It should be noted that the data in the southern polar region is not as good as in the northern hemisphere. The trough is not symmetric with respect to the magnetic equator. It starts at 250 km and continues all the way up to the satellite location at about 1000 km (no data available below 250 km and above 1000 km). The axis of the trough is almost vertical and located around 74° dip latitude

(44°N geographic latitude or 60°N magnetic latitude) at the height of 250 km. The electron densities are depressed by a factor ranging from 2 to 3 or more within 5 degrees of latitude.

In the low latitudes, the nighttime horizontal electron gradients, dn/ndy, are approximately 0.02% km^{-1} and 0.01% km^{-1} at 300 km and 1000 km levels respectively, while the vertical gradients, dn/ndz, are about 0.4% km^{-1} and 0.1% km^{-1} at the same heights. That is to say that the vertical gradient is at least one order of magnitude greater than the horizontal gradient throughout the whole ionosphere in the low latitudes. However, within the trough, the horizontal electron-density gradient increases quite a lot from the Alouette I results which are shown in Table 6.1. We see that at F2 peak the horizontal gradient is about one fifth of the vertical one. However, at 1000 km level, the horizontal gradient is greater than the vertical gradient. Fig. 1.7-1.13 show these facts. The trough has a seasonal variations (see 6.8).

Results from Alouette II show that the low electron density, $N = 100$ el/cm^{3}, were observed at all local times in the northern-hemisphere winter above 2000 km height. Most of the low electron densities were observed at geomagnetic latitudes greater than 65° near noon and greater than 55° near midnight (Timleck et al, 1969).

Liszka (1967) has analyzed the total electron content for 15-month period. The data collected by him is at Kiruna, Sweden (67°N, 20°E, geographic location) by using the 40 and 41 MHz beacon of the S-66 satellite. The trough positions in different seasons are listed in Table 6.2. for the purpose of a comparison with our results.

Table 6.1. Position of the trough axis; horizontal and vertical electron density gradients in the vicinity of the trough for different month and K_p index. dn/dy: N-S horizontal gradient; dn/dz: vertical gradient

Month	K_p	Location of axis (Mag. dip)		dn/ndy (km^{-1})		dn/ndz (km^{-1})		Remards
		at 300 km	at 1000 km	300 km	1000 km	300 km	1000 km	
2	0	above 80°N			0.06%		0.14%	Trough axis is above 85°N dip lat. Where data are not available
	2	above 80°N			0.06%		0.14%	
3	0	75°N	80°N	0.10%	0.38%	1.0%	0.2%	
	2	78°N	80°N	0.05%	0.23%	0.60%	0.30%	
	4	75°N	78°N	0.05%	0.15%	0.50%	0.32%	
5	1	70°N	72°N	0.12%	0.15%	1.2%	0.20%	
	4	50°N	51°N	0.13%		1.2%		
6	0		70°N		0.2%		0.11%	No trough below 600 km
	1		70°N		0.12%		0.11%	
	2							Data are not good
	3							Trough tends to be filled up
	4							Ditto

(to be continued)

Table 6.1. cont.

8	1	72°N	70°N	0.03%	0.02%	0.08%	0.08%	Below 400 km, the trough is filled up
	2	70°N	73°N	0.03%	0.06%	0.87%	0.10%	
	3	72°N	75°N	0.20%	0.13%	0.62%	0.32%	
9	1	75°N	78°N	0.03%	0.11%	0.40%	0.18%	
	2	70°N	68°N	0.04%	0.17%	0.70%	0.47%	
	3	72°N	75°N	0.20%	0.09%	0.50%	0.28%	
	4	70°N	70°N	0.15%	0.97%	1.7%	0.53%	
	5	69°N	69°N	0.18%	0.35%	0.42%	0.11%	
	6	69°N	70°N	0.10%	0.20%	0.35%	0.37%	
11	0			0.10%	0.31%	0.50%	0.29%	Trough axis is above 85°N
	1				0.27%		0.32%	ditto
	2	73°N	75°N	0.21%	0.39%	0.40%	0.24%	
	3	73°N	75°N	0.07%	0.03%	0.50%	0.31%	
12	0	77°N	80°N	0.01%	0.13%	0.25%	0.14%	
	1	77°N	82°N	0.02%	0.30%	0.55%	0.25%	
	3	76°N	80°N	0.04%	0.27%	0.50%	0.25%	

Table 6.2. Position of trough in total electron content (after Liszka, 1967).

Season	Geo-Lat.	Mag-Lat.	L.M.T.	Total content (el/m^2)
Winter 1964-65	55°N	53°N	00:00	1.5×10^{16}
Spring 1965	61.5°N	57°N	01:30	1.5×10^{16}
Summer 1965	not clear			
Autumn 1965	63°N	60°N	03:10	1.5×10^{16}

It is worthwhile to mention the terminology of the trough at this stage. A few different names such as "mid-latitude trough", "high latitude trough", and "main trough" were used by various authors, according to where does the low density region occur. Here we follow Nishida's proposal (1967), namely that there is only one trough. It is clear to see from our data analysis that there is only one such trough in existence. As Nishida (1967) explained it is due to auroral peaks which are superimposed on the trough and divide it into smaller parts, thus one trough looks like several.

6.3. K_p effect

The axis of the trough shifts a little bit towards lower latitude as K_p increases (see Table 6.1). But this shift does not depend on K_p very much. Power and Rush (1968) also found that no obvious relation between trough axis position and K_p index. However, as K_p index increases, the edge of the trough moves towards the south and the width of the trough is broaden.

It should be noted that in our analyses, we show both latitudinal as well as altitude variations of the electron density on the meridional plane, and the average values were examined. We emphasize the importance of examining the low density region change with the height besides knowing its latitudinal variations. Since all diagrams show that the low density region extends from F2 peak up to the satellite height, we have confidence to conclude that the trough is not due to redistribution of electrons vertically. This is the physical reason on which I process data in this way.

6.4. Current theories

6.4.1. Megill and Carleton (1964) have found that there is a marked decrease in electron density in the region of the red arc (λ = 6300-6364 A of atomic oxygen) in the midlatitudes. The electric field perpendicular to B is assumed to be 1 mv/cm. The explanation of the reduced electron densities in the red arc was given by Megill and Carleton (1964) as the joule heating effect. The ions and electron gas expand due to electric field heating, and those moving downward will encounter a larger recombination rate. Meanwhile, the heating itself can also cause an enhanced loss rate. However, there is no quantitative measurements. The red arc cannot explain the decrease of electron concentration at 1000 km height, because the 6300-6346 A spectrum is in the height range of 300-500 km.

6.4.2. Sharp (1966) has studied the mid-latitude trough by analyzing three months data (October-November, 1963) obtained from the flight of planar ion trap on a polar-orbiting satellite. He found that the trough occur both in the northern and the southern hemispheres. The width of the trough is inversely correlated with the intensity of electrons precipitated in the polar auroral zone. Several possible mechanisms of forming the trough have been discussed, such as the relation between the trough and the Carpenter knee, and the corpuscular radiations. However, no definite proposal was given by him.

6.4.3. Newell (private discussion) has thought that the auroral electrojet might be responsible for the nighttime ionospheric trough. The physical idea is this: the westward current is accompanied by a northward electric field, while the eastward current is driven by a southward electric field (see Fig. 6.2a). The plasma in the F-region thus drifts away due to the presence of such fields. The drift velocity is $V_d \approx E/B$. If $E = 50$ mv/m (Bostrom, 1967), we have $V_d \approx 1$ km/sec. Also if $n = 2x10^5 \ 1/cm^3$, and $\Delta x = 20^o$, then the decreasing rate of electrons will be approximately

$$\frac{\partial n}{\partial t} = - \frac{\partial n V_d}{\partial x} = \frac{-2x2x10^5x1}{20x100} = -200 \text{ el/cm}^3 \text{ -sec}$$

Newell proposed that this local decreasing rate may be counted for the formation of the trough.

6.4.4. Nishida (1967) analyzed more than 3000 N-h profiles collected by Alouette I during geomagnetically quiet intervals in the years of 1962, 1963, and 1964. He suggested that the plasma escape through the open field lines can destroy the diffusive equilibrium, and the escape loss is the physical cause of the trough formation.

6.5. Possible cause of the trough

6.5.1. Newell's hypothesis explains the storm time features of the trough quite well, but it cannot meet all the observational facts. The arguments are as follows:

First, according to the modern theory (Axford et al., 1965; Atkinson, 1966; Axford, 1967), the electrojet is caused by the interplanetary electric field conducted down along field lines to the ionospheric height at the time when open field lines returning to the closed form at geomagnetic tail. This jet is believed to cause the substorm. The nature of this jet is time dependent. It shifts rapidly poleward or equatorward even during a single event. The speed of shifting may reach 1 km/sec (Akasofu, 1965). Furthermore, the occurrence of the electrojet differs from day to day (Davis et al., 1966). From our analysis, the trough axis does not change much either with K_p or in different day or month. The trough still appears during magnetic quiet day at $K_p = 0$. Should the auroral electrojet be responsible for the electron trough, then the variation of the trough must correlate with the nature of the electrojet quite closely, but this is a lack of statistical evidence on this point. It should be noted that we do not mean that the effect from the electrojet can be ignored. The drifting process can certainly make the electron density decrease quite a lot. However, it can only be taken as a secondary effect which modifies the distribution of the electron density.

Secondly, the chemical time constant is given by

$$\tau_{chm} = (k_1 \, n(O_2) + k_2 \, n(N_2))^{-1}$$

Take $O_2 = 3x10^6$ cm^{-3}, $N_2 = 5x10^7$ cm^{-3}, $k_1 = 3x10^{-11}$ cm^{-3} sec^{-1}, and $k_2 = 2x10^{-12}$ cm^{-3} sec^{-1} at 300 km, we get $\tau_{chm} = 1.5$ hours The half life of the electron can be estimated by the following expression:

$$n/n_o = e^{-t/\tau_{chm}}$$

as $n/n_o = \frac{1}{2}$, we have $t_{half\ life} = \tau_{chm} x \ln 2 = 1$ hr.

Since τ_{chm} increases with the height, the electrons in the higher altitude should have longer life time, thus the electrons drifted away by the electrojet cannot be annihilated within the time when all electrons at the mid-night meridian were driven awy. (Take $\frac{\partial n}{\partial t} = -200$ el/cm^3 -sec, $n = 2x10^5$ 1/cm^3, the time required to drive all electrons away is about 17 minutes.) If this is true, we should expect that somewhere an accumulation of electron will occur, but this is lacking of observational evidence.

Another point is that in F region, it is a good approximation to set div $\vec{j} = 0$. Under this condition, the plasma driven away eastwesterly will be compensated by the incoming flow in the north-south direction (see streamlines in Fig. 6.2a). The net loss may not be serious.

6.5.2. According to the modern theory as well as the observations, the earth magnetic field has an open tail in the night side (Hess, 1968; King and Newman, 1967; Bame et al., 1967; Dessler, 1964; Dessler and O'Brien, 1965; Axford et al., 1965). Below 72-75° geomagnetic latitude, the field lines are thought to be closed and above that the lines are open (Axford, 1967; Timleck et al., 1969). The location of the closed-open field lines boundary has been detected by Burrows et al., (1969) and McDiarmid et al., (1968). They used the 35-kev electron flux obtained from Alouette II satellite as the tracer. They found that the 35-kev electron detector falls to the cosmic-ray level above about 70° of invariant latitude and suggested the location of the border-line.

Within the closed field lines, the plasma can be in hydrostatic equilibrium. However, in the open lines region, the plasma may escape from the ionosphere along the field lines to the geomagnetic tail where they get lost into space and probably drift away with the solar wind streams.

Dessler and Michel (1966) applied this open tail field model to the hydrogen ion loss, and suggested that the evaporation process can lead a subsonic flow of H^+ escaping from the magnetosphere and upper ionosphere. Mayr (1968) has shown that plasma escape can produce sufficiently large fluxes at latitudes where the field lines are open, thus significantly decrease the hydrogen-ion density. The formation of the plasmapause has been associated with the same concept by him. A recent paper by Banks and Holzer (1968) drew a conclusion that the depletion of H^+ and He^+ ions in the polar regions is a direct consequence of a large scale hydrodynamic expansion of plasma along the open lines of geomagnetic force.

The outgoing flux of protons has been detected by Explorer XXXI satellite. According to Hoffman (1969), there is an evidence from the phase difference of the maxima in the roll modulation curves that H^+ ions are flowing upward with a velocity of 10 to 15 km/sec.

The well-known paper by Carpenter in 1966 showed that the electron density exhibits an abrupt decrease in the equatorial plane at about 4 Re. The region of electron depletion is referred to as Carpenter knee. This knee has been proved to be a permanent feature of the magnetosphere-ionosphere. If we check the position of the knee by projecting it to the ionospheric height level along the field lines, we found that the edge of the knee is at about L = 4 which is the same position as our trough edge, see Fig. 6.1. The diurnal variation of the plasmapause was examined by Carpenter (1966). The formation mechanism of the plasmapause could be the joint action of geomagnetic convection and plasma escape from the open tail as suggested by Nishida (1966). It is quite acceptable that the trough in N_e is related to the phenomenon of the Wistler Knee (Nishida, 1967).

Since the neutral sheet is tilted, and the high latitude field lines which are swept into the lee of the earth by solar wind are asymmetric in the northern and southern polar regions, we may expect that the position of the N_e trough is also asymmetric. Our data show that this is true.

Alouette I satellite data show that the trough axis is at about 60°N magnetic latitude. The average position of the trough in Table 6.2 is about 57°N magnetic latitude which is close to our finding. The boundary between open and closed lines was suggested by Axford (1967) is higher than this. There is a discrepancy as far as the distance between the trough center and the open-close field lines boundary is concerned. This discrepancy of location could be eliminated, if the plasma circulation in the polar region is taken into consideration. According to convection theory (Axford and Hines, 1961, 1964; Axford, 1969) the viscous force produced by solar wind at the magnetopause can set the whole plasma within the magnetosphere in motion. The ionization at ionospheric heights, being frozen onto the field lines, will similarly convect. The convective system is expected to occur even during periods of relative calm, as a consequence of the more steadly streaming quiet-day solar wind, and there is evidence for the existence of a corresponding polar current at such times. Nagata and Kokubun (1962), Obayashi and Nishida (1967) have suggested that a twin current system is set up by the magnetospheric convection. The streamlines of the drifting motion due to DP2 are sketched in Fig. 6.2b. The streamlines corresponding to this twin current link day and night sides in polar region and can encompass the entire terrestrial globe (Nishida, 1968). As plasma circulates into the open field line region, a part of electron-ion pairs can escape along the field lines to the tail. The period of circulation depends on the length of the loop and the drifting velocity. The increase in electron density on the poleward side of the trough can be explained in terms of short stream loop which links day and night polar cap. The ionization created by solar EUV as well as by precipitating electrons in the polar region is sufficient on the day side, and this plasma can be transported to the night side. All our diagrams show that the electron densities in the nighttime meridional profiles increase at the place poleward of the trough. This may be the evidence of the transport effect from day side to the night side due to plasma circulation.

Another point is that the Axford's suggestion of boundary location shall need more evidence to prove and test, and cannot be taken for granted.

Summing up all the descriptions made above, I think that the plasma escape through the open tail plus the plasma circulation process in the polar cap due to DP2 field induced by plasma convection in the magnetosphere can meet the observational phenomena of the quiet day trough. In the disturbed times, the drift loss due to electrojet will enhance the depletion of the electrons, and thus create the large variations of the depleted region with K_p index. Furthermore, the formation of the Carpenter knee may have the same physical cause as to the trough formation.

In the next section we are going to demonstrate the electron depletion due to electrojet by solving continuity equation including east-west drifting term.

6.6. Electron density depletion due to electrojet

6.6.1 Formulation of equation

According to the hypothesis made by Newell that there is a east-west divergence of plasma out of the mid-night region due to electrojet at high latitude, it is worthwhile to include this east-west drifting term in equation (2.34) and solve it numerically. The N-S incoming flow was not included. The term which we omitted before is $\frac{1}{(a+z)\cos\phi}\frac{\partial \Phi_\lambda}{\partial \lambda}$, where Φ_λ is Nu_e .

$$\frac{\partial \Phi_\lambda}{\partial \lambda} = \frac{\partial (N u_e)}{\partial \lambda} = u_e \frac{\partial N}{\partial \lambda} + N \frac{\partial u_e}{\partial \lambda} \qquad (6.1)$$

The first term of equation (6.1) can be written as $u_e \frac{\partial t}{\partial \lambda} \frac{\partial N}{\partial t}$. This term is shifted to the left side of equation (2.34) and combined with the local change term, $\frac{\partial N}{\partial t}$. The second term of equation (6.1) can be combined with the chemical loss term. Thus, we have:

$$\frac{\partial N}{\partial t}\left\{1+\frac{u_e\frac{\partial t}{\partial \lambda}}{(a+z)\operatorname{Cos}\phi}\right\}=Q-\beta' N-\frac{\partial \Phi_z (a+z)^2}{(a+z)^2\partial z}-\frac{1}{(a+z)\operatorname{Cos}\phi}\frac{\partial \Phi_\phi \operatorname{Cos}\phi}{\partial \phi}$$

or
$$\frac{\partial N}{\partial t}=M\left\{Q-\beta' N-\frac{\partial \Phi_z (a+z)^2}{(a+z)^2\partial z}-\frac{1}{(a+z)\operatorname{Cos}\phi}\frac{\partial \Phi_\phi \operatorname{Cos}\phi}{\partial \phi}\right\} \qquad (6.2)$$

where

$$M=\frac{1}{1+\frac{u_e\,\partial t/\partial\lambda}{(a+z)\operatorname{Cos}\phi}}$$

and
$$\beta'=\beta+\frac{\partial u_e}{\partial \lambda}$$

Equation (6.2) is similar to equation (3.4). Consequently, it needs only a minor correction to the previous program and the new results can be obtained easily.

We assume that u_e occurs over the latitude range 67.6°-72.5°N and spans 22.5 degrees of longitude centered at mid-night hour. This is because that the electrojet appears at this location. Furthmore, u_e does not change with height. Then we have the following results.

6.6.2. Computer results

We started to assign u_e a value of $\pm$ 40 m/sec and make a 10 m/sec increment for successive step. The positive velocity is at the region of the post mid-night meridian corresponding to the westward current whereas the negative velocity is associated with eastward jet in the area of pre mid-night meridian. The following facts are found from computer results.

(a) The electron density starts to decrease in the mid-night section where there is a divergence due to electrojet.

(b) When the drifting velocity reaches 60 m/sec, the electron density at 300 km height and at 70°N is reduced to the value which is 40% compared with neighbor point at 5 degrees lower in latitude. In other words, the trough pattern appears at such drifting velocity of ± 60 m/sec. See Figs. 6.3-6.4.

(c) When $V_d = \pm 70$ m/sec, there is a negative value of electron density occuring at 72.5° latitude and at 350 km height. The number of grid points with negative values increase as the east-west drift velocity becomes greater than ± 70 m/sec.

6.6.3. The nighttime source

From above numerical calculations, it is clearly to see that the ionosphere cannot sustain a drifting velocity above 70 m/sec without a nighttime source of ionization. There is some evidence that the corpuscular radiation and the soft precipitated electrons are the major contributors to maintain the ionosphere during the night at high latitudes (Titheridge, 1968; Yonezawa, 1965b; Ivanov-Kholodny, 1965; Dalgarno, 1965). Newell also claimed that the nighttime source is required to balance the loss due to the electrojet. We will discuss more in detail about the energy and nighttime source in the next section.

6.7. Energy and flux

6.7.1. Escape flux

Dessler and Michel (1966) estimated that the escape flux of ionized hydrogen is about $10^8/\text{cm}^2$-sec. Nishida (1966) made a rough calculation and said that the plasma loss from ionospheric level is about 2×10^8 particle $\text{cm}^{-2}\ \text{sec}^{-1}$. A recent paper by Axford and Banks (1968) also agreed that a $10^8\ \text{cm}^{-2}\ \text{sec}^{-1}$ escape flux of H^+ is a reasonable quantity. An upward flow of protons has been observed by the mass spectrometer in Explorer XXXI (Hoffman, 1969) which indicates that the escape of charged particles from the earth is in existence.

6.7.2. Energy estimation

Let E be the energy required to pull out a particle with mass "m" from ionospheric height R to the outer space, we have:

$$E = \int_R^\infty \frac{GMm}{r^2}\,dr = \frac{GMm}{R} = gmR$$

For electron, $m = 9.1\times10^{-31}$ kg, and $R = 6.67\times10^6$ m, $g = 8.95\ \text{m/sec}^2$ (at 300 km).

$$E_e = 8.95 \times 9.1 \times 10^{-31} \times 6.67 \times 10^6 = 5.44\times10^{-23}\ \text{joule} = 3.4\times10^{-4}\ \text{ev}$$

Similarly, for 0^+, He^+ and H^+, we have

$$E_{O^+} \approx 10 \text{ ev}$$

$$E_{He^+} \approx 2.5 \text{ ev}$$

$$E_{H^+} \approx 0.62 \text{ ev}$$

The thermal energy of ambient electron is approximately on the order of 0.17 ev (for $T_e = 2000^\circ K$) which is much larger than the required energy to overcome gravitational force for the electron gas. However, the polarization field prevents further separation of electrons with ions, except that the ion and electron go together.

The above calculations tell us that a minimum energy of 0.62 ev is required to drive H^+-e pair out of the earth gravitational field and the more energy are necessary for He^+-e and 0^+-e pairs. Take $10^8/cm^2$-sec for escaping flux of ionized hydrogen, it needs 0.62×10^8 ev/cm^2-sec or 1×10^{-4} erg/cm^2-sec of energy flux to accomplish this job. Since the thermal energy is too small, an additional energy is required.

6.7.3. Energy source

There are two basic questions concerning the escape mechanism.

1) Where does the additional energy come from? Taking 9 hours for the length of night, and $10^8/cm^2/sec$ for the electron escape flux, then the total loss per cm^2 column is roughly on the order of $3 \times 10^{12}/cm^2$. The total electron content in the high latitudes during daytime is about the same amount. Actually, the ionosphere still remains in the antarctic region during the six month

winter night (Duncan, 1962). Then the second question is:

2) How to replenish the plasma which escaped from the ionosphere if the outward flow is continuous? According to Banks (private communication), the energy required to lift the ions in order to meet the requirements of gravitational potential energy and friction is supplied by the electron gas coming from outside of the ionosphere. Typical energy input rates of 0.1 ev cm^{-3} sec^{-1} are sufficient to maintain the polar wind and it appears that the polar wind is an unimportant factor in the electron gas energy budget.

Dessler and Michel (1966) proposed that the hot solar wind plasma can penetrate into ionospheric height through geomagnetic tail and ionize the neutral gas. The ionization rate must be large enough to maintain the polar ionosphere at night against recombination losses and the plasma escape.

Axford (1964) has calculated that the energy dissipation due to auroral process, ohmic losses and ring currents are approximately 10^{17} erg sec^{-1}, 10^{17} erg sec^{-1} and $2x10^{18}$ erg sec^{-1} respectively. The upper limit of the total energy loss is on the order of 10^{19} erg sec^{-1}. During a magnetic storm the flux of protons from the solar wind is on the order of $3x10^{19}$ cm^{-2} sec^{-1}, and the speed is about 1000 km sec^{-1} (Neugebauer et al., 1962). The total flux of energy was estimated by Axford as being around 10^{22} erg sec^{-1}. Therefore, he concluded that the energy from the solar wind is sufficient to cover all expenses for the disturbance losses.

The first measurements of the interplanetary plasma were those conducted by the U.S.S.R. in 1959 on the moon probe Lunik I. The results gave a positive ion flux of about $2x10^8/cm^2$-sec with ion energy per unit charge greater than 15 ev. In 1963, IMP I satellite measured the ion flux of 10^8-$10^9/cm^2$/sec with equivalent proton energy of 300-1000 ev. Thus only 1 per cent of solar plasma diffusing down the ionosphere is enough to cover the expenses of escape loss.

The energy flux required to produce 10^8 ion pair/cm^2/sec is about $3.5x10^9$ ev/cm^2/sec (The average energy expended in the production of an ion pair by a beam of fast electron absorbed in N_2 is about 35 ev). Again, the solar wind plasma possesses enough energy to accomplish this job.

Another energy source may come from the precipitating electrons. According to O'Brien (1964), there is always some precipitation of the electron in the auroral zone, even when $K_p = 0$. The flux of the precipitating electrons goes up roughly by a factor of 1000 for K_p going from 0 to 6. A downward-moving flux up to 1 erg/cm^2-sec has been found by him. Kamiyama (1966) has calculated the electron production rate due to precipitating electrons. For the electron flux of $5x10^6$ cm^{-2} sec^{-1} $ster^{-1}$, the maximum production rate of secondary electrons due to the impact ionization is estimated to be $2.2x10^2$ cm^{-3} sec^{-1} at the height of 115 km. Chase (1969) estimated that the precipitated electron flux is about 10^7 cm^{-2} sec^{-1} $ster^{-1}$ kev^{-1}. All these show that a continuous nighttime source is present which can compensate the losses through different processes.

6.8. Seasonal variation of the trough

From our extensive analysis of 3 years Alouette satellite data, we found that the nighttime trough has seasonal variations. In the months of September, and December, the trough is very clear. In May, the trough becomes weak, and in June, it is gone below 600 km and only a slight trace remains above 600 km height. Liszka (1968) analyzed 15 months data of ionospheric electron content made at Kiruna, Sweden ($\phi = 67^{\circ}N$, $\lambda = 20^{\circ}E$) and found the following features about the variations of the trough:

"In Winter, the trough is very clear during all nighttime. In Spring and Autumn, the trough is observed respectively at the beginning and end of the period. In Summer the trough does not show." See Table 6.2 for the positions of the trough.

We then ask: Why doesn't the trough show in Summer nights?

The possible explanation is that during the summer season, the north pole is deep in the sunlit side of the earth, and since the north pole is inclined $23\frac{1}{2}^{\circ}$ toward the sun, the sun's rays are shifted northward by the same amount and the tangent rays in the northern hemisphere pass over the pole and reach the Arctic Circle ($66\frac{1}{2}^{\circ}N$). The production of electron by solar radiation can thus reach the Arctic region day and night. The total production rate of electrons within the height range of 150 km to 1000 km by solar radiation at 70° latitude is on the order of $4\times10^{9}/cm^{2}$-sec which is much larger than the escape loss. Therefore the trough can be filled up easily. It is quite consistent that the trough tends to be filled up starting from low levels. This is because that the production rate is stronger in the lower altitudes.

By the same token, we can explain why the trough does not show in the day side of the ionosphere. It is the solar EUV radiation which can compensate the loss through escape process.

6.9. Conclusion

By examining three years data obtained from the Alouette I satellite, it can be concluded that the electron density trough is a permanent feature of the ionosphere. The low density region exists both in the northern and the southern hemispheres above about 60-65 degrees geomagnetic latitude under all magnetic conditions. This low density region extends from the F2 peak to the satellite height at 1000 km during the night hours. In the daytime, even though the trough does not exist in the lower ionosphere, it does occur at the higher altitudes. The boundary of low plasma region matches Carpenter's knee quite well. Since the outgoing flux of protons has been detected experimentally by Explorer XXXI (Hoffman, 1969), the escape of charged particles from the ionospheric level to the outerspace along the open field lines could be counted as the direct cause of the Muldrew's trough. The escape effect can reach to the region below 60° geomagnetic latitude through DP2 current system. In the disturbed day, the field associated with the electrojet can push the plasma out of the midnight sector and make the movement of the trough position vary with K_p index. The energy which is expended on the plasma escaping against the gravitational field and the viscous force may come from solar wind and the precipitating electrons.

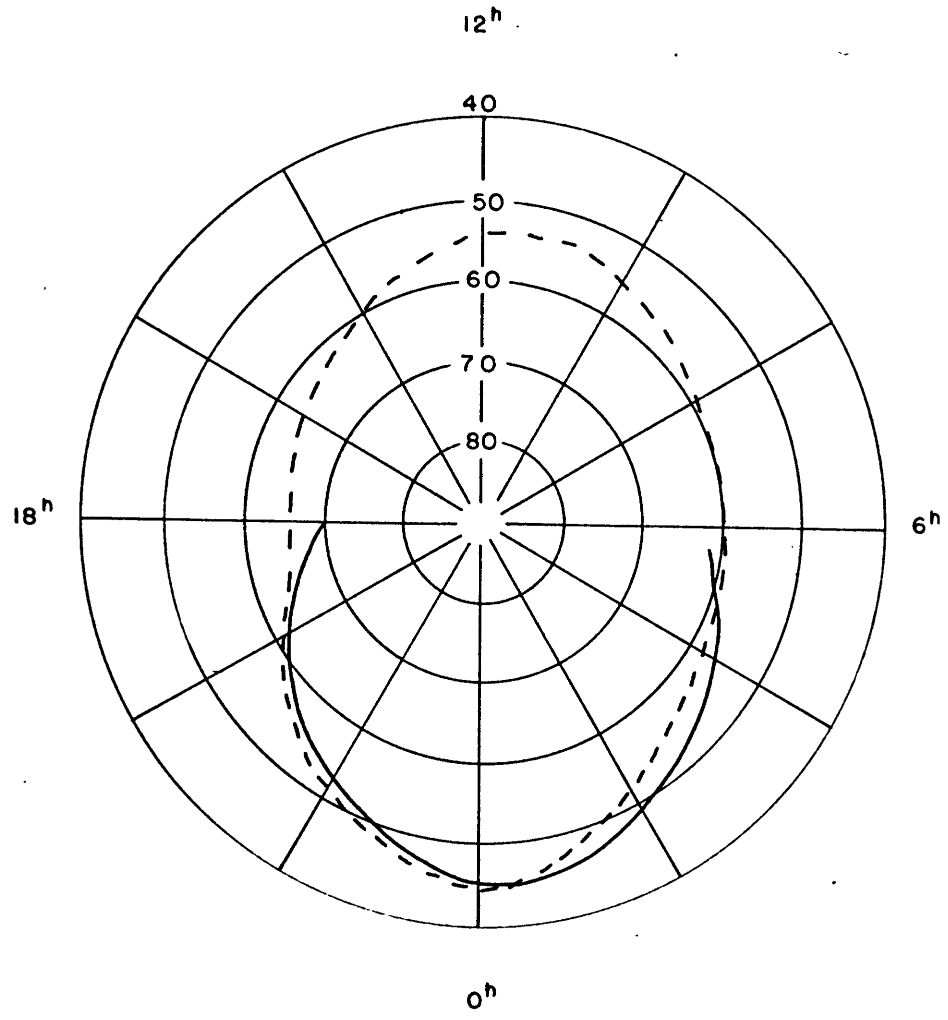

Fig. 6.1. Comparison between positions of the trough center and the Carpenter knee. The dashed curve shows the position of the Carpenter knee on the ionospheric height at 300 km (projected from Carpenter's paper, 1966), the solid curve for the trough center between the time of 16 UT to 05 UT, Oct. 24, 1962 (from Alouette I data). (In geographic coordinates).

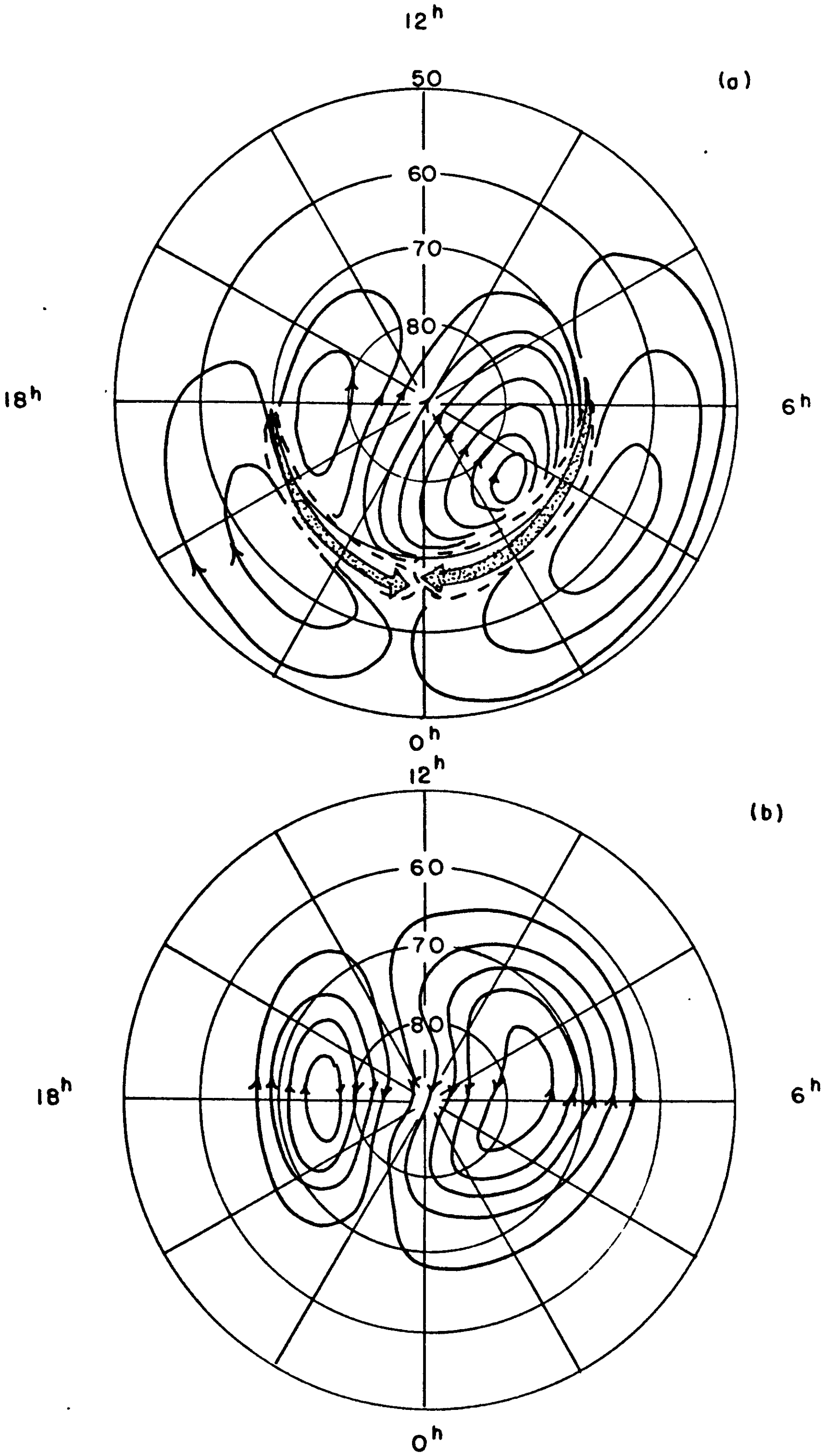
12^h
50
(a)
60
70
80
18^h
6^h
0^h
12^h
(b)
60
70
80
18^h
6^h
0^h

Fig. 6.2. (a) Equivalent current system of DP1 or auroral electrojet current system (after Hess, 1966)., (b) Equivalent current system of DP2 (after Obayschi and Nishida, 1968). (In geomagnetic coordinates).

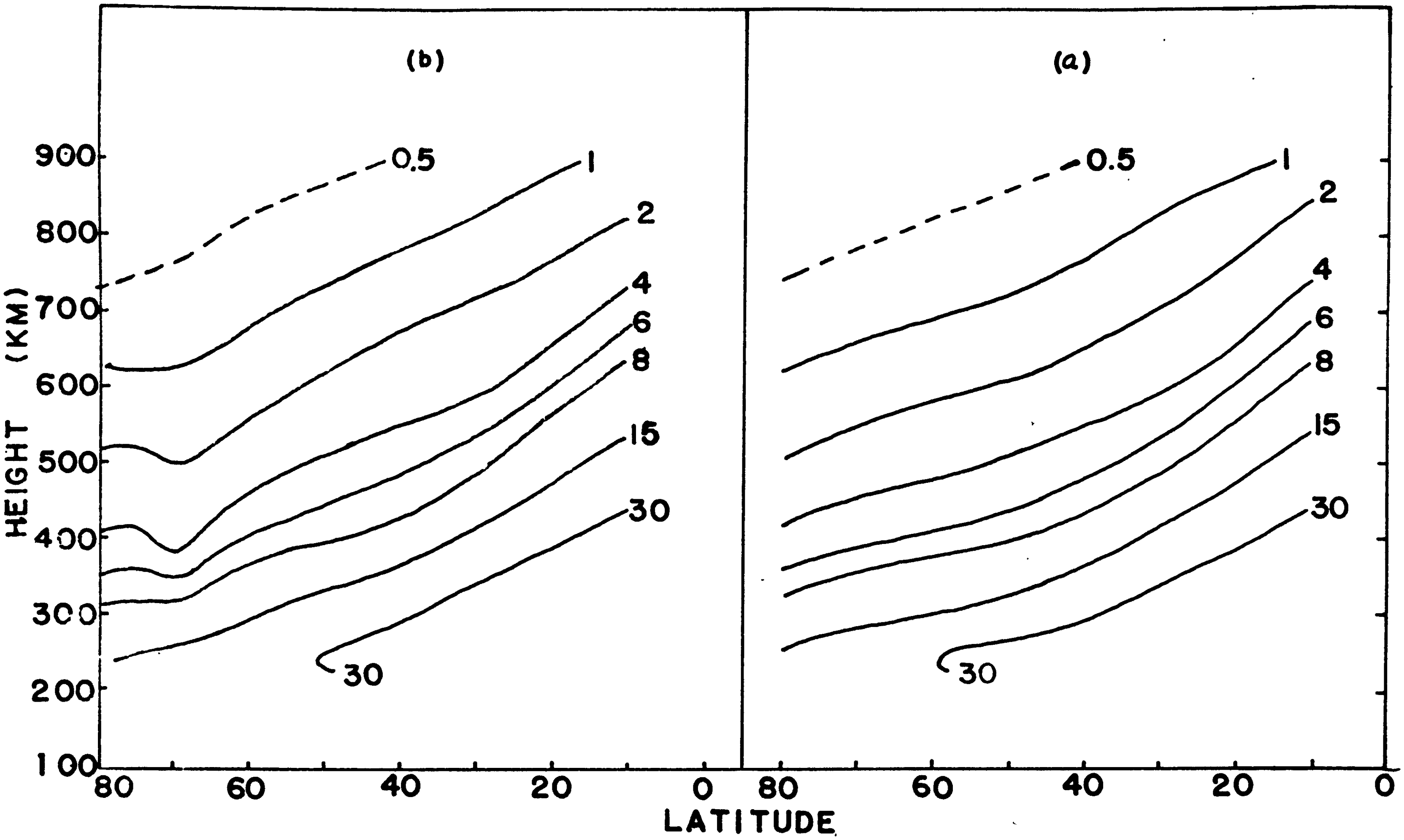

Fig. 6.3. Meridional cross sections of electron density at mid-night. Units: 10^4 el/cm^3. (a) without drift, (b) with east-west drift of ± 40 m/sec.

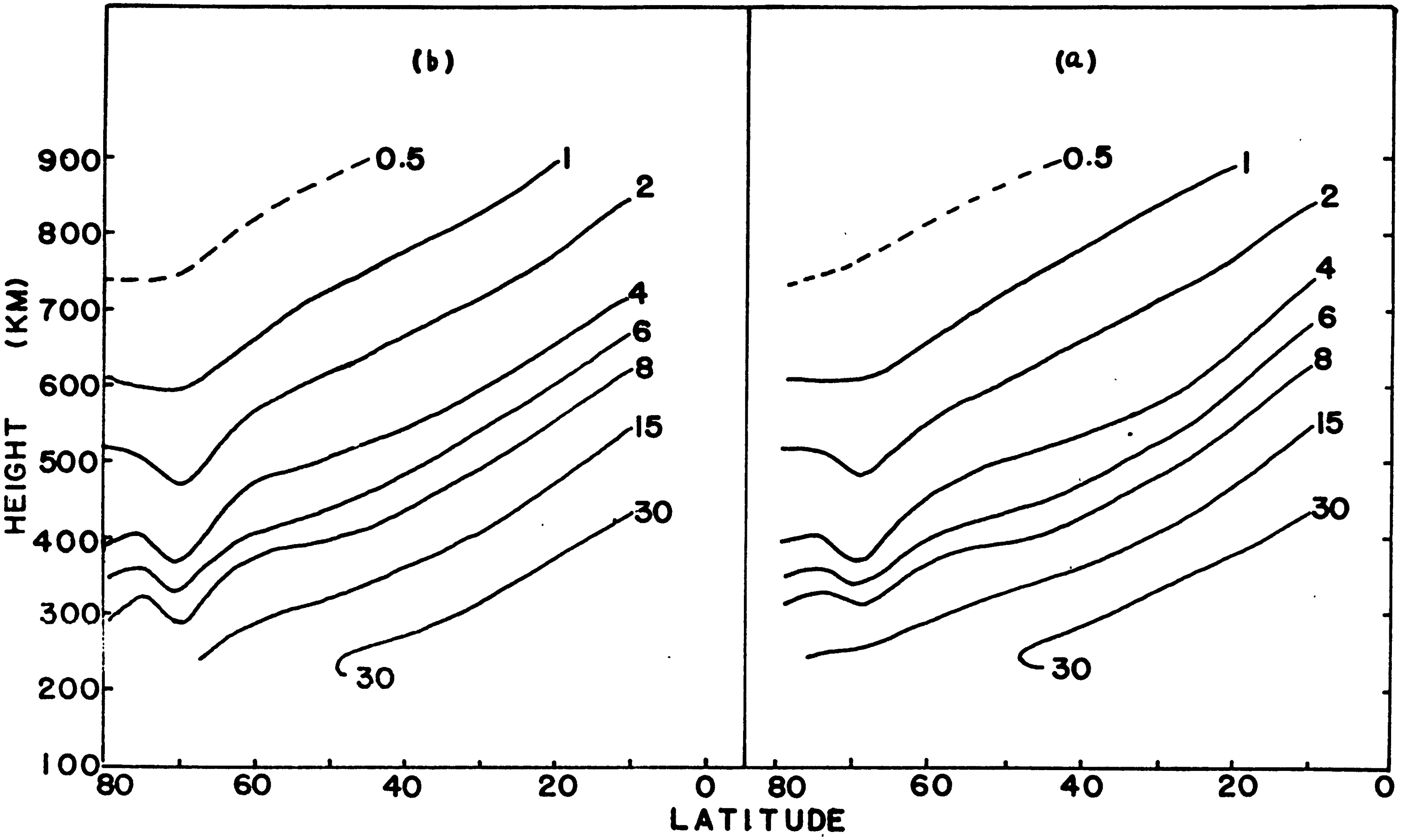

Fig. 6.4. Meridional cross sections of electron density at mid-night. Units: 10^4 el/cm^3. (a) with east-west drift of ± 50 m/sec, (b) with east-west drift of ± 60 m/sec.

CHAPTER 7

F2 PEAK HEIGHT AND VERTICAL TRANSPORT VELOCITY

7.1. Introduction

Since production rate decreases with height more slowly than the recombination coefficient above the F1 peak, the electron density, in the steady-state case, should increase monotonically with height if no diffusion occurs. However, in the actual case, the F2 peak does exist at a height of about 300 km. According to Yonezawa (1965a) and Rishbeth (1967b), the formation of the F2 peak is due to electron-ion diffusion in the gravitational field. Electrons and ions produced at higher levels tend to be distributed according to diffusive equilibrium, while a steady-state distribution is maintained at lower levels due to a slower diffusion rate, so that a peak of electron density appears at an intermediate height.

The F2 peak is approximately located at the height where the loss rate equals the diffusion rate. It is noted that in the stationary case, the pressure force, the gravity force and the electrostatic force are in balance, so that the effective ion mass is reduced due to the electrostatic force exerted by electron. The distributions of the neutral atmospheric constituents, temperature, dip angle and sunspot number all influence the location of the F2 peak. Based on bottomside ionospheric data Rishbeth (1968b) has summarized the general pictures of h_mF2 as follows:

1) h_mF2 increases with decreasing latitude.

2) h_mF2 is higher during the night than during the day at all latitudes except around the magnetic equator belt.

3) h_mF2 is higher in summer than in winter.

4) h_mF2 has a positive correlation with solar activity.

Yonezawa (1956, 1958) has shown that, in the steady-state case, upward drift motion of electrons and ions makes the F2 peak shift to a higher level accompanied by an increase in peak electron density while downward drift motion makes the F2 peak shift to a lower level accompanied by a decrease in peak electron density. Gliddon and Kendall (1962) have studied time-dependent cases and included vertical drift produced by motion of the neutral air and the electro-dynamic force. They found that h_mF2 is positively correlated with vertical drift. Rishbeth (1968a) has tabulated the various physical processes which govern daily variation of h_mF2. However, most of the results concerning h_mF2 variation come from the bottomside of the ionosphere, and the investigations are restricted to one fixed station. It is the purpose of this chapter to present a satellite view of the F2 peak. The great advantage of the satellite is that we can see the latitudinal changes of h_mF2 for the whole hemisphere within one hour or so. Furthermore, a rough calculation about the vertical transport velocity from the observational N-h profile was done. The correlation between h_mF2 and this velocity is also calculated so that we have a general idea of how important the vertical transport is to the F2 peak height under quiet as well as disturbed magnetic conditions.

7.2. Observational results of h_mF2

Figs. 7.1-7.4 show the detailed picture of F2 peak height during day and night times in different seasons and magnetic conditions. The general results can be described as follows:

7.2.1. Diurnal variation

F2 peak is higher in the equatorial region (Range 20^oN-20^oS magnetic dip) during day-time than during night-time, whereas in the mid and high latitudes, the reverse is true (Figs. 7.1-7.2).

7.2.2. Storm effect

(a) Equatorial area: the day-time F2 peak is lower for the solar quiet day than for the disturbed day. This shows in Figs. 7.3a-7.4a. Another set of data on September 19, 1963, at $K_p = 4$, shows the similar feature (not shown here).

The nighttime h_mF2 decreases a little when K_p is getting larger (Figs. 7.3b-7.4b).

(b) Mid and high latitudes: The day-time h_mF2 is higher in the Southern Hemisphere as the K_p index increases, whereas nighttime h_mF2 decreases a little during a disturbed day (Figs. 7.3a-7.4a).

7.2.3. Seasonal change: Day-time h_mF2 is higher in June than in December in the Northern Hemisphere, while the reverse is true for nighttime h_mF2 (Figs. 7.1b-7.2b and Fig. 4.3).

7.3. Vertical transport velocity

Chandra, Gibbons and Schmerling (1960) were the first group to calculate plasma vertical velocity from the equation of continuity. They took four IGY stations and found that the velocity is predominantly downward during the night and upward during the day at the equatorial stations. The vertical velocity is on the order of 25 m/sec. Doupnik and Rishbeth (1968) used the same equation to estimate the transport velocity at and above the F2 peak at Arecibo, Puerto Rico (18.29°N, 66.40°W). Their results gave 5, 10 and 24 m/sec at 250 km downward at local noon for the months of July, August and December respectively. Mitra et al., (1967) found that the vertical transport velocity is downward at Delhi (42.5°N) and has a nearly constant value of 6-7 m/sec during 00-03, while at Huancayo (2°N), the downward velocity varies from 12 to 16 m/sec during 00-03 hours.

The common drawback in the above mentioned authors' results is that they either use Chapman's theoretical formula or some other approximate method to calculate the electron production rate. Since the vertical transport velocity is proportional to the difference of the production rate and the recombination term, the error in Q can affect quite a lot the results. Here, our Q is calculated from actual solar flux data measured by Hinteregger et al., (1965) in the same year as the N-h profile data measured by Alouette I topside sounder.

7.3.1. Formula

We follow Chandra et al., (1960), but with further approximated adjustment in order to use our data.

Continuity equation:

$$\frac{\partial N}{\partial t} = Q - \beta N - \mathrm{div}\,(N\vec{v}) \qquad (7.1)$$

For mid and high latitudes, we can neglect horizontal flux comparing with vertical one, and since for the time at around local noon $\frac{\partial N}{\partial t}$ is small, (7.1) can be written as:

$$Q - \beta N - \frac{\partial (Nw)}{\partial z} \approx 0 \qquad (7.2)$$

Integrating (7.2) from z_1 to z_2, we have:

$$\int_{z_1}^{z_2} (Q - \beta N)\, dz = (Nw)_{z_2} + (Nw)_{z_1} \qquad (7.3)$$

If we choose z_1 and z_2 in such a way that at z_2 the $N(z_2)$ is at least one order of magnitude less than $N(z_1)$, while $W(z_2)$ does not differ by an order of magnitude between z_1 and z_2, then $(NW)z_2$ can be neglected comparing with $(NW)z_1$. We thus have an approximate formula for computing vertical transport velocity at local noon for mid and high latitudes:

$$w(z_1) = \frac{-\int_{z_1}^{z_2} (Q - \beta N)\, dz}{N(z_1)} \qquad (714)$$

The loss rate coefficient, β , was calculated by using a temperature dependent formula:

$$\beta = k_1 \, n(N_2) + k_2 \, n(0_2) \ \text{sec}^{-1}$$

where
$$k_1 = 3x10^{-12} \left(\frac{T_n}{300}\right)^{-1.5} \ \text{cm}^3/\text{sec}$$

$$k_2 = 4x10^{-11} \left(\frac{T_n}{300}\right)^{-1.5} \ \text{cm}^3/\text{sec}$$

T_n , $n(0_2)$, $n(N_2)$ were picked from CIRA 1965 data, and N from Alouette I data.

7.3.2. Results

N-h profiles in March, June, September and December in quiet day, $K_p \leqslant 3$, at local time between 1200 and 1300 were used. The vertical transport velocities computed from these N-h profiles are shown in Figs. 7.5-7.8. Fig. 7.7 also shows the vertical transport velocity on disturbed days, $K_p = 7$, in September. The results are as follows:

(a) The vertical transport velocity is maximum at the F2 peak and decreases with height. It should be noted that this conclusion may not hold for much higher altitudes where equation (7.4) is invalid.

(b) The velocities are downward around noon hours for all levels and all seasons (Figs. 7.5-7.8), except in December case in which the vertical velocities are upward at the F2 peak (Fig. 7.8). It is noted that these upward velocities only occur in the Northern Hemisphere and at the F2 peak. Above the F2 peak, the velocities in December are also downward. Another set of data on December 19, 1963, at $K_p = 2$ (not shown here) has similar features as shown in Fig. 7.8.

(c) At the F2 peak as well as at other constant height levels the downward velocities are largest at about 50°N and 40°S geographic latitudes and decrease both poleward and equatorward. The magnitude is on the order of 20 to 50 m/sec in the latitude range of 30 to 70 degrees.

(d) Below 30 degrees of latitude, the vertical transport velocity diminishes and approaches zero at the equatorial region for all seasons and all heights. We shall discuss this later.

7.4. The relation between F2 peak and the vertical transport velocity.

The correlation coefficients between h_mF2 and the vertical transport velocities have been calculated. Table 7.1 gives their values. The mean values of h_mF2 and the vertical transport velocity, and the number of data pairs for different months, are also given in the table. It is noted that the data points are in the latitude range of 30° to 65° both in the northern and southern hemispheres. The points below 30° of latitude are not included in the computations.

Table 7.1. Correlation coefficient between h_mF2 and vertical transport velocity.

R = correlation coefficient; $(h_mF2)_{mean}$ = Mean value of F2 peak with latitudes

$(W)_{mean}$ = Mean value of vertical transport velocity at F2 peak; N = No. of data pair

K_p	Data	N	R	$(h_mF2)_{mean}$ km	$(W)_{mean}$ m/sec
0	March 13, 1965	48	0.26	266.88	-19.93
0	March 17, 1965	29	0.30	236.14	-23.42
1	March 19, 1965	49	0.28	239.60	-46.52
2	March 25, 1965	12	0.41	256.25	-57.07
3	March 3, 1965	49	0.25	265.78	-20.36
6	March 10, 1965	40	0.50	272.67	-25.33
1	September 13, 1963	67	-0.24	236.88	-58.09
2	September 24, 1963	31	0.16	248.71	-35.37
2	September 12, 1963	72	0.25	257.65	-58.68
3	September 13, 1963	17	-0.37	231.06	-28.83
3	September 23, 1963	74	0.20	255.92	-52.45
7	September 14, 1963	127	0.58	284.04	-31.03

It is seen from Table 7.1 that the relation between h_mF2 and the vertical transport velocity is larger during storm times than under quiet conditions. General speaking, the downward velocity is smaller and the F2 peak averaged with latitude is higher during storm times than during quiet hours. We realize that it is hard to draw a definite conclusion based on our few samples. However, since this is a pioneer work, our purpose is to throw some light on this point and hope that further research will be carried on later.

7.5. Conclusion and discussion

(a) Strobel (1968), who made a simultaneous calculation coupling the equation of continuity of ions with the momentum equation of the neutral atmosphere, strongly suggests that the maintenance of the nighttime F-layer in the mid-latitudes could be due to upward motion of ions caused by neutral winds. From our analysis, it seems that F2 peak rises during the night in the mid-latitudes and shows evidence of upward motion. However, in the equatorial region, h_mF2 decreases during the night which may imply that the motion is downward. Our three-dimensional numerical solution of the equation of continuity has shown that the decreasing total electron content in the equatorial belt is accompanied by an increase in electron content at about 15° latitude during the early night. It is suggested from these results that the downward motion associated with horizontal divergence from equator toward both north and south should be considered as the important process to maintain nighttime electrons at subtropical zones.

(b) As we found in Figs. 1.1-1.6, the electron densities do not increase all over the world as $K_p > 4$. The present results show that during disturbed hours, h_mF2 goes higher and the correlation coefficient between h_mF2 and the vertical transport velocity is higher too. These seem to suggest that the alternation of h_mF2 is associated with upward and downward motions in the different regions, and it may imply that the electron density variations are also associated with the motions. King (1967) found that electrons are positively correlated with K_p in the equatorial region and negatively correlated above 20 degrees of magnetic dip. The heating effect is thought by him to be the most important factor to reduce the electron concentration. Sata (1968b), on the other hand, maintains that the electron drift induced by the magnetic disturbance is the main factor for the density changes in the various regions. We suggest that the bodily motions in the different regions should not be overlooked.

(c) Equation (7.4) is not a good approximate formula to be used to compute the vertical transport velocity in the low latitudes since the horizontal flux is comparable to the vertical flux below about 30 degrees latitude, and cannot be neglected. Theoretically speaking, the vertical motion is prohibited within the equatorial region where the field lines are horizontal. In the low latitudes, the electromagnetic force is the major factor to drive plasma into vertical motion, whereas in mid and high latitudes, this vertical motion can also be accomplished by the neutral winds, gravitational force and the pressure force in addition to the electromagnetic force. Consequently, it is expected that the vertical transport process should be slow as we approach the equator. This is exactly what we found in our results.

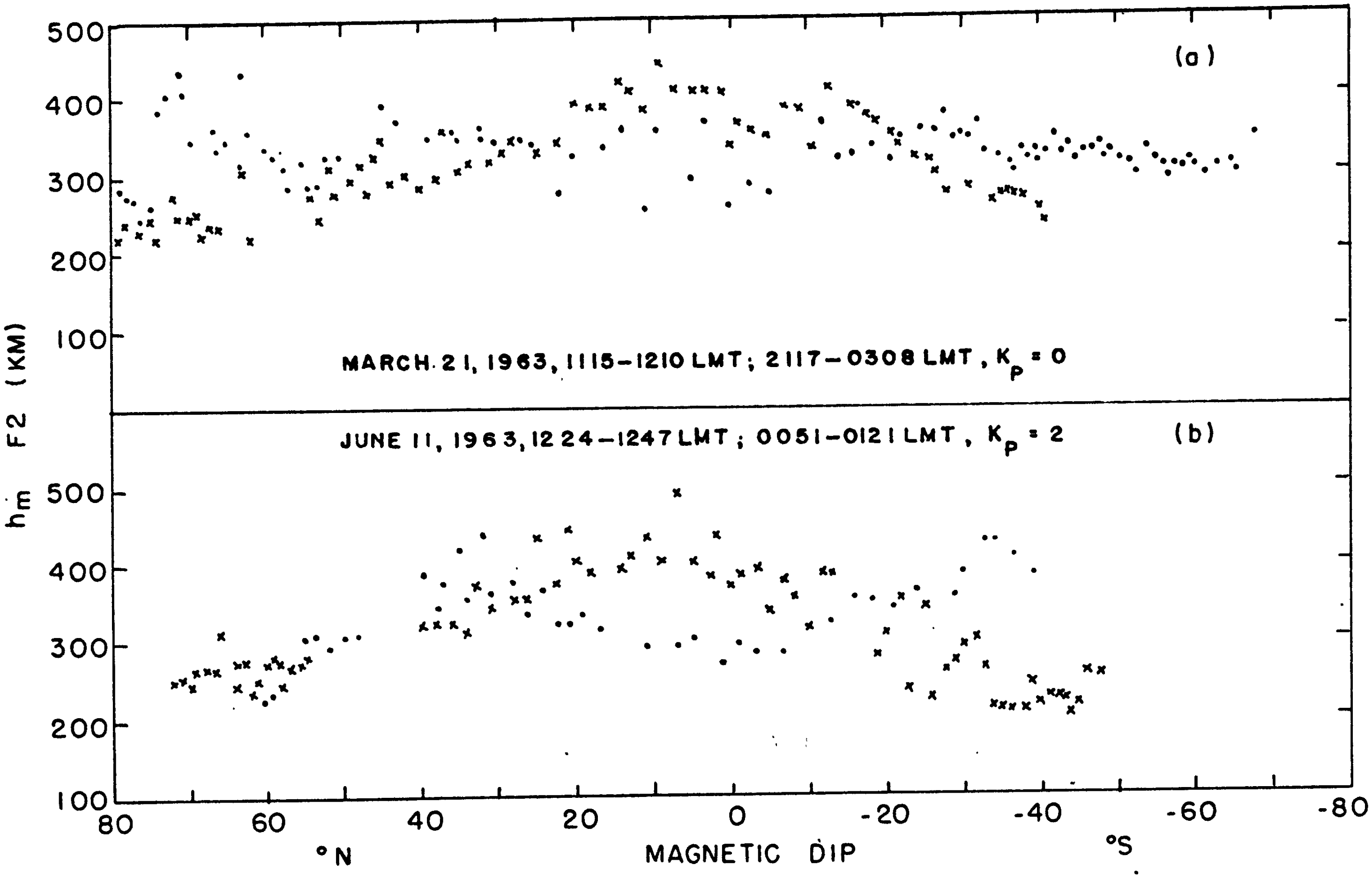

Fig. 7.1. Latitudinal variation of h_mF2 from Alouette I in March and June. The dots are in night-time, the cross in day-time.

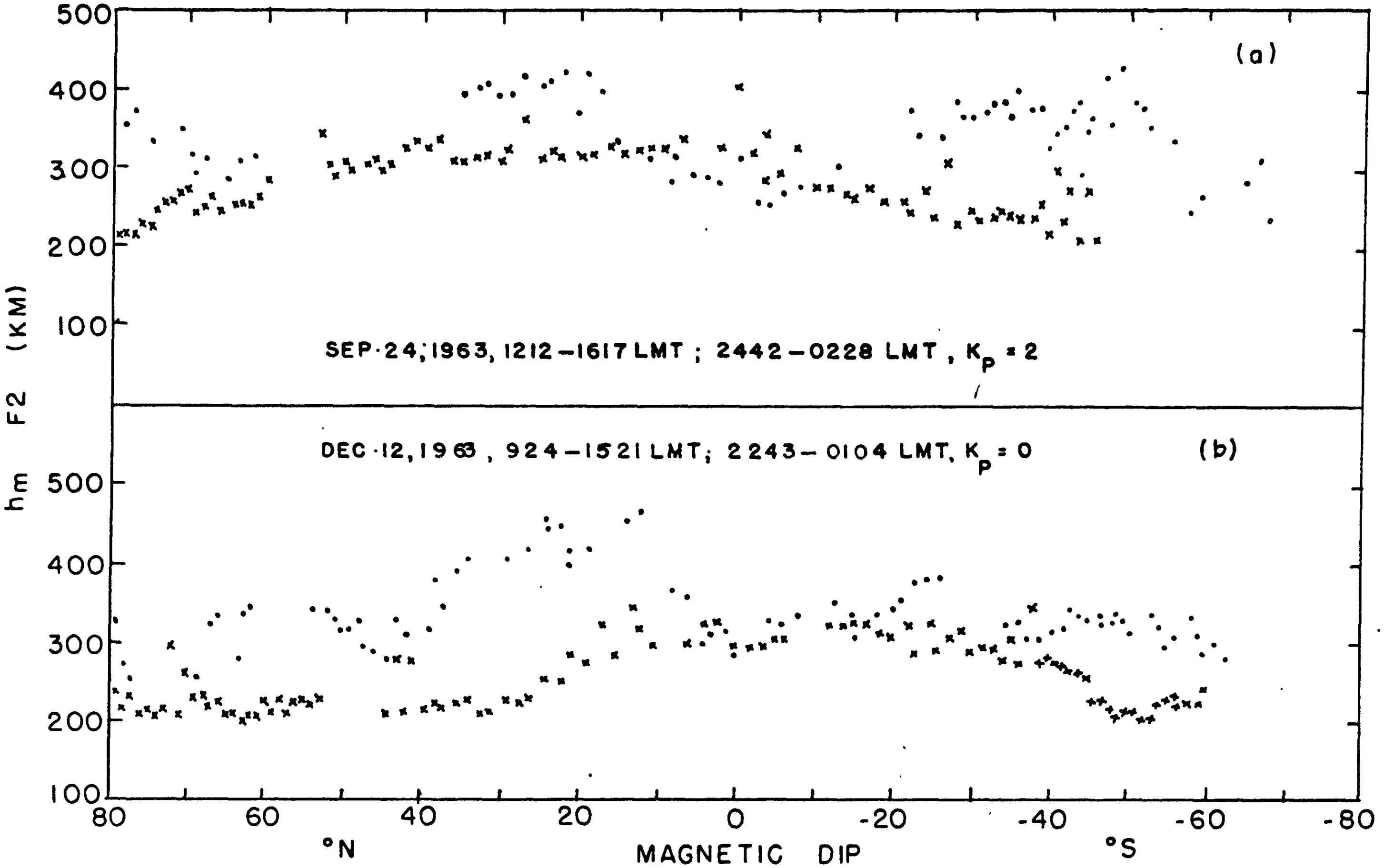

Fig. 7.2. Latitudinal variation of h_mF2 from Alouette I in September and December. The dots are in night-time, the cross in day-time.

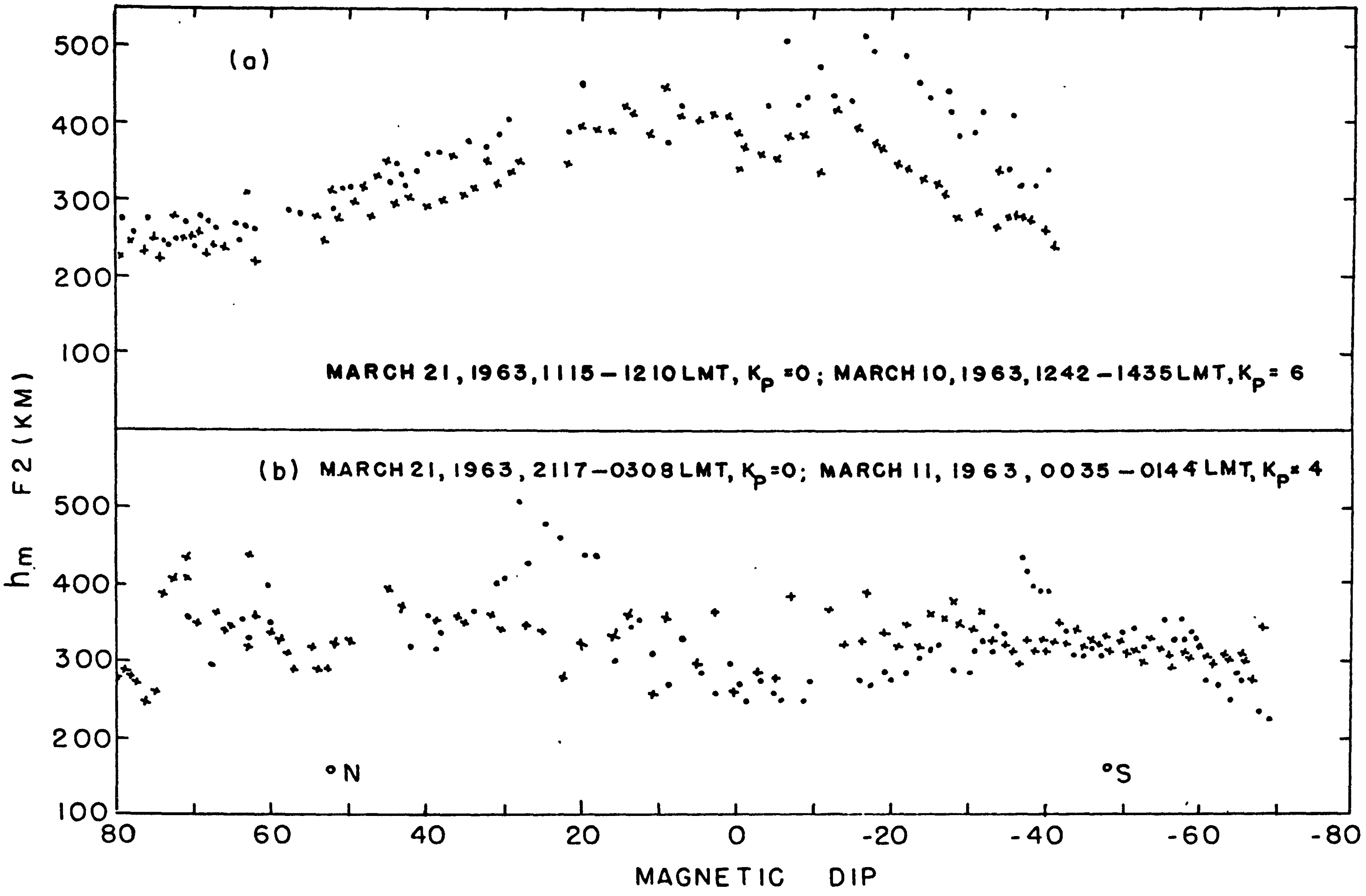

Fig. 7.3. Latitudinal variation of h_mF2 during storm and quiet times. The dots represent data in disturbed time, the cross in quiet condition.

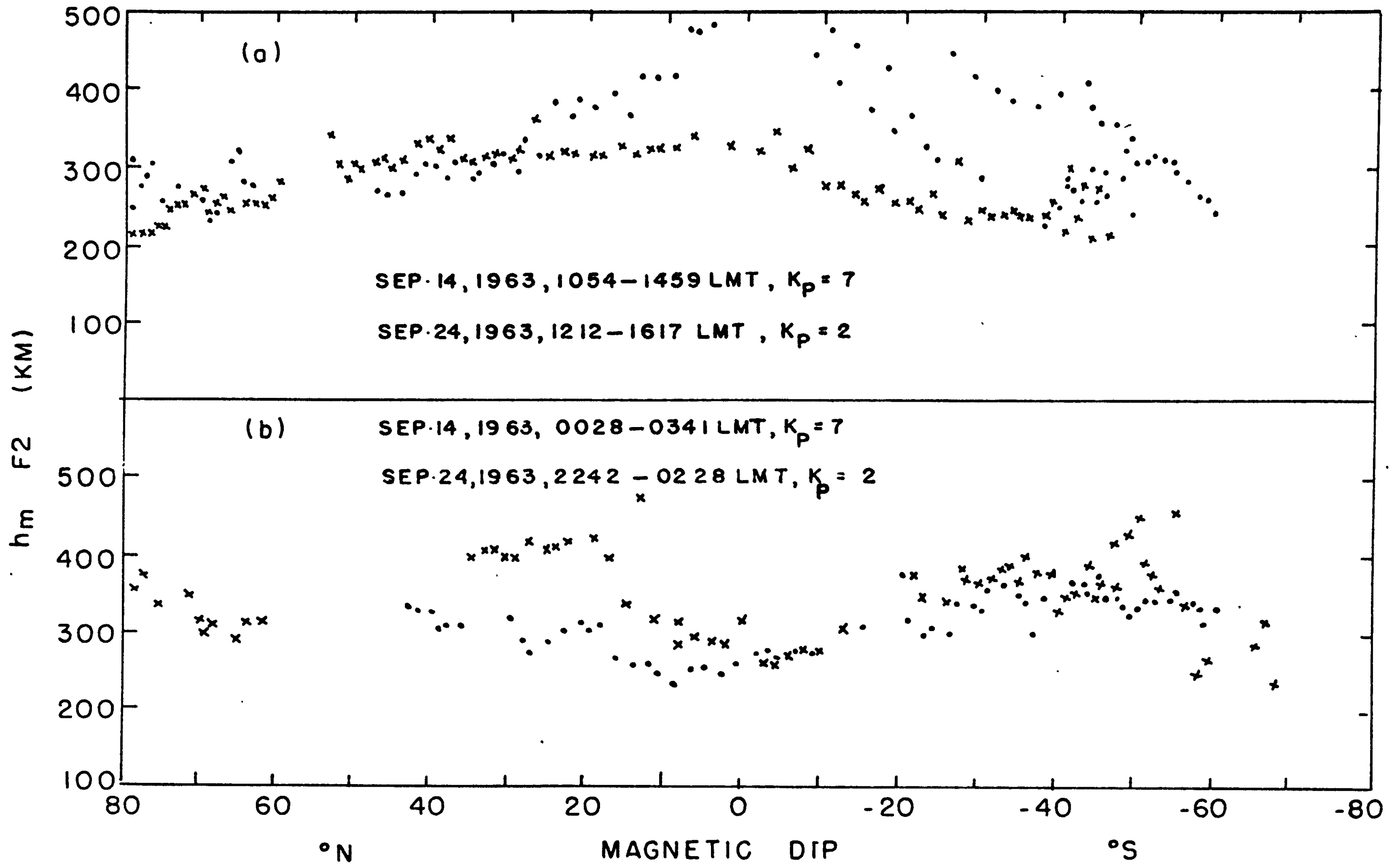

Fig. 7.4. Latitudinal variation of h_mF2 during storm and quiet times. The dots represent data in disturbed time, the cross in quiet condition.

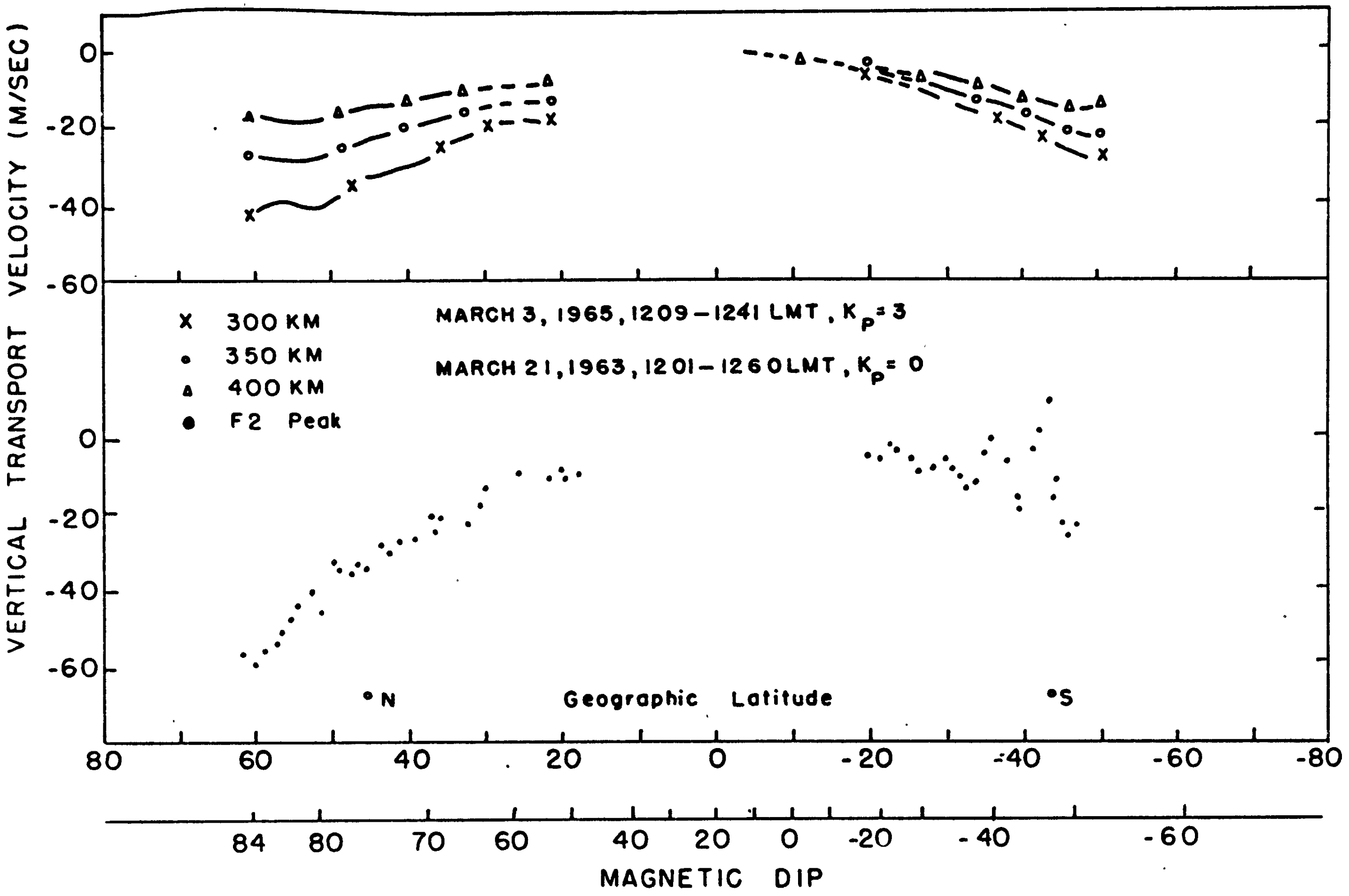

Fig. 7.5. Vertical transport velocity in March.

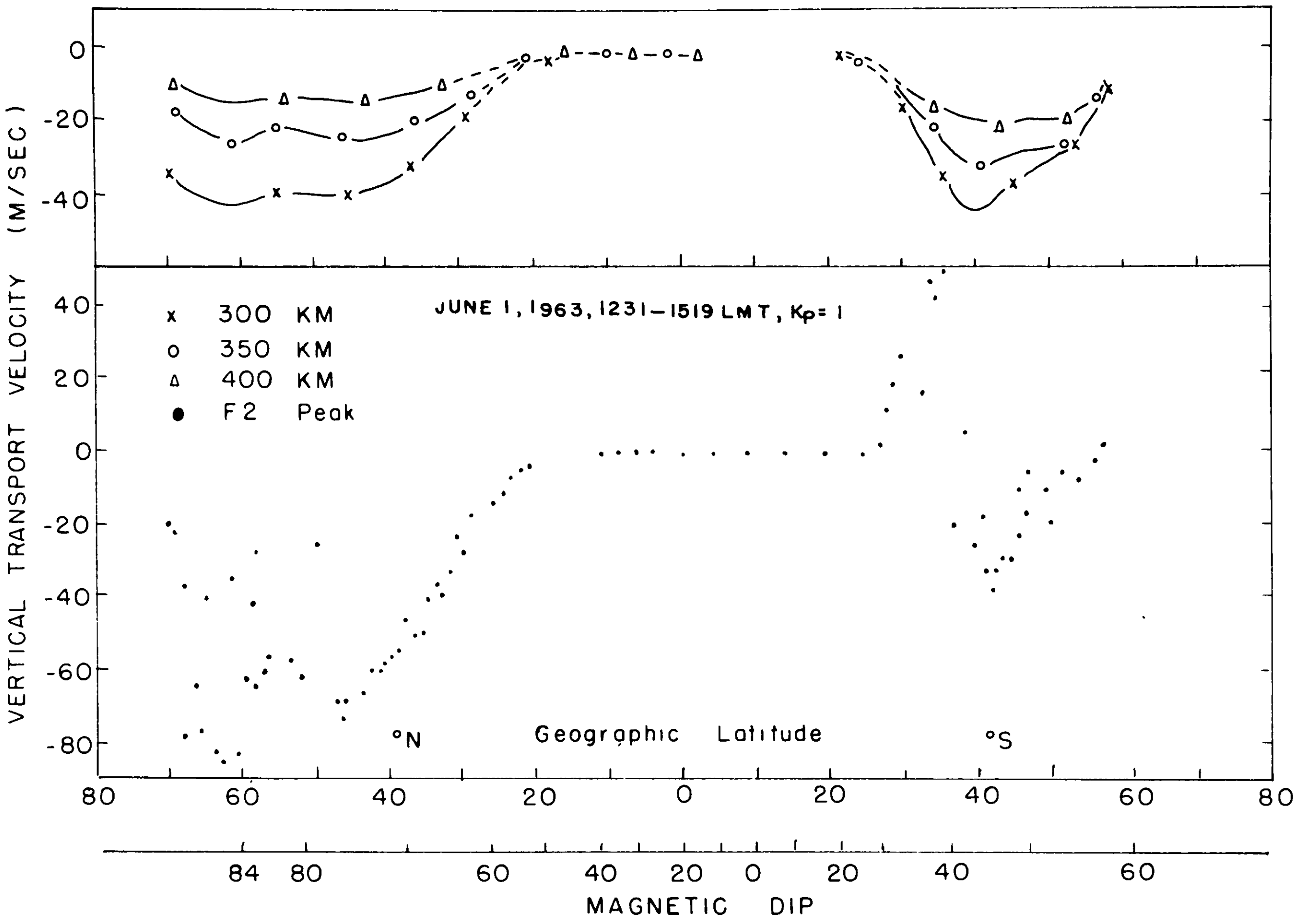

Fig. 7.6. Vertical transport velocity in June.

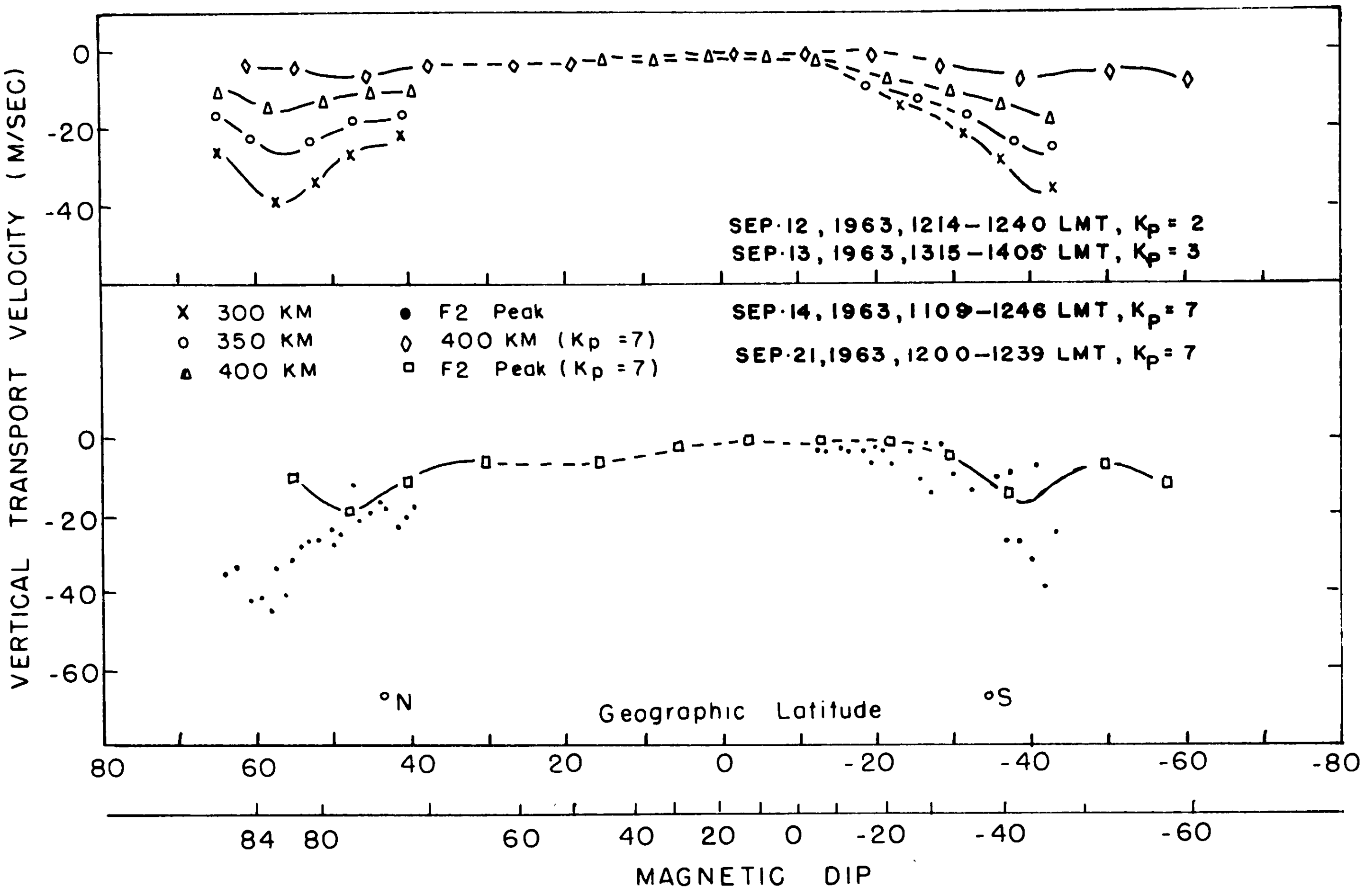

Fig. 7.7. Vertical transport velocity in September.

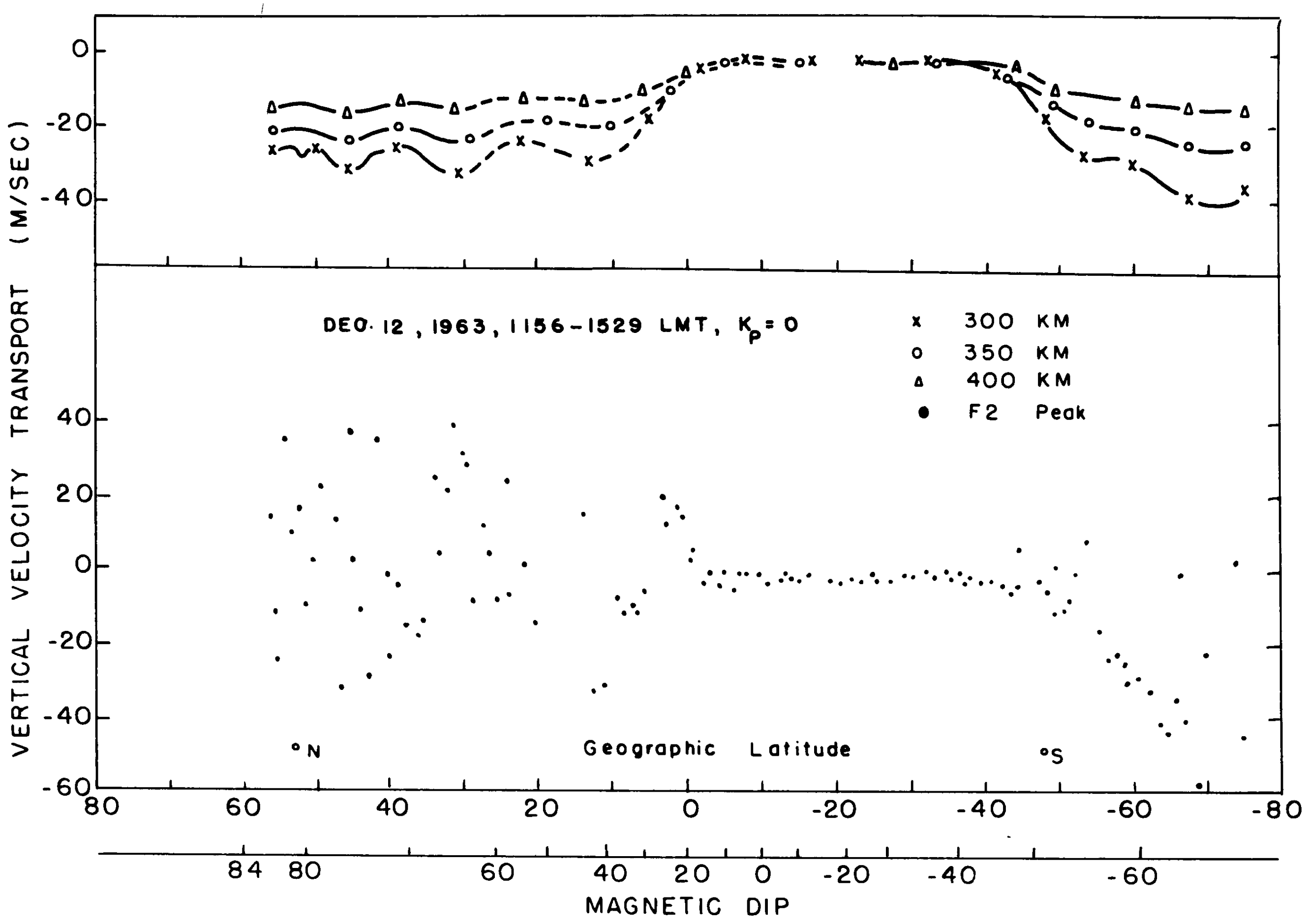

Fig. 7.8. Vertical transport velocity in December.

CHAPTER 8

SUMMARY AND CONCLUDING REMARKS

The object of this study is to present a satellite view of the F-region seasonal anomaly, the equatorial anomaly and the Muldrew trough. The possible physical causes are proposed through data analyses as well as theoretical calculations. The results of this investigation establish the following facts:

(I) The seasonal anomaly

The Alouette I satellite data show that the midday maximum electron densities at the F2 peak in the midlatitudes in the Northern Hemisphere are greater in December than in June. This fact agrees with the bottomside ionospheric observations. The total electron contents above the F2 peak do not have anomalous features, which also agrees with those results obtained from the ground radar stations. The continuity equation of electron density for the steady state case has been solved numerically. The solar zenith angle, the mean distance between the sun and the earth, and the plasma temperature difference between winter and summer seasons have been adjusted. In addition, we systematically increased the atomic oxygen density in the winter hemisphere and also increased the densities of the molecular gases, N_2 and O_2 in the summer hemisphere in the model calculations, so that the electron production rate increases in winter and the loss rate increases in summer. It is found that a 50% increase of O in winter and a 50% increase of N_2 and O_2 in summer are enough for the formation of the seasonal anomaly as compared with the observational facts. We searched the current literature for rocket and satellite data on the maximum change of the neutral atmospheric compositions from summer to winter. The evidence shows that a fifty percent change in the neutral atmospheric compositions is a reasonable amount. We thus conclude that the F-region seasonal anomaly could be produced by the seasonal change of the neutral atmospheric compositions.

(II) The equatorial anomaly

We shall not repeat the details of the results which were described in the text; but will merely list the general findings about the equatorial anomaly.

(a) Before 10:00 o'clock in the morning, the shape of the equidensity contour over the equatorial region is dome-like. A single maximum is located over the magnetic equator. There is no anomaly.

(b) At about 11:00 local time, two maxima of electron density appear on either side of the dip equator in all seasons.

(c) The anomaly is well formed around 12:00 local time and most developed in its depth and width near 16:00 LMT. The total length of time required to build this anomaly is on the order of 2 to 3 hours which agree with bottomside ionospheric observations.

(d) In general, the equatorial anomaly is not symmetric with respect to the magnetic equator. There is a seasonal variation on the life time of this anomaly, being longest during summer months and shortest in winter season.

A three dimensional continuity equation has been solved. The results show that a vertical drift velocity of 20 m/sec produced by the east-west electric field at the equator can be taken qualitatively as the production mechanism for the equatorial anomaly. It is also found that the plasma is likely to move directly toward the region of maximum density. The plasma flux does not go via the 840 km height in the equatorial plane as was thought by many ionospheric workers.

(III) The Muldrew trough

The electron trough is present for all magnetic conditions during the night. The electron densities are depressed by a factor ranging from 2 to 3 or more within 5 degrees of latitudes in the trough region. The location of the trough axis is around 74° dip latitude (44°N geographic latitude or 60°N geomagnetic latitude) in the North America sector. The low density region extends from 250 km up to the satellite location at about 1000 km height (no data available below 250 km and above 1000 km). The axis of the trough shifts only a little toward lower latitude as K_p increases. However, as K_p index increases, the edge of the trough moves toward the south and the width of the trough is broader. The trough has a seasonal variation. It is very clear in the months of September and December, but weak in May. In June, it does not show below 600 km height and only a slight trace remains above 600 km.

The physical cause of the electron trough is still in open debate. However, from experimental evidence as well as theoretical calculations, it is suggested that plasma escapes from the ionospheric level to the geomagnetic tail along the open field lines could be counted as the direct cause of this trough. The escape effect can reach to the region below 60° geomagnetic latitude through the DP2 current system which encompasses the entire terrestrial globe. It is also suggested that the effect from the electrojet as first proposed by Newell is also important during storm time. From our numerical calculations, we found that the east-west drift velocity of 60 m/sec is already enough to create the trough. The possible cause of the disappearance of the trough below 600 km height during the summer nights could be thought of as continuing sunshine over the region of the Arctic Circle. The solar wind and the precipitating electrons may be considered as the energy sources which supply escape loss as well as nighttime production source.

(IV) The F2 peak and the vertical transport velocity

The vertical transport velocities at the F2 peak are on the order of 20 to 50 m/sec and are downward during noon hours. The largest downward velocities are at about 50°N and 40°S geographic latitudes and decrease both poleward and equatorward. In the month of December the vertical velocities are upward at F2 peak in the Northern Hemisphere, while above F2 peak the velocities are still downward.

The correlation coefficient between h_mF2 and the vertical transport velocity has been calculated. It is found that the value of the correlation coefficients are higher during the storm time than during the quiet hours. We suggest that the upward and downward motions play an important role in altering the F2 peak height as well as electron density changes in the different regions.

References

Abur-Robb, M.F.K. and D.W. Windle, 1969: On the day night reversal in N_mF2 north-south asymmetry. Planet. Space Sci., 17, 99-106.

Abur-Robb, M.F.K., 1969: Combined world-wide neutral air wind and electrodynamic drift effects on the F2-layer. Planet. Space Sci., 17, 1269-1279.

Akasofu, S.I., S. Chapman and C.I. Meng, 1965: The polar electrojet. J. Atmosph. Terr. Phys., 27, 1275-1305.

Appleton, E.V., 1935: The seasonal variation of ionization in region F2 of the ionosphere. Phys. Rev., 47, 704.

Appleton, E.V. and R. Naismith, 1935: Some further measurements of upper atmospheric ionization. Proc. Roy. Soc. A, 150, 685-780.

Appleton, E.V., 1946: Two anomalies in the ionosphere. Nature, 157, 681.

Appleton, E.V., 1953: The seasonal variation of ionization in region F2 of the ionosphere. Phys. Rev., 47, 704.

Appleton, E.V., 1954: The anomalous equatorial belt in the F2-layer. J. Atmosph. Terr. Phys., 5, 348-351.

Atkinson, G., 1966: A theory of polar substorms. J. Geophys. Res., 71, 5157-5164.

Axford, W.I., 1964: Viscous interaction between the solar wind and the earth's magnetosphere. Planet. Space Sci., 12, 45-53.

Axford, W.I., H.E. Petschek and G.L. Siscoe, 1965: The tail of the magnetosphere. J. Geophys. Res., 70, 1231-1236.

Axford, W.I., 1967: Aurora and Airglow, edited by B.M. McCormac, New York, Reinhold Publishing Co., pp 500.

Axford, W.I., 1968: The polar wind and the terrestrial helium budget. J. Geophys. Res., 73, 6855-6859.

Bailey, D.K., 1948: The geomagnetic nature of the F2-layer longitude-effect. Terr. Magn. Atmos. Elec., 53, 35-39.

Bame, S.J., J.R. Asbridge, H.E. Felthanser, E.W. Hones and I.B. Strong, 1967: Characteristics of the plasma sheet in the Earth's magnetotail. J. Geophys. Res., 72, 113-129.

Bands, P.M., and T.E. Holzer, 1968: The polar wind. J. Geophys. Res., 73, 6848-6854.

Baxter, R.G. and P.C. Kendall, 1965: Diffusion equilibrium of the topside electron density in the F2 region. J. Atmosph. Terr. Phys., 27, 129-132.

Baxter, R.G., 1967: A numerical solution of the time-varying diffusion equation for the F2-layer. Planet. Space Sci., 15, 701-713.

Baxter, R.G., and P.C. Kendall, 1968: A theoretical technique for evaluating the time-dependent effects of general electrodynamic drifts in the F2-layer of the ionosphere. Proc. Roy. Soc., A, 304, 171-185.

Becker, W., 1966: The seasonal anomaly of the F region at midlatitudes and its interpretation. In Electron Density Distribution in Ionosphere and Exosphere. Ed. by J. Frihagen, 218-230.

Belrose, J.S., 1965: Physics of the Earth's Upper Atmosphere. Ed. by C.O. Hines, Prentice-Hall, New Jersey, pp 88.

Bostrom, R., 1967: Aurora and airglow, edited by B.M. McCormac, New York, Reinhold Publishing Co., pp 297.

Bowen, P.J., R.L. Boyd, W.J. Raitt and A.P. Willmore, 1964: Ion composition of the upper F-region. Proc. Royal Soc., 281, 504-552.

Brace, L.H., B.M. Reddy, and H.G. Mayr, 1967: Global behavior of the ionosphere at 1000 km altitude. J. Geophy. Res., 72, 265-283.

Bramley, E.N. and M. Peart, 1965: Diffusion and electromagnetic drift in the equatorial F2 region. J. Atmosph. Terr. Phys., 27, 1201-1211.

Brown, W.E., W.R. Steiger and F.E. Roach, 1968: Maintenance of the tropical night-time F layer. Nature, 220, 559-560.

Calvert, W., 1966: Steep horizontal electron density gradients in the topside F-layer. J. Geophy. Res., 71, 3665-3669.

Carpenter, D.L., 1966: Whistler studies of the plasmapause in the magnetosphere. J. Geophy. Res., 71, 693-725.

Chandra, S. and R.A. Goldberg, 1964: Geomagnetic control of diffusion in the upper atmosphere. J. Geophys. Res., 69, 3187-3198.

Chapman, S. and T.G. Cowling, 1965: Math. theory of non-uniform gases, Cambridge Univ. Press.

Copsey, M.J., D. Smith and J. Sayers, 1966: Laboratory afterglow studies of O^+ ions in helium-oxygen and helium-oxygen-nitrogen mixtures. Planet. Space Sci., 14, 1047-1055.

Cospar International Reference Atmosphere (CIRA), 1965, North-Holland Publishing Co.-Amsterdam.

Crank, J. and P. Nicholson, 1947: A practical method for numerical integration of solution of partial differential equation of heat conduction type. Proc. Cambridge Philos. Soc., 43, 50.

Croom, S.A., A.R. Robbins, and J.O. Thomas, 1960: Variation of electron density in the ionosphere with magnetic dip. Nature, 185, 902-903.

Dalgarno, A. and F.J. Smith, 1962: The thermal conductivity and viscosity of atomic oxygen. Planet. Space Sci., 9, 1-2.

Dalgarno, A., 1965: Corpuscular bombardment and N_2 radiation Planet. Space Sci., 13, 1008-1009.

Davis, T.N. and M. Sugiura, 1966: Auroral electrojet activity index AE and its universal time variations. J. Geophy. Res., 71, 785-800.

Dessler, A.J., 1964: Length of magnetospheric tail. J. Geophys. Res., 69, 3913-3918.

Dessler, A.J., B.J. O'brien, 1965: Penetrating particle radiation, in Satellite Environment Handbook, second edition, edited by F.S. Johuson, pp 64, Stanford University press, Stanford, California.

Dessler, A.J. and F.C. Michel, 1966: Plasma in the geomagnetic tail. J. Geophy. Res., 71, 1421-1426.

Donahue, T.M., 1966: Ionospheric reaction rates in the height of recent measurements in the ionosphere and the laboratory. Planet. Space Sci., 14, 33-48.

Doupnik, J.R. and J.S. Nishbet, 1968: Fluctuations of electron density in the daytime F-region. J. Atmosph. Terr. Phys., 30, 931-961.

Duncan, R.A., 1960: The equatorial F region of the ionosphere. J. Atmos. Terr. Phys., 18, 89-100.

Duncan, R.A., 1962: Universal-time control of the arctic and antartic F-region. J. Geophy. Res., 67, 1823-1830.

Duncan, R.A., 1969: F-region seasonal and magnetic-storm behaviour. J. Atmosph. Terr. Phys., 31, 59-70.

Evans, J.V., 1967: Midlatitude F-region densities and temperatures at sunspot minimum. Planet. Space Sci., 15, 1387-1405.

Fehsenfeld, F.C., Schmeltakoph, A.L. and E.E. Ferguson, 1965: Some measured rates for oxygen and nitrogen ion molecule reactions of atmospheric importance, including $O^+ + N_2 \rightarrow NO^+ + N$. Planet. Space Sci., 13, 219-223.

French, A.G., 1966: Seasonal variation of some F-region parameters at sunspot minimum. J. Atmosph. Terr. Phys., 28, 9-16.

Geisler, J.E., 1966: Atmospheric winds in the middle latitude F region. J. Atmosph. Terr. Phys., 28, 703-720.

Geisler, J.E., 1967: A numerical study of the wind system in the middle thermosphere. J. Atmosph. Terr. Phys., 29, 1469-1482.

Gliddon, J.E.C. and P.C. Kendall, 1962: A mathematical model of the F-region. J. Atmosph. Terr. Phys., 24, 1073-1099.

Goldberg, R.A. and E.R. Schmerling, 1962: The distribution of electrons near the magnetic equator. J. Geophys. Res., 67, 3813-3816.

Goldbery, R.A., P.C. Kendall, and E.R. Schmerling. 1964: Geomagnetic control of the electron density in the F region of the ionosphere. J. Geophys. Res., 69, 417-428.

Goldberg, R.A., 1969: A review of the theories concerning the equatorial F2 region ionosphere. Proc. IEEE., 57, 1119-1126.

Hanson, W.B. and R.J. Moffet, 1966: Ionization transport effects in the equatorial F region. J. Geophys. Res., 71, 5559-5572.

Hanson, W.B. and I.B. Ortenburgen, 1961: The coupling between the protonophere and the normal F region. J. Geophy. Res., 66, 1425-1435.

Hess, W.N., 1965: Introduction to space science. pp 45, Gorden and Breach Science Publishers.

Hess, W.N., 1968: The radiation belt and magnetosphere. p. 37-41, Ginn Blaisdell Publishing Co.

Hines, C.O., 1964: Hydromagnetic motions the magnetosphere. Space Sci. Review. 3, No. 3, 342-379.

Hinteregger, H.E., L.A. Hall and G. Schmidtke, 1965: Solar EUV radiation and neutral particle distribution in July 1963 thermosphere. Space Res., V, 1175-1190, North-Holland Pub. Co.

Hoffman, J., 1969: The ion-mass spectrometer on Explorer XXXI satellite. Proc. IEEE., 57, 1063-1067.

Ivanov-Kholodny, G.S., 1965: Energy source to maintain night-time ionosphere. Space Res., V, 19-42.

Johson, F.S., 1964: Composition changes in the upper atmosphere. In Electron Density Distribution in Ionosphere and Exosphere, Edited by Thrane. 81-84, North-Holland Publishing Co.

Kaufman, A.N., 1960: Plasma transport theory in the theory of neutral and ionized gases. Ed. C. Dewitt and J.F.Deteouf, 293-253.

Keating, G.M. and J. Priou, 1967: Latitudinal and seasonal variations in atmospheric densities obtained during low solar activity by means of the inflatable air density satellite. Space Res., VII, 1119-1131.

Kellogg, W.W., 1961: Chemical heating above the polar mesopause in winter. J. Meteorology, 18, 373-381.

Kendall, P.C., 1962: Geomagnetic control of diffusion in the F2 region of the ionosphere-I. The form of the diffusion operator. J. Atmosph. Terr. Phys., 24, 805-811.

Kendall, P.C. and D.W. Windle, 1965: A possible explanation of the Appleton anomaly of the F2 layer; Dougherty's theory of ion drag. J. Atmosph. Terr. Phys., 27, 795-802.

Kendall, P.C. and D.W. Windle, 1968: Ion drag with electrodynamic drift; a computer experiment for the F2 layer. Geophys. J.R. Astr. Soc., 15, 147-156.

King, G.A.M., 1961: Analysis of the F1-F2 transition region. J. Geophys. Res., 66, 2757-2762.

King, G.A.M., 1964: The dissociation of oxygen and high level circulation in the atmosphere. J. Atmosph. Sci., 21, 231-237.

King, J.W., P.A. Smith, D. Eccles, G.F. Fooks and H. Heom, 1964: Preliminary investigation of the structure of the upper ionosphere as observed by the topside sounder satellite Alouette. Royal Soc. Proc., 281, 464-487.

King, J.W., and H. Kohl, 1965: Upper atmospheric winds and ionospheric drifts caused by neutral air pressure gradients. Nature, 206, 699-701.

King, J.W., W.S. Newman, 1967: Solar-terrestrial physics, edited by J.W. King and W.S. Newman, Academic press, London.

King, J.W., K.C. Reed, E.O. Olatunji and A.J. Legg, 1967: The behaviour of the topside ionosphere during storm bondition. J. Atmosph. Terr. Phys., 29, 1355-1363.

King, J.W., R. Pratt and W.S. Newman, 1968: Sporadic-E and the F2-layer at middle latitudes. J. Atmosph. Terr. Phys., 30, 463-476.

Kohl, H., 1966: The possible effect of diffusion between magnetically conjugate points on the seasonal anomaly of the F-layer, in Electron Density Distribution in Ionosphere and Exosphere, Edited by J. Frihagen, North-Holland Publishing Co., 231-238.

Kohl, H. and J.W. King, 1967: Atmospheric winds between 100 and 700 km and their effects on the ionosphere. J. Atmosph. Terr. Phys., 29, 1045-1062.

Linhart, J.G., 1961: Plasma physics, 2nd ed. North-Holland Publishing Co.-Amsterdam, pp 184.

Liszka, L., 1967: The high-latitude trough in ionospheric electron content. J. Atmosph. Terr. Phys., 29, 1243-1257.

Maeda, H., 1963: Worldwide pattern of ionization drifts in the ionospheric F region as deduced from geomagnetic variations. The Ionosphere. London: Inst. of Phys. and the Physical Soc., 187-190.

Mahoney, J.R., 1968: A numerical study of the variable structure of the lower thermosphere. Meteorological monographs., 9, No. 31, 90-97.

Martyn, D.F., 1953: Electric currents in the ionosphere, 3, Ionization drift due to winds and electric fields, Phil. Trans. Soc., London. A 246, 306-320.

Martyn, D.F., 1954: Theory of height and ionization density changes at the maximum of a Chapman-like region taking account of ions production, decay, diffusion and tidal drift. Physical Soc., London, Conference in the Physics of the ionosphere, pp 259.

Martyn, D.F., 1959: The normal F region of the ionosphere, Proc. I.R.E. 47, 147.

Mauersberger, K., D. Muller, D. Offermann and U.V. Zahn, 1968: A mass spectrometric determination of the neutral consituents in the lower thermosphere above Sardina. J. Geophs. Res., 73, 1071-1076.

Mayr, H.G., 1968: The plasmapause and its relation to the ion composition in the topside ionosphere. Planet. Space Sci., 16, 1045-1414.

Megill, L.R. and N.P. Carleton, 1964: Excitation by local electric fields in the aurora and airglow. J. Geophys. Res., 69, 101-122.

Mitra, S.K., 1946: Geomagnetic control of region F2 of the ionosphere. Nature, 158, 668-669.

Mitra, S.K., R. Narasinga and K.K. Mahajan, 1967: Determination of loss coefficient and vertical transport velocity in the ionosphere F-region. J. Atmosph. Terr. Phys., 29, 43-59.

Muldrew, D.B., 1965: F-layer ionization troughs deduced from Alouette data. J. Geophys. Res., 70, 2635-2650.

Nagata, T. and S. Kokubun, 1962: On the earth storm IV. Polar magnetic storms, with special reference to relation between geomagnetic disturbances in the Northern and Southern auroral zones. Rep. Ionos. Res., Japan, 6, 273-290.

Nelson, G.J., 1968: Total ionospheric electron content at middle latitudes during sunspot minimum. J. Atmosph. Terr. Phys., 30, 513-526.

Nergebauber, M. and C.W. Snyder, 1962: The mission of mariner II: Preliminary observations. Science, 138, 1095-1097.

Nishida, A., 1966: Formation of plasmapause, or magnetospheric plasma knee, by the combined action of magnetospheric convection and plasma escape from the tail. J. Geophys. Res., 71, 5669-5679.

Nishida, A., 1967: Average structure and storm-time change of the polar topside ionosphere at sunspot minimum. J. Geophys. Res., 72, 6051-6061.

Nishida, A., 1968: Geomagnetic DP2 fluctuations and associated magnetosphere phenomena. J. Geophys. Res., 73, 1795-1803.

Norton, R.B. and J.M. Warnoch, 1968: Seasonal variation of molecular oxygen near 100 km. J. Geophy. Res., 73, 5789-5800.

Obayschi, T. and A. Nishida, 1968: Large-scale electric field in the magnetosphere. Space Sci. Review, 8, 1-31.

O'Brien, B.J., 1964: Whistler studies of the plasmapause in the magnetosphere. J. Geoph. Res., 69, 13-43.

Peterson, V.L. and W.R. Steiger, 1966: F-region night glow emmissions of atomic oxygen. J. Geoph. Res., 71, 2256-2277.

Piddington, J.H., 1964: Ionospheric and magnetospheric anomalies and disturbance. Planet. Space Sci., 12, 553-566.

Power, C.F. and C.M. Rush, 1968: The ionization maximum in polar latitudes ionosphere. Ionospheric Radio Communication, Plenum press, 46-57.

Rao Narasinga, B.C., 1963: The postsunset rise of f_oF2 in the transition region and its dependence on the postsunset rise of h'F in the equatorial region. J. Geophys. Res., 68, 2551-2557.

Rasgogi, R.G., 1960: Abnormal features of F2 region of the ionosphere at some southern high latitude stations. J. Geoph. Res., 65, 585-592.

Ratcliffe, J.A., 1960: Physics of the Upper Atmosphere.Academic Press New York and London, pp 116.

Richtmyer, R.D., 1967: Difference methods for initial-value problem. 2nd edition, New York, Interscience Publishers. pp 206-208.

Rishbeth, H. and C.S.G.K. Setty, 1961: The F-layer at sunrise. J. Atmosph. Terr. Phys., 20, 263-276.

Rishbeth, H., 1967a: The effect of winds on the ionospheric F2-peak J. Atmosph. Terr. Phys., 29, 225-238.

Rishbeth, H., 1967b: A review of ionospheric F-region theory. Proc. IEEE., 55, 16-35.

Rishbeth, H., 1968a: On explaining the behavior of the ionospheric F region. Review of Geophys., 6, No. 1, 33-71.

Rishbeth, H., 1968b: The effect of winds on the ionospheric F2-peak-II. J. Atmosph. Terr. Phys., 30, 63-71.

Rothwell, P., 1963: Diffusion of ions between F layers at magnetic conjugate points., in procedings of the international conference on the ionosphere, 217-221, Institute of physics and physical Sco., London.

Sato, T. and G.F. Rourke, 1964: F-region enhancements in the Antarctic. J. Geoph. Res., 69, 4581-4608.

Sato, T., 1966: Night-time abnormal enhancement of ionospheric F2-region electron density in low and equatorial latitudes. Rep. of ionosphere and Space Res. Japan, 20, No. 2, 150-171.

Sato, T., 1968a: Abnormally large electron concentration in the ionosphere F2 region at summer-night in middle latitides. J. Geoph. Res., 73, 127-142.

Sato, T., 1968b: Electron concentration variations in the topside ionosphere between 60^oN and 60^oS geomagnetic latitude associated with geomagnetic disturbances. J. Geophy. Res., 73, 6225-6241.

Sharp, G.W., 1966: Midlatitude trough in the night ionosphere. J. Geoph. Res., 71, 1345-1356.

Shercliff, J.A., 1965: A textbook of Magnetohydrodynamics. 1st ed., Oxford, New York, Pergamon Press, pp 23.

Skinner, N.J., R.A. Brown and R.W. Wright, 1954: Multiple stratification of the F2-layer at Ibadan. J. Atmosph. Terr. Phys., 5, 92-100.

Smith, D. and R.A. Fouracre, 1968: The temperature dependence of the reaction rate coefficent of O ions with molecular oxygen and nitrogen. Planet. Space Sci., 16, 243-252.

Spitzer, L.Jr., 1962: Physics of fully ionized gases. 2nd ed. New York, Interscience Publishers, pp 146.

Strobel, D.F., 1968: On the ionospheric F2-layer and its maintenance at night by thermospheric winds. PH.D. thesis at Harvard Univ.

Stubbe, P., 1968: Frictional forces and collision frequences between moving ion and neutral gases. J. Atmosph. Terr. Phys., 30, 1965-1985.

Thomas, G.R. and F.H. Venables, 1967: The effect of diurnal temperatures changes on the F2-layer. J. Atmosph. Terr. Phys., 29, 621-640.

Thomas, J.O., 1964: The electron density distribution in the F2-layer of the ionosphere in winter. Electron Density Distribution in Ionosphere and Exosphere. Editored by Thrane, 226-242.

Thomas, L., 1963: Recent developments in the theory of the F-region Electron Density Distribution in Ionosphere and Exosphere. Editored by Thrane, 77-80.

Thompson, P.D., 1961: Numerical weather analysis and prediction. The Macmillan Co., New York.

Timleck, P.L. and G.L. Nelms, 1969: Electron densities less than 100 el/cm^3 in the topside ionosphere. Proc. IEEE., 57, 1164-1171.

Titheridge, J.E., 1968: The maintenance of the night ionosphere. J. Atmosph. Terr. Phys., 30, 1857-1875.

Valley, S.L., 1965: Handbook of Geophysics and Space Environments. Airforce Cambridge Research Laboratories.

Wright, J.W., 1960: A model of the F region above h_mF2. J. Geoph. Res., 65, 185-191.

Wright, J.W., 1964: Diurnal and seasonal variations of the atmosphere near the 100 km level. J. Geophy. Res., 69, 2851-2853.

Yeh, K.C. and H. Fritz, 1968: An investigation of F2 region ionospheric behavior by computer methods. Tech. Rep. No. 35, Dept. of Electrical Engineering, Univ. of Illinois.

Yonezawa, T., 1956: A new theory of formation of the F2 layer. J. Radio Res. Labs. (Japan) 3, 1.

Yonezawa, T., 1958: On the influence of electron-ion diffusion exerted upon the formation of the F2 layer. J. Radio Res. Labs. (Japan) 5, 165-187.

Yonezawa, T., 1965a: Theory of formation of the ionosphere. Space Sci., Review, 5, 3-56.

Yonezawa, T., 1965b: Maintenance of ionization in the night time F2 region. Space Res., V, 49-60.

APPENDIX

FINITE DIFFERENCE METHOD

1. Introduction

This note describes the finite difference method for solving equation of continuity which models the density of electrons in the ionosphere. Let the variables z, ϕ and t represent the altitude, latitude and time, respectively. Let N = N(z, ϕ, t) represent the electron density in the ionosphere. Then equation (3.4) can be expressed in the following form:

$$\frac{\partial N}{\partial t} = C_1(z,\phi,t)\frac{\partial^2 N}{\partial z^2} + C_2(z,\phi,t)\frac{\partial^2 N}{\partial z \partial \phi} + C_3(z,\phi,t)\frac{\partial^2 N}{\partial \phi^2} + C_4(z,\phi,t)\frac{\partial N}{\partial z} + C_5(z,\phi,t)\frac{\partial N}{\partial \phi} + C_6(z,\phi,t)N + C_7(z,\phi,t) \quad (1)$$

Where $z_1 < z < z_2$, $\phi_1 < \phi < \phi_2$ and $t > 0$.

(a) Boundary conditions

$$N(z_1,\phi,t) = N_1(\phi,t)$$
$$N(z_2,\phi,t) = N_2(\phi,t)$$
$$N(z,\phi_1,t) = N_3(z,t) \qquad \text{for} \quad t > 0$$
$$N(z,\phi_2,t) = N_4(z,t)$$

(b) Initial condition

$N(z,\phi,0) = N_0(z,\phi)$ for $z_1 \leq z \leq z_2$, $\phi_1 \leq \phi \leq \phi_2$

The boundary values, forcing term, and all the coefficients are periodic in nature with periods of 24 hours. The solution of N is also a periodic function.

2. Finite difference equation

We use implicit scheme (backward difference for $\frac{\partial N}{\partial t}$ and central difference of Crank-Nicolson method for other terms).

$$\frac{\partial N}{\partial t} = \frac{N^{n+1}(I,J) - N^{n}(I,J)}{\Delta t}$$

$$\frac{\partial N}{\partial z} = \frac{1}{4\Delta z}\left\{ N^{n+1}(I,J+1) - N^{n+1}(I,J-1) + N^{n}(I,J+1) - N^{n}(I,J-1) \right\}$$

$$\frac{\partial N}{\partial \phi} = \frac{1}{4\Delta \phi}\left\{ N^{n+1}(I+1,J) - N^{n+1}(I-1,J) + N^{n}(I+1,J) - N^{n}(I-1,J) \right\}$$

$$\frac{\partial^2 N}{\partial z^2} = \frac{1}{2(\Delta z)^2}\left\{ \left[N^{n+1}(I,J+1) - 2N^{n+1}(I,J) + N^{n+1}(I,J-1) \right] \left[N^{n}(I,J+1) - 2N^{n}(I,J) + N^{n}(I,J-1) \right] \right\} \tag{2}$$

$$\frac{\partial^2 N}{\partial \phi^2} = \frac{1}{2(\Delta \phi)^2}\left\{ \left[N^{n+1}(I+1,J) - 2N^{n+1}(I,J) + N^{n+1}(I-1,J) \right] \left[N^{n}(I+1,J) - 2N^{n}(I,J) + N^{n}(I-1,J) \right] \right\}$$

$$\frac{\partial^2 N}{\partial z \partial \phi} = \frac{1}{8\Delta z \Delta \phi}\left\{ N^{n+1}(I+1,J+1) - N^{n+1}(I-1,J+1) - N^{n+1}(I+1,J-1) + N^{n+1}(I-1,J-1) \right.$$

$$+ N^n(I+1, J+1) - N^n(I-1, J+1) - N^n(I+1, J-1) + N^n(I-1, J-1)\Big\}$$

Here

$t = n\Delta t \qquad n = 0,1,2,\ldots$

$\phi = i\Delta\phi \qquad i = 0,1,2,\ldots L$

$z = j\Delta z \qquad j = 0,1,2,\ldots M$

Substitute equation (2) into equation (1) and rearrange the terms in such a way that all N of time step n+1 are transported to the LHS and the other terms in the RHS.

Thus the equation of finite different scheme can be written as a system

$$M\, N_{i,j}^{n+1} = U\, N_{i,j}^{n} \qquad (3)$$

of linear equations, where M is a matrix.

The computer program solves this system of equation by using Gaussian elimination method which is an internal scientific subroutine stored in the IBM 360.

3. Locations of the grid points and the time interval

The subscripts i, j, n are used to denote the latitude, altitude and time mesh points respectively. We start numbering the grid points in the horizontal direction with i = 1 at 2.5 degrees away from the equator and i = 2 at 5° latitude, etc.; the last one i = L is at 87.5° latitude. Similarly, we number from the bottom boundary to the top boundary from J = 1 to M. The mesh intersection labeled i, j is ith from the equator and the jth from the bottom boundary. In the first calculation, the height interval Δz is 50 km, the latitide interval is 2.5° and the time increment is 15 minutes. The total number of mesh points in the meridional plane is 560. In the second calculation, Δz is reduced to 25 km, $\Delta\phi$ remains the same and Δt is 5 minutes. The mesh points are 1120. We also used $\Delta z = 50$ km, $\Delta\phi = 5^{\circ}$, and $\Delta t = 15$ minutes for the third calculation. The results calculated by using different mesh size were compared. It is found that the maximum difference between any two sets of results is less than 5%. Finally, we decided to use 560 mesh points in our entire calculations.

BIOGRAPHICAL NOTE

Mao-Fou Wu was born in Nanking, China on July 28th, 1932. He attended the Naval College of Technology in Taiwan in 1950, and obtained his B.S. degree with honor in December, 1955. After graduation, he served in the chinese Navy for seven years. He worked successively as an engineer at the Naval Shipyard (in Taiwan), as a surveyor at the Harbour Bureau (in Taiwan), and as an instructor at the Naval Post Graduate School. In 1963, he was awarded a fellowship for study at the University of Chicago where he gained his M.S. degree in 1965. Then he came to M.I.T. to pursue his advanced studies. He got married in December, 1966.